

# UC Irvine

## UC Irvine Electronic Theses and Dissertations

### Title

Multifunctional Cementitious Materials with Damage Tolerance and Self-Sensing Capacity for the Protection of Critical Infrastructure

### Permalink

<https://escholarship.org/uc/item/0dd2v2dn>

### Author

Li, Xiaopeng

### Publication Date

2018

Peer reviewed|Thesis/dissertation

UNIVERSITY OF CALIFORNIA,  
IRVINE

Multifunctional Cementitious Materials with Damage Tolerance and Self-Sensing Capacity for  
the Protection of Critical Infrastructure

DISSERTATION

submitted in partial satisfaction of the requirements  
for the degree of

DOCTOR OF PHILOSOPHY

in Civil Engineering

by

Xiaopeng Li

Dissertation Committee:  
Assistant Professor Mo Li, Chair  
Professor Lizhi Sun  
Associate Professor Farzin Zareian

2018



## **DEDICATION**

To

my parents Tingquan Li and Xiulan Liu,

and my wife Weiwei Wu

# TABLE OF CONTENTS

	Page
<b>LIST OF FIGURES</b> .....	viii
<b>LIST OF TABLES</b> .....	xviii
<b>ACKNOWLEDGMENTS</b> .....	xix
<b>CURRICULUM VITAE</b> .....	xxi
<b>ABSTRACT OF THE DISSERTATION</b> .....	xxiii
<b>CHAPTER 1: INTRODUCTION</b> .....	1
1.1 Background.....	1
1.2 Emerging Distributed Sensing Technologies for SHM.....	3
1.2.1 Fiber Optic Sensors .....	4
1.2.2 Digital Image Correlation .....	5
1.2.3 Wave propagation-based detection .....	5
1.2.4 X-ray or Gamma ray .....	8
1.3 Electrical Methods and Self-Sensing Cementitious Composites .....	9
1.4 Research Objectives and Dissertation Outline .....	13
<b>CHAPTER 2: UNDERSTANDING ELECTRICAL MICROSTRUCTURE AND RESPONSES OF CEMENTITIOUS MATERIALS</b> .....	18
2.1 Introduction .....	18
2.2 Basics of Electrochemical Impedance Spectroscopy .....	22
2.3 Experimental Methodology.....	24
2.3.1 EIS test setup.....	24
2.3.2 Materials.....	25
2.4 Results and Discussion .....	26
2.4.1 Effect of age .....	26
2.4.2 Effect of water/binder ratio .....	30
2.4.3 Effect of composites.....	32
2.5 Equivalent Circuit Model .....	41

2.6 Conclusions .....	46
<b>CHAPTER 3: MATERIAL DESIGN OF MULTIFUNCTIONAL STRAIN-HARDENING CEMENTITIOUS MATERIALS.....</b>	<b>48</b>
3.1 Introduction .....	48
3.2 Electrical Microstructure Design Guided by Electrical Impedance Spectroscopy.....	50
3.2.1 Initial mix design incorporating carbon black nanoparticles .....	50
3.2.2 Specimen preparation.....	52
3.2.3 Four-point electrical impedance spectroscopy .....	53
3.2.4 Effect of carbon black nanoparticles on electrical microstructure and parameters.....	54
3.3 Design for Tensile Strain-hardening Behavior with Improved Ductility Guided by Micromechanics-based Theory .....	61
3.3.1 Energy criterion.....	62
3.3.2 Strength criterion.....	62
3.3.3 Conditions for high-density multiple microcracking and large tensile ductility.....	64
3.3.4 Effect of carbon black nanoparticles on tensile behavior .....	65
3.3.5 Effect of carbon black nanoparticles on fiber-bridging behavior and matrix toughness .....	67
3.3.6 Material re-designs for improved tensile ductility and strength .....	72
3.4 Conclusions .....	75
<b>CHAPTER 4: MSC ELECTROMECHANICAL BEHAVIOR .....</b>	<b>77</b>
4.1 Introduction .....	77
4.2 Electromechanical Behavior of MSC .....	77
4.2.1 Electromechanical experiment details.....	77
4.2.2 Electromechanical response under cyclic tension and compression within elastic stage .....	80
4.2.3 Electromechanical response under monotonic tension up to material failure.....	84
4.2.4 Electromechanical response under cyclic loading beyond elastic stage .....	90
4.3 Effects of Temperature and Humidity on Electromechanical Behavior of MSC .....	93
4.4 Conclusions .....	99
<b>CHAPTER 5: EFFECTS OF DAMAGE AND HEALING ON THE IMPEDANCE OF MSCS - A MULTI-SCALE MODEL .....</b>	<b>102</b>
5.1 Introduction .....	102

5.2 The Multi-Scale Model.....	104
5.2.1 Model establishment .....	104
5.2.2 Bulk impedance.....	107
5.2.3 Model details.....	108
5.3 Experimental Validations .....	118
5.3.1 Validation test 1 .....	118
5.3.2 Validation test 2 .....	120
5.4 Results and Discussions: Validation Test 1.....	123
5.4.1 Single crack opening test results .....	123
5.4.2 Impedance ~ crack opening relation at single cracking scale .....	124
5.4.3 Impedance ~ strain relation at multiple cracking scale .....	127
5.4.4 Parameter study.....	130
5.5 Results and Discussions: Validation Test 2.....	132
5.5.1 Impedance ~ crack opening relation at single cracking scale .....	132
5.5.2 Impedance ~ strain relation at multiple cracking scale .....	134
5.5.3 Effect of crack self-healing .....	137
5.6 Conclusions .....	140
<b>CHAPTER 6: SPATIAL DAMAGE SENSING IN MSCS THROUGH TIME- DIFFERENCE ELECTRICAL IMPEDANCE TOMOGRAPHY .....</b>	<b>143</b>
6.1 Introduction .....	143
6.2 Electrical Impedance Tomography.....	146
6.3 Electrical Properties Characterization of Cementitious Materials .....	149
6.4 Parameter Study.....	151
6.5 Experimental Methodology .....	157
6.5.1 Materials and specimens .....	157
6.5.2 EIT measurement system .....	160
6.5.3 Mechanical test methodology .....	162
6.5.4 Finite element modeling.....	164
6.6 Results and Discussion .....	165
6.6.1 Validation of the EIS system.....	166
6.6.2 Damage sensing of 2D localized cracks.....	169
6.6.3 Damage sensing of 2D distributed cracks .....	176

6.6.4 Damage sensing of 3D crack in the beam specimen.....	182
6.7 Conclusions .....	201
<b>CHAPTER 7: SPATIAL DAMAGE SENSING IN MSCS THROUGH FREQUENCY-DIFFERENCE ELECTRICAL IMPEDANCE TOMOGRAPHY .....</b>	<b>203</b>
7.1 Introduction .....	203
7.2 Frequency-dependent Impedance of Cracking.....	205
7.2.1 Materials and specimens .....	206
7.2.2. Single crack opening test with impedance measurements .....	206
7.2.3 Frequency-dependent impedance.....	209
7.3 Frequency-difference EIT Test and Image Reconstructions .....	215
7.3.1 Frequency-difference EIT system for cementitious materials .....	215
7.3.2 Test methodology.....	217
7.4 Frequency-difference EIT Test and Image Reconstructions .....	219
7.5 Results and Discussions .....	220
7.5.1 Validation test .....	220
7.5.2 Damage sensing of the localized damage .....	223
7.5.3 Damage sensing of distributed damage.....	232
7.5.4 Damage sensing of beam specimen .....	249
7.6 Conclusions .....	258
<b>CHAPTER 8: CORROSION SENSING IN MSCS.....</b>	<b>261</b>
8.1 Introduction .....	261
8.2 Chemical Sensing: a feasibility study.....	263
8.3 Tracking Chloride Penetration.....	267
8.4 Spatial Corrosion Sensing Using EIT.....	274
8.4.1 Materials and test setup.....	274
8.4.2 Corrosion test results.....	279
8.4.3 EIT image reconstructions .....	285
8.5 Conclusions .....	289
<b>CHAPTER 9: CONCLUSIONS AND FUTURE RESEARCH.....</b>	<b>291</b>
9.1 Conclusions .....	291
9.2 Future Research .....	293



**References** ..... 295

## LIST OF FIGURES

	Page
Figure 1.1 A schematic outline of the major topics presented in this dissertation .....	15
Figure 2.1 Equivalent circuit model proposed by Mccarter et al. [175] .....	19
Figure 2.2 Equivalent circuit model proposed by Gu et al. [176-179] .....	20
Figure 2.3 Equivalent circuit model proposed by Song et al. [180, 181] .....	21
Figure 2.4 Illustration of test framework in this chapter .....	22
Figure 2.5 EIS setup: (a) EIS measurement circuit; (b) Test setup and specimen dimensions ....	25
Figure 2.6 Bode plot for C+W (0.21) .....	26
Figure 2.7 Bode plot for C+W (0.28) .....	27
Figure 2.8 Bode plot for C+W+S (0.21) .....	27
Figure 2.9 Bode plot for C+W+S (0.28) .....	27
Figure 2.10 Bode plot for C+W+F (0.28) .....	28
Figure 2.11 Bode plot for CB+C 1% .....	28
Figure 2.12 Bode plot for CB+C 4% .....	28
Figure 2.13 Bode plot for C+W+S+F .....	29
Figure 2.14 Bode plot for C+W+S+F+P .....	29
Figure 2.15 Bode plot for C+W+S+F+CB1% .....	29
Figure 2.16 Bode plots of C+W specimens with water/binder ratios of 0.21 and 0.28, at the age of (a) 7 days, (b) 14 days, (c) 21 days, (d) 28 days, and (e) 180 days .....	31
Figure 2.17 Bode plots of C+W+S specimens with water/binder ratios of 0.21 and 0.28, at the age of (a) 7 days, (b) 14 days, (c) 21 days, (d) 28 days, and (e) 180 days .....	32

Figure 2.18 Bode plots of C+W+S 0.21 specimens and C+W 0.21 specimens, at the age of: (a) 7 days, (b) 14 days, (c) 21 days, (d) 28 days, and (e) 180 days.....	34
Figure 2.19 Bode plots of C+W+S 0.28 specimens and C+W 0.28 specimens, at the age of: (a) 7 days, (b) 14 days, (c) 21 days, (d) 28 days, and (e) 180 days.....	35
Figure 2.20 Bode plots of C+W 0.28 specimens and C+W+F 0.28 specimens, at the age of: (a) 7 days, (b) 14 days, (c) 21 days, (d) 28 days, and (e) 180 days.....	36
Figure 2.21 Bode plots of C+W+S+F 0.28 specimens and C+W+F+S+P 0.28 specimens, at the age of (a) 14 days, (b) 21 days, (c) 28 days, (d) 42 days, (e) 63 days and (f) 180 days .....	37
Figure 2.22 Bode plot comparison for C+W specimen, CB+C 1% specimen, and CB+C 4% specimen. (a) 7day, (b) 14 day, (c) 21 day, (d) 28 day, and (f) 180 day.....	38
Figure 2.23 Evolution of impedance magnitude with age .....	39
Figure 2.24 Impedance magnitude comparisons of different designs at the age of 180 days .....	41
Figure 2.25 Equivalent circuit model.....	42
Figure 2.26 Typical Nyquist plot of a cementitious material .....	43
Figure 2.27 Typical Nyquist plot results of cementitious materials at the age of 180 days .....	43
Figure 2.28 Nyquist plot of (a) C+F+S+W+P and (b) C+F+S+W at different ages .....	44
Figure 2.29 Typical Nyquist plots of cementitious materials and corresponding model results. (a) C+W 0.21; (b) C+W 0.28; (c) C+W+S 0.28.....	45
Figure 2.30 Effects of material composition on continuous conductive path $R_1$ and partially conductive path $R_2$ at the age of 180 days .....	46
Figure 3.1 The concept of MSCs: (a) cementitious matrix with conductive particles. (b) elastic strain sensing. (c) nonlinear strain sensing.....	49
Figure 3.2 EIS specimen details.....	53
Figure 3.3 EDS mapping of carbon black distribution in a cementitious matrix. (a) EDS element map of carbon black, (b) Binary image of carbon black distribution .....	55

Figure 3.4 Complex Nyquist plots and equivalent circuit modeling results of cementitious composite materials with (a) 0%, (b) 2.5%, (c) 5%, and (d) 10% carbon black nanoparticles ....	57
Figure 3.5 Effect of carbon black nanoparticles on equivalent circuit model parameters: (a) resistance $R_1$ , (b) resistance $R_2$ , (c) capacitance $C_2$ , and (d) capacitance $C_1$ .....	59
Figure 3.6 Typical crack bridging stress $\sim$ crack opening relation $\sigma(\delta)$ for tensile strain-hardening composite .....	63
Figure 3.7 Uniaxial tension test setup.....	66
Figure 3.8 Effect of carbon black nanoparticles on the tensile stress-strain relation of the cementitious composite material.....	66
Figure 3.9 Single crack opening test: (a) specimen details, (b) test setup .....	67
Figure 3.10 Matrix fracture toughness test. The cementitious matrix does not contain any fibers .....	69
Figure 3.11 Fiber bridging stress vs. crack opening ( $\sigma \sim \delta$ ) relation: (a) effect of carbon black nanoparticles, (b) initial and redesign with 2.5% CB, (c) initial and redesign with 5% CB, (d) initial and redesign with 10% CB .....	70
Figure 3.12 Effect of carbon black nanoparticles on cementitious matrix fracture toughness ( $K_m$ ) for both initial design and re-design .....	71
Figure 3.13 Tensile stress-strain relations of redesign.....	74
Figure 3.14 Crack distribution in 5% MSC .....	74
Figure 4.1 Electromechanical test under uniaxial tension .....	78
Figure 4.2 Electromechanical test under uniaxial compression.....	79
Figure 4.3 Electromechanical behavior of (a) 0% SHC, (b) 2.5% MSC, (c) 5% MSC and (d) 10% MSC during elastic stage under cyclic uniaxial tension .....	80
Figure 4.4 Electromechanical behavior of (a) 0% SHC, (b) 2.5% MSC, (c) 5% MSC and (d) 10% MSC during elastic stage under cyclic uniaxial compression .....	83

Figure 4.5 Electromechanical behavior of (a) 0% SHC, (b) 2.5% MSC, (c) 5% MSC and (d) 10% MSC during elastic, strain-hardening and tension softening stages up to failure. $ Z $ is impedance magnitude, $Z_r$ stands for real part of the impedance, and $ Z_m $ stands for absolute value of imaginary part of the impedance.....	85
Figure 4.6 Equivalent circuit model of the material-crack system .....	86
Figure 4.7 Microscopy of a pulled-out fiber after testing.....	89
Figure 4.8 Electromechanical behavior of (a) 0% SHC, (b) 2.5% MSC, (c) 5% MSC and (d) 10% MSC under reversed cyclic loading.....	92
Figure 4.9 The change of average impedance magnitude in terms of measurement time.....	94
Figure 4.10 Desiccator with 6 chambers.....	95
Figure 4.11 Impedance magnitude of 5% MSC under different relative humidity conditions.....	96
Figure 4.12 Gage factor corresponding to different relative humidity levels.....	97
Figure 4.13 Instron temperature chamber .....	98
Figure 4.14 Change in impedance magnitude corresponding to varying temperature .....	99
Figure 5.1 Overview of the model: (a) specimen before crack; (b) a single crack; (c) multiple cracks .....	105
Figure 5.2 Equivalent circuit model of the bulk material .....	107
Figure 5.3 A short fiber embedded in the MSC material.....	108
Figure 5.4 Determination of contact resistance $R_{f\text{-contact}}$ between the fiber and matrix.....	109
Figure 5.5 Determination of $Z_{f\text{-total}}$ .....	113
Figure 5.6 Plot of single crack opening v.s. single crack tensile stress, and corresponding single fiber pull-out stress-strain relations .....	113
Figure 5.7 Algorithm to determine the ratio of fibers fully pulled out or ruptured .....	115
Figure 5.8 Single cracking equivalent circuit model .....	116

Figure 5.9 Single crack opening test: (a) specimen geometry, and (b) test setup.....	119
Figure 5.10 Uniaxial tension test: (a) test setup; (b) specimen details .....	119
Figure 5.11 Single crack opening behavior ( $\sigma \sim \delta$ relation) of SHC. EIS was performed at different crack opening values as marked on the curve .....	122
Figure 5.12 Tensile stress-strain curve ( $\sigma \sim \varepsilon$ relation) and multiple microcracking behavior of SHC. EIS was performed at different strain values as marked, corresponding to different damage levels within SHC .....	122
Figure 5.13 Single crack stress v.s. crack opening relations .....	123
Figure 5.14 The ratio of bridging fibers calculated based on single crack opening test results. (a) 0% SHC. (b) 5% MSC .....	124
Figure 5.15 Relations of impedance change v.s. crack opening of 0% SHC: (a) Impedance magnitude; (b) Phase degree .....	125
Figure 5.16 Relations of impedance change v.s. crack opening of 5% MSC: (a) Impedance magnitude; (b) phase degree .....	126
Figure 5.17 Tensile stress-strain relation and average crack width of 0% SHC.....	128
Figure 5.18 Relation of tensile strain vs. impedance magnitude .....	128
Figure 5.19 Relation of tensile strain v.s. impedance magnitude .....	129
Figure 5.20 Relation of tensile strain vs. impedance: (a) impedance magnitude; (b) phase degree .....	130
Figure 5.21 Parameter study of the model (a) cracking relative permittivity; (b) fiber-matrix contact resistivity; (c) initial fiber number.....	131
Figure 5.22 EIS Nyquist plots of 0% SHC at different crack openings .....	132
Figure 5.23 Effects of single crack opening on $R_c$ and $Q_c$ .....	134
Figure 5.24 EIS Nyquist plots of SHC at different tensile strain levels .....	134
Figure 5.25 Effect of tensile strain on statistical distribution of crack width .....	135

Figure 5.26 Effects of tensile strain on (a) impedance magnitude and (b) phase angle at different AC frequencies.....	136
Figure 5.27 Optical microscopy and SEM images of self-healing phenomenon in SHC.....	137
Figure 5.28 EIS Nyquist plots of SHC before loading, after preloading to 2% tensile strain, during self-healing. ....	138
Figure 5.29 Effect of self-healing on statistical distribution of crack width .....	139
Figure 5.30 Effects of self-healing on (a) impedance magnitude and (b) phase angle at different AC frequencies.....	140
Figure 6.1 Electrical Impedance response of the normal cementitious material. (a) impedance magnitude; (b) phase degree .....	150
Figure 6.2 Relationship between signal-to-noise ratio and impedance magnitude .....	150
Figure 6.3 Finite element mesh.....	151
Figure 6.4 Comparisons of image reconstructions in terms of signal-to-noise ratio and element number .....	153
Figure 6.5 Comparisons of image reconstructions in terms of the signal-to-noise ratio and the electrode number.....	154
Figure 6.6 Comparisons of image reconstructions in terms of the signal-to-noise ratio and the impedance magnitude level.....	155
Figure 6.7 Comparisons of image reconstructions in terms of the signal-to-noise ratio and the uniformity variation .....	156
Figure 6.9 Procedures to apply silver paste and copper electrodes .....	158
Figure 6.10 Beam specimen with 24 electrodes on one single side: (a) beam specimen illustration; (b) electrode setup; (c) one beam specimen .....	159
Figure 6.11 Electrical Impedance Tomography test setup.....	160
Figure 6.12 Design of switch matrix.....	160

Figure 6.13 Uniaxial tensile test setup.....	162
Figure 6.14 Beam specimen under four-point bending test: (a) test setup and dimension; (b) crack in the mid-span of the beam .....	163
Figure 6.15 Finite element model of (a) coupon specimen with 32 electrodes; (b) beam specimen with 24 electrodes; (c) panel specimen with 16 electrodes.....	164
Figure 6.16 Image reconstructions of square panel specimen (a) square specimen with 16 electrodes; (b) damage in the middle of the specimen; (c) image reconstruction .....	166
Figure 6.17 Damage within a specimen of N1 .....	167
Figure 6.18 Electrical impedance tomography image reconstructions of (a) N1 and (b) C1 .....	168
Figure 6.19 Image reconstructions of coupon specimen N2 with a localized crack.....	173
Figure 6.20 Image reconstructions of coupon specimen C2 with a localized crack.....	175
Figure 6.21 Specimens with distributed cracks and processed images: (a) N1; (b) C1.....	177
Figure 6.22 Image reconstructions of coupon specimen N1 with distributed cracks .....	179
Figure 6.23 Image reconstructions of coupon specimen C1 with distributed cracks .....	181
Figure 6.24 Relation of fixture extension and load.....	183
Figure 6.25 Crack details of N2 beam .....	184
Figure 6.26 Image reconstructions of the coupon specimen (C2) with a single crack .....	192
Figure 6.27 3D slice of the beam (Image reconstruction based on impedance magnitude at 1 Hz) .....	193
Figure 6.28 Crack details of C2 beam .....	193
Figure 6.29 Image reconstructions of the coupon specimen (C2) with a single crack .....	200
Figure 6.30. 3D slice of the image reconstructions showing crack location and depth.....	201
Figure 7.1 Single crack opening test on C1 with four-probe impedance measurement: (a) test setup; (b) DIC results showed crack opening .....	206



Figure 7.2 Single crack opening behavior ( $\sigma \sim \delta$ relation) of C1. EIS was performed at different crack opening values as marked on the curve.....	208
Figure 7.3 High-resolution images of a single crack opening .....	209
Figure 7.4 Frequency-dependent behaviors of the impedance with crack opening increases: (a) impedance magnitude; (b) real part of impedance; (c) imaginary part of impedance .....	212
Figure 7.5 Frequency-dependent real part of impedances measured with crack openings of 0.00 mm and 0.85 mm .....	213
Figure 7.6 The change parameter ( $\xi$ ) of different crack openings at different frequencies: (a) impedance magnitude; (b) real part; (c) imaginary part .....	214
Figure 7.7 Frequency-difference Electrical Impedance Tomography test setup in this study....	215
Figure 7.8 Electrode setup on the coupon specimen.....	215
Figure 7.9 Measured frequency-dependent impedance data based on established EIT system: (a) real part of impedance; (b) imaginary part of impedance.....	216
Figure 7.10 Beam specimen with 27 electrodes on one single side.....	216
Figure 7.11 Uniaxial tensile test setup.....	218
Figure 7.12 Flexure test setup.....	218
Figure 7.13 Image reconstructions reflected damage in the middle of the specimen.....	221
Figure 7.14 Image reconstructions reflected water presence.....	222
Figure 7.15 Localized damage in the coupon specimen.....	223
Figure 7.16 Image reconstructions for damage detection of localized damage.....	230
Figure 7.17 Distributed damage in the coupon specimen.....	232
Figure 7.18 Image reconstructions for detection of distributed damage .....	240
Figure 7.19 Distributed damage in the coupon specimen.....	241
Figure 7.20 Image reconstructions for detection of distributed damage .....	248

Figure 7.21 localized damage in the beam specimen .....	249
Figure 7.22 Image reconstructions of beam based on frequency-difference EIT .....	256
Figure 7.23 Image reconstructions for damage depth detection .....	257
Figure 8.1 Comparisons of image reconstructions in terms of damage detection .....	262
Figure 8.2 Chemical sensing test setup: (a) before dropping the liquid; (b) after dropping the water and 5% NaCl solution .....	265
Figure 8.3 FEM model for image reconstruction.....	267
Figure 8.4 Image reconstruction for chemical sensing .....	267
Figure 8.5 Chloride penetration monitoring using EIT technology.....	268
Figure 8.6 Chloride penetration monitoring using EIT .....	269
Figure 8.7 Specimen details and electrode setup .....	270
Figure 8.8 FEM model for image reconstructions .....	271
Figure 8.9 Image reconstructions for (a) 5% MSC (b) concrete.....	273
Figure 8.10 Accelerated corrosion test setup: (a) corrosion test up details; (b) overview of the corrosion test setup .....	275
Figure 8.11 Specimen details and electrode setup: (a) specimen details; (b) specimen with copper electrodes; (c) specimen with alligator clips.....	277
Figure 8.12 EIT test setup.....	277
Figure 8.13 Current injection and voltage measurement pattern.....	278
Figure 8.14 Change of current in terms of time for different specimens.....	279
Figure 8.15 0% SHC at different corrosion stage. (a) during accelerated corrosion test; (b) one month under non-accelerated corrosion.....	280
Figure 8.16 5% MSC at different corrosion stage. (a) during accelerated corrosion test; (b) one month under non-accelerated corrosion.....	281

Figure 8.17 0% Mortar at different corrosion stage. (a) during accelerated corrosion test; (b) one month under non-accelerated corrosion.....	282
Figure 8.18 5% Mortar at different corrosion stage. (a) during accelerated corrosion test; (b) one month under non-accelerated corrosion.....	283
Figure 8.19 FEM model used for image reconstructions.....	285
Figure 8.20 Image reconstructions for corrosion sensing of 5% Mortar .....	286
Figure 8.21 Image reconstructions for corrosion sensing of 5% MSC.....	287

## LIST OF TABLES

	Page
Table 1.1 NDT test methods for structural health monitoring.....	3
Table 2.1 Design of tested specimens.....	26
Table 3.1 Mix designs investigated in this study.....	51
Table 4.1. Gage factors and signal-to-noise ratios during elastic stage.....	82
Table 4.2 Relative humidity and desiccants .....	95
Table 5.1 Mixing proportion of SHC in Validation test 2 .....	121
Table 5.2 Exponent parameter $\lambda$ in terms of crack opening .....	126
Table 6.1 Parameters considered in this study.....	151
Table 6.2 Material design in this chapter.....	158
Table 8.1 Mix design .....	274

## ACKNOWLEDGMENTS

First of all, I would like to express my deepest gratitude to my advisor, Professor Mo Li, for her enthusiasm, inspiration, encouragement, financial support, and guidance. She is a teacher, a friend, an inspiration, and a role model for me. I really appreciate that she gave me the opportunity to pursue Ph.D. study in University of Houston and University of California, Irvine. She opened my eyes to beauties of research, and convincingly conveyed a spirit of curiosity and creativity with regard to research and scholarship. Without her able guidance, this work could not have been completed. I shall eternally be grateful to her for her mentorship.

Furthermore, my utmost gratitude is given to my Ph.D. dissertation committee members, Professor Lizhi Sun and Professor Farzin Zareian for their support during the course of my study and for evaluation of my research work. Their suggestions are critically important to complete this dissertation. I also would like to thank Professor Anne Lemnitzer and Professor Lorenzo Valdevit for serving on my Ph.D. qualifying exam committee, and for their constructive comments.

A note of thanks goes to my great friends in University of Houston and University of California, Irvine, Dr. Prakash Bhat, Dr. Shuai Fan, Ing Lim, Yun-Chen Wu, Mengyang Jiang, Dongxu Liu, Jingming Cai, Chang Wu, Dr. Guang Yang, Dr. Cheng Shi, and Dr. Botong Zheng for making this working experience inspirational and joyful. I am very grateful for my HCC Mandarin Student Christian Fellowship. Especially, I would like to thank Gary Ge, Betty Wu, Zhihong Huang, Hua Lin, Yaohui Lu, Bing Tian, Chuan Luo, Bing Lv, Shuishui Feng, Huirong Zhu, and Jian Wu for their support.

I am forever grateful for my parents (Tingquan Li and Xiulan Liu), my brother (Zhihong Li), and my sister in law (Liyang Yao) for their conditional love and support. My wife, Weiwei Wu, is my source of strength. Weiwei has been extremely supportive of me throughout this entire Ph.D. study and has made countless sacrifices to help me. I also would like to thank my children Daniel and Enoch who never let things get dull or boring.

The research is performed using funding received from U.S. Department of Energy, Office of Nuclear Energy's Nuclear Energy University Program, under Contract Number DE-AC07-05ID14517 Standard Research # 168284.

# CURRICULUM VITAE

**Xiaopeng Li**

## EDUCATION

- 2018            Doctor of Philosophy in Civil Engineering, University of California, Irvine
- 2012            Master of Science in Transportation Engineering, Shandong University, China
- 2009            Bachelor of Science in Structural Engineering, Shandong University, China

## FIELD OF STUDY

Multifunctional concrete materials and structures, damage sensing, structural health monitoring

## PUBLICATIONS

### Published

- [1] Fan, S., Li, X., & Li, M. (2018). The effects of damage and self-healing on impedance spectroscopy of strain-hardening cementitious materials. *Cement and Concrete Research*, 106, 77-90.
- [2] Li, X., Li, M., & Song, G. (2015). Energy-dissipating and self-repairing SMA-ECC composite material system. *Smart Materials and Structures*, 24(2), 025024.
- [3] Li, X., & Li, M. Effect of cracking and fracture on the electromechanical response of HPCFRCC. *9th International Conference on Fracture Mechanics of Concrete and Concrete Structures*, 2016.

### Submitted

- [4] Li, X., & Li, M. Multifunctional cementitious materials with damage tolerance and self-sensing functionality. *Cement and Concrete Research*, in review, 2018.
- [5] Li, X., & Li, M. A novel frequency-difference impedance tomography method for distributed damage sensing in cement-based materials. *Cement and Concrete Research*, in review, 2018.

- [6] Li, X., & Li, M. Cyclic behavior and constitutive modeling of shape memory alloy reinforced Engineered Cementitious Composites. *Smart Materials and Structures*, in review, 2018.

In Preparation

- [7] Li, X., & Li, M. Electrical Impedance Tomography for cracking sensing in cementitious materials. In preparation, 2018.
- [8] Li, X., & Li, M. A multi-scale electro-mechanical model for Multifunctional Cementitious Materials. In preparation, 2018.
- [9] Li, X., & Li, M. Effect of carbon-based nanomaterials on the electrical and mechanical properties of cementitious materials. In preparation, 2018.



# **ABSTRACT OF THE DISSERTATION**

Multifunctional Cementitious Materials with Damage Tolerance and Self-Sensing Capacity for  
the Protection of Critical Infrastructure

by

Xiaopeng Li

Doctor of Philosophy in Civil Engineering

University of California, Irvine, 2018

Professor Mo Li, Chair

Early detection of damage in concrete infrastructure is critical to prolonging structural service life through timely maintenance, ensuring safety and preventing failure. Current management practices rely on regular visual inspections, which can be subjective and limited to accessible locations. In the field of structural health monitoring (SHM), the key limitations are: (1) Indirect damage sensing, which requires complex\_physics-based models and algorithms to correlate structural response measurements to damage state; (2) Point-based sensors, such as strain gages or accelerometers, cannot accurately identify spatially distributed damage such as cracking and corrosion. To address the limitations, distributed sensing methods have been explored, such as ultrasonic guided waves and acoustic emission. These methods require expensive instrumentation, intricate network of sensors, and suffer from data contamination due to background noise and secondary sources. Most importantly, they are significantly more difficult to apply to concrete structures than steel structures. Therefore, distributed sensing method that can provide the spatial resolution to localize and quantify the severity of concrete infrastructure deterioration and damage is urgently needed.

In lieu of reliance on point-based sensors, this dissertation develops a *distributed, direct* damage and strain sensing approach based on novel multifunctional strain-hardening and self-sensing cementitious materials (MSCs). In this work, multifunctional cementitious materials are encoded with damage tolerance and spatial self-sensing capacity. The sequential formation of steady-state microcracks, rather than localized cracking, enables a prolonged and intrinsically controlled damage process, while allowing detection of microcracking damage level in the material long before failure occurs. The beauty of multifunctional concrete materials is two-fold: First, it serves as a major structural material component for infrastructure systems with greatly improved resistance to deterioration under service loading conditions, and to fracture failure under extreme events compared to conventional concrete. Second, it offers capacity for distributed and direct sensing of cracking and straining, while eliminating the need for sensor installation and maintenance.

The dissertation research is driven by two central hypotheses: (I) Cementitious materials exhibit an AC frequency-dependent electrical response, which would depend on its heterogeneous microstructure. Mechanical straining and damage process would lead to a change in the microstructure, thus affecting the frequency-dependent electrical response. A strong, high signal-to-noise coupling between cementitious material electrical response and mechanical behavior at different length scales would enable a self-sensing functionality during elastic and post-cracking stages; (II) Using electrical stimulation and advanced tomography methods, spatial mapping offering a visual depiction of concrete damage and deterioration can be gained. Spatial sensing of damage location and level inside a structural element can be achieved through electrical probing only from the boundaries.

This dissertation generates new understandings on how the composition and microstructure affect the frequency-dependent electrical response of cementitious materials. 4-point AC impedance spectroscopy is integrated with equivalent circuit modeling analysis to reveal the electrical microstructures and properties of cementitious materials, and their interfaces with electrodes. The work also elucidates whether and how cracking and healing (as a reversed damage process) lead to changes in material electrical response. An idealized model circuit is formulated to predict the frequency-dependent electrical behavior of cementitious composite materials at various cracking and healing levels. The model is tested and validated through a series of experimental measurements. Analyzing the changes of model parameters due to material composition, mechanical strain, and damage processes reveal the mechanisms that contribute to the overall electromechanical response of cementitious materials.

This dissertation develops novel multifunctional cementitious composite materials that integrate self-sensing functionality with a pseudo-strain-hardening behavior accompanied by multiple steady-state microcracking process. The macroscopic electro-mechanical properties, which are strongly coupled through high signal-to-noise ratios, are achieved by tailoring the material electrical microstructure as well as micromechanical parameters. Through experimental investigation, the dissertation reveals the material strain sensing behavior at elastic, pseudo-strain-hardening, and tension softening stages under various loading scenarios and environmental conditions. In addition, a modeling framework is established to link length scales from single fiber/matrix interfacial electromechanical behavior, to a single crack bridged by numerous fibers with statistically random embedment lengths and orientation, and to multiple cracking process and final localized failure. The analytical model couples micromechanics theory with equivalent

circuit model, to bring mechanistic insights into the material electromechanical response as the basis for self-sensing.

Furthermore, this dissertation realizes spatial sensing and visual depiction of damage through combining with advanced electrical impedance tomography (EIT) methods. It establishes two EIT methods that are suitable for solid heterogeneous concrete elements: time-difference EIT and frequency-difference EIT. It evaluates different variables, e.g., material type, real or imaginary parts of impedance, probing frequency, and finite element algorithm, on the effectiveness of EIT methods and image reconstruction. Impedance reconstruction is an ill-posed inverse problem. Finite element models that describe the forward problem are implemented, and the inverse solution is solved using regularized least square analysis. This work makes it possible to spatially visualize impedance and damage distribution within multifunctional cementitious elements upon voltage measurements collected from probe locations at element boundaries. It demonstrates the effectiveness of the EIT methods using 2D (plate) and 3D (beam) specimens with different levels of cracking damage. Finally, the EIT methods are further extended for corrosion sensing in reinforced concrete specimens.

# CHAPTER 1: INTRODUCTION

## 1.1 Background

Civil infrastructure such as buildings, bridges, roadways, and pipelines, are critical to providing residency, operations, mobility, clean water, and other elements essential to every citizen's quality of life. While the importance of infrastructure to national prosperity is clear, its level of disrepair is alarming. The American Society of Civil Engineer's 2017 Report Card for America's Infrastructure assigned a national grade of "D+" to US infrastructure with a total investment of \$4.6 trillion needed for repairs [1-4]. In addition to direct repair costs borne by government agencies and owners, user costs such as \$160 billion annual burden on US drivers for wasted time and fuel further emphasize the need for improved infrastructure [5-8]. The environmental impact is also vast: the cement industry is responsible for 5-8 % of total worldwide man-made CO<sub>2</sub> generation [9-12], roughly the CO<sub>2</sub> equivalent of 305 million automobiles. Although standardized building codes and design methodologies are adopted to ensure the safety and reliability of reinforced concrete structures, deterioration cannot be avoided once they are built and used [13-16]. While the current problems facing the aging American infrastructure are overwhelming, they only look to get worse into the future. To compound the problem, the economic resources available to maintain our infrastructure are shrinking at an alarming rate [17, 18].

Underlying this problem is the limitation of concrete material and the current health monitoring method. Concrete is inherently quasi-brittle, with a low fracture energy on the order of 0.1 kJ/m<sup>2</sup> [19]. Consequently, it is highly susceptible to cracking and fracture failure under combined mechanical loads and environmental effects. Cracking causes local distress, and

greatly impairs the transport properties of concrete, leading to other common deterioration mechanisms such as embedded steel corrosion [20]. Therefore, early detection of strain and cracking in concrete is critical in minimizing maintenance costs, prolonging structure service life, ensuring safety, and preventing failure [21-26].

Current management practices rely on regular visual inspections. Although visual inspections can be aided by a number of tools, such as telescopes, borescopes, magnifying lenses, real-time videos, cameras, rulers, measuring tapes, crack width gauges, light hammers, etc., they are still subjective and limited to accessible locations [27]. For example, the tap method can be used on the concrete. If the hammer is struck on good concrete, a ringing sound is heard. If cracks occur, the striking of the hammer produces a drum-like sound. However, determining the sound is subjective and this type of method cannot detect deep defects in the structural member.

A new paradigm, structural health monitoring (SHM), was proposed to objectively evaluate the structural health condition and to essentially reduce the economic burden of maintaining the inventory of aging and damaged structures. In recent years, great technological advances have been made in the field of structural health monitoring. The state of the art is the cabled and wireless structural health monitoring system, which employs a variety of point-based-sensors, namely accelerometers, strain gages, linear voltage displacement transducers (LVDT), etc., connected to a centralized data repository [28]. However, there remain few implementations of SHM systems in operational structures. The key limitations of SHM systems are [21, 28-30]: (1) Indirect damage sensing: the sensors generally do not directly detect damage. Rather, the sensors make measurements of structural response such as strain or displacement. Physics-based models are required to correlate structural response measurements to damage

state. Given the many complexities inherent to this inverse problem, robust algorithms that can pinpoint and quantify damage remain elusive [31-33]. (2) Point-based sensors: Commonly used sensors such as strain gages and accelerators are point-based, which cannot accurately identify spatially distributed damage such as cracking and corrosion. A dense network of point-based sensors is thus necessary for analytical models to extrapolate the point measurements to predicted component behavior [34, 35], but they are highly costly.

## 1.2 Emerging Distributed Sensing Technologies for SHM

To address the limitations of current SHM systems, researchers have begun to explore distributed sensing methods, such as Fiber Optic Sensors (FOS), Digital Image Correlations (DIC), wave propagation-based detection methods, X-ray or Gamma-ray, etc. Distributed sensing methods provide sensing functionalities of one certain region (area, line, or volume) in the structure, instead of one point. A brief overview of these technologies is presented. Undoubtedly, each of these sensor technologies has improved the state of the art in SHM. Table 1.1 summarizes the advantages and disadvantages of the distributed sensing methods.

Table 1.1 NDT test methods for structural health monitoring

Inspection method	Parameters measured	Advantages	Disadvantages	Cost
Visual inspection	Surface condition	Quick	Superficial; subjective	Low
Fiber Optic Sensor	Optical frequency domain reflectometry, wavelength	Light, small, distributed sensing	Limited distributed sensing (point based)	Moderate
Passive wave propagation	Wave mode	Collects damage event occurrence	Does not give quantitative information; easy to be contaminated by environmental noise	Moderate

Active wave propagation	Signal attenuation	Quantitative results are available	Lack of consensus on how to define attenuation	Moderate
X-ray and gamma-ray	Radiation of X-ray and gamma-ray	Easy to interpret data; Visual images	It needs to have access to both sides of a structure	High
Electrical method	Relative conductivity	Quick; gives relative conductivities over a large area	Low signal-to-noise ratio when conductivity is low.	Low

### *1.2.1 Fiber Optic Sensors*

Optical fibers were first proposed in the 1960s as the light wave guiding media and have been explosively developed since 1980s. Fiber Optical Sensor [36-38] can be defined as a means through which a measurement interacts with light guided in an optical fiber or guided to an interaction region by an optical fiber to produce an optical signal related to the parameter of interest. Compared with traditional sensors, FOSs have inherent advantages, such as high sensitivity, remote sensing, small size, light weight, wide bandwidth, electromagnetic immunity, etc. Also, an optical fiber communication network allows the user to carry out measurements at different points along the transmission line. This provides a method to collect information distributionally over an extended length. Various applications in SHM using FOSs have been investigated [39, 40]. FOSs can be applied to conduct different measurements, such as the temperature of the environment [41], the local strain of a structure, moisture and humidity of an area [42]. Due to evident advantages compared with traditional sensors, fiber optic sensors have been widely utilized in SHM systems [38, 43-45].

While the advantages are evident, it is still challenging to attain two-dimensional or three-dimensional distributed sensing. Although FOS can be theoretically used for distributed



sensing along the line, the number of sensors on one cable is limited to as few as four due to limitations of usable frequency range [46].

### *1.2.2 Digital Image Correlation*

DIC is an optical non-contact 2D and 3D surface deformation measurement technique. It captures sets of high-resolution images before and after deformation of an object to represent different non-deformed and deformed stages. DIC system captures images from high-resolution cameras and digitizes the images to grayscale. The displacement of a regular grid of points on the specimen surface based on the grayscale images was calculated. DIC has been utilized on reinforced concrete structures for decades. Corr et al. [47] validated the feasibility of using DIC technique to precisely determine the bond constitutive laws. Alam et al. [48], Kozicki et al. [49], and Shah et al. [50] utilized DIC technology to observe the fracture behaviors of reinforced concrete composites and measure crack openings. Gencturk et al. [51] utilized DIC technique for full-scale testing of prestressed concrete structures. The results showed that the DIC technique could provide very accurate and detailed information, including the in-plane and out-of-plane strains and their spatial variations, and the locations of high tensile and compressive strains which at later stages of loading result in cracking or crushing of concrete. Although Digital Image Correlation is able to accurately reflect cracking and deformation on the surface of structures, the application of DIC technique requires painting on the surface of objects and is limited to the damage which emerges from the surface.

### *1.2.3 Wave propagation-based detection*

Wave propagation-based detection includes passive sensing method (i.e., acoustic emission, etc.) and active sensing method (i.e., ultrasonic guided waves, impact echo method, etc.). The passive sensing method senses the signal from objectives of interest by collecting

signals released from objectives. Active sensing approach provides a controllable probing signal (frequency, direction, energy, etc.) and detects the received signal.

Acoustic emission (AE) is one of the most commonly used passive sensing methods. When a crack occurs in the object, the cracking event induces energy which propagates in the structure in terms of a stress wave, which can be collected by acoustic emission sensors preinstalled in the structure [52]. Therefore, researchers have tried to install acoustic emission sensors to monitor the health condition of structures. Carpinteri et al. applied acoustic emission technique to monitor the structural health based on the counting of events [53]. Farhidzadeh et al. monitored the fracture process of a reinforced concrete shear wall due to cyclic loading. A *b*-value analysis Gaussian filter was investigated to measure the crack propagation. Contributed by a cluster analysis based on the k-means, tensile and shear cracks can be classified automatically [54]. Choi et al. deployed distributed piezoelectric sensors into a beam and investigated an identification system consisting of a system model and a response comparator to identify the impact load and location [41]. Song et al. embedded piezoceramic transducers in a model concrete bridge girder and successfully detected the level of damage due to a collision impact. A linear relation between the output of sensor energy and the impact energy was found. Elfergani et al. [55] validated the feasibility to use AE to detect corrosion and crack propagation in representative structures. Shiotani et al. [56] conducted a study using AE technique to characterize the structural condition of a concrete bridge. This study showed that the evaluation of AE activity leads to information about any specific part of the structure that requires attention. In practice, AE systems are merely able to qualitatively evaluate damage presence; It is necessary to conduct other tests to determine damage details, i.e., depth, geometry, extent, severity, etc. Also, AE systems have an obvious drawback, which is low signal-to-noise ratio in

loud service environment.

Compared with the passive sensing method, the active sensing method is more reliable as the probing signal is deliberately provided with certain features, leading to the data collection with less noise. Experimental results validated that the cracking and debonding damage can be detected by the active sensing system. Wu et al. proposed to use piezoelectric elements in reinforced concrete for debond detection [43, 44]. Song et al. [57] proposed piezoceramic-based smart aggregates so that they can be embedded into the desired location before the casting of the concrete structure. The smart aggregate-based active sensing system was able to monitor the hydration of early-age concrete [58, 59], impact [60], damage evolution in the reinforced concrete structures [61-63], water presence in the concrete structure [64], bond slip [65], etc. Kong et al. [66, 67] designed and fabricated one new type of embeddable spherical smart aggregate for structural health monitoring. This smart aggregate enables generating and receiving omnidirectional stress waves that can significantly improve the detection aperture.

The limitations of wave propagation-based detection methods are: (1) Wave attenuation in concrete is severe, leading to the limited use of this method [68-71]. (2) The degradation of the piezoelectric actuator is a serious concern [72, 73]. The acoustic emission method uses an array of sensors installed on structures to detect propagating elastic waves released by newly formed damage surfaces. (3) Data contamination is a major challenge due to background noise and secondary sources such as the slight movement of the structure, impact loading, friction, and liquid flow [74-76]. This concern is even more severe for concrete structures due to the higher heterogeneity than steel structures [77]. Also, without an improved understanding of characteristics of elastic waves, it is difficult to obtain quantitative results of damage [78].

#### *1.2.4 X-ray or Gamma ray*

X-ray and Gamma-ray methods are robust techniques to obtain visual images of the interior of structures [79]. The main advantages of these methods are that they are easy to understand and have a wide base of acceptance. X-ray and gamma-ray techniques involve positioning a radiographic energy source on one side of an object and a recording medium such as film on the other side. An X-ray or gamma ray travels through the object and then exposes the film. As cracks in the object or corrosion of steel change the local material density [80], a two-dimensional picture of density variation in the object is able to reflect the crack or damage in the object. Recently, portable X-ray or gamma-ray sources are developed, which become possible to replace traditional film-based radiographs with digital records [45]. Furthermore, the object can be radiographed at various orientations and then a three-dimensional image can be reconstructed, which is called computed tomography (CT). Garboczi [81] described a mathematical procedure using spherical harmonic functions which can characterize concrete aggregate particles and other particles of the same nature based on X-ray tomography. Fukuda et al. [82] investigated the sealing of a crack in high-strength and ultra-low permeability concrete in water using micro-focus X-ray computed tomography. Shuai and Li [83] adopted X-ray computed microtomography to derive three-dimensional morphological data on microcracks before and after healing in Engineered Cementitious Composites (ECC). The results unveiled the nonuniform healing in the microcrack. The main limitations of X-ray and gamma techniques are obvious: they require accessibility to both sides of objects for measurements, which is difficult to be achieved in practice.

### 1.3 Electrical Methods and Self-Sensing Cementitious Composites

Electrical method regards measuring the electrical responses of the cementitious materials to reflect the mechanical states of the cementitious materials. This method has been explored as a sensing functionality for hydration monitoring [84-87], composition and pore structure assessment [88-91], and currently as an emerging method to quantify a material's mechanical state [92-95]. There is a standard ASTM testing method to quantify the resistivity of concrete materials [79] so that the health practices and safety of concrete materials can be evaluated.

The electrical response of a cementitious material strongly depends on its microstructure, including the distribution and connectivity of pores, the interconnecting layers of C-S-H gels, and their interfaces [21-23]. Since the microstructure of the cementitious material is highly age-dependent and heterogeneous, the concept of self-sensing concrete was proposed with conductive additives dispersed into the cementitious matrix to tailor the electrical microstructure of the cementitious materials and hence provide sensing functionality [92, 96, 97]. Conductive additives tailor the electrical microstructure of the cementitious materials so that high signal-to-noise ratio and piezoresistive behaviors can be attained. Researchers proposed to develop self-sensing concrete with different conductive additives. They can be categorized into four groups:

- Fibers, i.e., carbon fibers [92, 95, 96, 98-119], steel fiber[120], etc.
- Conductive particles, i.e., nickel powder [121, 122], graphite [123, 124] , etc.
- Nano-materials, i.e., carbon black nanoparticles [125-132], carbon nanotube [133-141], carbon nanofiber [142, 143], etc.
- Hybrid fillers [123, 124, 126, 131, 138].

Following are some of the featured studies. Seminal works by Chung et al. [93, 101, 105, 119, 120, 126, 144] explored multi-point DC probing of the plain cementitious matrix and cementitious pastes with conductive carbon-based fibers and revealed that the electrical properties of cementitious materials can be correlated with their mechanical behaviors, especially within the elastic range. Azhari et al. [138] proposed cement-based sensors involving carbon fibers and carbon nanotubes, and validated that the changes in resistivity mimic both the changes in the applied load and the measured material strain with high fidelity. Baeza et al. [145] investigated the influence of aspect ratio of the carbon fibers on electrical, mechanical, and functional properties of the carbon fiber-based self-sensing cementitious composites. Galao et al. [146] reported both strain and damage sensing properties of carbon nanofiber cement composites. The damage sensing was achieved via defining parameters to indicate irreversible damage. Gonzalez et al. [147] proposed to use CNT-based thin films to modify the cement-sand particles interface, which enhanced the electromechanical or sensing properties of the cementitious composites. In the above studies, the linear relations between elastic strain (tension and compression) and bulk resistance were established for sensing purpose; a nonlinear change in the bulk resistance indicated the occurrence of the material damage.

Despite the great advances in self-sensing cementitious materials, knowledge gaps remain. The fundamental issue is that DC resistance measurements were performed for sensing purpose, which are prone to unstable data collection due to the polarization effect of cementitious materials. Polarization effect of the cementitious materials is attributed to the electrical microstructure of the cementitious materials, which involves the interaction of different phases (conductive and nonconductive). Therefore, a cementitious material is not an ideal resistor whose resistance value is independent of measurement time and frequency, but an

equivalent circuit involving both resistor effect and capacitor effect. In contrast, alternating current (AC) is able to diminish the polarization effect of cementitious materials due to the periodically reversed direction. The piezoresistive behaviors (impedance magnitude vs. elastic strain relation) of the self-sensing cementitious materials under AC are hence desired to be revealed. Furthermore, the strain sensing capacity of “self-sensing concrete” is limited within the elastic strain range (0~0.3% in compression and 0~0.01% in tension). Once cracking, strain sensing is not attainable due to rupture failure of the cementitious materials. Although instant changes of the electrical resistance upon cracking of the cementitious materials indicate the occurrence of the damage [113, 114, 146], they cannot accurately track the damage evolution. The demand of sensing damage, however, requires understanding and establishing post-cracking electromechanical behaviors of the cementitious materials.

Recently, researchers also studied the electromechanical responses of Fiber-Reinforced Cementitious Composites (FRC) during cracking or damage evolution. FRCs are cementitious materials with fibers (i.e., steel fiber, carbon fiber, PVA fiber, etc.) dispersed in the cementitious matrix so that the cracking development is controlled by the reinforcing effect of fibers. Peled et al. [148] first reported post-cracking electromechanical behaviors of carbon and steel fiber reinforced cementitious composites based on AC electrical impedance spectroscopy. Electrical impedance spectroscopy was able to reveal the differences of conductive fibers vs. cementitious matrix phases in the contribution of the electrical response. This work found a strong correlation between the electrical responses (real part of impedance) and crack mouth opening displacement during crack growth (localized crack on a notched specimen). Among FRCs, Strain-hardening Cementitious Composites (SHC) feature a pseudo strain-hardening behavior under tension with tensile strain capacity hundreds of times that of normal concrete or FRC, exhibiting distributed

damage through multiple microcracking with self-controlled crack width at the micrometer scale [149]. Tensile piezoresistivity of SHCs was first experimentally studied by Hou et al. [150]. Hou's work showed that the resistivity of SHC can be correlated to mechanical strain during both elastic and strain-hardening stages. Li et al. [130, 132] utilized the carbon black particles to modify the electrical properties of SHC and proved that the change in resistivity of carbon black SHC behaved differently during elastic, strain-hardening, and tension softening stages. Most recently, Ranade et al. [151] investigated the influence of microcracking on the resistivity of strain-hardening cementitious materials through 2-point AC probing under a fixed frequency (1 kHz), and established one multi-scale framework from single cracking to multiple cracking to interpret the electromechanical behavior of strain-hardening cementitious materials. Above studies revealed that the post-cracking electromechanical responses were affected by the multiple microcracking process during the strain-hardening stage and the single crack opening during the tension softening stage. Still, there are some fundamental questions. (1) The electrical responses of cementitious materials cannot be fully represented by resistivity. As described above, a cementitious material is not an ideal resistor and thus capacitor effect cannot be neglected. Capacitor effect is further evident when cracks are present in cementitious materials. In this sense, impedance is a more accurate measure than resistance for cementitious materials. (2) How the different mechanical stages (elastic, strain-hardening, tension softening) impact the impedance of cementitious materials and whether the impedance is able to differentiate the strain-hardening and tension softening stages are still unknown and desirable to be studied. In SHC, the strain-hardening stage is characterized as steady-state multiple microcracking, but the tension softening stage is governed by a single crack evolution accompanied by the failure of the structural element. It is thus necessary to identify the final damage occurrence in the tension



softening stage for sensing purposes. (3) The differences between different parts of the impedance (impedance magnitude, the real part, and the imaginary part) corresponding to cracking have yet to be identified. The imaginary part is attributed to the capacitor effect of the crack; however, the real part is contributed to the resistor effect of the crack. Studying such difference allows achieving optimized sensing performance.

#### **1.4 Research Objectives and Dissertation Outline**

Above discussion indicates that there remains a significant need for distributed sensing of damage and strain in reinforced cementitious composites. The research questions are:

(1) What are the mechanisms responsible for the electrical and electromechanical behavior of cementitious materials?

(2) Is the electrical behavior of cementitious materials frequency-dependent?

(3) Can we harness the electrical properties of cementitious materials to achieve strain and damage self-sensing?

In order to answer the above questions, following hypotheses are made. (1) Cementitious materials exhibit an AC frequency-dependent electrical response, depending on its heterogeneous microstructure. Mechanical straining and damage would lead to a change in the microstructure, thus affecting the frequency-dependent electrical response. Therefore, A strong, high signal-to-noise coupling between electrical and mechanical behavior at different length scales would enable self-sensing functionality during elastic and post-cracking stages. (2) Using advanced tomography methods, spatial mapping offering a visual depiction of concrete impedance distribution can be gained. Therefore, spatial sensing of damage location and level inside a structural element is possible through electrical probing only from the boundaries.

The objectives of this dissertation are:

(1) Generate fundamental understandings on how the composition and microstructure affect the frequency-dependent electrical response of cementitious materials.;

(2) Develop novel multifunctional strain-hardening cementitious composite (MSC) integrating distributed cracking behavior with self-sensing capacity;

(3) Elucidate the electromechanical behavior and mechanisms of MSC through experiments and modeling;

(4) Establish advanced EIT methods for realizing distributed damage sensing in MSC members.

To achieve the objectives, the research tasks and corresponding chapters are summarized in Figure 1.1.

Chapter 2 focuses on understanding how the composition and microstructure affect the frequency-dependent electrical response of cementitious materials. Specifically, electrical impedance spectroscopy was performed to reveal the frequency-dependent impedance of cementitious materials. Equivalent circuit model analysis was conducted to explain how the electrical microstructure affects the frequency-dependent electrical response of cementitious materials and their interfaces with electrodes.

Chapter 3 describes the design of multifunctional cementitious materials that integrate damage tolerance with self-sensing functionality. The material design was accomplished through tailoring the material micromechanical as well as electrical parameters to achieve a desired macroscopic electromechanical behavior.

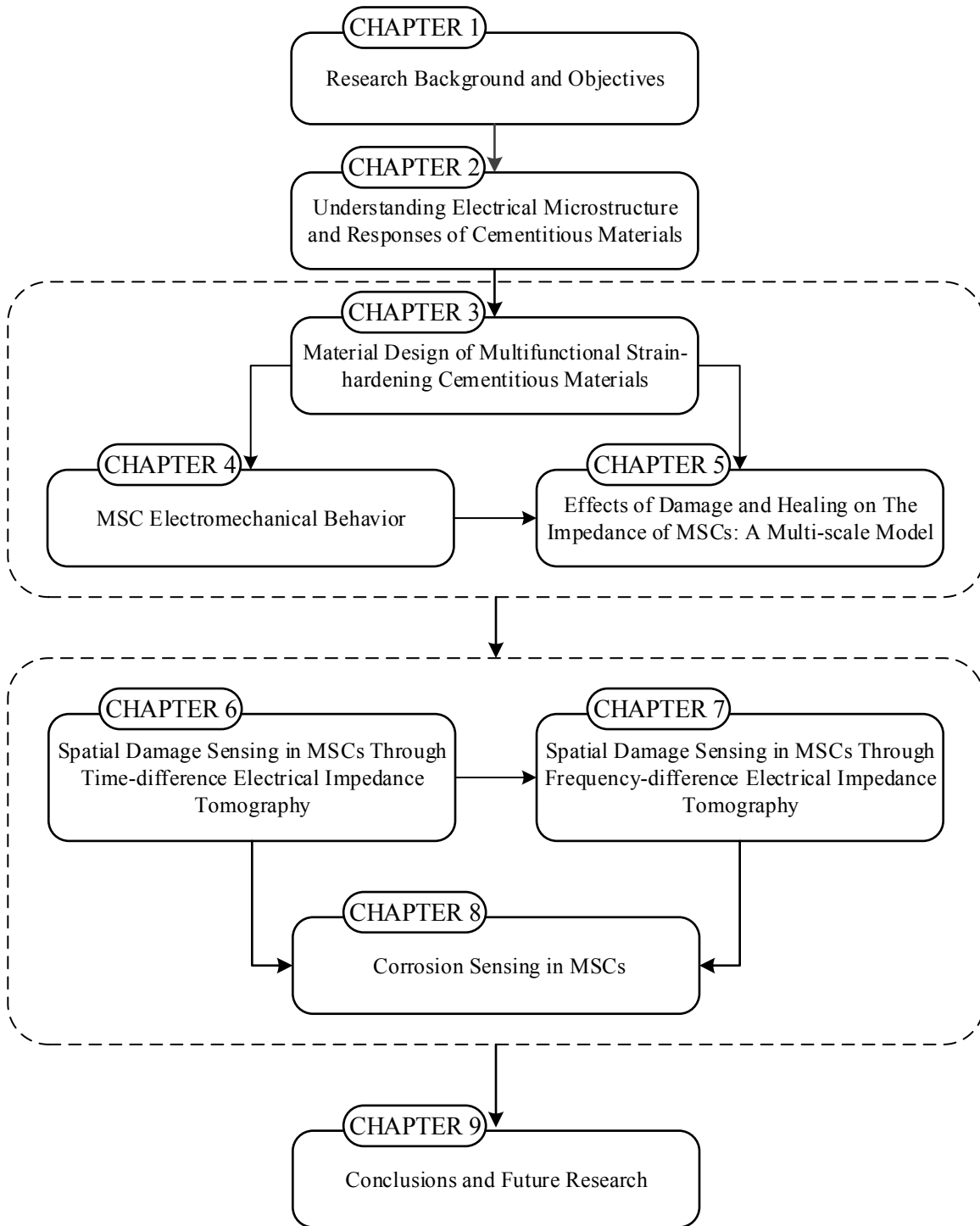


Figure 1.1 A schematic outline of the major topics presented in this dissertation

Chapter 4 reveals the unique electromechanical properties of MSCs under monotonic and cyclic tension and compression. MSC shows strongly-coupled, high signal-to-noise ratio

electromechanical behavior during elastic, strain-hardening, and tension softening stages while exhibiting the ductile behavior with tensile strain capacity more than 3%. The results indicate the potential of strain and damaging self-sensing in MSCs long before the localized fracture occurs.

Chapter 5 elucidates the effects of damage and healing on the frequency-dependent impedance of MSCs. A multiscale model was formulated to explain the mechanisms of impedance change, and its frequency-dependence, due to damage and healing processes within MSCs. This model links scales from the electromechanical behavior of single fiber pull-out, to single crack opening, and then to multiple cracking process. The model was validated using designed experiments. Also, the model was used to predict the frequency-dependent electrical response of cementitious materials during damage evolution and autogenous self-healing process.

Chapter 6 focuses on achieving spatial damage sensing in MSCs through advanced electrical impedance tomography (EIT) method. It established the EIT setup for MSCs. It generates understandings on the frequency dependency of EIT image reconstructions for cementitious materials, the selection of probing method, and the EIT finite element algorithms. It successfully demonstrates the distributed sensing of single localized crack as well as distributed multiple microcracks within MSC specimens.

Chapter 7 develops a frequency-difference electrical impedance tomography approach for damage sensing in MSCs. This approach tackles the challenges of time-difference EIT method that the reference state before damage is not always available and the influences of temperature and humidity can introduce secondary noise.. Frequency-difference EIT requires potential measurements at two different frequencies simultaneously, among which one is considered as the reference state and the other measurement is considered as a change-of-state. Image reconstructions based on two frequencies showed the contrast between damage region and un-

damaged region. A frequency-difference EIT system (frequency range: 0.1 Hz ~ 32 MHz) was established for cementitious materials in this study. Then image reconstructions for 2D and 3D damage sensing based on frequency-difference EIT were demonstrated in MSC specimens.

Chapter 8 explores corrosion sensing in MSCs through EIT method and image reconstruction of chloride penetration profile and concrete cover cracking damage during the steel reinforcement corrosion process. Due to the distinctive electrical behavior of MSCs and its possible effect on the electrochemical process during corrosion, the corrosion resistance of MSCs was investigated and validated in this study, in comparison with conventional reinforced concrete and reinforced strain-hardening cementitious composite.

Chapter 9 concludes this dissertation by identifying potential directions for future research.

## CHAPTER 2: UNDERSTANDING ELECTRICAL MICROSTRUCTURE AND RESPONSES OF CEMENTITIOUS MATERIALS

### 2.1 Introduction

Cementitious materials are heterogeneous in terms of their microstructure and physiochemical properties. Besides ingredients such as sand, coarse aggregates, pozzolans, etc., cement paste microstructure includes several parts: pores, cement hydration products, outer products, and unhydrated clinkers. Pores include capillary pores, entrapped air voids, and the entrained air system. Hydrated cement particles consist of high-density C-S-H, and in some cases an interior core of unhydrated cement. The outer product can be a solid C-S-H gel, gel pores, calcium hydroxide, calcium sulfoaluminate phases. Humidity exists in pore solution and C-S-H layer solution. For pore humidity, there are different ions inside:  $\text{Na}^+$ ,  $\text{K}^+$ ,  $\text{Ca}^{2+}$ ,  $\text{SO}_4^{2-}$ ,  $\text{OH}^-$ , etc. For pore solution or gel pore solution, conductivity is higher than 10 S/m [152, 153] after 1 day curing. The conductivity of C-S-H and other solid phase composites is several thousand times lower than that of the pore solution [154]. Under an applied steady electric field, the ions in pore water are mobilized to create the electrical current. Therefore, the electrical response of a cementitious material strongly depends on its heterogeneous microstructure, including the distribution and connectivity of pores, the interconnecting layers of C-S-H gels, and their interfaces. Also, the microstructure of cementitious materials is age-dependent. In addition, humidity content within pores also changes from time to time, due to cement hydration process as well as ambient relative humidity changes in the exposure environment.

Resistance (under DC) or impedance (under AC) of cementitious materials has been explored as a sensing functionality for hydration monitoring [85, 86, 155-160], composition and

pore structure assessment [88-90, 161-166], chloride penetration evaluation [89, 167, 168], and has recently emerged as a method for measuring the material's mechanical state [94, 95, 169-174]. Compared with resistance, frequency-dependent electrical impedance is more suitable for cementitious materials, which enables unveiling the microstructure features of the cementitious materials and avoiding polarization effect occurring in cementitious materials under direct current. Electrical impedance spectroscopy (EIS) is such a technology that explains fundamental electrical properties of materials and also provides means of analytical prediction of material electrical response through equivalent circuit modeling.

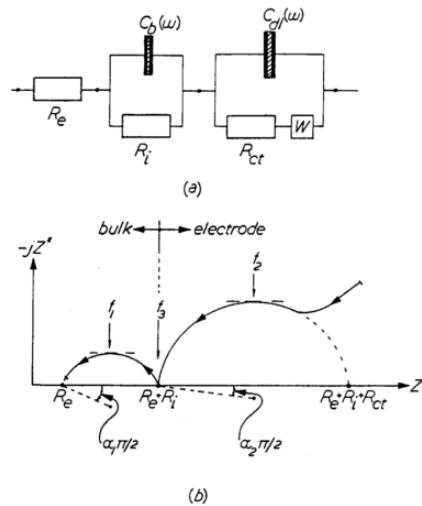


Figure 2.1 Equivalent circuit model proposed by Mccarter et al. [175]

An equivalent circuit refers to a theoretical circuit that retains all of the electrical characteristics of a given circuit. A simple circuit can be a resistor. However, a cementitious material is not an ideal resistor whose resistance is time and frequency independent, due to the complex microstructure as described above. Electrical impedance spectroscopy has been utilized on cementitious materials for around three decades, and researchers proposed different equivalent circuit models to interpret the electrochemical responses of the cementitious materials. It should be noted that most of those works focused on the cementitious materials at an

early age. McCarter et al. [175] firstly published EIS results on cement paste. He proposed one equivalent circuit model (Figure 2.1), separating electrical response of cement into two distinct regions. One is relating to electrode-cement interface processes and other is due to bulk processes. Also, considering the slow ionic diffusion effects at the electrode-cement interface, the model includes a Warburg impedance element. Gu et al. [176-179] proposed a model to physically interpret microstructural elements of the cement paste. The model considers a solid-liquid interface unit cell to illustrate the cement paste matrix, as shown in Figure 2.2. With this model, he was able to link the high-frequency arc of the Nyquist plot to ionic concentration of pore solution, porosity and pore size distribution. Song et al. [180, 181] proposed a new equivalent circuit model (Figure 2.3). According to the proposed model, the parameters demonstrated by the experimental Nyquist plot have clear meanings. In particular, he proposed the concept of the electrical microstructure, considering that the cementitious materials include three paths: conductive paths representing the continuous ion conductivity, non-conductive paths representing capacitor effect of the matrix, and partially conductive paths reflecting the discontinuous ion conductivity.

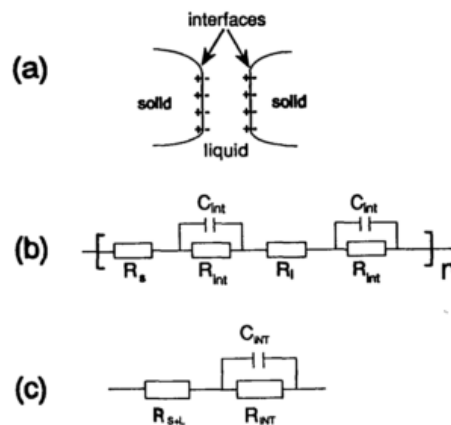


Figure 2  
 (a). Schematic of the "solid-liquid interface unit cell" model; (b). The corresponding equivalent circuit for a single layer of cement paste; (c). The simplified equivalent circuit for one layer of cement paste.

Figure 2.2 Equivalent circuit model proposed by Gu et al. [176-179]



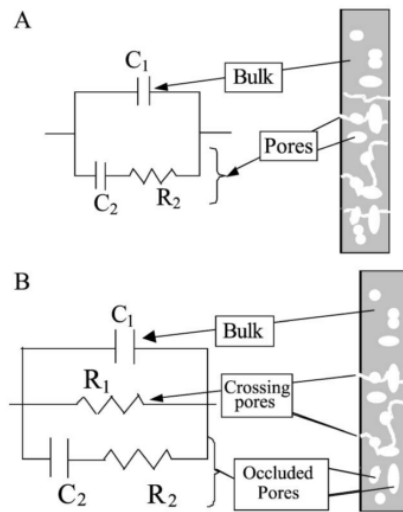


Figure 2.3 Equivalent circuit model proposed by Song et al. [180, 181]

In this study, electrical impedance spectroscopy (EIS) was conducted on cementitious materials with two variables: age and composition. The electrical response of porous cementitious materials with a wide frequency range from 1 Hz to 1 MHz reflected the movement of ions in the pore solution and hence was linked to microstructure characterization. In order to fundamentally understand the electrical behavior, especially the complex impedance of cementitious materials, EIS and equivalent circuit analysis were performed on various mixtures with different binder ingredients, water/binder ratios, incorporation of conductive nano-materials, and age effects. The equivalent circuit model was further refined to better reflect the contribution of different phases, interfaces, components and ingredients on the electrochemical behavior of the material. The results laid the groundwork for the systematic development of MSCs. A comprehensive electrical impedance study, coupled with equivalent circuit analysis, allowed us to tailor the physical and chemical parameters MSC materials to exhibit a strong correlation between complex impedance and material strain, crack width, damage level, and healing.

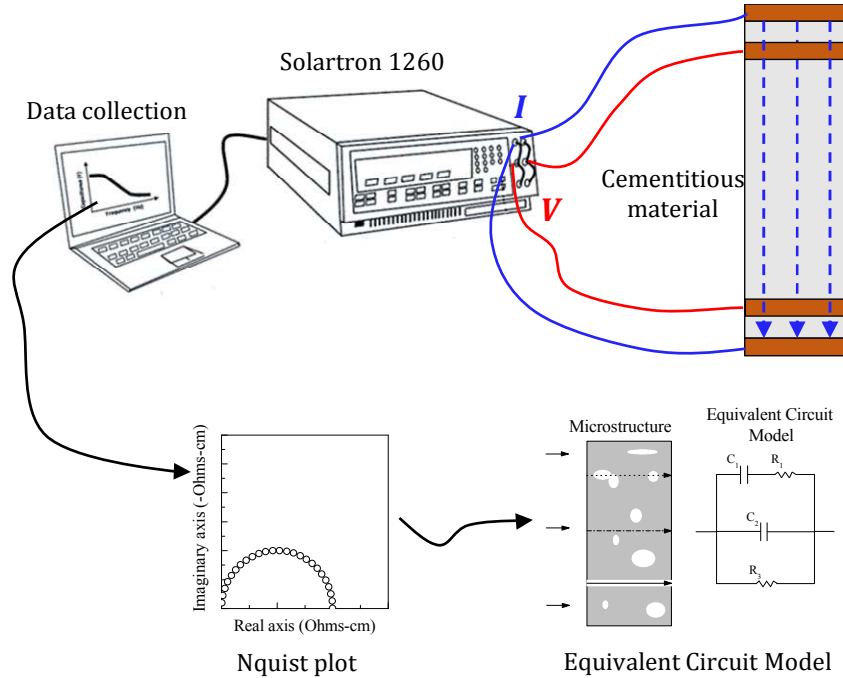


Figure 2.4 Illustration of test framework in this chapter

The test framework of this study is shown in Figure 2.4. First, the impedance analyzer was used to measure the impedance of cementitious materials. The collected data were then analyzed with equivalent circuit model. Equivalent circuit model allows interpreting the electrical microstructure of the cementitious materials.

## 2.2 Basics of Electrochemical Impedance Spectroscopy

Impedance spectroscopy is a new and powerful method for characterizing electrical properties of materials and their interfaces with electrodes. It can be utilized to investigate the dynamics of bound or mobile charge in the bulk or interfacial regions of solid or liquid materials, including ionic, semiconducting, dielectric and mixed electronic-ionic materials. Its fundamental theory can be shown below. For ideal Ohms law:

$$R = \frac{V(t)}{I(t)} \quad (2.1)$$

With small excitation signal, a sinusoidal potential excitation is applied. The response to this potential is an AC current signal, containing excitation frequency and harmonics. The excitation signal, expressed as a function of time, has the form of:

$$V(t) = V_0 \cos(\omega t) \quad (2.2)$$

$$I(t) = I_0 \cos(\omega t - \phi) \quad (2.3)$$

For a linear system, the impedance is written as:

$$Z(t) = \frac{V(t)}{I(t)} = \frac{V_0 \cos(\omega t)}{I_0 \cos(\omega t - \phi)} = Z_0 \frac{\cos(\omega t)}{\cos(\omega t - \phi)} \quad (2.4)$$

With Euler's relationship

$$\exp(i\phi) = \cos\phi + i\sin\phi \quad (2.5)$$

$$V(t) = V_0 \exp(i\omega t) \quad (2.6)$$

$$I(t) = I_0 \exp(i\omega t - i\phi) \quad (2.7)$$

The impedance can be re-written as a complex number:

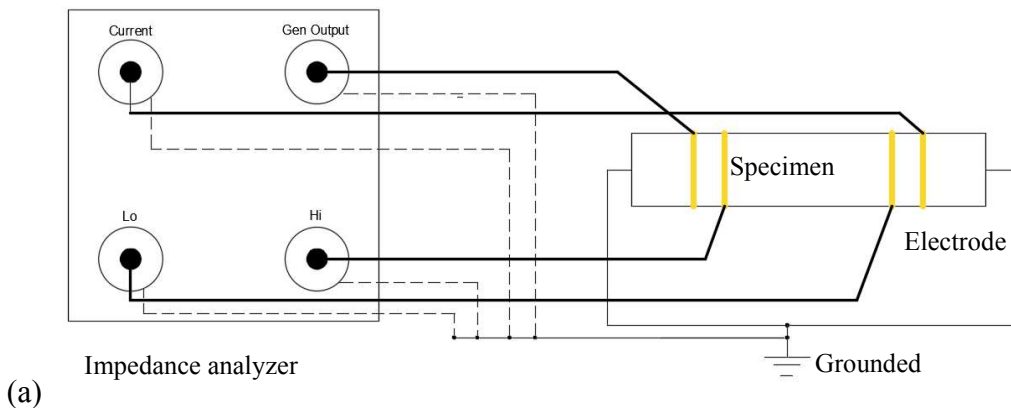
$$Z = \frac{V}{I} = Z_0 \exp(i\phi) = Z_0 (\cos\phi + i\sin\phi) \quad (2.8)$$

When the complex number is plotted on the complex Coordinate, a Nyquist plot is obtained. When the impedance magnitude or phase degree is plotted corresponding to the frequency, a bode plot is attained.

## 2.3 Experimental Methodology

### 2.3.1 EIS test setup

Four copper electrodes were attached to the specimen surfaces with conductive silver colloidal paste (Figure 2.5). The two outer electrodes were used to inject AC current at frequencies ranging from 0.1 Hz to 10 MHz into the specimen. The two inner electrodes were used to measure the *in-situ* voltage within the specimen. The electrodes were parallel to each other and spaced with sufficient distance in order for the current to be continuous and perpendicular to the electrodes. The EIS measurements were carried out using an impedance analyzer configured for a 100 mV amplitude excitation, which was slight enough to ensure that the material system was a linear system. Data were collected with 35 points per decade. The impedance as a function of frequency was then plotted, yielding the impedance spectrum. The specimen had the thickness of 12.7mm, the width of 51 mm and the length of 254 mm. The gauge length between two internal electrodes was 102 mm.



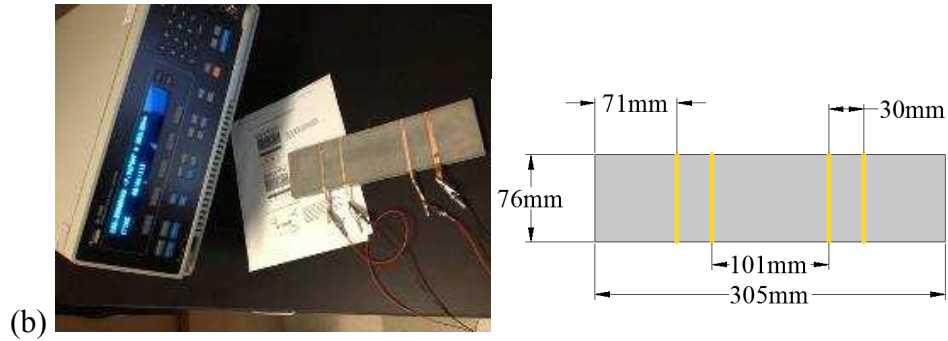


Figure 2.5 EIS setup: (a) EIS measurement circuit; (b) Test setup and specimen dimensions

### 2.3.2 Materials

Specimens were made of different mixture designs shown in Table 2.1. C stands for cement; F stands for fly ash; W stands for water; S stands for silica sand; P stands for PVA fiber; CB stands for carbon black nanoparticles. 1% and 4% means the volume proportions of carbon black. 0.28 and 0.21 are water/binder ratios. All specimens were prepared at controlled room temperature of  $20 \pm 1^\circ\text{C}$  and relative humidity of  $50 \pm 5\%$ . All dry particles such as cement, fly ash, silica sand, and carbon black nanoparticles were first mixed for 3 minutes. Water was then added together with the superplasticizer to form a homogeneous mortar with the optimum rheology favoring uniform dispersion of PVA fibers and carbon black. The fresh mixture was cast into coupon specimens ( $305\text{ mm} \times 76\text{ mm} \times 12.5\text{ mm}$ ). After casting, the specimens were covered with plastic sheets and demolded after 24 hours. The specimens were water-cured until the age of 7 days, and then air-cured with an ambient temperature of  $20 \pm 1^\circ\text{C}$  and relative humidity of  $45 \pm 5\%$ . EIS was performed on the specimens at 7, 14, 21, 28, 42, 63 and 180 days. For each measurement, data collection rate was 35 points per decade, where a decade is a 10-times increase in frequency.

Table 2.1 Design of tested specimens

Specimen no.	Composition & Description	Specimen no.	Composition & Description
1	C+W (0.21)	7	C+W+CB1% (0.28)
2	C+W (0.28)	8	C+W+CB4% (0.28)
3	C+W+S (0.21)	9	C+W+S+F (0.28)
4	C+W+S (0.28)	10	C+W+F+S+PVA
5	C+W+F (0.28)		
6	C+W+F+S+ +CB1%		

## 2.4 Results and Discussion

### 2.4.1 Effect of age

The effects of age on complex impedance of cementitious materials are shown in Figure 2.6-2.15. The age was increased from 7 days to 180 days. The results were plotted as impedance magnitude vs. frequency. It was found that impedance increased with specimen age, and the increase became more significant after 28 days. This was the case for all mix designs. The change in electrical response of cementitious materials was due to the hydration process that led to a decrease in pore water and an increase in the nonconductive path formed by increasing amount of hydration products.

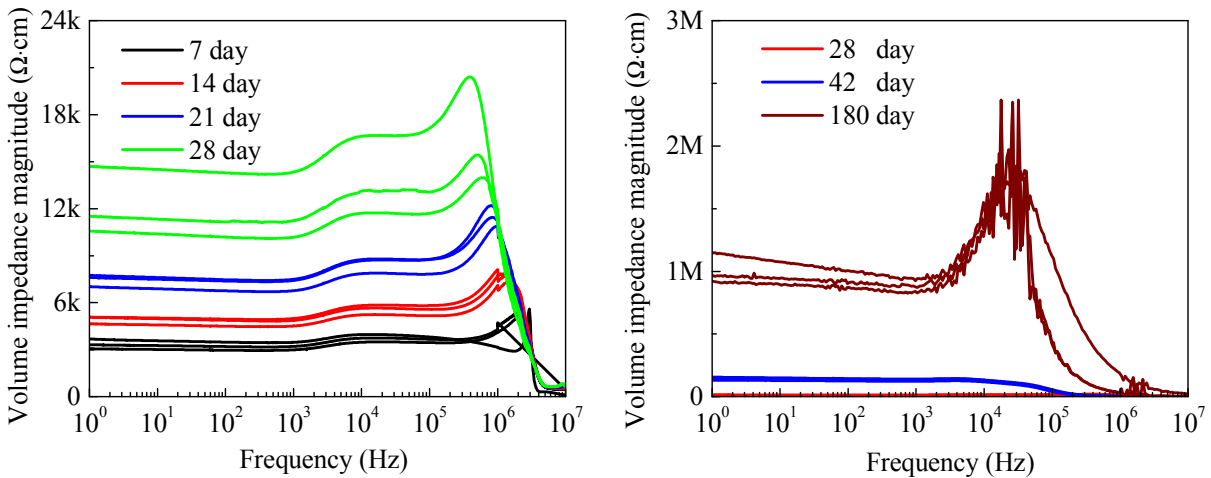


Figure 2.6 Bode plot for C+W (0.21)

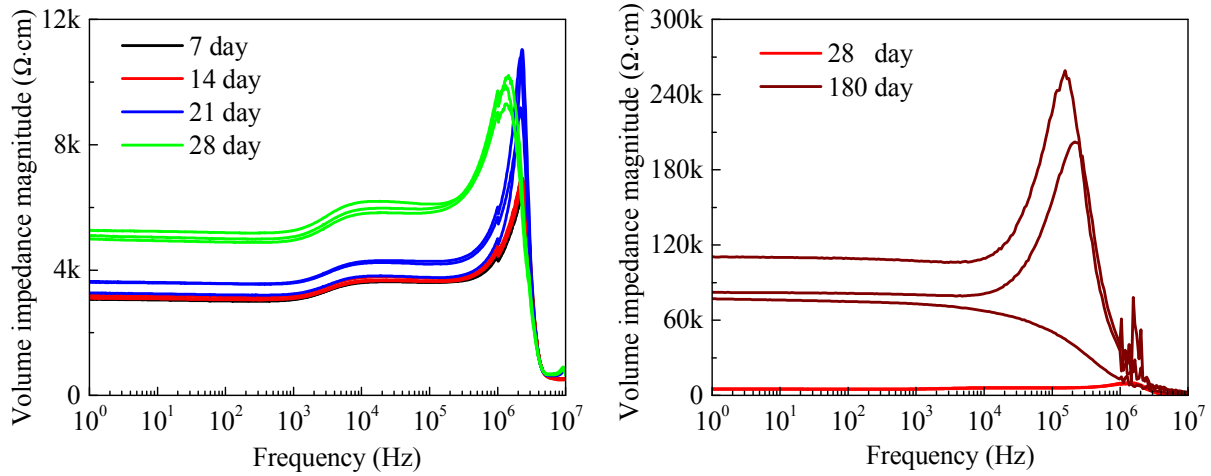


Figure 2.7 Bode plot for C+W (0.28)

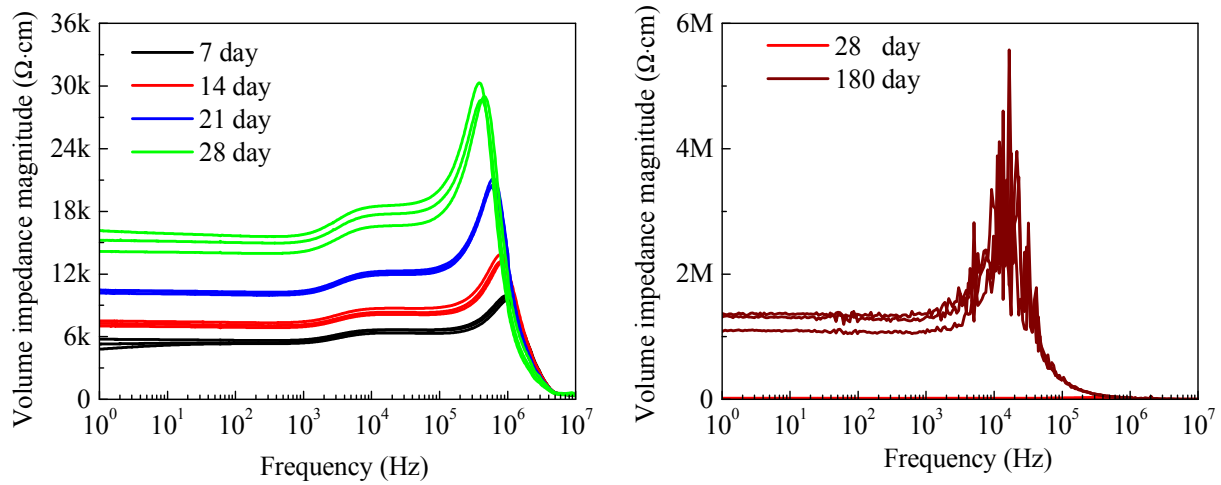


Figure 2.8 Bode plot for C+W+S (0.21)

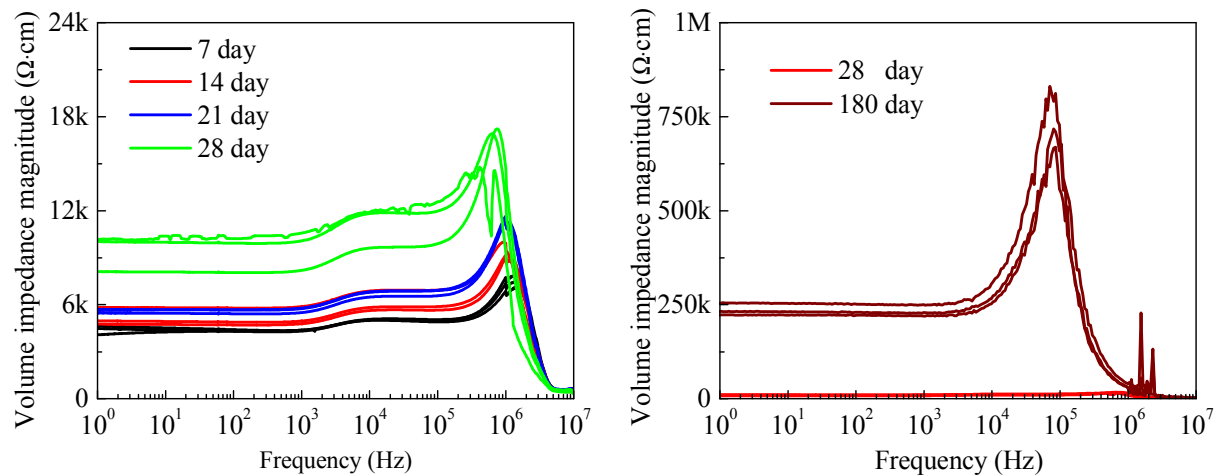


Figure 2.9 Bode plot for C+W+S (0.28)

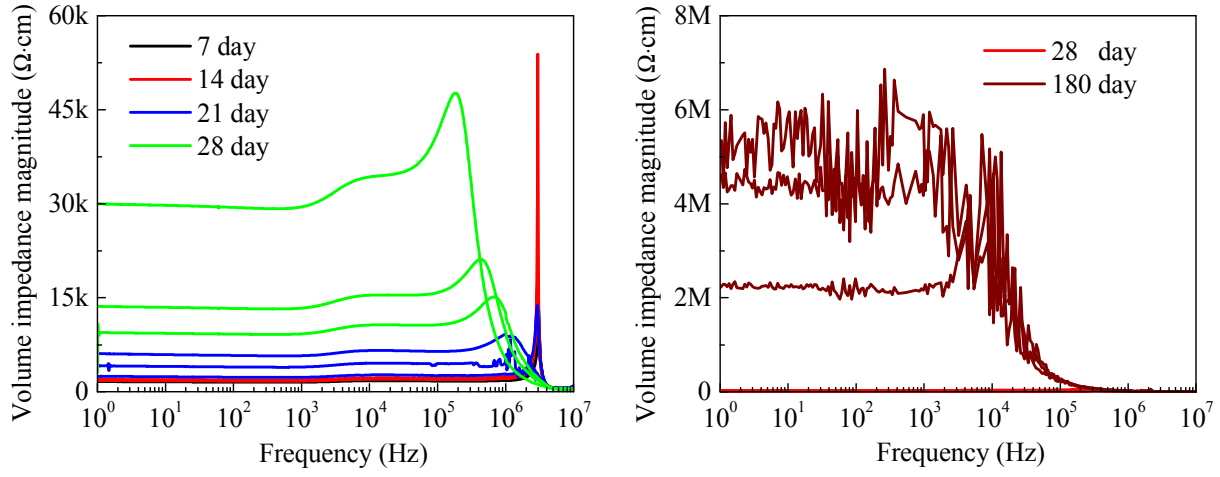


Figure 2.10 Bode plot for C+W+F (0.28)

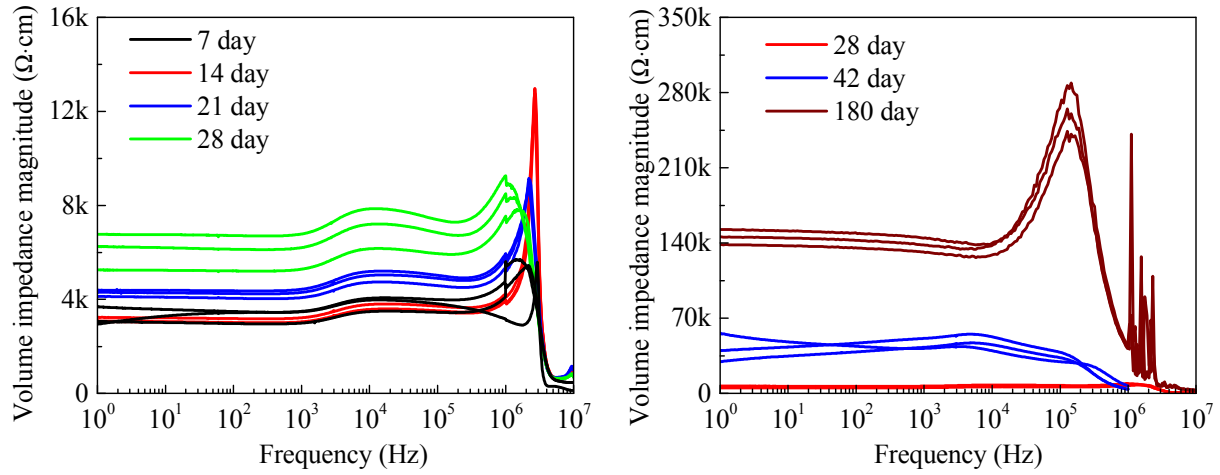


Figure 2.11 Bode plot for CB+C 1%

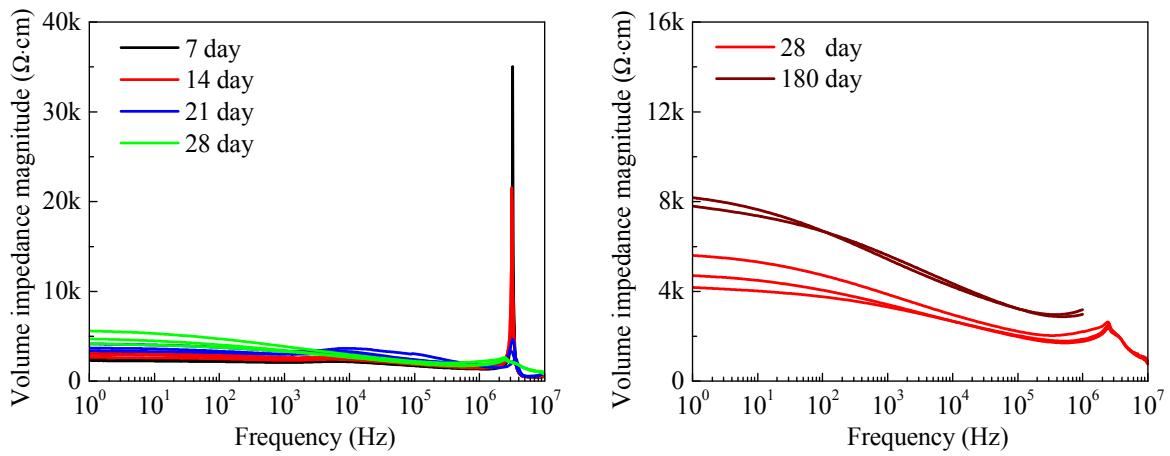


Figure 2.12 Bode plot for CB+C 4%



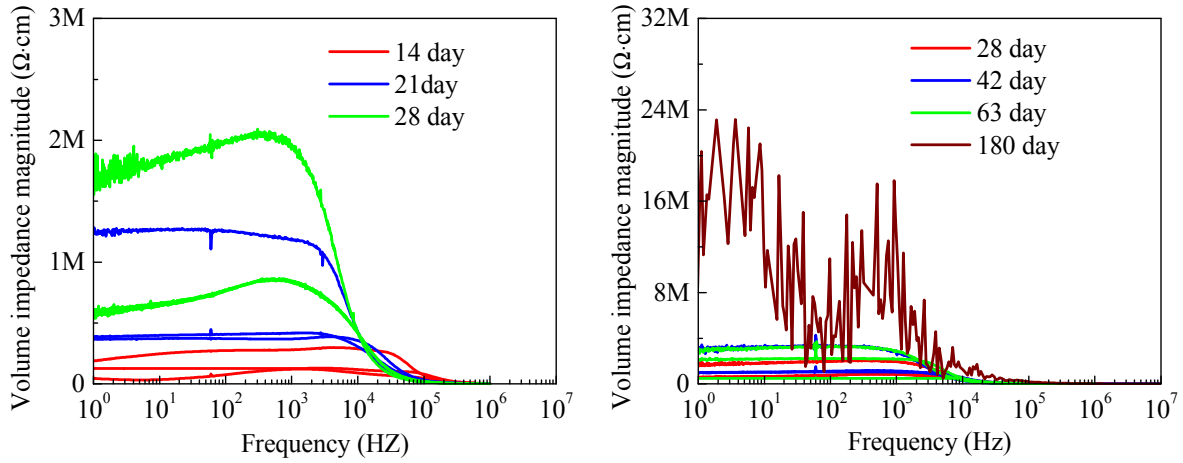


Figure 2.13 Bode plot for C+W+S+F

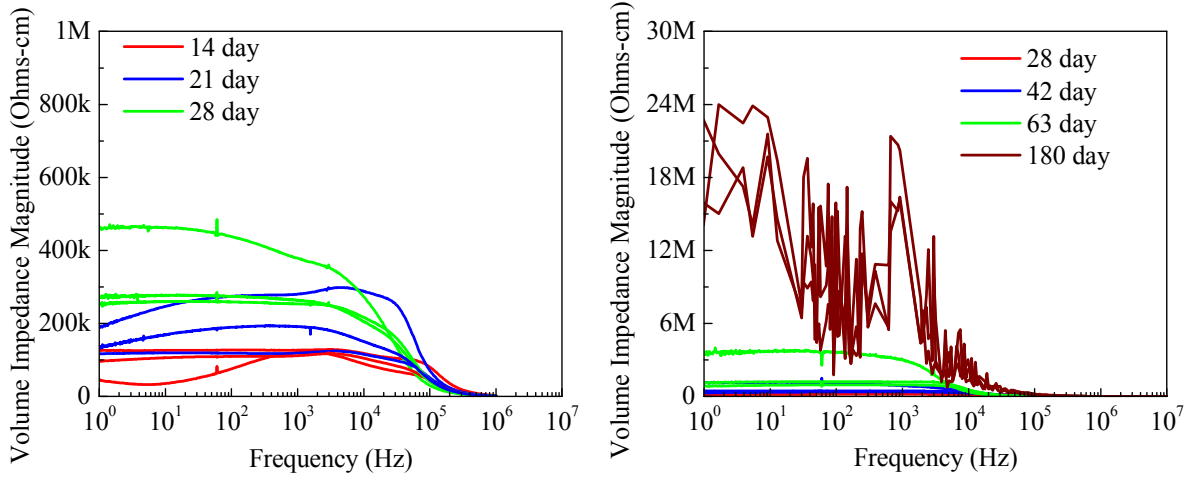


Figure 2.14 Bode plot for C+W+S+F+P

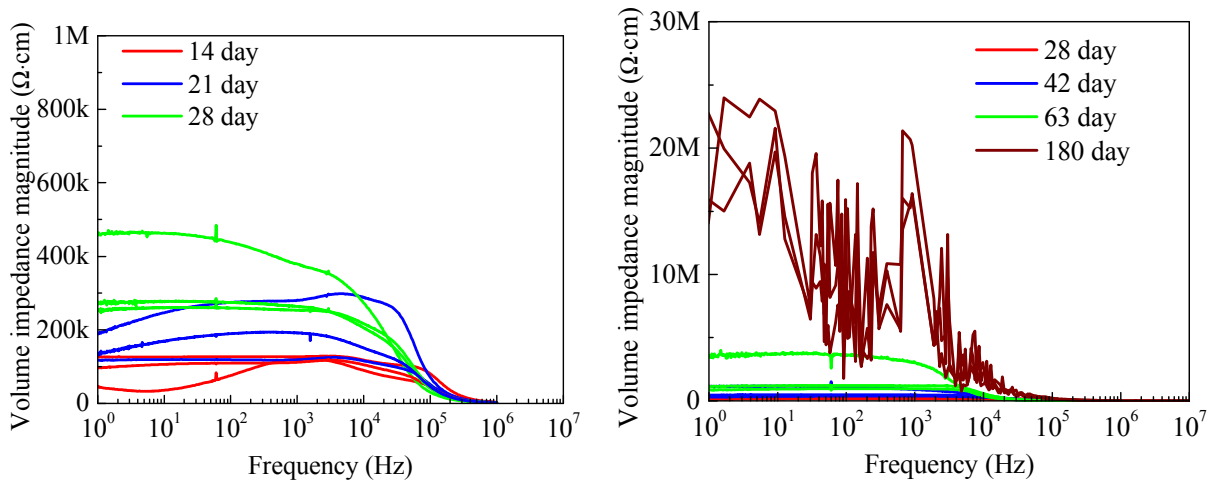
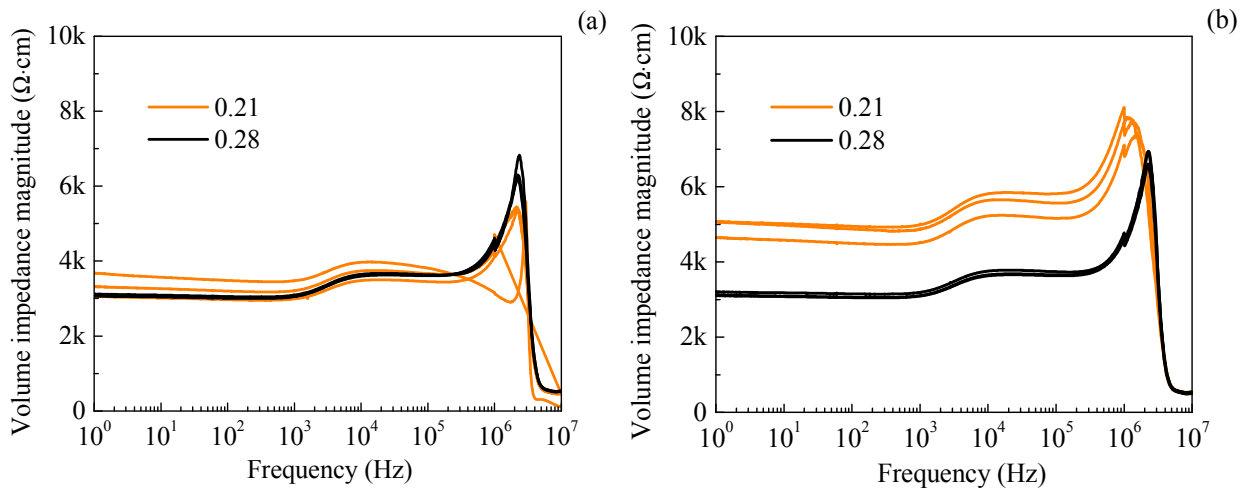


Figure 2.15 Bode plot for C+W+S+F+CB1%

### 2.4.2 Effect of water/binder ratio

The effects of water/binder ratios on complex impedance of cementitious materials are shown in the bode plots in Figure 2.16 and 2.17. Two water/binder ratios were investigated: 0.21 and 0.28. It was found that water/binder ratio had less effect at earlier ages than later ages. At the age of 7 days, complex impedances did not show any significant difference between the specimens with water-binder ratios of 0.21 and 0.28. At lower frequency, the impedance of C+W 0.21 specimens was slightly higher than that of C+W 0.28. After the age of 14 days, the impedance difference between C+W 0.21 and C+W 0.28 specimens became significant. The specimens with lower water/binder ratio exhibited higher impedance magnitude. At the age of 180 days, the impedance magnitude of C+W 0.21 specimens were 10 times higher than C+W 0.28 specimens.



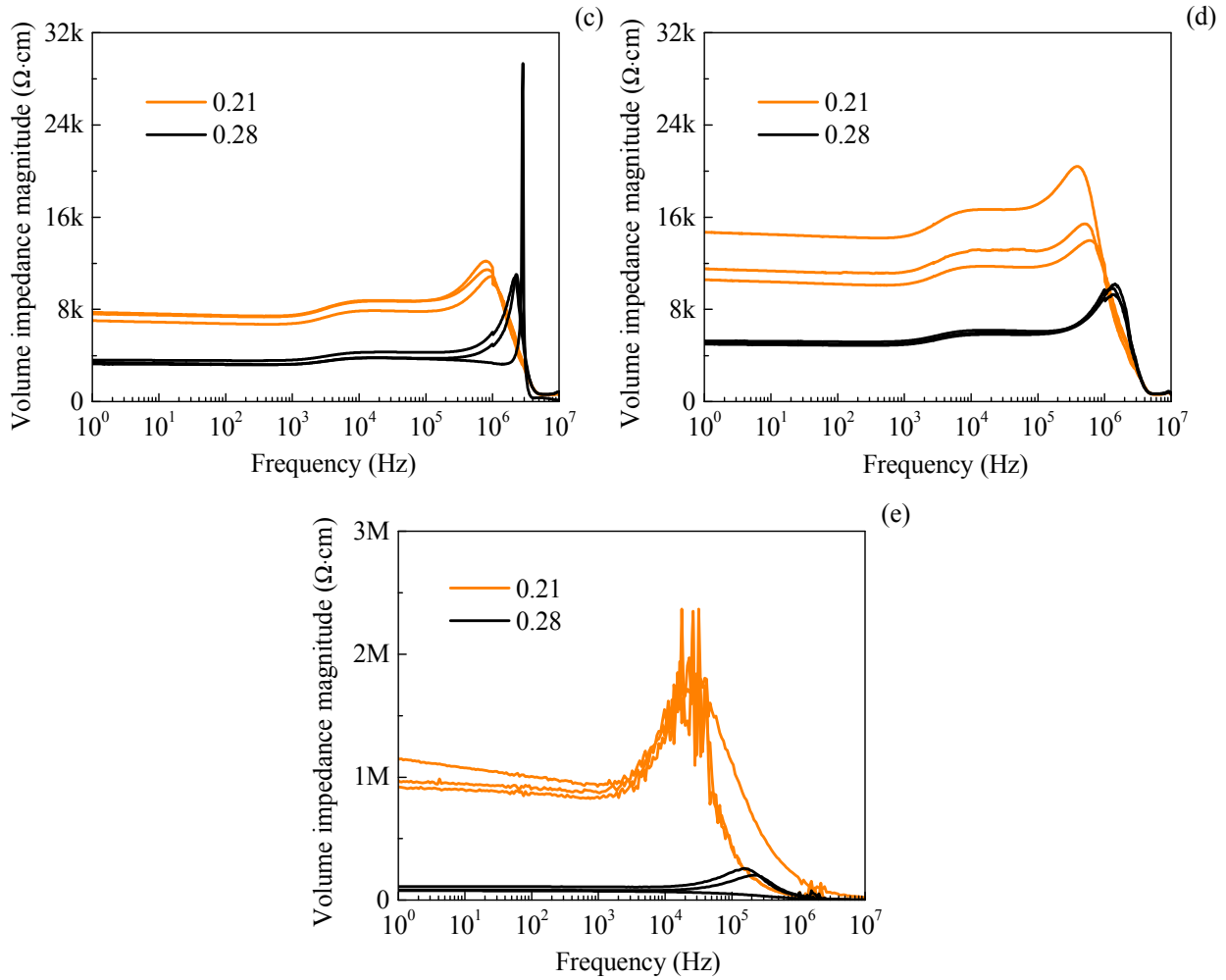
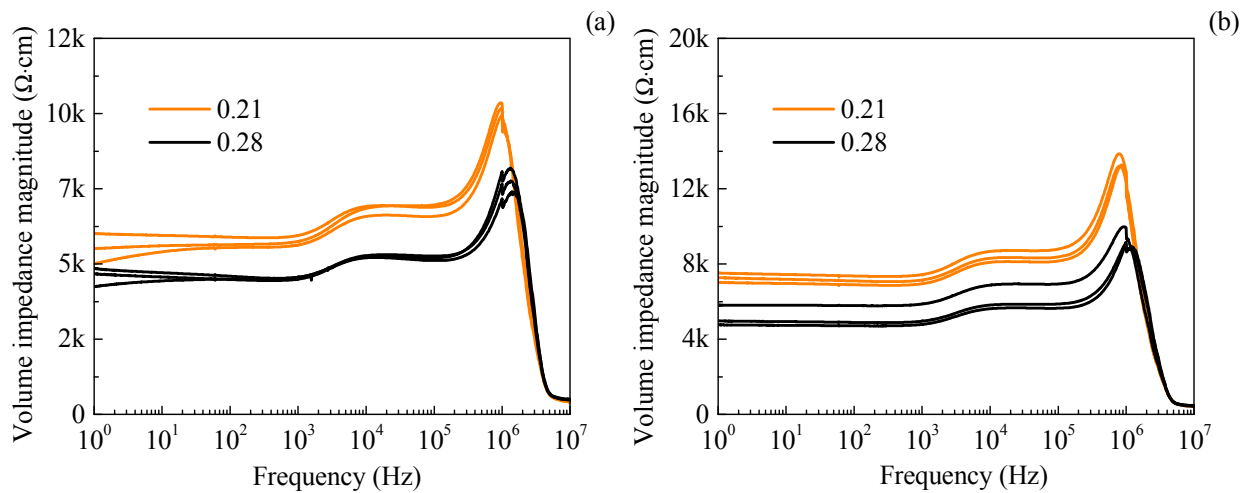


Figure 2.16 Bode plots of C+W specimens with water/binder ratios of 0.21 and 0.28, at the age of (a) 7 days, (b) 14 days, (c) 21 days, (d) 28 days, and (e) 180 days



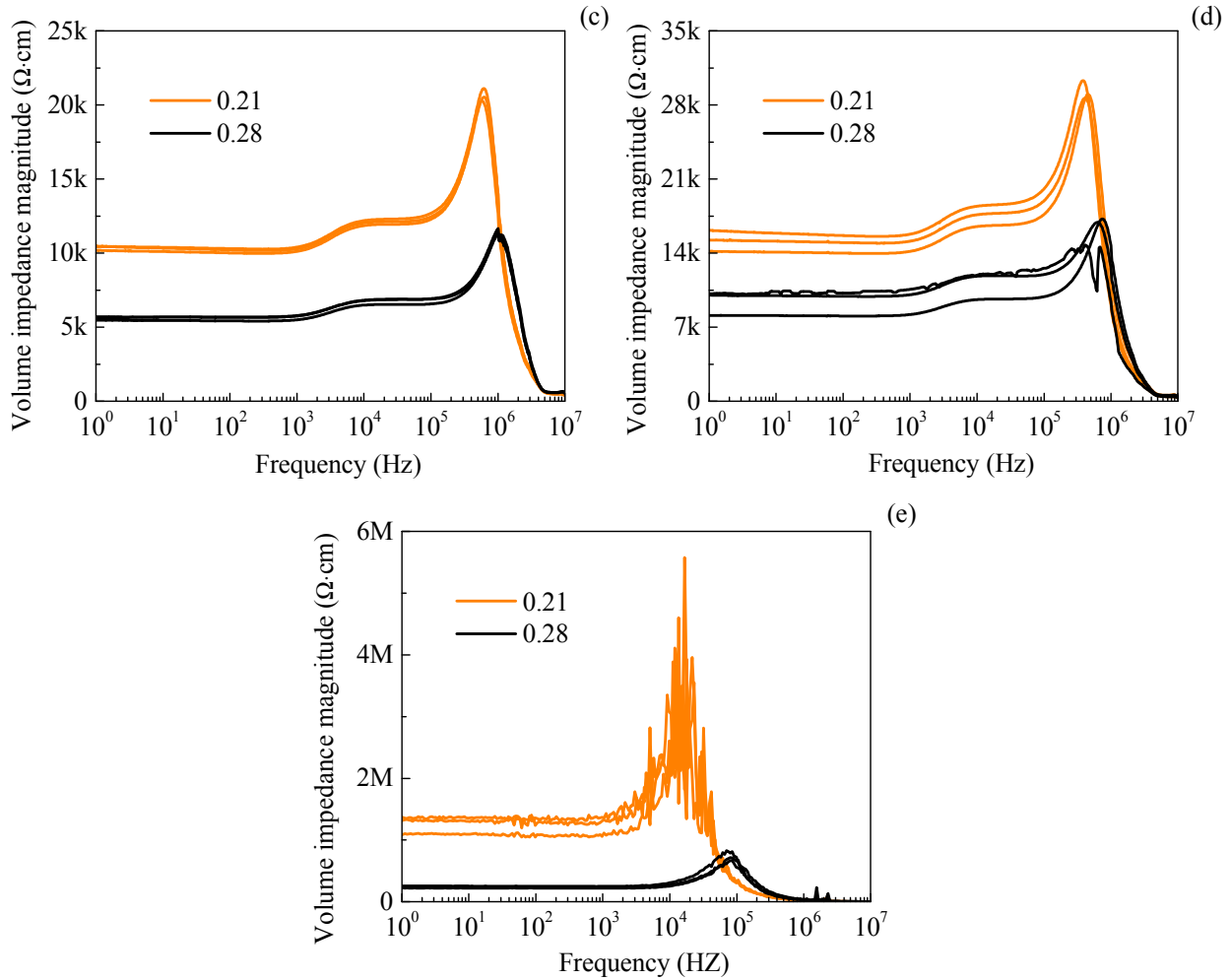
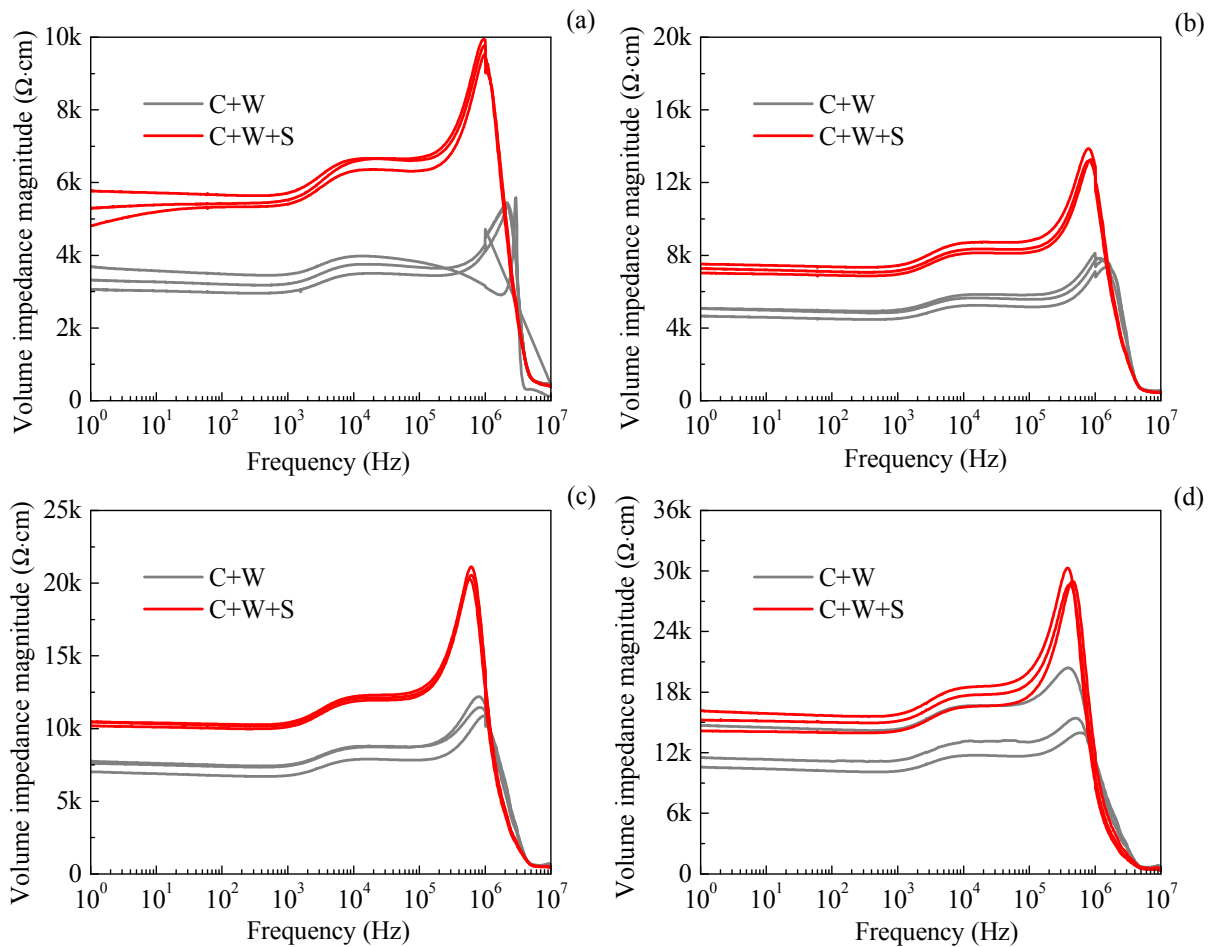


Figure 2.17 Bode plots of C+W+S specimens with water/binder ratios of 0.21 and 0.28, at the age of (a) 7 days, (b) 14 days, (c) 21 days, (d) 28 days, and (e) 180 days

### 2.4.3 Effect of composites

The effects of fine aggregates, i.e., sands, on complex impedance of cementitious materials are shown in the bode plots in Figure 2.18 and 2.19. At all ages, and for two different water/binder ratios, the presence of sands in the cementitious material led to an increase in impedance magnitude; such increase was more prominent for later ages. The results elucidated the role of silica sands as nonconductive paths for a wide range of frequencies in cementitious materials.

The effects of fly ash on complex impedance of cementitious materials are shown in the bode plots in Figure 2.20. Two scenarios were investigated: with and without fly ash. It was found that the effects of fly ash on electrical response of cementitious materials were different from sand. At the ages of 7 days and 14 days, specimens with fly ash exhibited lower impedance magnitudes. The difference became negligible at the age of 21 days. At the age of 28 days and 180 days, specimens with fly ash exhibited higher impedance magnitudes with larger variation and noise. The impedance magnitude of C+W+F 0.28 specimen was more than 40 times higher than that of C+W 0.28 specimens.



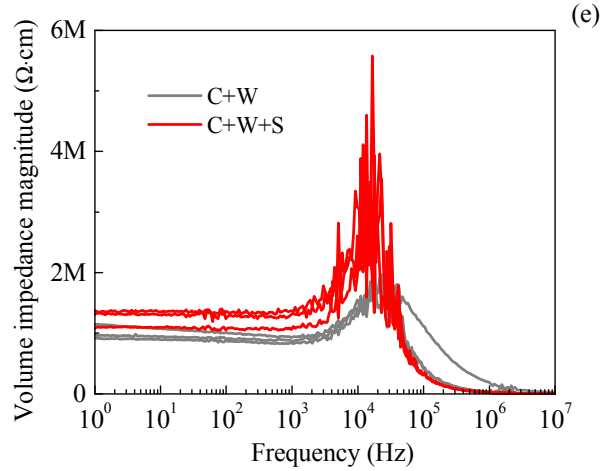
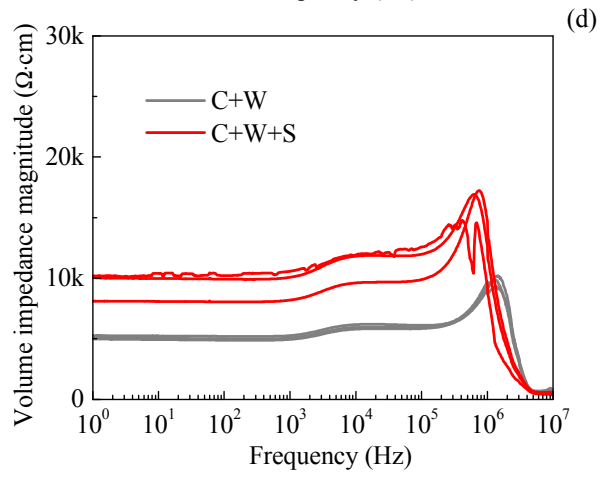
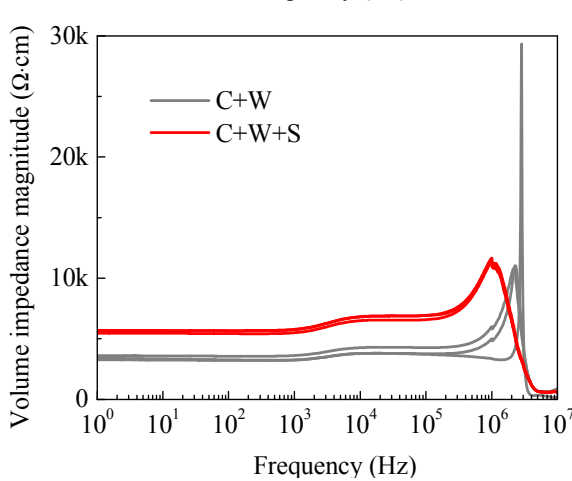
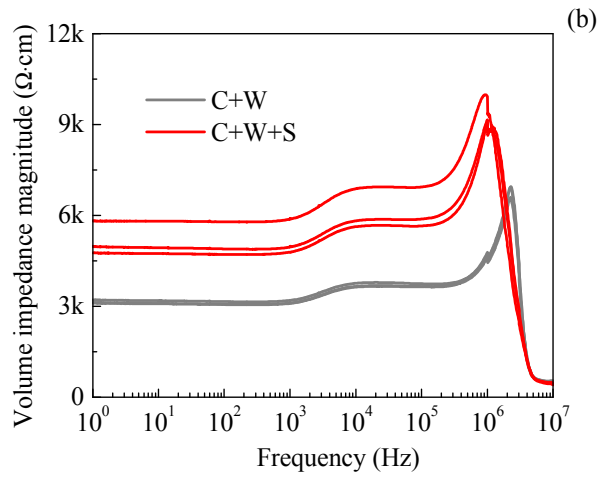
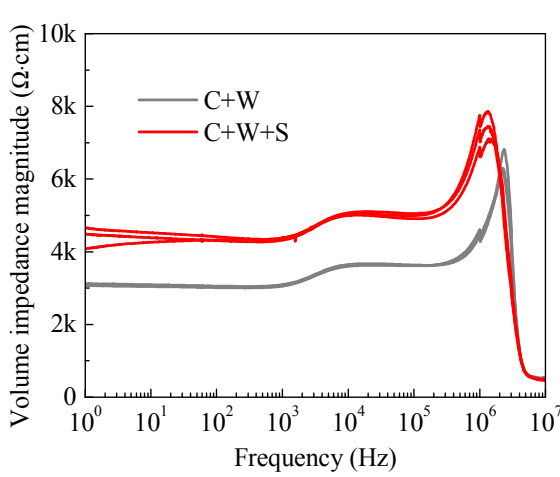


Figure 2.18 Bode plots of C+W+S 0.21 specimens and C+W 0.21 specimens, at the age of: (a) 7 days, (b) 14 days, (c) 21 days, (d) 28 days, and (e) 180 days



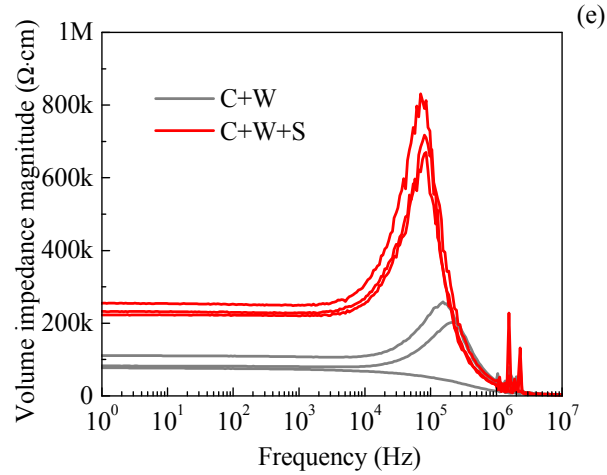
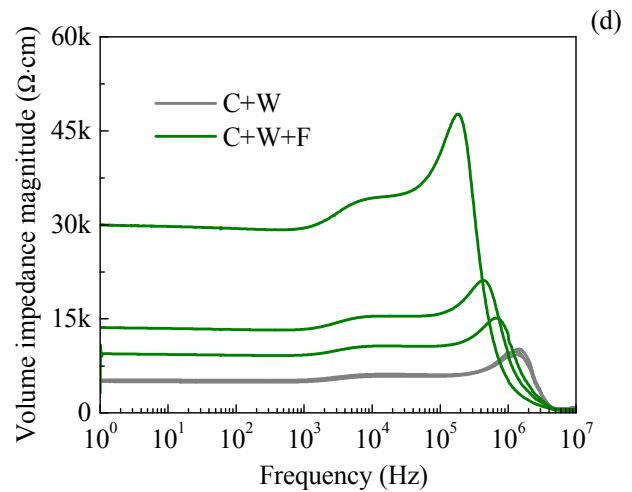
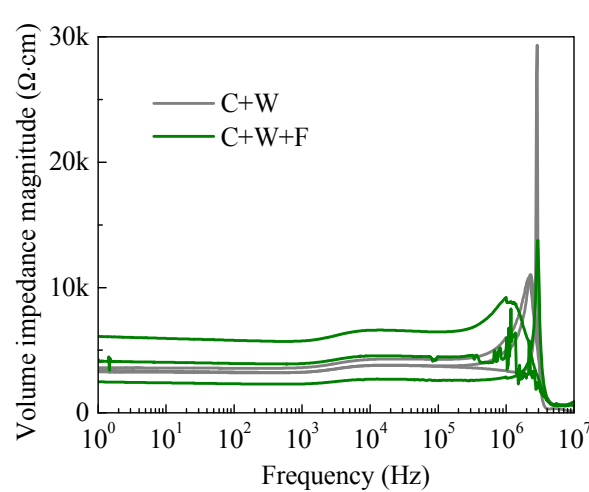
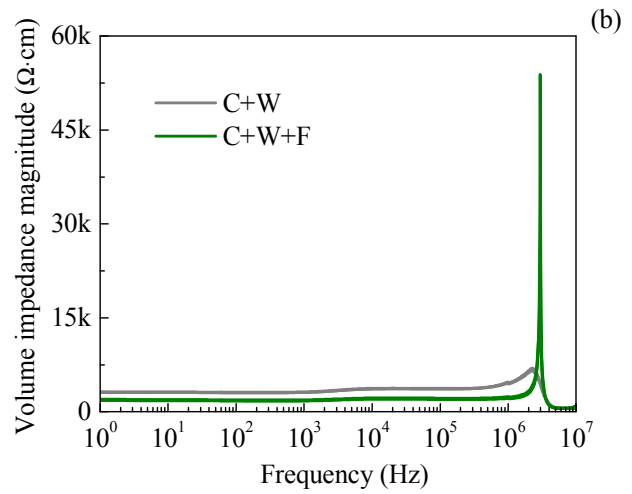
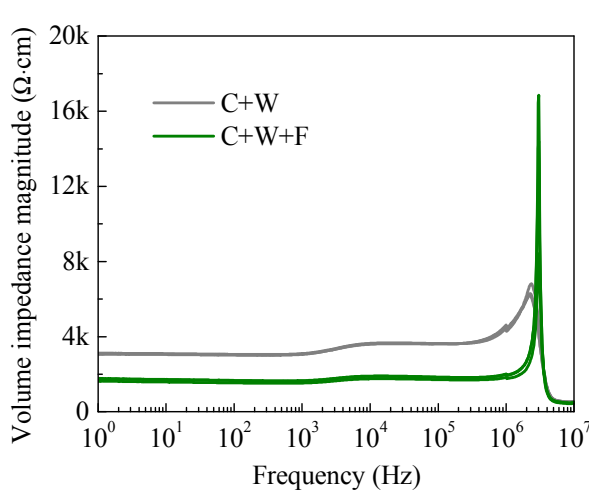


Figure 2.19 Bode plots of C+W+S 0.28 specimens and C+W 0.28 specimens, at the age of: (a) 7 days, (b) 14 days, (c) 21 days, (d) 28 days, and (e) 180 days



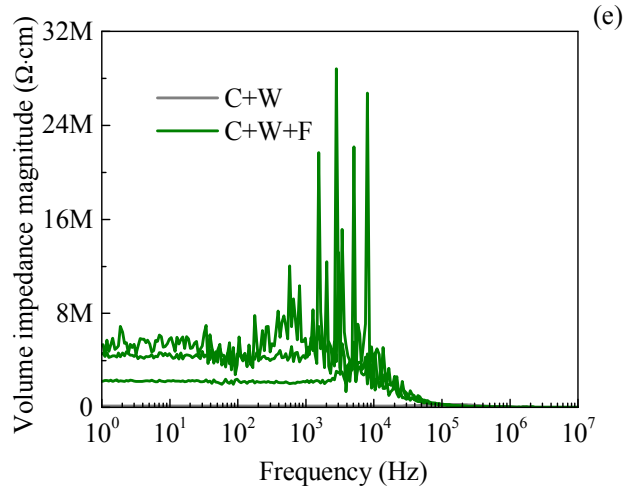
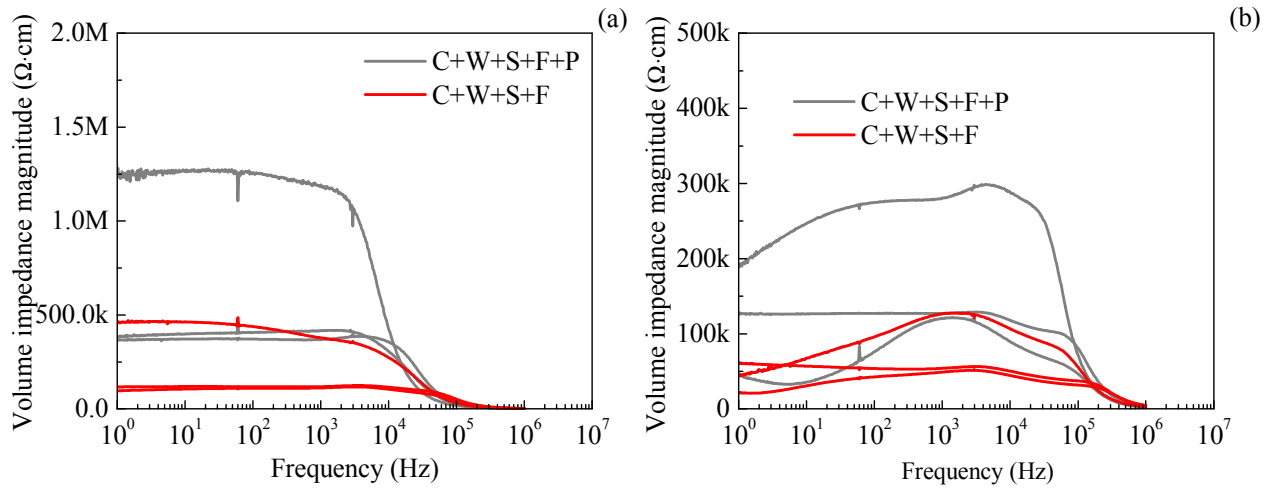


Figure 2.20 Bode plots of C+W 0.28 specimens and C+W+F 0.28 specimens, at the age of: (a) 7 days, (b) 14 days, (c) 21 days, (d) 28 days, and (e) 180 days





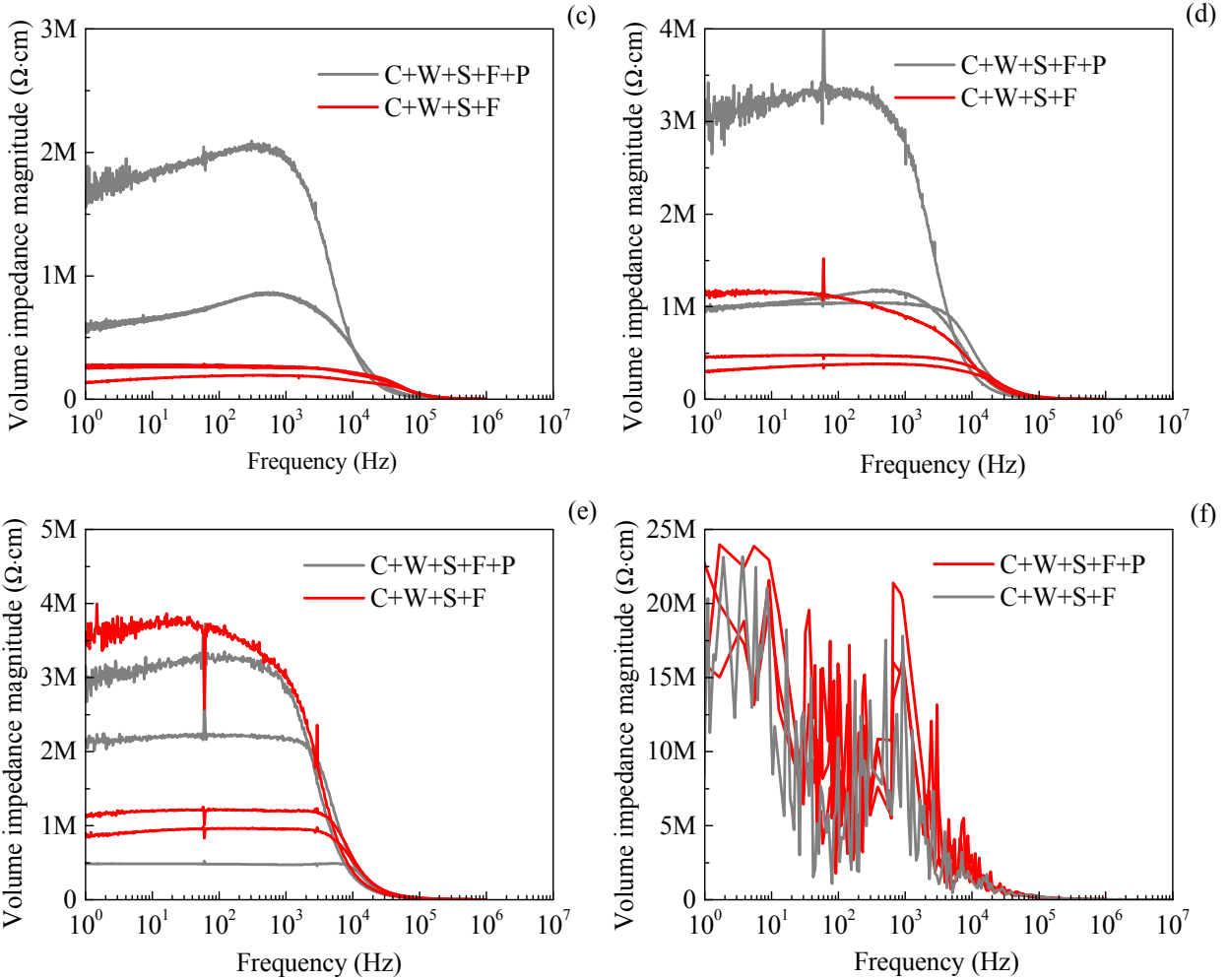
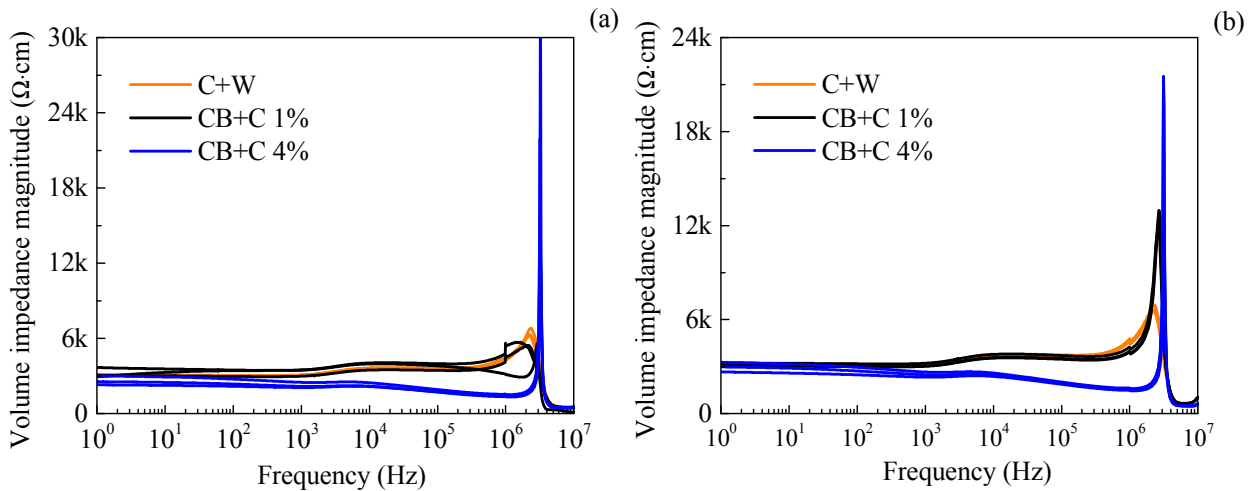


Figure 2.21 Bode plots of C+W+S+F 0.28 specimens and C+W+S+F+P 0.28 specimens, at the age of (a) 14 days, (b) 21 days, (c) 28 days, (d) 42 days, (e) 63 days and (f) 180 days



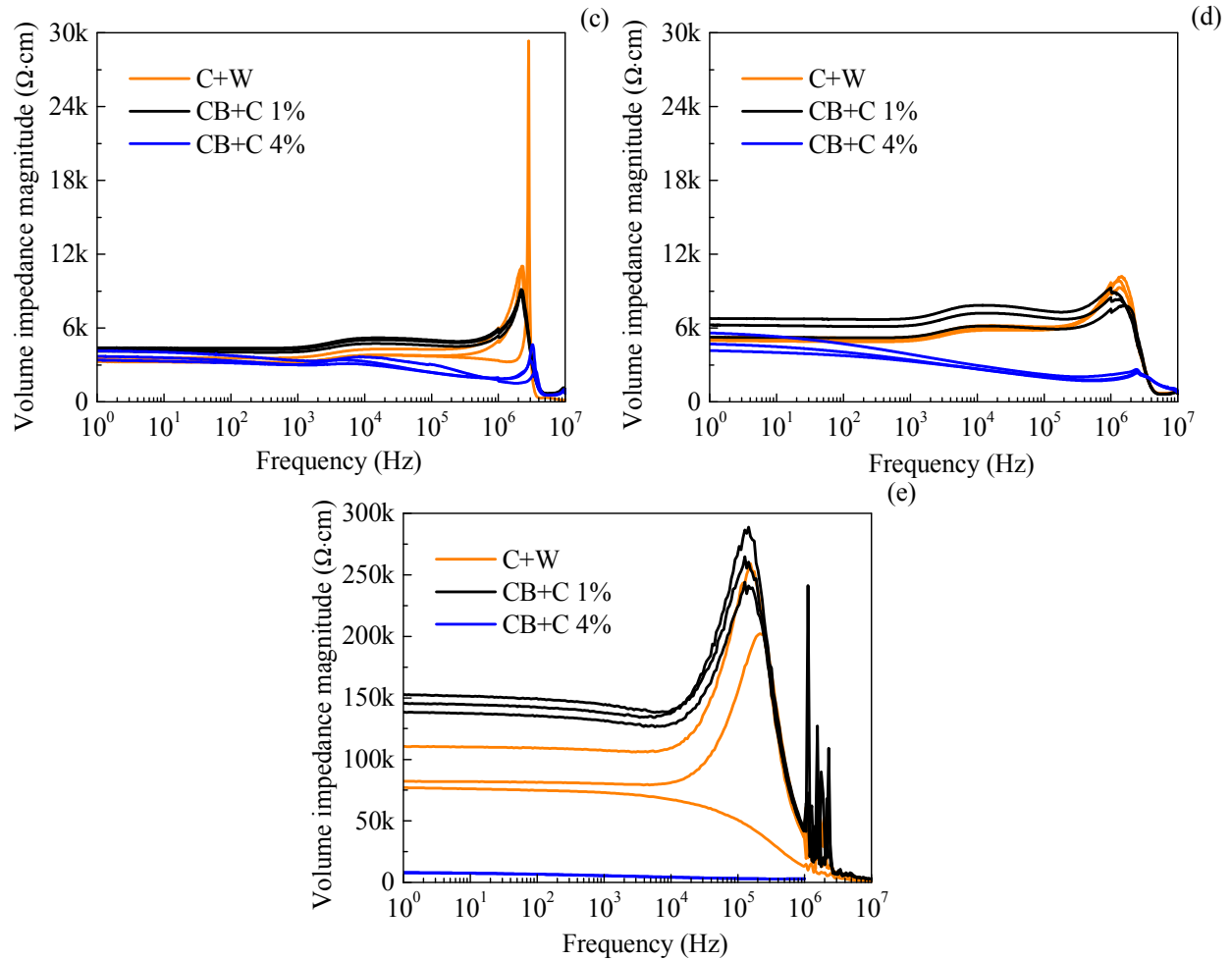


Figure 2.22 Bode plot comparison for C+W specimen, CB+C 1% specimen, and CB+C 4% specimen. (a) 7day, (b) 14 day, (c) 21 day, (d) 28 day, and (f) 180 day

The effects of PVA fibers on complex impedance of cementitious materials are shown in the bode plots in Figure 2.21. The specimens with PVA fibers exhibited higher impedance magnitudes at early ages. At later ages, i.e., 63 days and 180 days, no obvious difference was observed. In fact, the variation in the impedance results made it difficult to conclude that specimens with PVA fibers had higher impedance magnitude at most of the frequencies than specimens without fibers.

The effects of conductive nanoparticles, e.g. carbon black nanoparticles, on the complex impedance of cementitious materials are shown in the bode plots in Figure 2.22. Three scenarios

were investigated: 0%, 1% and 4% addition of carbon black nanoparticles. It was found that the addition of carbon black nanoparticles reduced impedance magnitudes, especially at later ages. Most interesting, the specimens with 4% of carbon black nanoparticles showed negligible age effect on impedance magnitudes. At the age of 180 days, the impedance magnitude of specimens with 4% of carbon black nanoparticles was three orders lower than specimens without and with 1% carbon black nanoparticles.

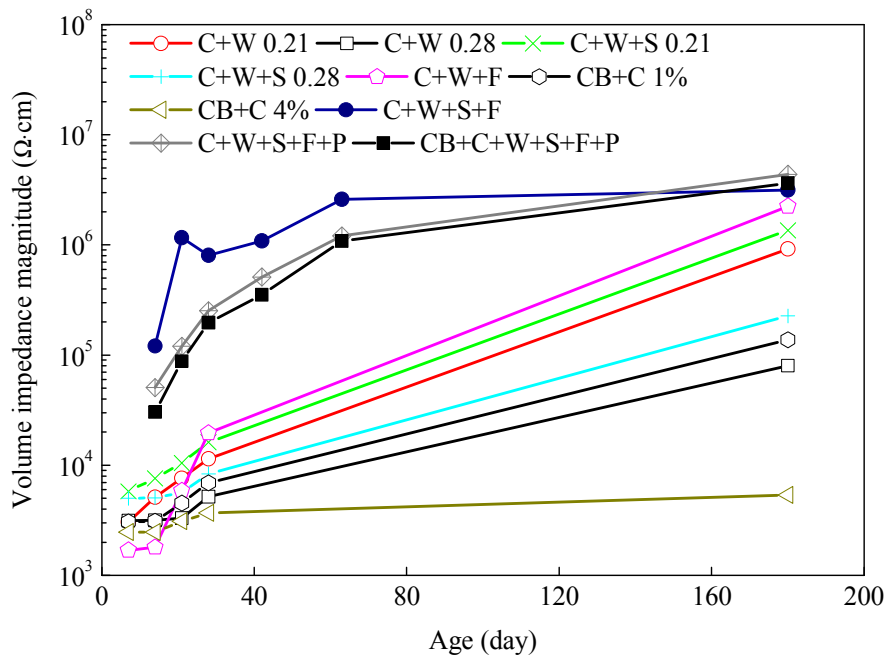


Figure 2.23 Evolution of impedance magnitude with age

The impedance magnitude changes with specimen age for all mixture designs at a fixed frequency of 1,500 Hz were plotted in Figure 2.23. The 180-day impedance magnitude of different mixture designs was further compared in Figure 2.24. Based on electrical impedance spectroscopy studies, the following conclusions were drawn:

- Material composition, proportion, and age all contributed to the changes of complex impedance at a wide range of excitation frequencies. Material aging led to increased

impedance magnitude, indicating the effect of hydration process on the change of the material microstructure, which subsequently resulted in less conductive paths within the cementitious material.

- Water/binder ratio played an important role in the electrical response of cementitious materials. A higher water/binder ratio led to lower impedance magnitude. This difference was small at specimen early age due to a lower hydration degree and thus higher amount of pore water containing ions that can be mobilized to generate current; however, the difference became significantly large at later ages of cementitious materials, as the hydration process consumed more water.
- Silica sand dispersed in cementitious matrix acted as nonconductive paths, leading to increases in impedance magnitude for a wide range of excitation frequencies, and for both early and later ages.
- Fly ash had an age-dependent effect on the impedance magnitude: specimens with fly ash exhibited lower impedance at earlier ages, but higher impedance at later ages compared with specimens without fly ash. This effect was due to the lower hydration rate at earlier ages and increased pozzolanic reaction at later ages.
- Introducing PVA fibers into cementitious materials led to an increase of impedance; such increase was more significant at earlier ages and became negligible at later ages. In addition, the Bode plots of specimens with PVA fibers had higher noise, probably due to the increased porosity and nonhomogeneity of material microstructure.
- Adding conductive carbon black nanoparticles into cementitious materials was an effective way to reduce impedance magnitude while minimizing the effect of age on the electrical response of cementitious materials.

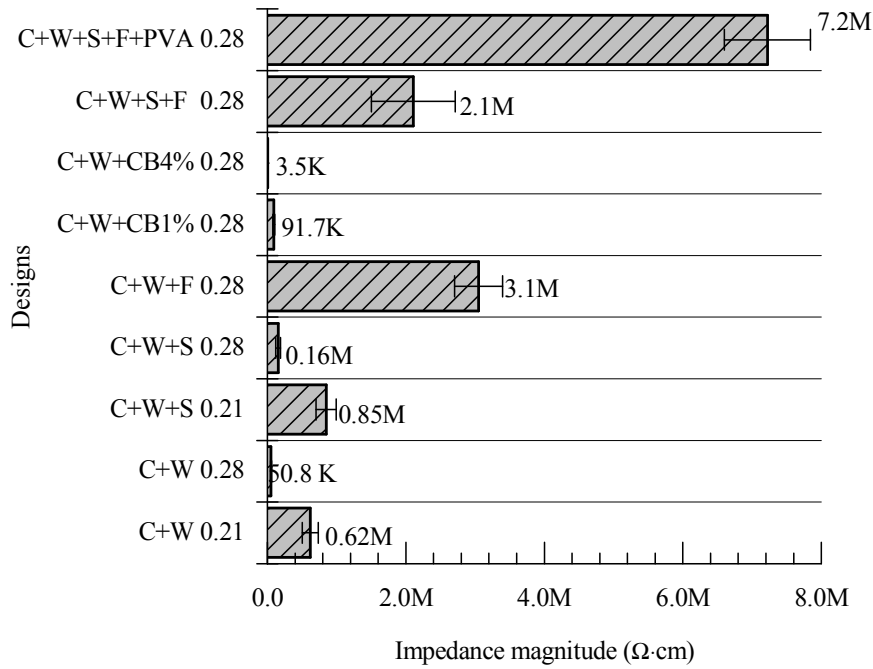


Figure 2.24 Impedance magnitude comparisons of different designs at the age of 180 days

## 2.5 Equivalent Circuit Model

Through impedance spectroscopy, the frequency-dependent electrical behavior of the cementitious composite material was represented by an idealized model circuit consisting of discrete electrical components. Analyzing the changes of model parameters revealed the mechanisms that contribute to the overall electromechanical response of the cementitious composite material. In the equivalent circuit model, the material is represented by an equivalent parallel circuit containing a capacitor and a resistor connected in series, in parallel with a capacitor, and a resistor (Figure 2.25). The total impedance ( $Z$ ) of the bulk material is described as Eq. (2.9).

$$Z = \frac{1}{\frac{1}{R_1} + \frac{1}{R_2 + \frac{1}{j\omega C_2}} + j\omega C_1} \quad (2.9)$$

where  $j$  is the imaginary number, and  $\omega$  is the angular frequency of the sinusoidal signal.  $R_1$  represents the overall resistance of the conductive paths in the direction of the electrical current, which is the well-connected pore structure where ions can be mobilized to generate current. For the cementitious materials with carbon black nanoparticles, conductive paths were formed by adjacent carbon black nanoparticles that were electrically connected through direct contact or tunnel effect [128, 182].  $C_2$  and  $R_2$  connected in series represent the overall electrical behavior of the partially conductive paths, for which the partially connected pores and carbon black nanoparticles (if any) in the direction of the electrical current behave as a resistor; the regions in between the connected pores (and carbon black nanoparticles) behave as dielectrics in between conductors, providing a capacitor effect ( $C_2$ ).  $C_1$  represents the overall capacitor effect of the nearly nonconductive paths along the direction of AC current in the cementitious material. The electrical insulation is attributed to the presence of calcium silicate hydrate gel binding the silica aggregates and nonconductive PVA fibers.

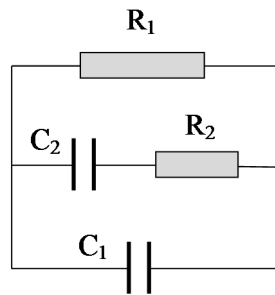


Figure 2.25 Equivalent circuit model

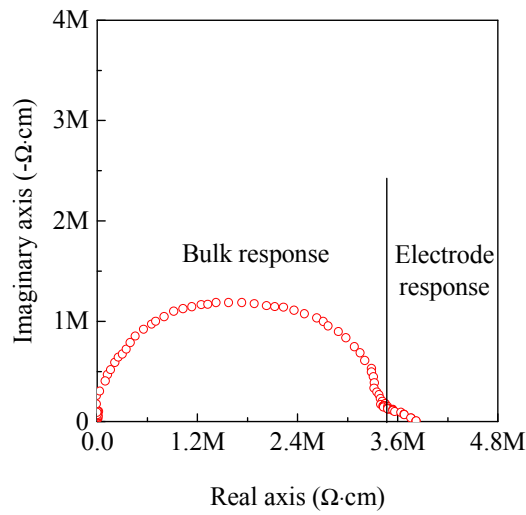


Figure 2.26 Typical Nyquist plot of a cementitious material

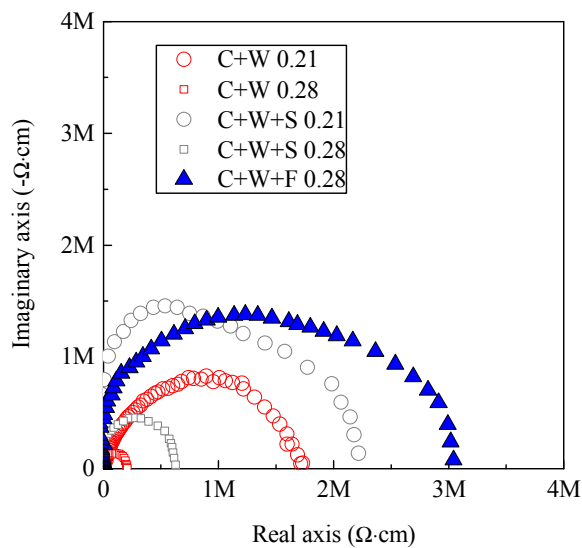


Figure 2.27 Typical Nyquist plot results of cementitious materials at the age of 180 days

Nyquist plot is such plot that the electrical impedance magnitude and the phase degree were comprehensively considered, and the impedance was represented by a complex number. Figure 2.26 shows a typical Nyquist plot of a cementitious material. Therefore, the plot includes two parts: low-frequency arc and the high-frequency depressed semicircular arc. It is believed that the high-frequency arc is related to the bulk responses, while the low-frequency arc is

attributed to the electrode-bulk interfacial responses. Nyquist plots also allow revealing the age effects and composite effects on the electrical responses of the cementitious materials. Figure 2.26 shows the represented Nyquist plots of cementitious materials showing the composite effects at the age of 180 days. It is observed that the changing water/binder ratio from 0.21 to 0.28 (for C+W and C+W+S) results into the change of the high-frequency arc: the center of the arc moved from right to left and the radius decreased. Similarly, involving sand and Fly ash into the matrix leads to following phenomena: radius increased, and the center moved to the right. Figure 2.27 shows the represented Nyquist plots showing the age effects. It can be observed that increasing age leads to a corresponding increase in the radius and a movement of the center of the arc from left to right gradually. Above observations can be modeled and interpreted by the model in Figure 2.25.

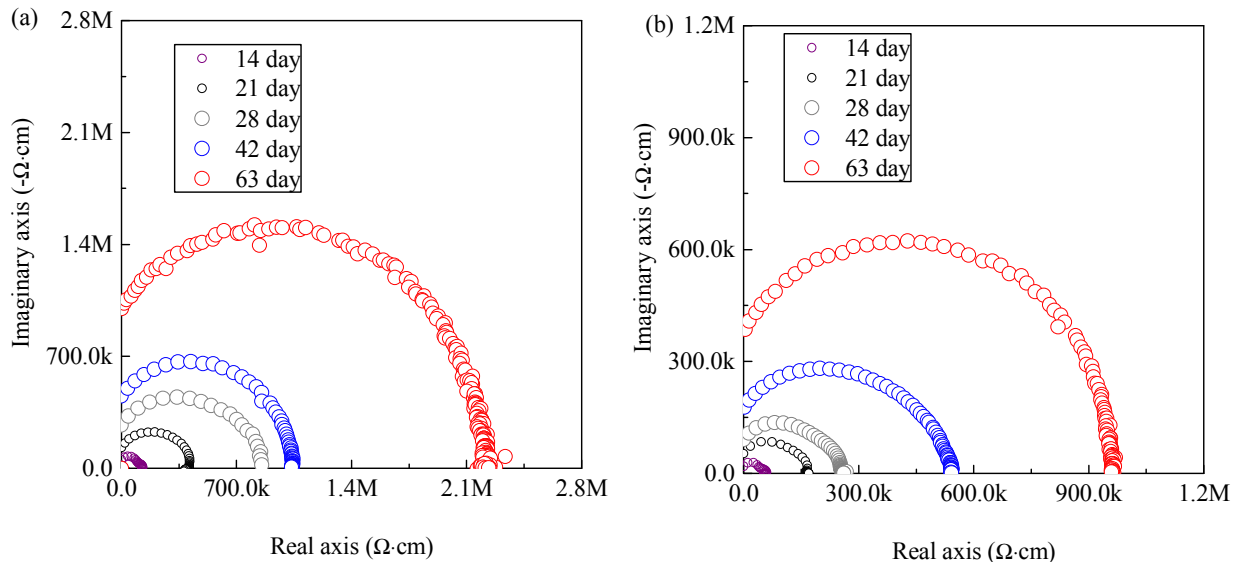


Figure 2.28 Nyquist plot of (a) C+F+S+W+P and (b) C+F+S+W at different ages



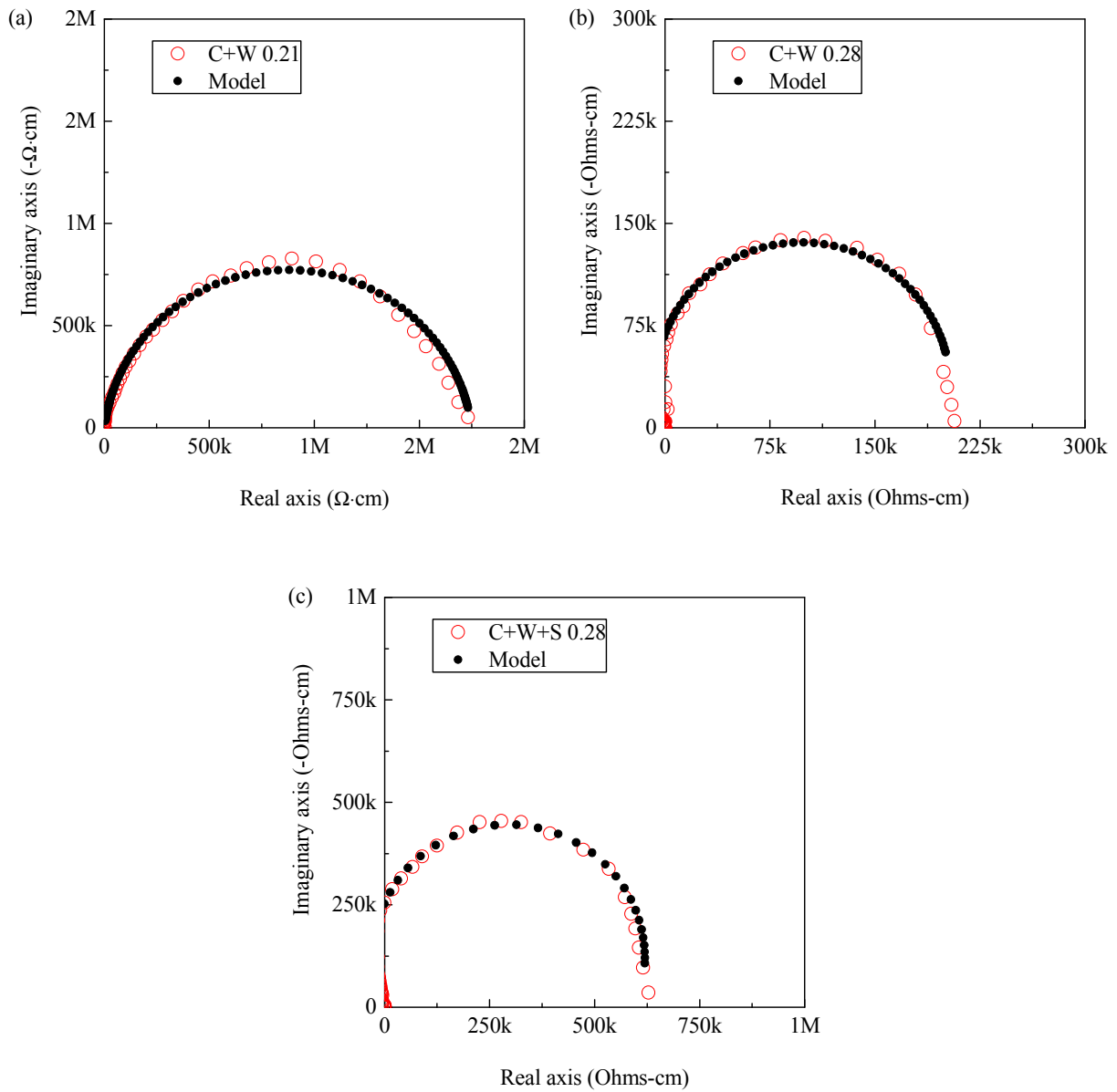


Figure 2.29 Typical Nyquist plots of cementitious materials and corresponding model results. (a) C+W 0.21; (b) C+W 0.28; (c) C+W+S 0.28

Figure 2.29 shows the typical Nyquist plots of cementitious materials and corresponding model results: (a) C+W 0.21, (b) C+W 0.28, and (c) C+W+S 0.28. It is observed that there is a good matching between the model results and the experimental results, validating the conclusions drawn based on the equivalent circuit model. The conductive path resistance  $R_1$  and

the partially conductive path resistance  $R_2$  are plotted in Figure 2.30. It is observed that the conductive paths in above cementitious materials are fewer than the partially conductive paths. C+W+S+F+P has the highest conductive path resistance, suggesting that sand, fly ash and PVA fibers contribute to fewer conductive paths in the cementitious materials.

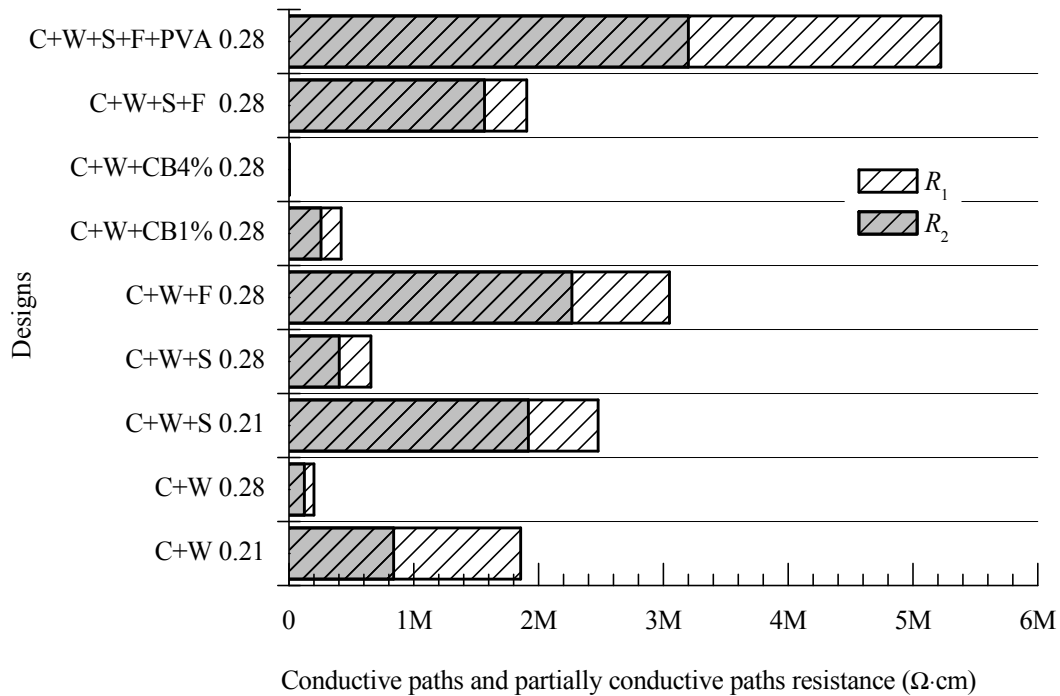


Figure 2.30 Effects of material composition on continuous conductive path  $R_1$  and partially conductive path  $R_2$  at the age of 180 days

## 2.6 Conclusions

Using the EIS and equivalent circuit model allows understanding the electrical responses of cementitious materials, unveiling the effects of aging and composites on the electrical microstructure of the cementitious materials. The following conclusions are drawn:

1. The cementitious material is modeled by an equivalent parallel circuit containing a capacitor and a resistor connected in series, in parallel with a capacitor, and a resistor. In this

sense, the electrical microstructure of cementitious material can be represented by three types of paths: conductive path, partially conductive path, and nearly nonconductive path.

2. Aging of cementitious materials leads to increased impedance. With increasing age, the hydration of cementitious materials results into formation of nonconductive hydration products, such as C-S-H. At the same time, porosity and internal moisture level decreases. This leads to fewer conductive paths and partially conductive paths.

3. A higher water/binder ratio leads to lower impedance, suggesting that higher water/binder ratio enhances the conductive paths in the cementitious matrix. Conductive paths are formed by connected pore solutions in matrix. Increasing water/binder ratio results into an increase of internal moisture level, and thus increases conductive paths.

4. Silica sand and PVA fibers acts as nonconductive particles, blocking the conductive paths in the cementitious matrix. Therefore, involving silica sand and PVA fibers leads to an increase in impedance.

5. Fly ash has an age-dependent effect on the impedance: specimens with fly ash exhibit lower impedance at earlier ages, but higher impedance at later ages compared with specimens without fly ash.

6. Adding conductive carbon black nanoparticles into cementitious materials is an effective way to tailor electrical property of cementitious materials. The carbon black nanoparticles have an average size of 40 nm, which favors highly uniform dispersion. More conductive paths are formed by adjacent carbon black nanoparticles that are electrically connected through direct contact or tunnel effect.

## **CHAPTER 3: MATERIAL DESIGN OF MULTIFUNCTIONAL STRAIN-HARDENING CEMENTITIOUS MATERIALS**

### **3.1 Introduction**

This chapter aims to achieve strain-hardening, crack width control and enhanced piezoresistivity behavior simultaneously within a single material platform, named MSC. It is achieved by incorporating conductive carbon black nanoparticles into the strain-hardening cementitious composites system with non-conductive polymeric fibers to tailor composite rheological, mechanical and electrical properties (Figure 3.1(a)). Carbon black particles, as well as pore solution, form a conductive network. The change of the conductive network caused by mechanical stimulus results in the change of impedance measurement for sensing purpose (Figure 3.1(b) and (c)). The uniqueness of this study is two-fold: First, strain sensing capacity is not limited to an initial elastic stage ( $0 \sim 0.3\%$  in compression and  $0 \sim 0.01\%$  in tension) as self-sensing concrete. Second, nonlinear strain sensing due to strain-hardening behavior makes early warning feasible long before final failure. For elastic strain sensing, under mechanical strain, the conductive network is changed correspondingly, resulting in the linear relation between strain and electrical response (Figure 3.1(b)). For strain-hardening and tension softening strain sensing, microcracks divide the matrix with the conductive network into several parts, inducing a change in electrical response (Figure 3.1(c)). A linear change of electrical response is harvested from the elastic strain, and a nonlinear change of electrical response is harvested from the strain-hardening and tension softening stage.

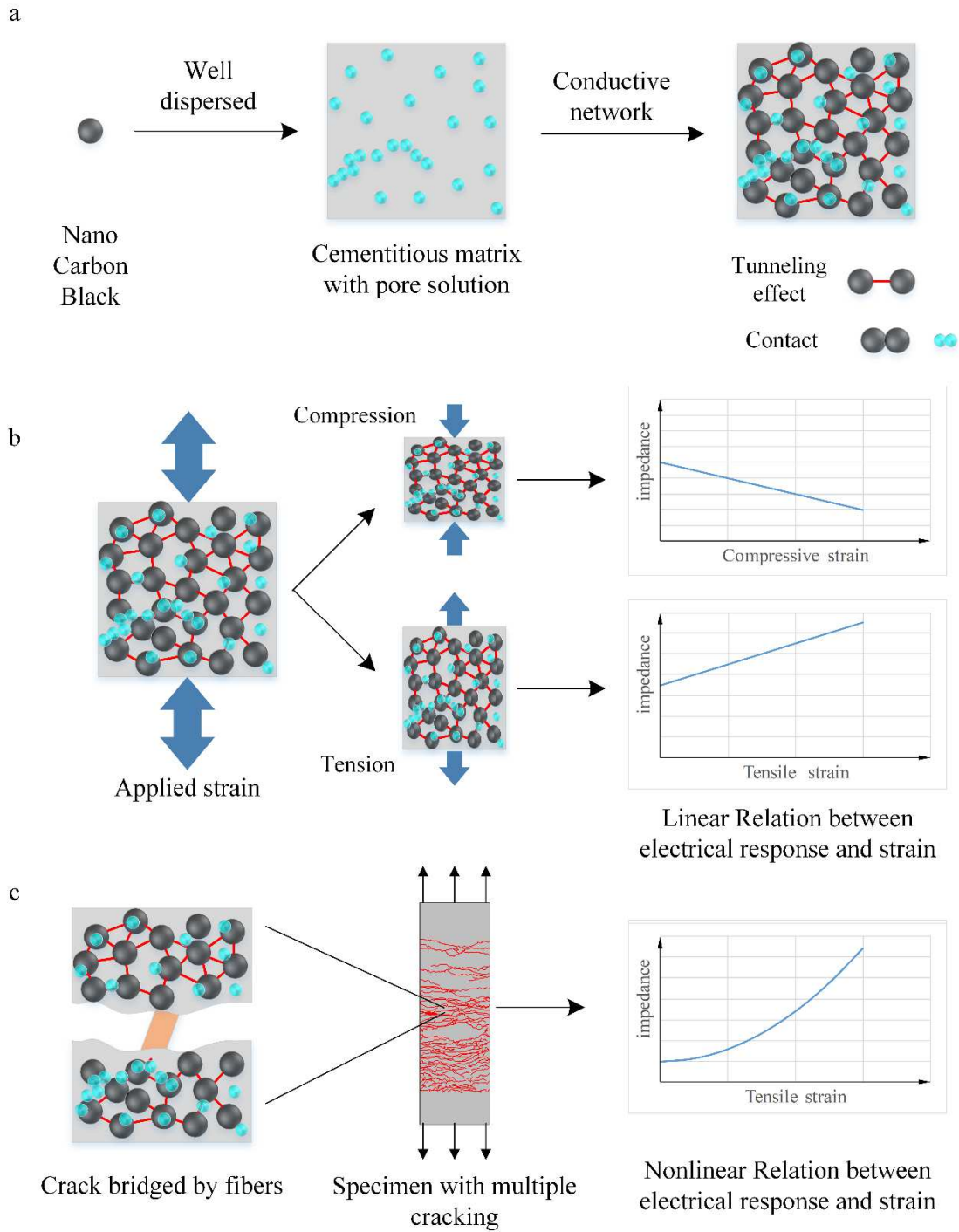


Figure 3.1 The concept of MSCs: (a) cementitious matrix with conductive particles. (b) elastic strain sensing. (c) nonlinear strain sensing

### **3.2 Electrical Microstructure Design Guided by Electrical Impedance Spectroscopy**

Designing self-sensing and strain-hardening into fiber reinforced cementitious composite materials requires understanding and tailoring material microstructure to achieve the desired macroscopic electromechanical properties. In this study, electrical impedance spectroscopy (EIS) was performed on cementitious specimens with different mix designs to understand how the microstructure, which contains a combination of electrically conductive, nonconductive and partially conductive paths, affects the material frequency-dependent electrical response. It is hypothesized that the electrical parameters of the cementitious matrix can be tailored by incorporating conductive nanoparticles, e.g., carbon black nanoparticles, within an optimum range to achieve a strong piezoresistive behavior with a high signal-to-noise ratio. During material elastic straining stage, a stronger piezoresistive behavior indicates that a small change in elastic strain can induce a larger change in electrical impedance, leading to a higher sensing sensitivity. In addition, a high signal-to-noise ratio is necessary for achieving the sensing accuracy with a low background noise, during material elastic straining as well as post-cracking stages. It is further hypothesized that the incorporation of carbon black nanoparticles would impact the micromechanical parameters of the cementitious matrix (e.g. matrix toughness) and the fiber/matrix interfaces (e.g. interfacial bonds), consequently changing the material cracking behavior. The cracking behavior would then affect the material electrical response during both strain-hardening and tension softening stages. These effects will be investigated through impedance spectroscopy, mechanical, and electromechanical measurements in this study.

#### *3.2.1 Initial mix design incorporating carbon black nanoparticles*

Four different mixing proportions were initially designed, as shown in Table 3.1. The control mix design (0% SHC) was adopted from Li et al [183], which features a tensile strain-

hardening behavior through the sequential formation of multiple microcracks under increasingly applied tensile strain. The control mix contained water, Portland type I cement, fine silica sand (mean grain size = 270  $\mu\text{m}$ ), class F fly ash ( $\text{CaO} < 7\%$ ), a poly-carboxylate-based superplasticizer, and Polyvinyl alcohol fibers (length = 8 mm, diameter = 40  $\mu\text{m}$ , 1.5% oil coating, strength = 1,300 MPa). In addition, carbon black nanoparticles were introduced into the fiber-reinforced cementitious composite at different volume percentages of 2.5%, 5%, and 10%, respectively. These three mix designs are called 2.5% MSC, 5% MSC and 10% MSC, respectively, with “MSC” standing for multifunctional strain-hardening cementitious composite. Carbon black nanoparticles are inexpensive ingredients, and are most commonly used as a pigment and in automobile tires [184, 185]. The carbon black nanoparticles have an average size of 40 nm, a conductivity of 0.1 S/cm, and a density of 1.8  $\text{g/cm}^3$ . For all mix designs, the ratios between cement, fly ash and sand were kept the same. Due to the porous structure of the carbon black nanoparticles and their large surface area, the water-to-binder ratio was increased with the higher amount of carbon black to achieve appropriate rheology during processing. The water-to-binder ratio was kept between 0.25 and 0.30.

Table 3.1 Mix designs investigated in this study

Design	Water $\text{kg/m}^3$	Cement $\text{kg/m}^3$	Sand $\text{kg/m}^3$	Fly ash $\text{kg/m}^3$	Carbon Black $\text{kg/m}^3$	Superplast icizer $\text{kg/m}^3$	Fiber Vol-%	Silica Fume $\text{kg/m}^3$	Water- binder ratio	28-day compressive strength MPa
<b>Initial Design</b>										
0% SHC	312	292	456	935	0	2.7	2	0	0.25	44.6
2.5% MSC	312	285	445	912	12.5	2.7	2	0	0.26	36.6
5% MSC	314	277	433	888	25	2.7	2	0	0.27	32.5
10% MSC	330	263	410	842	51	2.7	2	0	0.30	30.2

<b>Re-design</b>										
0% SHC	312	292	456	935	0	2.7	2	0	0.25	44.6
2.5% MSC	277	243	380	584	12.5	2.7	2	113	0.33	42.1
5% MSC	296	243	380	600	25	3.5	2	115	0.35	40.3
10% MSC	313	243	380	611	51	4.0	2	117	0.37	38.2

### 3.2.2 Specimen preparation

All specimens were prepared at controlled room temperature of  $20 \pm 1^\circ\text{C}$  and relative humidity of  $50 \pm 5\%$ . All dry particles such as cement, fly ash, silica sand, and carbon black nanoparticles were first mixed for 3 minutes. Water was then added together with the superplasticizer to form a homogeneous mortar with the optimum rheology favoring uniform dispersion of PVA fibers and carbon black. The PVA fibers were then added and mixed for 2 minutes until uniformly dispersed. Owing to the small size of carbon black nanoparticles, inter-particle interactions are subjected to Van Der Waals forces, leading to a high tendency of particle agglomeration [86, 186, 187]. Therefore, a high shear rate is necessary to separate the agglomerates into smaller aggregates or single primary particles [87, 188]. In this study, the high-structure carbon black rather than the low-structure carbon black was adopted, due to its high electrical conductivity, easier dispersion, and less dense packing [85, 189, 190]. The less dense packing in high-structure carbon black allows more space to be accessible to the cementitious binder with increased entanglement and lower inter-aggregate attractive forces; both mechanisms facilitate the dispersion of the carbon black nanoparticles in the cementitious matrix [84, 191, 192]. The fresh mixture was cast into two types of specimens: (1) Coupon specimens ( $254\text{ mm} \times 51\text{ mm} \times 12.5\text{ mm}$ ) for uniaxial direct tension tests. Some of the specimens were further cut into  $165\text{ mm} \times 51\text{ mm} \times 12.5\text{ mm}$  specimens for EIS measurements;



(2) Cylinder specimens with a height of 152 mm and a diameter of 76.2 mm for uniaxial compression tests. After casting, the specimens were covered with plastic sheets and demolded after 24 hours. Then, the specimens were water-cured till the age of 7 days, and then air-cured with ambient temperature of  $20 \pm 1^\circ\text{C}$  and relative humidity of  $45 \pm 5\%$  till the age of 28 days. Afterward, the specimens were exposed to the outdoor environment until the age of 42 days for testing.

### 3.2.3 Four-point electrical impedance spectroscopy

Frequency-dependent 4-point AC impedance spectroscopy and equivalent circuit analysis were performed to understand the effect of carbon black nanoparticles on the electrical parameters of the cementitious specimens based on the understanding in Chapter 2.

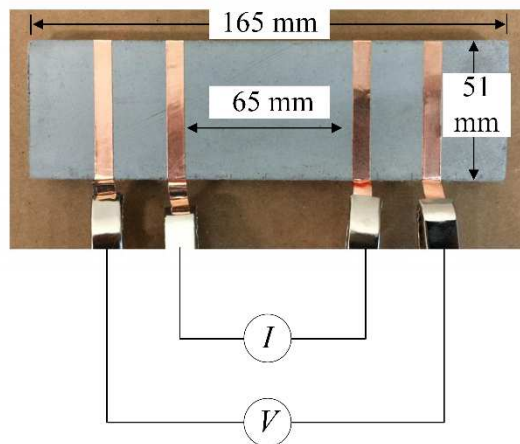


Figure 3.2 EIS specimen details

Four copper electrodes were attached to the specimen surfaces with conductive silver colloidal paste (Figure 3.2). The two outer electrodes were used to inject AC current at frequencies ranging from 0.1 Hz to 10 MHz into the specimen. The two inner electrodes were used to measure the in-situ voltage within the specimen. The electrodes were parallel to each other and spaced with sufficient distance in order for the current to be continuous and perpendicular to the electrodes.

### 3.2.4 Effect of carbon black nanoparticles on electrical microstructure and parameters

Through impedance spectroscopy, the frequency-dependent electrical behavior of the cementitious composite material was represented by an idealized model circuit consisting of discrete electrical components in Figure 2.25. Analyzing the effects of carbon black nanoparticles on the changes of model parameters revealed the mechanisms that contribute to the overall electromechanical response of the cementitious composite material.

In this study, for the older specimens at the age of 42 days, there were limited conductive paths due to the less connected pore structure. When carbon black nanoparticles were dispersed in the cementitious matrix, more conductive paths were formed by adjacent carbon black nanoparticles that were electrically connected through direct contact or tunnel effect [128, 182].  $C_2$  and  $R_2$  connected in series represent the overall electrical behavior of the partially conductive paths, for which the partially connected pores and carbon black nanoparticles (if any) in the direction of the electrical current behave as a resistor; the regions in between the connected pores (and carbon black nanoparticles) behave as dielectrics in between conductors, providing a capacitor effect ( $C_2$ ).  $C_1$  represents the overall capacitor effect of the nearly nonconductive paths along the direction of AC current in the cementitious material. The electrical insulation is attributed to the presence of calcium silicate hydrate gel binding the silica aggregates and nonconductive PVA fibers.

As the material electrical microstructure strongly depends on the dispersion and connectivity of carbon black nanoparticles, scanning electron microscopy (SEM) and X-ray spectroscopy (EDS) were conducted to map the dispersion of carbon black nanoparticles in the cementitious matrix. 10 mm × 10 mm × 10 mm samples were carefully cut and cleaned in an ultrasonic bath for 1 minute, then slowly dried in a vacuum chamber to remove the vapor inside

the pore space. The sample surfaces were not coated because the conductivity of carbon black reduced the charging effect. SEM (FEI Quanta Dual Beam) was performed on the samples under a low-vacuum condition at 10 kV voltage and probe current of 180 pA using back-scattered electron signal. EDS (INCA, Oxford Instruments) mapping was performed to analyze carbon element for a total of 600 data points ( $30 \times 20$  rectangular area,  $1\mu\text{m}$  increments). The carbon element mapping of the cementitious sample with 5% carbon black is shown in Figure 3.3(a). The image was further converted into a binary image shown in Figure 3.3(b). The images clearly reflect the carbon black nanoparticles network and the three possible electrical paths within the material microstructure: conductive, partially conductive, and nonconductive paths.

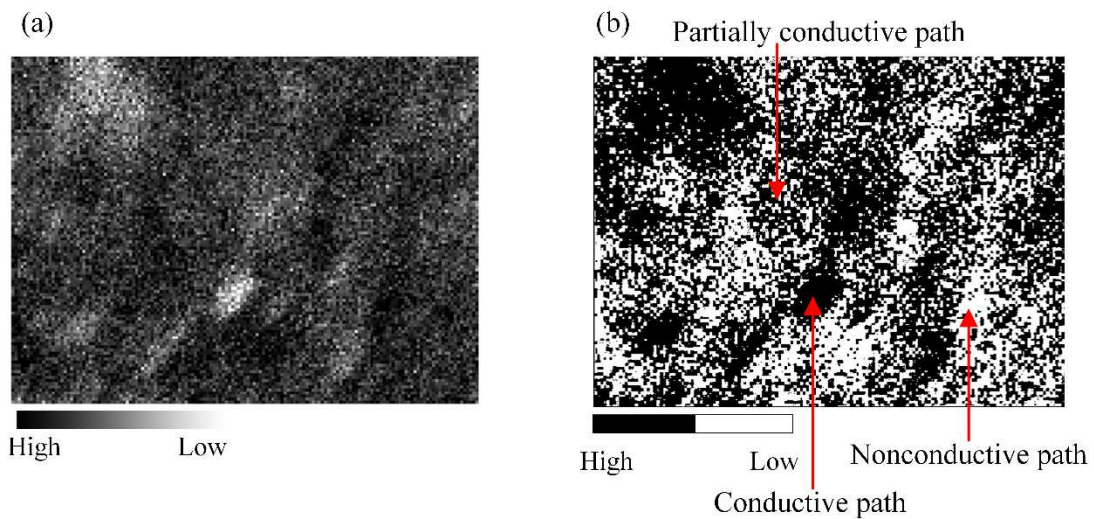


Figure 3.3 EDS mapping of carbon black distribution in a cementitious matrix. (a) EDS element map of carbon black, (b) Binary image of carbon black distribution

Figure 3.4 shows the Nyquist plots of the AC impedance spectra of cementitious specimens containing 0%, 2.5%, 5% and 10% carbon black nanoparticles. Each impedance spectrum exhibits a high-frequency depressed semicircular arc (left) describing the electrical response of the bulk material, and a depressed arc (right) ascribed to the electrode-interface behavior. Only the high-frequency semicircle arc was considered for the equivalent circuit

model. The center of the arc was displaced away from the real axis because the material system contained distributed elements, leading to a relaxation time that was not single-valued but continuously distributed [54]. When the amount of carbon black nanoparticles increased from 0% to 10%, the impedance spectrum moved from right to left along the real axis, indicating that the material impedance decreased at high and also low AC frequencies. Meanwhile, the arc diameter significantly decreased from around  $1.34 \text{ M}\Omega\cdot\text{cm}$  to around  $3.23 \text{ }\Omega\cdot\text{cm}$ , suggesting a decrease in the imaginary part of material complex impedance and a reduction in the capacitor effect of the material. The imaginary part represented the phase lag between voltage and current and also the energy storage of the circuit elements. Based on the impedance spectra measured by EIS, the electrical parameters of the equivalent circuit model were determined. The two capacitors in the equivalent circuit model,  $C_1$  and  $C_2$ , were considered as constant phase elements, i.e., imperfect capacitors, to more accurately represent the compressed high-frequency arc. The modeling results are shown in Figure 3.4 in comparison to the experimental data. It should be noted that the capacitors were considered as constant phase elements in the simulation.

The effects of carbon black nanoparticles on the equivalent circuit model parameters are shown in Figure 3.5. Note that the electrical parameters are plotted on a log-scale. With increasing amount of carbon black nanoparticles, both  $R_1$  and  $R_2$  decreased and both  $C_1$  and  $C_2$  increased, indicating an increase in the conductive and partial-conductive paths and a decrease in nonconductive paths in the material.

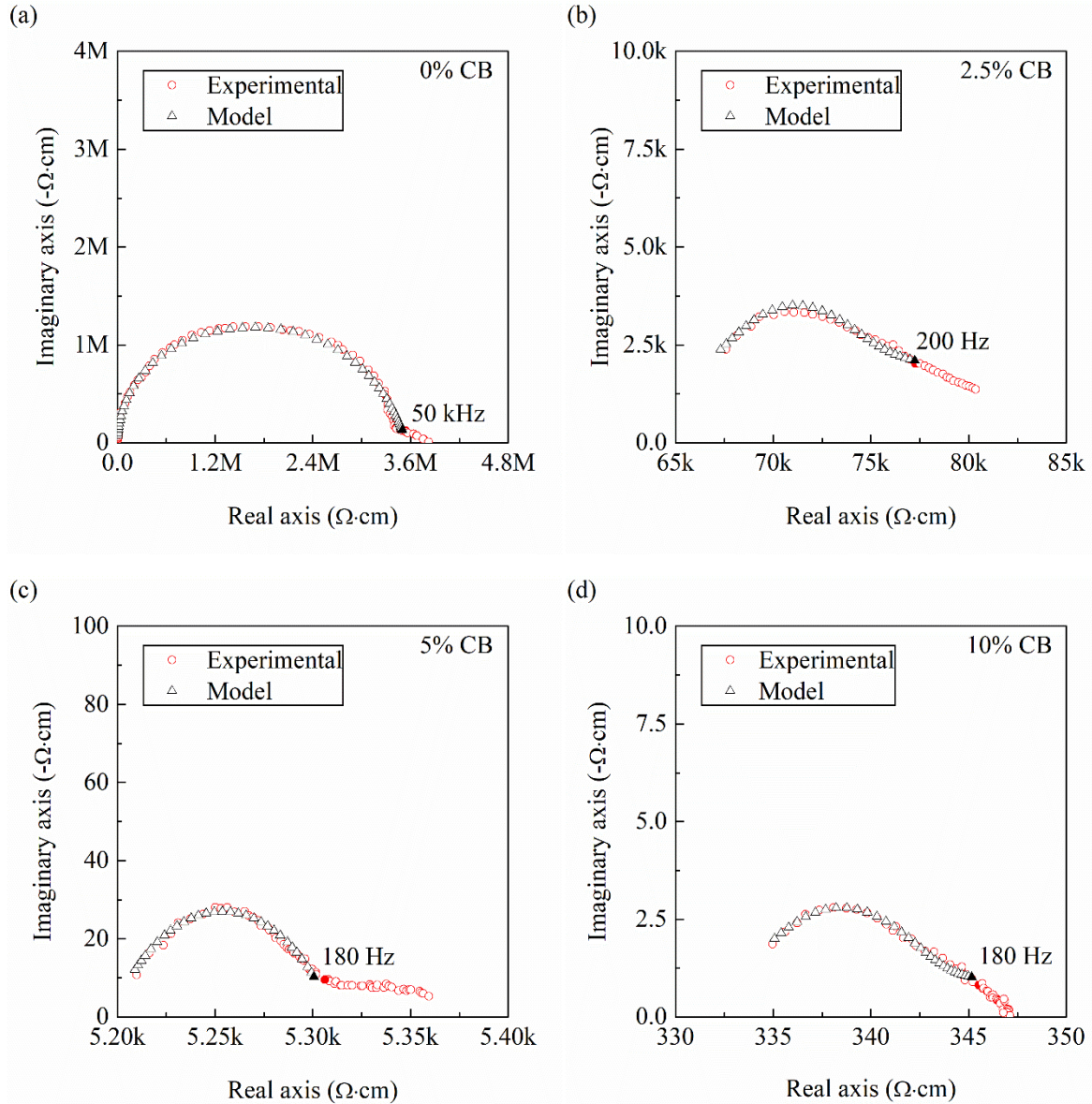
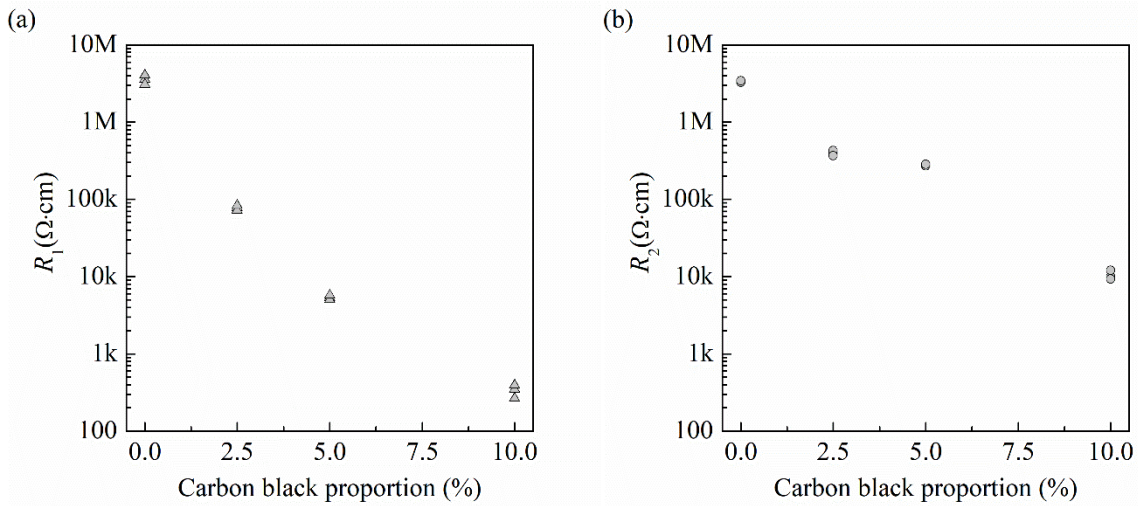


Figure 3.4 Complex Nyquist plots and equivalent circuit modeling results of cementitious composite materials with (a) 0%, (b) 2.5%, (c) 5%, and (d) 10% carbon black nanoparticles

The fastest drop in  $R_1$  and  $R_2$  both occurred between 0% and 2.5% of carbon black amount, while the decrease in  $R_1$  was more prominent than the decrease in  $R_2$ . This revealed that increasing carbon black from 0 to 2.5% led to the formation of a larger number of conductive paths than partially conductive paths, suggesting two simultaneous processes: a portion of the partially conductive paths changed into conductive paths, while an even higher portion of the

nonconductive paths changed into partially conductive paths. This is further supported by the evidence of an increase in  $C_2$  accompanying the decrease in  $R_2$ , indicating the increase in both capacitor effect ( $C_2$ ) and resistor effect ( $R_2$ ) due to the overall increasing amount of partially conductive paths. It was also found that the decreasing trend in  $R_1$  and  $R_2$  became slower at a higher amount of carbon black, i.e., from 5% to 10%, while the increasing trend in  $C_2$  became much larger. This suggested that at such a high content of carbon black nanoparticles, the material system prevalently contained conductive and partial-conductive paths; therefore, further increasing carbon black amount only led to a limited decrease in  $R_1$  and  $R_2$  which were already low. However, the additional carbon black nanoparticles filled in the regions within the partially conducted paths that behaved as dielectrics in between conductors.



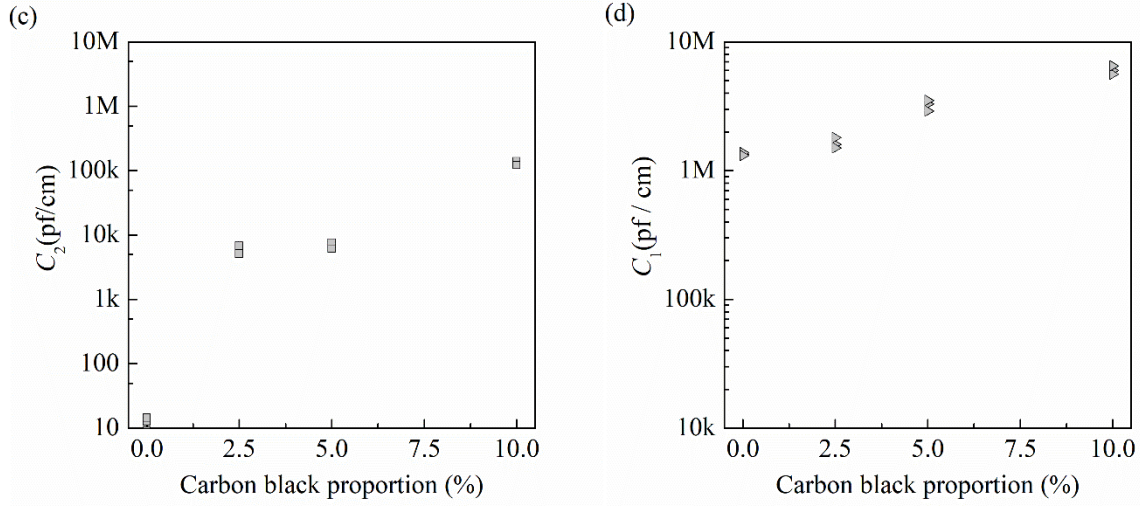


Figure 3.5 Effect of carbon black nanoparticles on equivalent circuit model parameters: (a) resistance  $R_1$ , (b) resistance  $R_2$ , (c) capacitance  $C_2$ , and (d) capacitance  $C_1$

This led to a fast decrease in  $d$  and an increase in  $A$ , and consequently a fast increase in  $C_2$ , where  $d$  can be treated as the separation between the plates in the parallel-plate capacitor model Eq. (3.1) [180] and  $A$  represents the area of the plates.

$$C_2 = \kappa_r \kappa_0 \frac{A}{d} \quad (3.1)$$

where  $C_2$  is the capacitance of the partially conductive path,  $\kappa_r$  is the dielectric constant describing the relative static permittivity of the dielectrics material between the plates (i.e., between the conductors along the partially conductive path), and  $\kappa_0$  is the electric constant.

Understanding the effects of carbon black nanoparticles on the electrical microstructure of the cementitious composite material sheds lights on the material design to achieve enhanced piezoresistive behavior with a high signal-to-noise ratio ( $SNR_{db}$ ). A strong piezoresistive behavior is quantified as a high value of large gage factor  $\alpha$ , as defined in Eq. (3.2).

$$\alpha = \frac{Z_f}{\varepsilon}; \quad (3.2)$$

$$Z_f = \frac{\Delta Z}{Z_b}$$

where  $Z_f$  is the fractional change in impedance magnitude,  $Z_b$  is the initial impedance magnitude of the unstrained bulk material, and  $\Delta Z$  is the change in impedance magnitude due to straining, and  $\varepsilon$  is the strain.

The signal-to-noise ratio is defined in Eq. (3.3):

$$SNR_{db} = 10 \log_{10} \left( \frac{P_{signal}}{P_{noise}} \right) \quad (3.3)$$

where  $P_{signal}$  is the power of the signal, and  $P_{noise}$  is the power of the noise.

In order to achieve a large gage factor, it is thus preferred that (1) a small amount of applied strain shall induce a significant change in the electrical impedance ( $\Delta Z$ ) of the material, and (2) the initial impedance ( $Z_b$ ) of the bulk material at unloaded state shall not be too high. In order to achieve a larger signal-to-noise ratio, it is desired that the material exhibits low bulk impedance and a less heterogeneous electrical microstructure.

Implied in these conditions is that the material system shall contain a significant amount of partial-conductive paths as well as conductive paths. It is important to have them both. The sufficient amount of conductive paths leads to a low initial impedance of the bulk material. In addition, it is necessary that sufficient amount of partially conductive paths also exist in the bulk material to enable a large change in electrical impedance with a small amount of applied strain. During the material pre-cracking stage, i.e., the elastic stage, when a strain is applied, the distances between adjacent carbon black nanoparticles in the partially conductive path will increase under tension, or decrease under compression, consequently inducing a change in bulk impedance. Compressive strain will convert some of the partially conductive paths into conductive paths due to the electron tunneling effect, which occurs when the carbon black



nanoparticles get sufficiently close; Tensile strain will increase the distances between adjacent carbon black nanoparticles along the partially conductive path, and will also convert some of the conductive paths into partially conductive paths, resulting in a strong piezoresistive behavior. The results shown in Figure 3.5 suggest that the strongest piezoresistive behavior (i.e., the largest gage factor) can be achieved at around 5% carbon black content; this is because beyond 5%, the decrease in  $R_2$  slows down and the increase in  $C_2$  becomes much faster (note the log scale), indicating further increasing carbon black content leads to a reduction in partially conductive paths because more of them turn into conductive paths.

### **3.3 Design for Tensile Strain-hardening Behavior with Improved Ductility Guided by Micromechanics-based Theory**

Incorporating carbon black nanoparticles into fiber reinforced cementitious composite materials can affect the micromechanical parameters, such as the toughness of the cementitious matrix, the fiber/matrix interfacial chemical and frictional bonds, and the fiber bridging “spring law” across the crack. The “spring law” describes the fiber bridging stress vs. crack opening relation, i.e., the  $\sigma \sim \delta$  relation, which indicates the interaction between the fibers and the cementitious matrix during crack opening and propagation [149]. These effects will thus further impact the crack opening and propagation mode, potentially leading to the deterioration or even loss in the tensile strain-hardening behavior of the material. Therefore, experiments were conducted to study the effects of the different amount of carbon black nanoparticles on the material tensile stress-strain relation, as well as on the matrix toughness and  $\sigma \sim \delta$  relation to evaluate the strain-hardening criteria. These results guided us to further tailor the material to ensure that both strain-hardening within improved tensile ductility and self-sensing can be achieved. The tensile pseudo strain-hardening behavior can be achieved through the formation of

series of matrix multiple fine cracks. The tight cracks are bridged by randomly distributed fibers in the matrix. Two micromechanics-based fundamental conditions [193-196] are required to be satisfied for tensile strain-hardening of the composite.

### 3.3.1 Energy criterion

This energy-based criterion governs the crack propagation mode by ensuring whether the crack formation mode is steady-state flat cracking or Griffith cracking. To ensure steady-state flat cracking, the crack tip toughness  $J_{\text{tip}}$  must be less than the complementary energy  $J_b'$ . The complementary energy ( $J_b'$ ) is the total available crack driving energy of crack bridging which can be estimated by fiber bridging relation  $\sigma(\delta)$  expressed in equation (3.4). For brittle matrices, such as mortars, the resistance of the composite to crack propagation ( $J_{\text{tip}}$ ) can be approximated to fracture energy of matrix ( $G_m$ ), which can be determined by matrix fracture toughness ( $K_m$ ) and Young's modulus of elasticity ( $E_m$ ) using equation (3.5). Equation (3.4) employs the concept of energy balance ( $J_{\text{tip}}$ ) between external work done to the body ( $\sigma_0\delta_0$ ) and energy absorption through fiber/matrix interface debonding and sliding ( $\int_0^{\delta_0} \sigma(\delta)d\delta$ ) during flat crack formation.

$$J_{\text{tip}} \leq \sigma_0\delta_0 - \int_0^{\delta_0} \sigma(\delta)d\delta \equiv J_b' \quad (3.4)$$

$$J_{\text{tip}} \cong G_m = \frac{K_m^2}{E_m} \quad (3.5)$$

where  $J_{\text{tip}}$  is crack tip toughness (crack tip energy absorption through matrix breakdown);  $J_b'$  is the complementary energy (total available crack driving energy);  $\sigma$  is fiber bridging stress;  $\delta$  is crack opening;  $\sigma_0$  is maximum fiber bridging stress corresponding to  $\delta_0$ ;  $G_m$  is fracture energy of matrix;  $K_m$  is matrix fracture toughness; and  $E_m$  is matrix young's modulus.

### 3.3.2 Strength criterion

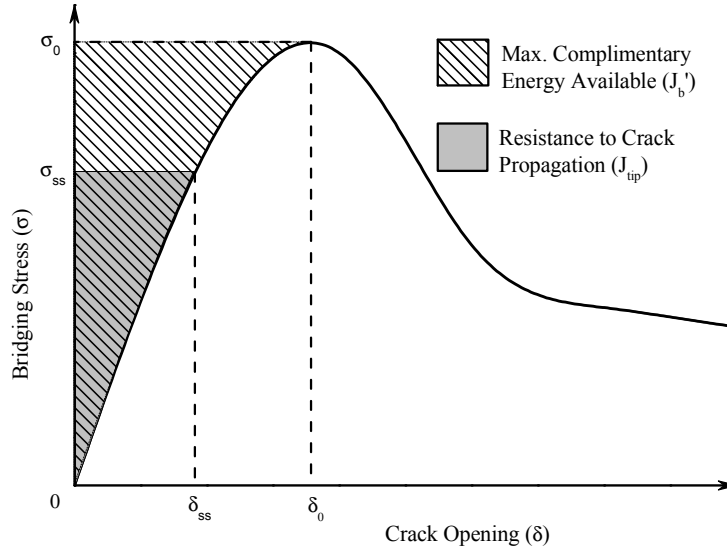


Figure 3.6 Typical crack bridging stress ~ crack opening relation  $\sigma(\delta)$  for tensile strain-hardening composite

The second necessary condition for tensile strain-hardening is strength criterion or crack initiation criterion, which requires the matrix cracks to initiate at stresses lower than the bridging capacity of the least bridged crack ( $\min[\sigma_0]$ ) as shown in Eq.(3.6). Crack initiation stress for the first crack ( $\sigma_{ci}$ ) and subsequent cracks can be determined by matrix fracture toughness ( $K_m$ ) and pre-existing internal flaw size ( $a_0$ ) using Irwin's fracture criterion; and bridging capacity ( $\sigma_0$ ) can be determined from the crack bridging behavior relation ( $\sigma-\delta$ ). All micro-cracks in a multiple cracking composite have different  $\sigma_0$  due to inhomogeneity of fiber dispersion, and therefore, the minimum of these bridging capacities ( $\min[\sigma_0]$ ) is critical for determining the upper bound for crack initiation stress ( $\sigma_{ci}$ ). The mathematical expression of strength criteria is given by

$$\sigma_{ci} \leq \min[\sigma_0] \quad (3.6)$$

Where  $\sigma_{ci}$  is matrix tensile crack initiation stress and  $\sigma_0$  is maximum fiber bridging stress corresponding to  $\delta_0$ .

### 3.3.3 Conditions for high-density multiple microcracking and large tensile ductility

Besides, robust high-density multiple microcracking and large tensile ductility is critically dependent on the uniformity of fiber dispersion, which determines the fiber bridging strength, complementary energy, critical flaw size and degree of multiple cracking saturation [149]. Fresh rheology of the matrix directly governs fiber dispersion, which influences both the feasibility and density of multiple cracking. Therefore, Li & Li [149] recommended to optimize plastic viscosity, control the rheology and fiber dispersion during material processing of strain-hardening cementitious materials.

The crack bridging stress  $\sim$  crack opening relation as shown in Figure 3.6 depends on fiber dispersion. When a specimen is under uniaxial tension, poor fiber distribution in the specimen results into a reduced effective fiber volume at the weakest cross section, leading to a low crack bridging stress. Therefore, fiber bridging capacity exhausts prematurely and hence the crack bridging stress  $\sim$  crack opening relation shifts downward, leading to the reduced complimentary energy and thus the violation of the energy criterion.

High density multiple microcracking requires saturated formation of multiple cracks. The number of the microcracks are determined by (1) the maximum fiber bridging stress  $\sigma_0$  and (2) the pre-existing flaw size distribution and matrix flaw toughness. Each crack is activated corresponding to the weakest cross-section which is determined by the largest flaw along the section in the material. The critical flaw size,  $c_{mc}$ , is the lower bound of flaw size such that only those flaws larger than this critical size can be activated and contributed to multiple cracking. Poor fiber dispersion leads to a reduction of maximum fiber bridging stress  $\sigma_0$  and hence increases the critical flaw size. In this sense, large tensile ductility cannot be achieved.

Therefore, the ideal rheology should be achieved during material processing to optimize fiber dispersion to a uniform random distribution state.

### *3.3.4 Effect of carbon black nanoparticles on tensile behavior*

Uniaxial tension tests were conducted on coupon specimens with the initial mix designs shown in Table 3.1. The test used a servo-hydraulic testing system with a capacity of 50 kN at a fixed displacement rate of 0.0025 mm/sec (Figure 3.7). The specimens were gripped at both ends by the testing system with a gripping length of 51 mm. Two LVDTs were attached with a gauge length of 152 mm. Figure 3.8 shows the measured tensile stress-strain curves. It was observed that increasing carbon black nanoparticles led to a decrease in tensile strain capacity, ultimate tensile strength, and first-cracking tensile stress. The tensile strain capacity is defined as the strain corresponding to the ultimate tensile strength. The first-cracking stress is defined as the tensile stress where the first microcrack occurs in the specimen. The tensile strain capacity decreased from above 5% to less than 2% when carbon black nanoparticles were added. The ultimate tensile strength decreased by 19%, 26% and 57%, at carbon black content of 2.5%, 5% and 10%, respectively. The first-cracking tensile stress decreased by 14%, 28%, 57%, at carbon black content of 2.5%, 5% and 10%, respectively. The reduction in tensile properties needs explanations on how the nanoparticles affect the matrix and fiber/matrix interfacial properties, and requires re-tailoring the material to improve mechanical properties.

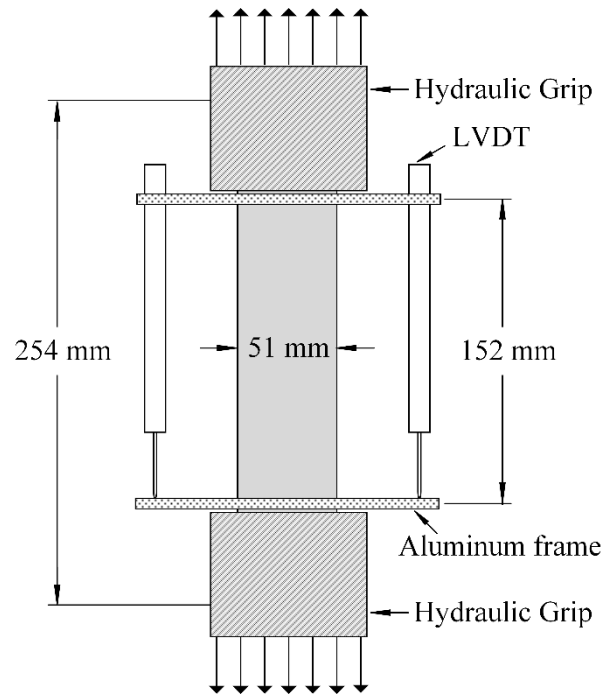


Figure 3.7 Uniaxial tension test setup

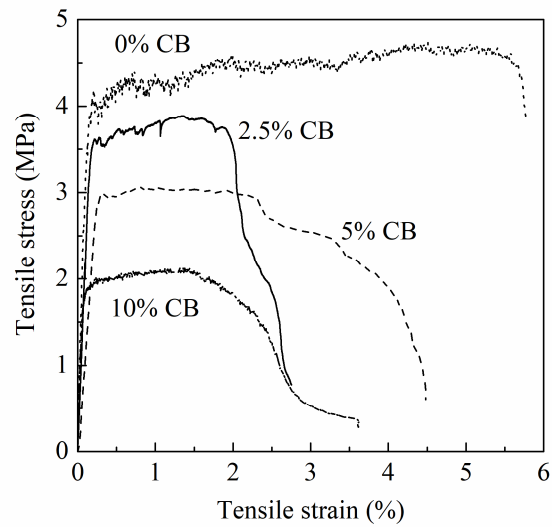


Figure 3.8 Effect of carbon black nanoparticles on the tensile stress-strain relation of the cementitious composite material

### 3.3.5 Effect of carbon black nanoparticles on fiber-bridging behavior and matrix

#### toughness

To ensure tensile strain-hardening behavior in a fiber-reinforced brittle-matrix composite material, the synergistic interaction between the fibers, cementitious matrix, and fiber/matrix interface needs to be tailored based on the micromechanics theory [42]. Based on the two criterion described above, the theory requires that steady-state crack propagation is prevalent, rather than Griffith-type crack propagation. Steady-state crack propagation requires that the matrix crack tip toughness  $J_{tip}$  must be less than the complementary energy  $J_b'$  calculated from the fiber bridging stress  $\sigma$  versus crack opening  $\delta$  relation (i.e., the fiber bridging “spring law”); and that the maximum fiber bridging capacity  $\sigma_0$  must be higher than the matrix cracking strength  $\sigma_{fc}$  [197]. In addition to the steady-state crack propagation criteria, a sufficient number of intrinsic flaws larger than the critical flaw size should exist in the matrix; upon loading, these flaws can be activated during multiple microcracking processes before the fiber bridging capacity is exhausted. More activated flaws will lead to a larger number of microcracks formed before crack localization, resulting in a larger tensile ductility.

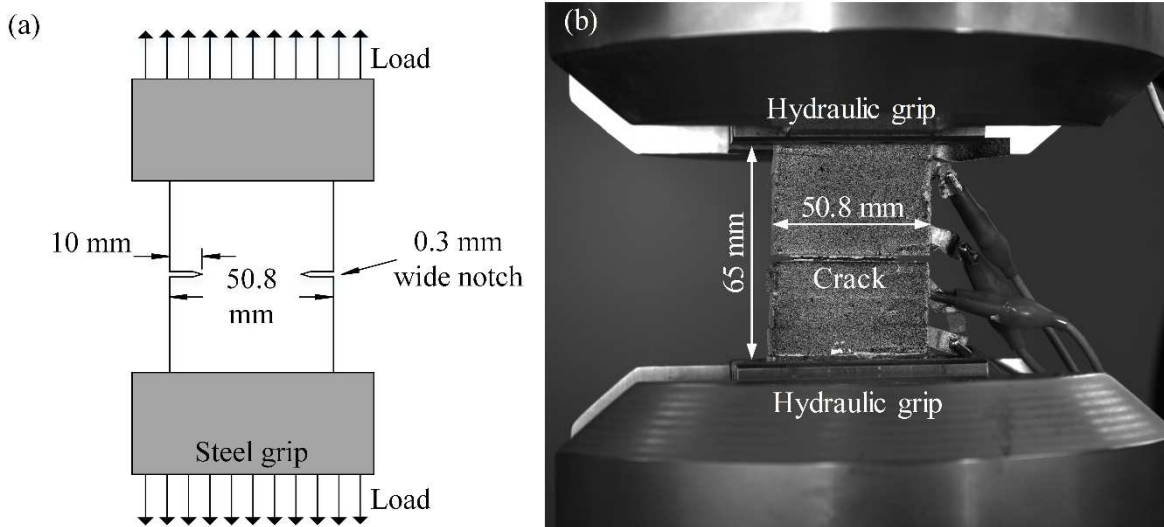


Figure 3.9 Single crack opening test: (a) specimen details, (b) test setup

To understand the observed negative impact of carbon black nanoparticles on the tensile ductility and strength of the fiber reinforced cementitious composite, two types of experimental investigations were performed: (1) single crack opening test, to measure the fiber bridging stress  $\sigma$  versus crack opening  $\delta$  relation; The relation reflects the fiber/matrix interfacial bonding properties, and can be used to determine complementary energy  $J_b$ , (2) matrix fracture toughness test, to determine the matrix (without fibers) crack tip toughness  $J_{tip}$ . The single crack opening test was performed on double-notched coupon specimens measuring 76.2 mm  $\times$  50.8 mm  $\times$  12.7 mm under uniaxial tension (Figure 3.9(a)). At each side of the specimen middle section, a straight through slot terminating in a sharpened *V*-notch (0.3 mm wide and 10 mm deep) was prepared. The double notches allowed the formation of a single crack along the notched cross-section. The specimen was tested using a hydraulic testing system with a controlled displacement rate of  $8.5 \times 10^{-5}$  mm/s (Figure 3.9(b)). During loading, a digital image correlation (DIC) system [47] was used to accurately measure the crack opening. The matrix fracture toughness test was conducted on notched beam specimens (305 mm  $\times$  76 mm  $\times$  38 mm) under three-point bending (Figure 3.10). Four specimens were prepared for each mix designs in Table 3.1, but without including fibers, to reflect only matrix fracture property. This test was similar to ASTM E399 “Standard Test Method for Plane-Strain Fracture Toughness of Metallic Materials” [198] and followed the RILEM recommendations [199]. The test allows using different geometry specimens, such as bending specimens and compact tension specimens, to measure the fracture toughness value. Before the test, an artificial single-edge straight-through notch was made on the mid-span of the specimen, with 38 mm in the depth and 2 mm in the opening. To facilitate cracking, the root radius for the *V*-notch of the straight-through notch was 0.08 mm. the loading actuator applied force on the mid-span of the specimen at the rate of 1  $\mu$ m/s. For each matrix



design, there were four specimens tested and the average is reported.

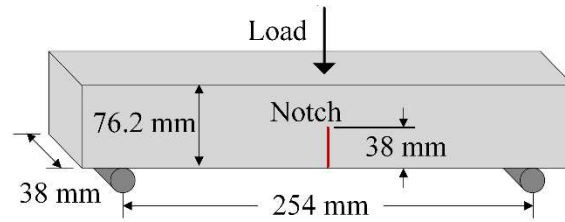
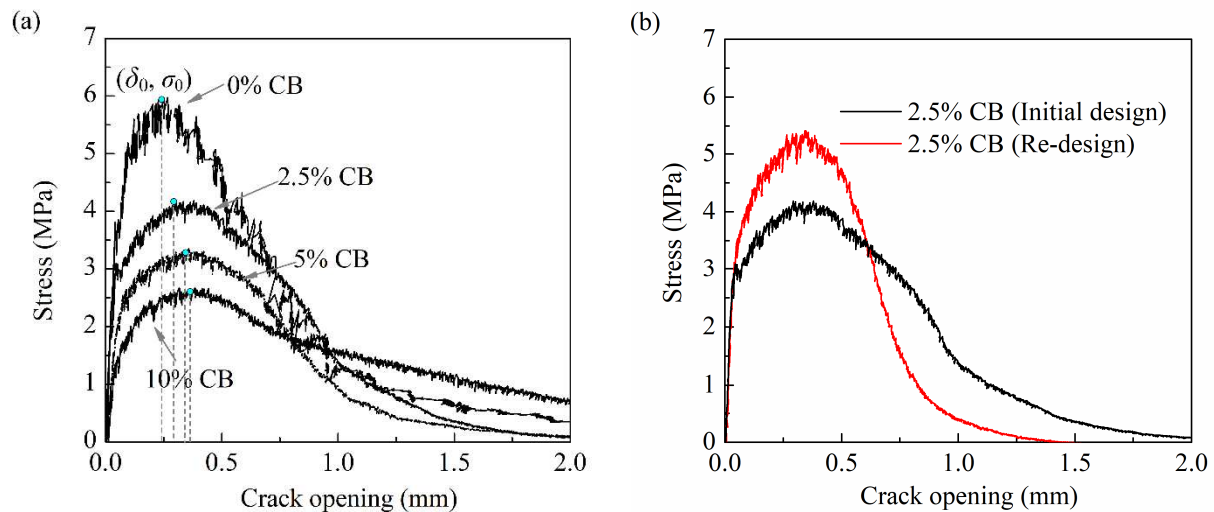


Figure 3.10 Matrix fracture toughness test. The cementitious matrix does not contain any fibers

The single crack opening test results are shown in Figure 3.11 (a). The fiber bridging stress  $\sigma_0$  was plotted against crack opening  $\delta$ . It was observed that increasing amount of carbon black nanoparticles led to a decrease in the peak fiber bridging stress  $\sigma_0$  across the crack.  $\sigma_0$  decreased by 33%, 43% and 58%, at carbon black content of 2.5%, 5% and 10%, respectively. Increasing carbon black content also led to an increase in the critical crack opening  $\delta_0$  which corresponds to  $\sigma_0$ . Because the fiber parameters and volume were the same for the different mix designs, the decrease in  $\sigma_0$  and increase in  $\delta_0$  indicated a decrease in fiber/matrix interfacial bond. PVA fibers generally have a hydrophilic nature. Therefore, they tend to form an overly strong bond with a cementitious matrix [200-202].



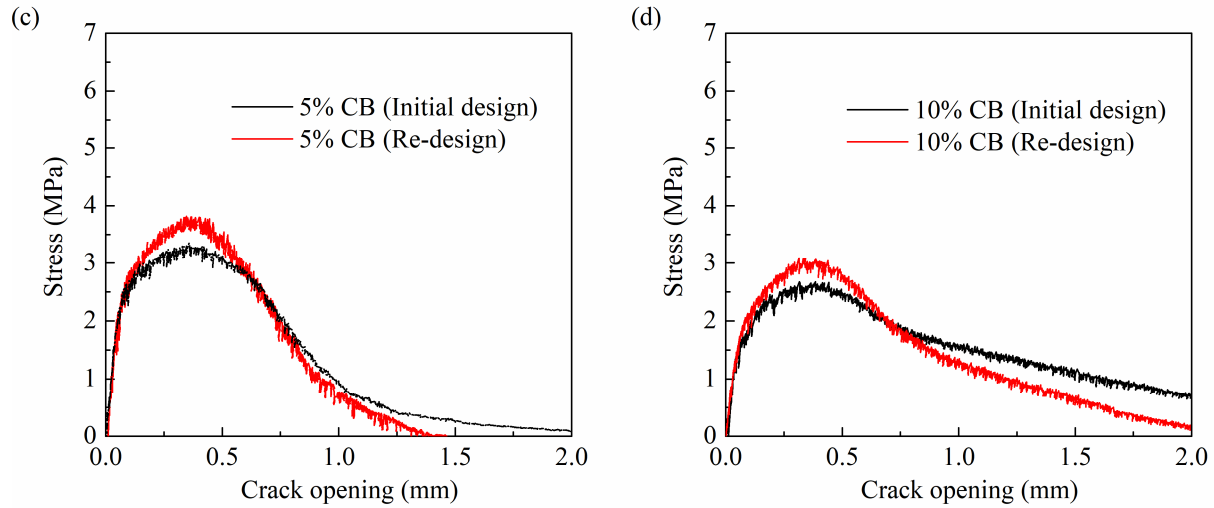


Figure 3.11 Fiber bridging stress vs. crack opening ( $\sigma \sim \delta$ ) relation: (a) effect of carbon black nanoparticles, (b) initial and redesign with 2.5% CB, (c) initial and redesign with 5% CB, (d) initial and redesign with 10% CB

As a result, PVA fibers are prone to rupture rather than being pulled out from the cementitious matrix under loading, leading to a small complementary energy  $J_b'$  which disfavors steady-state crack propagation and strain-hardening behavior. Therefore, PVA fibers with 1.2% oil-coating were used to reduce fiber/matrix interfacial bond to increase  $J_b'$ . However, when a large amount of carbon black nanoparticles were introduced to the system, the fiber/matrix interfacial bond was further reduced due to the well-known “lubricant” effect of carbon black nanoparticles. This significantly weakened the effectiveness of fiber bridging during fiber pullout stage. Consequently, the reduction of fiber bridging capacity  $\sigma_0$  had three negative effects on the tensile behavior of the cementitious composite material: (1) it led to the decrease in complementary energy  $J_b'$ ; a low  $J_b'$  can potentially violate the steady-state crack propagation criteria, leading to a reduction or loss of tensile strain-hardening behavior; (2) Before the maximum fiber bridging capacity  $\sigma_0$  was reached, less amount of intrinsic flaws preexisting in the cementitious matrix could be activated to form microcracks; Less microcracking before crack

localization resulted in a smaller tensile strain capacity; (3) a lower fiber bridging capacity  $\sigma_0$  lead to a lower ultimate tensile strength of the cementitious composite material. These are consistent with the observations from the tensile stress-strain relations shown in Figure 3.8.

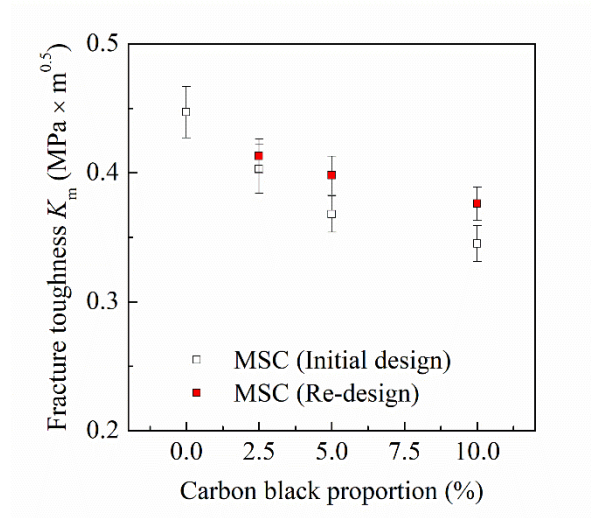


Figure 3.12 Effect of carbon black nanoparticles on cementitious matrix fracture toughness ( $K_m$ ) for both initial design and re-design

Figure 3.12 shows that the cementitious matrix fracture toughness decreased by 11%, 15% and 24% in average with increasing carbon black percentage at 2.5%, 5%, and 10%, respectively. The reduction in matrix fracture toughness well explained the decrease in the first crack strength as shown in Figure 3.8. However, the reduction in matrix fracture toughness also implies a decrease in  $J_{tip}$ , which favors the steady-state crack propagation and strain-hardening criteria. This supports the observation from Figure 3.8 and Figure 3.11 (a) that even at a large amount of carbon black nanoparticles with a decreased  $J_b'$ , the materials still exhibited multiple cracking and strain-hardening behavior. Two mechanisms could contribute to the reduction of matrix fracture toughness: (1) large amount of porous carbon black nanoparticles behaved as inert fillers and “flaws” among the cementitious matrix, leading to a “dilution” effect; (2) The “lubricant” effect of carbon black nanoparticles weakened the bond between aggregates and cementitious

binder. This compromised the effectiveness of aggregate bridging at the crack tip, facilitating crack propagation.

### *3.3.6 Material re-designs for improved tensile ductility and strength*

Based on the findings in Sections 3.1 and 3.2, the material tensile strain capacity and strength were improved to abate the negative impacts of carbon black nanoparticles. The improvements were achieved through increasing the fiber/matrix interfacial bond, increasing the fiber bridging capacity, and increasing the matrix fracture toughness. The re-designed mixing proportions are shown in Table 3.1. Silica fume (150 nm particle size) was added by 13% by weight of the cementitious binder. Due to the pozzolanic reaction and the small particle size, it was found that replacing cementitious binder by up to 15% of silica fume increased packing density, refined pore structure and densified cementitious microstructure [141, 203, 204], consequently improving matrix strength and toughness. Silica fume can densify the fiber/matrix interface, increasing the fiber/matrix interfacial bond and thus the maximum fiber bridging capacity across the crack. In addition, the water-to-binder ratio was adjusted in the re-designs to improve the rheology of the cementitious binder containing carbon black nanoparticles, which are porous and absorptive in nature. This resulted in the formation of a more homogeneous mixture with less entrapped larger air pores, and more uniform fiber dispersion to improve the fiber bridging capacity. The fracture toughness test results (Figure 3.12) show that compared with the initial mixture designs, the new designs incorporating 13% by volume of silica fume exhibited increased matrix fracture toughness by 2.5%, 8.2%, and 9.0% for the carbon black content of 2.5%, 5%, and 10%, respectively. In addition, the single crack opening test results (Figure 3.11) show that the maximum fiber bridging capacity  $\sigma_0$  increased by 32%, 22%, and 25%

for the carbon black content of 2.5%, 5%, and 10%, respectively, validating the improvement of fiber/matrix interfacial bond due to the densification effect of silica fume.

Figure 3.13 shows all the re-designed mixtures exhibited tensile strain-hardening behavior. Compared to the initial mixture designs (Figure 3.8), the re-designs had significant improvements in both tensile strength and tensile strain capacity at different carbon black contents. For example, the tensile strength was improved by 26%, 24% and 31% at 2.5%, 5% and 10% of carbon black content, respectively. This macroscopic observation proved the effectiveness of fiber/matrix interface tailoring at the microscopic scale, which significantly improved the fiber bridging capacity. Meanwhile, the tensile strain capacity increased from 1.8% to 5.6% at 2.5% of carbon black content, from 2.3% to 3.7% at 5% of carbon black content, and from 1.5% to 3% at 10% of carbon black content. These results further validated the improvements in the fiber/matrix interfacial bond and fiber bridging capacity, which led to the increase in the complementary energy  $J_b'$  to promote more intensive multiple microcracking and larger tensile ductility. Furthermore, increase in the first cracking stress was observed, especially for the specimens containing 5% and 10% carbon black nanoparticles, resulting from the improvement in matrix fracture toughness.

Compression test results (Table 3.1) showed that compared to the initial design, the re-designed mixtures exhibited improved 28-day compressive strength by 26.5%, 24% and 13.1% for 10%, 5% and 2.5% carbon black content, respectively. This reflects the combined effects of increased matrix strength and toughness due to denser particle packing, pozzolanic reaction of silica fume, improved rheology that reduces larger flaws, and increased fiber bridging capacity. The macroscopic results validated the micromechanics-based material re-design to incorporate

carbon black nanoparticles into strain-hardening cementitious composite materials without scarifying key mechanical properties.

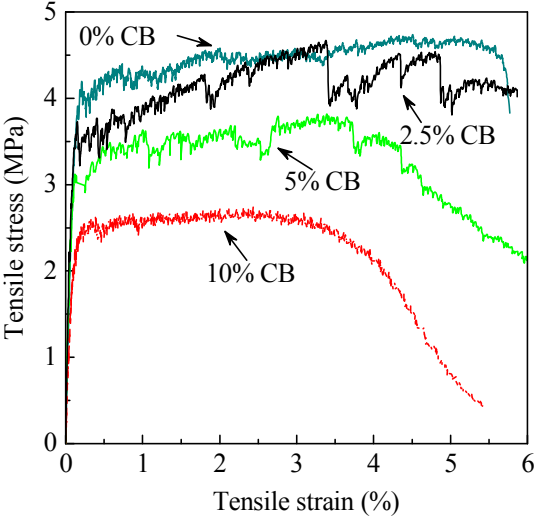


Figure 3.13 Tensile stress-strain relations of redesign

Figure 3.14 shows the distributed damage pattern on the surface of the 5% MSC specimen. As the specimen is black, microscope was utilized to take pictures of each region of specimen and then all pictures were added together. The results show that saturated distributed multiple cracks were attained for the MSCs. The average crack width was below 65  $\mu\text{m}$ .

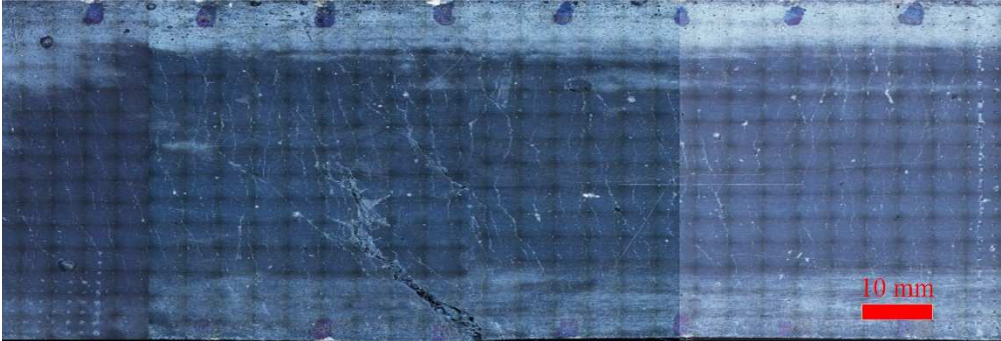


Figure 3.14 Crack distribution in 5% MSC

### 3.4 Conclusions

The following conclusions are drawn from this chapter:

1. A set of multifunctional strain-hardening cementitious composites (MSCs) is developed based on electrical impedance spectroscopy and micromechanics theory. The EIS method offers insights on the electrical microstructure of cementitious materials, leading to a guideline to tailor the piezoresistive behaviors of the material in the elastic stage. The micromechanics theory guides us to evaluate the impact of carbon black nanoparticles on matrix and fiber/matrix interfacial properties, resulting in re-designing the material for achieving tensile strain-hardening capacity.

2. Increasing amount of carbon black nanoparticles leads to a reduction in the peak fiber bridging stress  $\sigma_0$  across the crack.  $\sigma_0$  decreases by 33%, 43% and 58%, at carbon black content of 2.5%, 5% and 10%, respectively. The reduction of fiber bridging capacity  $\sigma_0$  has three negative effects on the tensile behavior of the cementitious materials. (1) it leads to the decrease in complementary energy  $J_b'$ . (2) less amount of pre-existed flaws can be activated to form microcracks before the maximum fiber bridging capacity is reached. (3) it leads to a lower ultimate tensile strength of cementitious material.

3. Increasing amount of carbon black nanoparticles also leads to a reduction in matrix fracture toughness by 11%, 15% and 24% for carbon black percentage at 2.5%, 5%, and 10%, respectively. It is due to the “dilution” effect and “lubricant” effect of carbon black, which weakened the cross-section of specimens, and the bond between aggregates and cementitious binder.

4. The redesign is achieved by (1) the introduction of silica fume, and (2) the adjustment of water-to-binder ratio. Due to the pozzolanic reaction and the small particle size, silica fume

can densify the fiber/matrix interface, increasing the fiber/matrix interfacial bond and thus the maximum fiber bridging capacity across the crack, which favors strain-hardening behavior. Water-to-binder ratio is adjusted so that optimal rheology can be achieved to favor uniform fiber dispersion and reduced entrapped larger air pores. The maximum fiber bridging capacity  $\sigma_0$  after redesign increases by 32%, 22%, and 25% for the carbon black content of 2.5%, 5%, and 10%,

5. The tensile ductility and tensile strength of the redesign significantly increases compared with the initial design. The tensile strength is improved by 26%, 24% and 31% at 2.5%, 5% and 10% of carbon black content, respectively. After the redesign, MSCs all demonstrate tensile strain-hardening behavior with strain capacity more than 3%. The average crack width was below 65  $\mu\text{m}$ .



## CHAPTER 4: MSC ELECTROMECHANICAL BEHAVIOR

### 4.1 Introduction

In this chapter, the electromechanical behavior of MSC is presented. In the elastic stage, the reversible impedance ~ strain relations were established. During strain-hardening and tension softening stages, the monotonic impedance ~ strain relations were revealed. Furthermore, the reversible impedance ~ strain relations were extended from elastic stage to early strain-hardening stage. Also, the effects of humidity and temperature on electromechanical behaviors of MSCs were studied.

### 4.2 Electromechanical Behavior of MSC

#### *4.2.1 Electromechanical experiment details*

The self-sensing functionality of MSC is based on the coupling between the material electrical response with mechanical state. The electromechanical behaviors of MSCs were experimentally studied. The electromechanical test under uniaxial tension was conducted on coupon specimens with four different mixture re-designs shown in Table 3.1. The specimen geometry was the same as Figure 3.6. Four copper electrodes were attached to the surfaces of the coupon specimen with conductive silver colloidal paste (Figure 4.1). In addition, epoxy was applied to the gripped region of the specimen to electrically isolate and mechanically protect the electrodes and the specimen from the steel grip, which was electrically grounded. Three types of loading scenarios were considered: (1) monotonic loading up to specimen failure. (2) cyclic loading with a peak strain within the material elastic range. The maximum strain was 0.015%, and the minimum strain was 0. Eight loading cycles were applied to each specimen. (3) cyclic loading with increasing peak strain from 0.1% to 0.3% and 0.5% for every 5 loading cycles. In

this scenario, the applied peak strains reached material inelastic (i.e., post-cracking) stage where multiple microcracking had occurred. The minimum strain was 0. During each loading scenario, electrical impedance was continuously measured within a gauge length of 152 mm, by applying an AC current at 1,500 Hz to the specimen via outer electrodes and recording the amplitude and phase shift of the resulting voltage. The impedance data were collected with 20 points per minute. Meanwhile, the mechanical displacement within the gauge length was measured using DIC method to calculate tensile strain. By this means, the relation between electrical impedance and tensile strain was established.

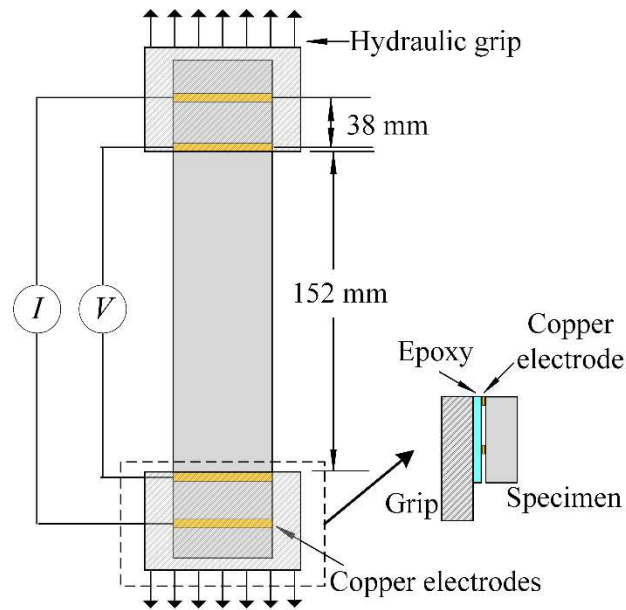


Figure 4.1 Electromechanical test under uniaxial tension

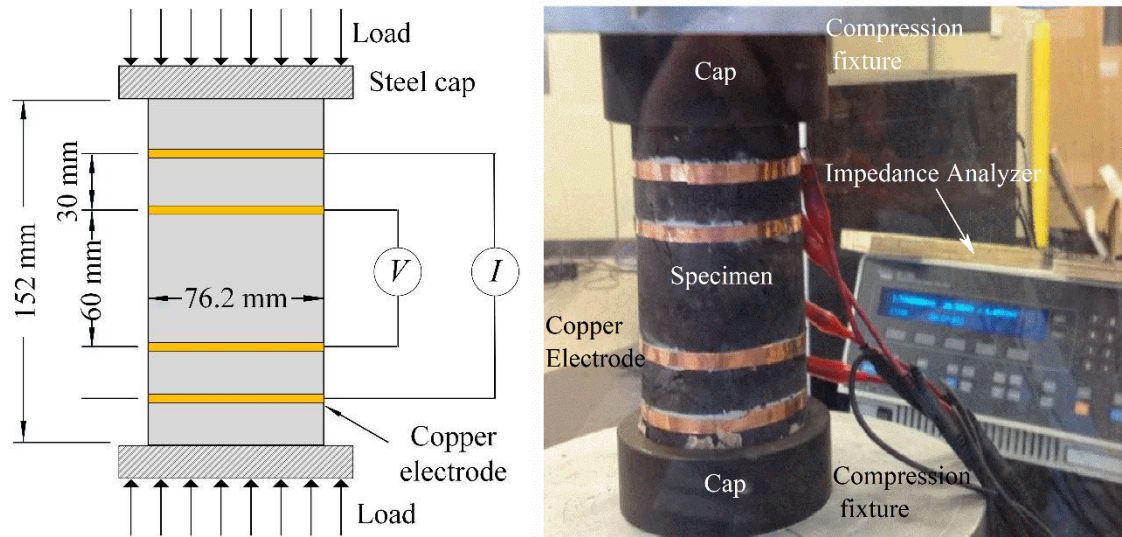


Figure 4.2 Electromechanical test under uniaxial compression

The electromechanical test under uniaxial compression was conducted on 152 mm (height) by 76.2 mm (diameter) cylinder specimens. Four copper electrodes (Figure 4.2) were attached to the surfaces of the cylinder specimen by surrounding the specimen. The AC current injection and four-point probing method were the same as the uniaxial tension test. Epoxy was applied onto the top and bottom surfaces of the cylinder specimen, in order to electrically insulate the specimen from the metal caps. The specimen was loaded under cyclic compression with a peak compressive strain of 0.05% and minimum strain of 0. Eight loading cycles were applied to each specimen. During loading, the electrical impedance was measured at a fixed frequency of 1,500 Hz. The relation between material electrical impedance and compressive strain under cyclic loading was then established.

#### 4.2.2 Electromechanical response under cyclic tension and compression within elastic stage

stage

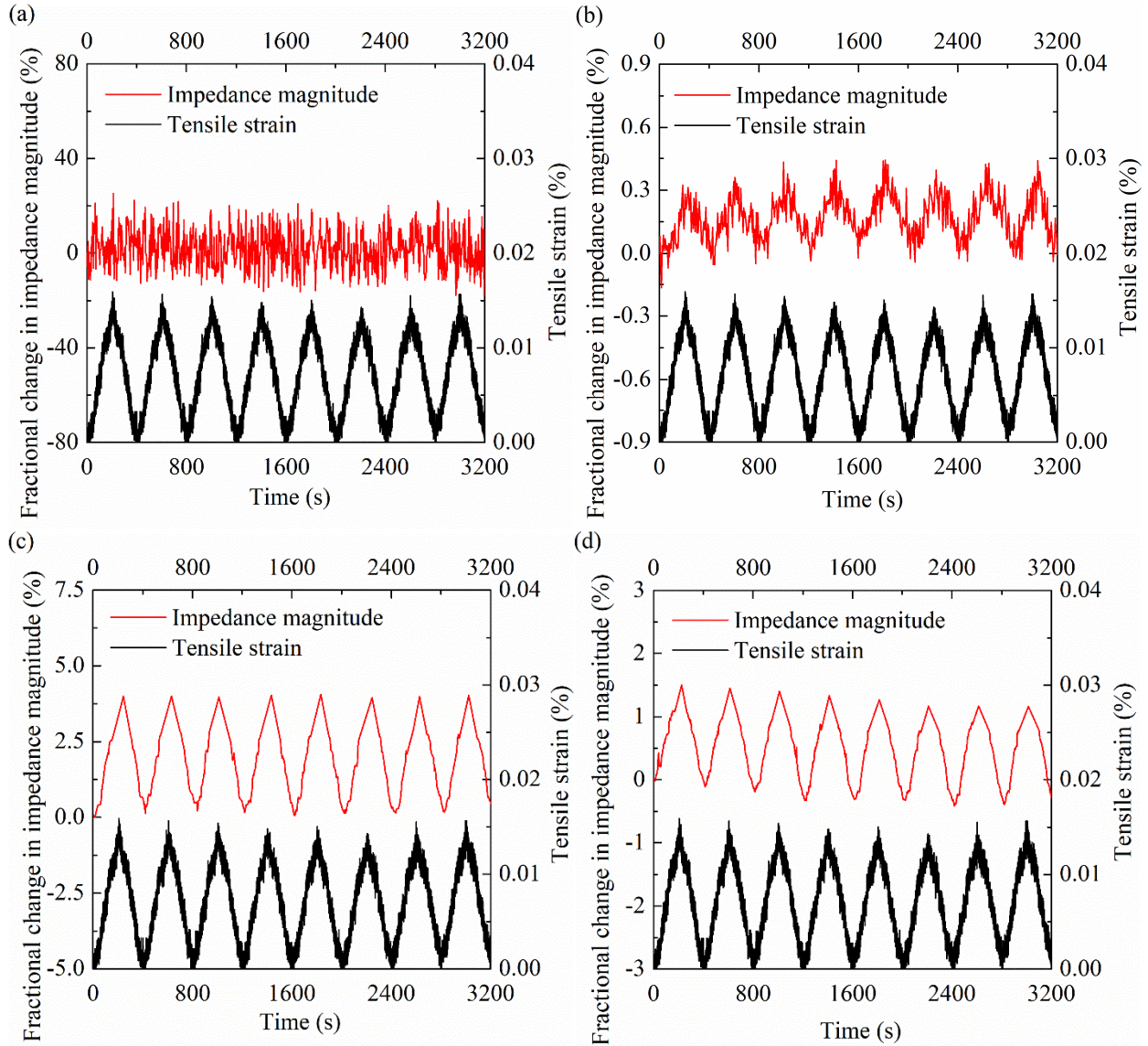


Figure 4.3 Electromechanical behavior of (a) 0% SHC, (b) 2.5% MSC, (c) 5% MSC and (d) 10% MSC during elastic stage under cyclic uniaxial tension

Figure 4.3 shows the electromechanical behavior of MSCs in comparison with the control 0% SHC under cyclic uniaxial tension within the material elastic stage. Both tensile strain and the fractional change in impedance magnitude were plotted versus loading time. The fractional change in impedance ( $I_f$ ) is defined in Eq. (3.2). The 0% SHC without carbon black nanoparticles

did not show a clear trend of impedance magnitude change with tensile strain.  $I_f$  fluctuated around a constant value, suggesting that the measurements were accompanied by a high level of noise. An overall high impedance magnitude was also observed, at the order of  $1 \times 10^7 \Omega \cdot \text{cm}$ . The phenomena were attributed to the electrically highly heterogeneous microstructure and a large number of nonconductive and partially conductive paths in the 0% SHC specimen, especially at a low humidity level at the age of 42 days.

In contrast, a linear correlation between  $I_f$  and the tensile strain was clearly observed for the 2.5%, 5%, and 10% MSC specimens. For the 2.5% MSC, although  $I_f$  was accompanied by a certain level of noise, it is clearly seen that  $I_f$  nearly linearly increased with increasing tensile strain, and decreased with decreasing tensile strain. For the 5% and 10% MSC specimens, the linear relation between  $I_f$  and tensile strain had little noise. Overall, the results show that compared to the control 0% SHC, the newly designed MSCs (2.5%, 5%, and 10%) exhibited significantly higher signal-to-noise ratios and stronger piezoresistive behavior under elastic tensile straining. Furthermore, the piezoresistive behavior of MSCs was stable and repeatable under cyclic loading with increasing loading cycles. The high signal-to-noise ratios, and the strong and stable piezoresistive behavior of MSCs demonstrate a robust strain self-sensing capacity during its elastic stage under tension.

The signal-to-noise ratios and gage factors during elastic tension stage were calculated based on Eq. (3.3) and (3.2) and shown in Table 4.1. It was observed that the signal-to-noise ratio increased with increasing carbon black content. This proved the material design hypothesis in Section 3.2 that dispersing carbon black nanoparticles throughout the cementitious matrix improved the electrical homogeneity of the material microstructure, increased the total amount of conductive and partially-conductive paths, while decreasing the overall bulk impedance; these

mechanisms contributed to larger signal-to-noise ratios. The results also revealed that increasing carbon black content from 2.5% and 5% increased the gage factor from  $45 \pm 15.2$  to  $254 \pm 16$ . However, further increasing carbon black content from 5% to 10% decreased the gage factor to  $102 \pm 9$ . The data thus validated another material design hypothesis in Section 4.2 that the material system shall contain a significant amount of partial-conductive paths as well as conductive paths, in order to achieve a large gage factor. Apparently, these conditions were optimally satisfied in 5% MSC. Further increasing carbon black content from 5% to 10% decreased partially conductive paths, leading to a decrease in the gage factor. The change in gage factor with increasing carbon black content was consistent with the findings in Figure 3.5, which suggested that the strongest piezoresistive behavior can be achieved at around 5% carbon black content.

Figure 4.4 shows electromechanical behaviors of MSCs in comparison with the control 0% SHC under cyclic uniaxial compression within the material elastic stage. Similar to the cyclic tensile testing results, the 0% SHC did not show a clear trend of impedance magnitude change with the change in compressive strain. The data contained large noise, indicating a low signal-to-noise ratio resulting from the high bulk impedance and heterogeneous electrical microstructure of the 0% SHC. In contrast, the 2.5%, 5%, and 10% MSCs all exhibited strong piezoresistive behavior under cyclic compression; the impedance magnitude decreased with increasing compressive strain, and increased with decreasing compressive strain, in a nearly linear manner.

Table 4.1. Gage factors and signal-to-noise ratios during elastic stage

Material		0% SHC	2.5% MSC	5% MSC	10% MSC
Gage factor	Tension	- -	$48 \pm 15.2$	$254 \pm 16$	$102 \pm 9$
	Compression	- -	$69 \pm 5.2$	$323 \pm 27$	$108 \pm 5.5$
Signal-to-noise ratio (db)	Tension	- -	$8.34 \pm 1.4$	$19.4 \pm 2.0$	$20.2 \pm 1.3$
	Compression	- -	$12.4 \pm 1.8$	$18.6 \pm 0.9$	$19 \pm 1.5$

- - : Hard to determine due to extremely high noise level

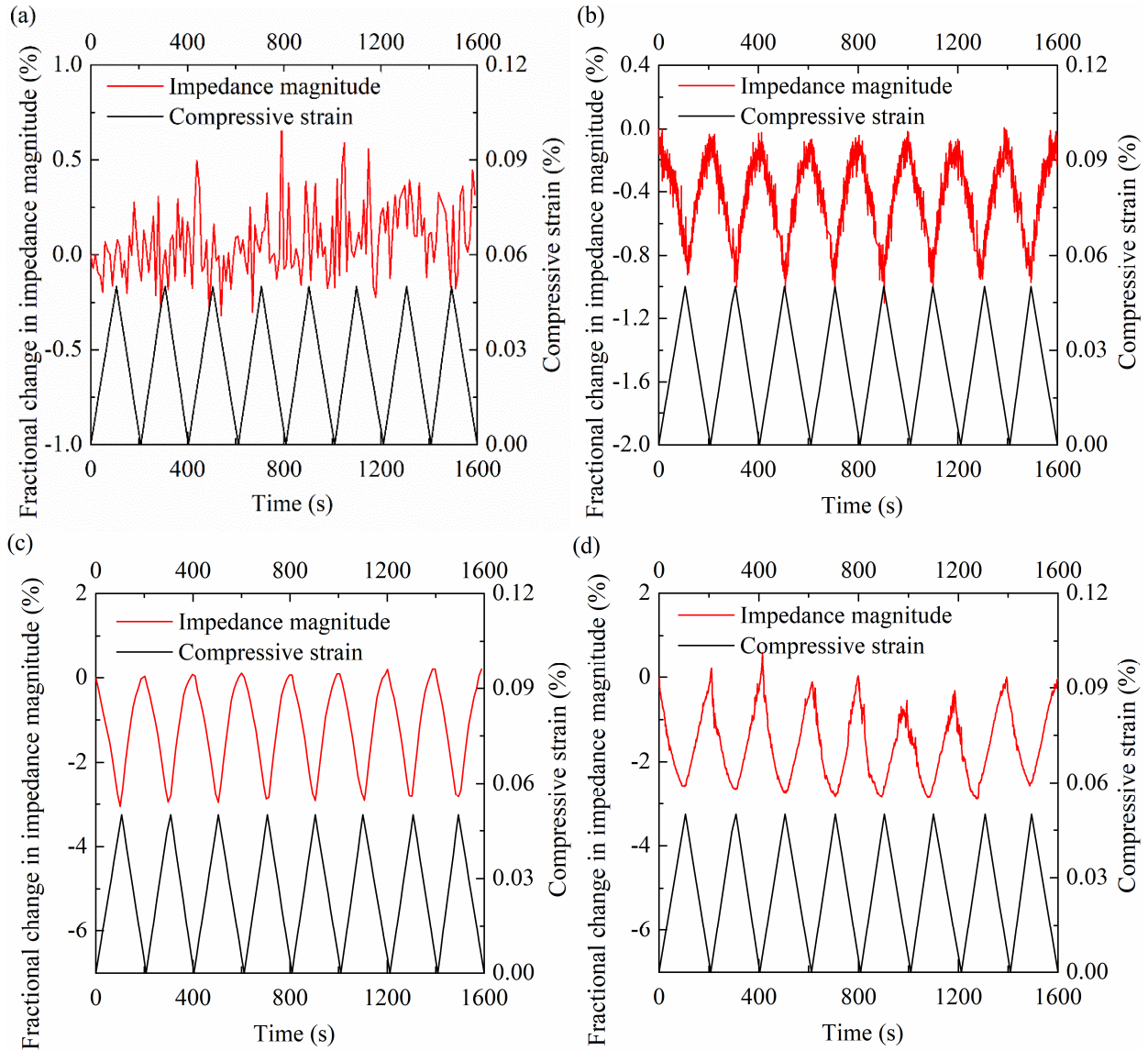


Figure 4.4 Electromechanical behavior of (a) 0% SHC, (b) 2.5% MSC, (c) 5% MSC and (d) 10% MSC during elastic stage under cyclic uniaxial compression

As shown in Table 4.1, the 5% MSC had the largest gage factor ( $323 \pm 27$ ) under compression, followed by 10% MSC ( $108 \pm 5.5$ ) and 2.5% MSC ( $69 \pm 5.2$ ). The trend was consistent with the impact of carbon black nanoparticles content on the tensile gage factors. This further supported the material design hypothesis that a strong piezoresistive behavior with a high

signal-to-noise ration can be achieved by tailoring the electrical parameters (e.g.,  $R_1$ ,  $R_2$ ,  $C_2$ , and  $C_1$ ) of the cementitious composite material by incorporating an optimum range of conductive nanoparticles.

#### *4.2.3 Electromechanical response under monotonic tension up to material failure*

Figure 4.5 shows electromechanical behaviors of MSCs in comparison with the control 0% SHC under monotonic uniaxial tension up to specimen failure. The tensile stress, impedance magnitude, impedance real part and imaginary part were plotted against the tensile strain in the same figure. The tensile stress-strain relations of the four materials similarly contained three major stages: (1) the initial elastic stage; (2) the tensile strain-hardening stage, which started when the first microcrack occurred in the specimen, followed by the sequential formation of more and more steady-state microcracks with self-controlled crack width, and ended before localized fracture occurred at one of the microcracks. During this multiple micro-cracking stage, the tensile stress continued to increase with tensile strain, thus called “pseudo-strain-hardening” or “strain-hardening”. This stage contributed to the large tensile ductility and damage tolerance of the materials; (3) the tension softening stage, which corresponded to the final crack localization with increasingly applied deformation. At this stage, the tensile stress dropped continuously accompanied by the increasing opening of the final failure crack.

Apparently, the multiple microcracking process during the strain-hardening stage, and the localized single crack opening during the tension softening stage, strongly affected the electrical response of MSC materials. For the control specimens made from 0% SHC, the impedance magnitude, real and imaginary parts all increased with increasing tensile strain during strain-hardening and tensile-softening stages, despite their unclear trend in during elastic stage. The data, however, were associated with a significant amount of noise. It was also noted that the



fractional increase was greatly larger in the imaginary part of impedance than the real part and magnitude of impedance.

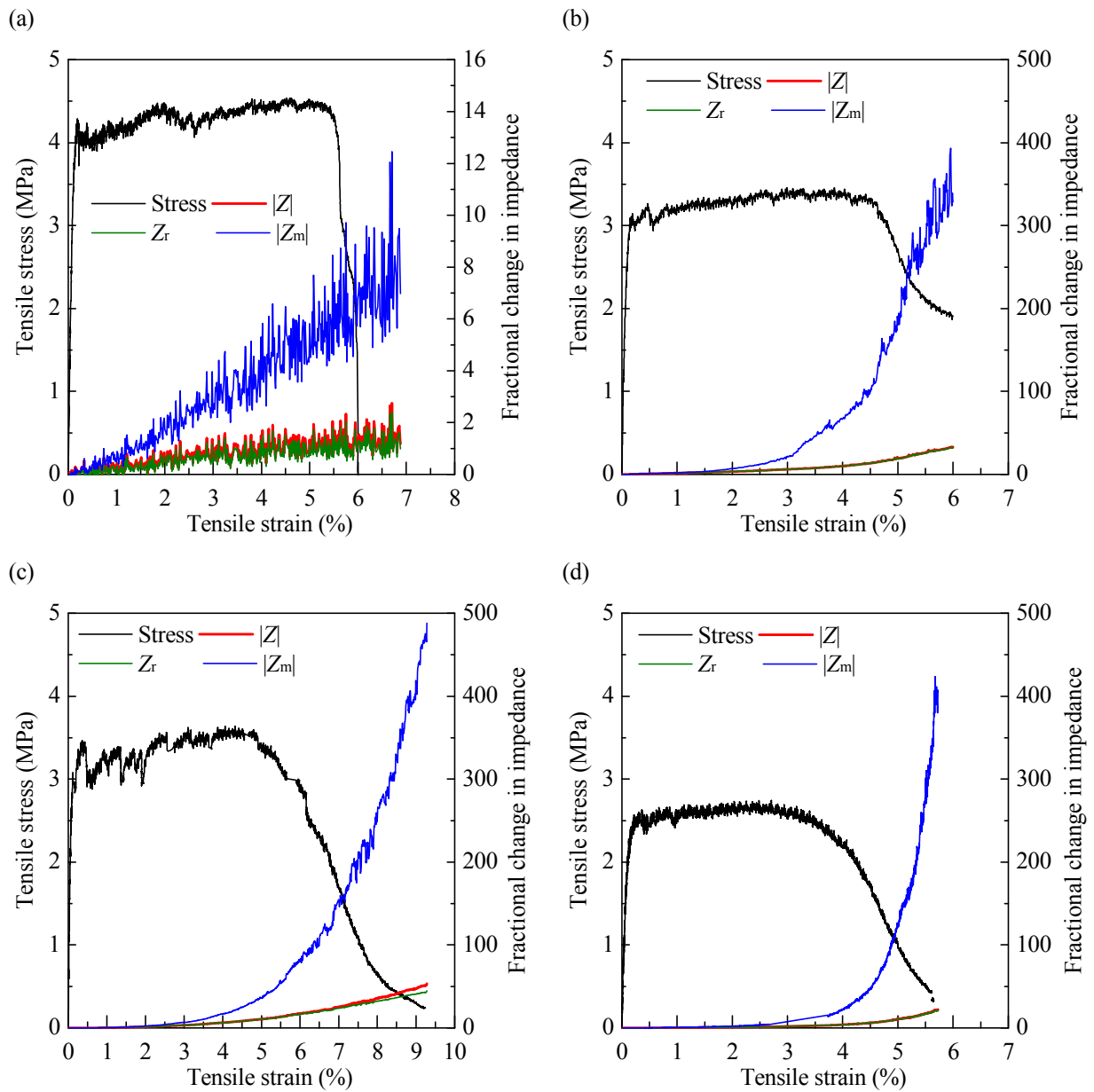


Figure 4.5 Electromechanical behavior of (a) 0% SHC, (b) 2.5% MSC, (c) 5% MSC and (d) 10% MSC during elastic, strain-hardening and tension softening stages up to failure.  $|Z|$  is impedance magnitude,  $Z_r$  stands for real part of the impedance, and  $|Z_m|$  stands for absolute value of imaginary part of the impedance

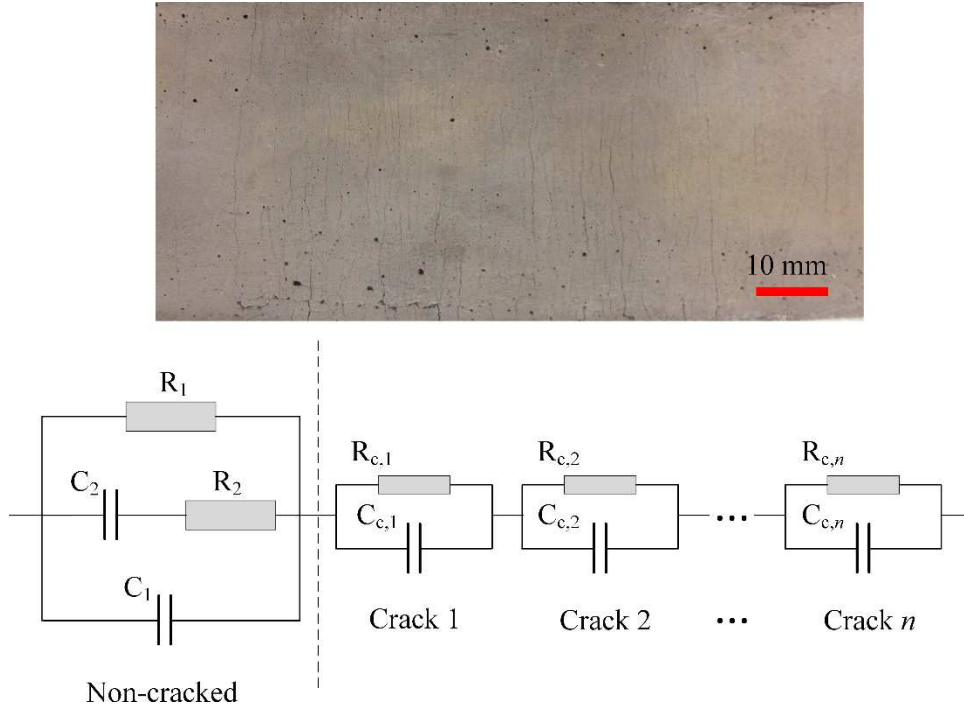


Figure 4.6 Equivalent circuit model of the material-crack system

This observation suggested that the  $i$ th crack in a cementitious matrix can be described as an equivalent circuit, i.e., the “crack circuit”, with a capacitor ( $C_{c, i}$ ) and a resistor ( $R_{c, i}$ ) connected in parallel (Figure 4.6). The crack capacitor ( $C_{c, i}$ ) can be described by Eq. (4.1), for which the two walls of the crack represents the two plates in an ideal capacitor:

$$C_{c,i} = \varepsilon_{r,c} \varepsilon_0 \frac{A_c}{d_i} \quad (4.1)$$

where  $C_{c, i}$  is the capacitance of the crack,  $\varepsilon_{r,c}$  is the dielectric constant describing the relative static permittivity of the material between the two walls of the crack, which are collectively contributed by the loose cementitious particles and the nonconductive polymeric fibers that have been ruptured or pulled out inside the crack,  $\varepsilon_0$  is the electric constant,  $A_c$  is the area of overlap of the two crack walls, and  $d_i$  is the crack opening.

The crack resistor ( $R_{c,i}$ ) describes the collective effect of moisture and well-connected cementitious particles within the crack, if any, the fibers that are still bridging the crack, which provides electrical resistance to reduce current flow. Consequently, the multiple crack process can be idealized as an increasing number of crack circuits connected in series, assuming that the cracks are not interconnected. The impedance change ( $Z_{c,i}$ ) due to a single crack effect is given in Eq. (4.2). The impedance change ( $Z_{c,m}$ ) due to multiple cracking is described in Eq. (4.3).

$$Z_{c,i} = \frac{1}{\frac{1}{R_{c,i}} + j\omega C_{c,i}} \quad (4.2)$$

$$Z_{c,m} = \sum_{i=1}^n Z_{c,i} \quad (4.3)$$

where  $j$  the imaginary unit,  $\omega$  is the angular frequency of the current, and  $n$  is the number of cracks.

The faster increase in the impedance imaginary part than the real part of during the multiple cracking process suggested that cracking had a predominant capacitor effect. At the probing AC frequency of 1,500 Hz, the uncracked cementitious composite material had a relatively low initial capacitor response and high initial resistor response, as shown in Figure 3.4. Because of the strong capacitor effect of the cracks, the fractional increase in the imaginary part of the impedance exhibited a much faster rate than the increase in the real part of impedance, during the strain-hardening as well as tension softening stages.

It should be noted that for 0% SHC, distinguishing between material strain-hardening stage and tension softening stage based on impedance fractional change was unattainable. The linear increasing trend of impedance continued from the strain-hardening stage into the tension softening change, without significant change in the increasing slope. This phenomenon implied

the predominant capacitor effect and weak resistor effect of the cracks in 0% SHC. Because the conductivity of the substances (e.g. fibers, air) between the crack walls is low, each crack can be approximated as an ideal capacitor. According to Eq. (4.1) - (4.3), when  $R_{c,i}$  has a very large value, the material impedance change due to cracking becomes linearly proportional to the crack opening  $d_i$ . During the strain-hardening stage when multiple microcracking occurs, the impedance change is described by  $Z_{c,m}$  (Eq. (4.3)); during the tension softening stage when crack localization occurs, the impedance change is described by  $Z_{c,i}$  (Eq. (4.2)). It can be mathematically proven that the same level of applied tensile deformation would induce the same change in the total crack opening of the multiple microcracks during the strain-hardening stage as in the single crack opening during the tension softening stage, thus leading to the same rate of change in impedance.

For the 2.5%, 5% and 10% MSCs, the magnitude, real and imaginary parts of impedance all increased with increasing tensile strain during the strain-hardening stage as well as the tension softening stage. However, compared to the 0% SHC, MSC exhibited three fundamental differences: (1) the data contained significantly low noise level, indicating a lower bulk impedance and reduced heterogeneity of material electrical microstructure; (2) the impedance increase exhibited nonlinearity, implying that the cracks in MSCs can no longer be approximated as ideal capacitors; (3) the strain-hardening stage was clearly distinguished from the strain-hardening stage, based on a significantly increased rate of impedance change versus strain. These differences resulted from the modified electrical parameters at fiber/matrix interfaces during the cracking stage. The presence of carbon black nanoparticles around PVA fiber surfaces provided additional conductive paths through the fibers across the crack. Therefore, the crack resistor effect became significantly stronger in the MSCs than the 0% SHC. The combined

resistor  $R_{c,i}$  and capacitor  $C_{c,i}$  effects of each additional microcrack led to the nonlinear increase in electrical impedance during the multiple micro-cracking stage (i.e., the strain-hardening stage). When the MSC material entered the tension softening stage, sequential multiple micro-cracking ended and localization of one failure crack occurred. This led to the continued opening of one single failure crack and rapid loss of the number of fibers bridging the failure crack, because more fibers were experienced rupture or complete pullout. Consequently, the resistance of the failure crack fast increased, and the capacitor effect of the failure crack gained dominance. Therefore, the impedance increasing trend became significantly faster, delineating the transition from the strain-hardening stage into the tension softening stage. At a very large applied deformation, the crack again behaved as an ideal capacitor, and the impedance increase curved showed a linear behavior.

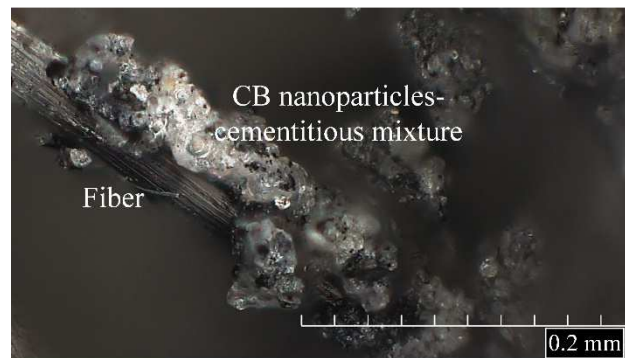


Figure 4.7 Microscopy of a pulled-out fiber after testing

This phenomenon was experimentally observed, as shown in Figure 4.7. When the strain level increases during the strain-hardening stage, more microcracks form while the crack width for each microcrack slightly increases up to the critical crack opening  $\delta_0$  (Figure 3.10) for steady-state cracking [205]. At lower strain levels, the fibers across the microcrack are mostly at fiber debonding or pullout stage, thus still bridging the microcrack. At higher strain levels, more and more fibers experience rupture or complete pullout, thus no longer bridging the crack. For 2.5%

MSC, the fibers provide conductive paths due to the carbon black nanoparticles “coating” at fiber surface.

Similar electromechanical behavior was observed for 2.5%, 5% and 10% MSCs: (1) They all exhibited high signal-to-noise ratios, compared to 0% SHC; the ratios increase with increasing amount of carbon black; (2) The increase in impedance with increasing strain all exhibited nonlinear behavior, due to the effects of electrical modification of fiber surfaces with carbon black nanoparticles; (3) based on the impedance (especially imaginary part) increasing rate, the tensile-softening stage can be well differentiated from the strain-hardening stage, and the change of increasing rate is more significant in 10% MSC. (4) Furthermore, the impedance change is significantly more sensitive to tensile strain change during both strain-hardening and tension softening stages, for MSC containing carbon black nanoparticles in comparison with 0% SHC. For example, when the tensile strain increases to 3%, the fractional imaginary part of impedance change in 0% SHC, 2.5%, 5% and 10% MSCs are 4.02 (with significant noise), 21.30, 8.66, and 8.56, respectively. When the tensile strain reaches the tensile strain capacity of each material, i.e., the material is just about to enter its tensile-softening stage, the fractional imaginary part of impedance change in 0% SHC, 2.5%, 5% and 10% MSCs are 6.01 (with significant noise), 101.2, 49.3, and 22.2, respectively. All these features in (1) - (4) are critical properties of MSC, which allows accurate sensing of strain levels with minimal noise as well as providing early warning before the material enters the tension softening stage.

#### *4.2.4 Electromechanical response under cyclic loading beyond elastic stage*

Figure 4.8 shows the electromechanical responses of the MSCs loaded under reversed uniaxial tension up to different peak strain levels, 0.1%, 0.3% and 0.5%, as described in Scheme 3 in Section 4.2.1. The experiment was conducted to test the strain sensing capacity and

robustness of different MSCs when subjected to reversed loading cycles. It was observed that 0% SHC exhibits significant noise in its impedance magnitude, and there is no obvious correlation between impedance magnitude change and strain levels. This means 0% SHC does not possess a strain sensing capacity, although the material does show a correlated electromechanical behavior during strain-hardening and tension softening stage. This is especially true when MSC is not under a “wet” or water-saturated condition; the specimens were under natural outdoor conditions with relative humidity of 40 - 50% for our study. The low signal-to-noise ratio exhibited by 0% SHC and its highly heterogeneous electrical properties overwhelmed the weak linkage between its mechanical behavior and electrical response, making self-sensing unattainable.

In contrast to 0% SHC, the 2.5%, 5% and 10% MSCs clearly exhibited strain sensing capacity under reversed uniaxial cyclic loading. With low noise, the impedance magnitude increased with increasing tensile strain, and decreased with decreasing tensile strain. The nearly linear correlation between impedance magnitude and tensile strain remained consistent during increasing loading cycles, and increasing peak strain levels. Such nearly reversible material electromechanical response under cyclic loading is necessary for robust strain sensing. It was further observed that impedance magnitudes of 5% and 10% MSCs were nearly fully reversible when the tensile strain decreased to zero. However, for the 2.5% MSC, residual impedance magnitude remained at zero tensile strain; furthermore, the residual impedance magnitude increased after each loading cycle. The phenomenon was attributed to the alternation in the electrical microstructure of the cementitious materials at different carbon black content. Under tensile strain which goes beyond the material elastic stage, cracking in MSC matrix takes place. Each microcrack created a new phase, or an electrical interface, in the material system.

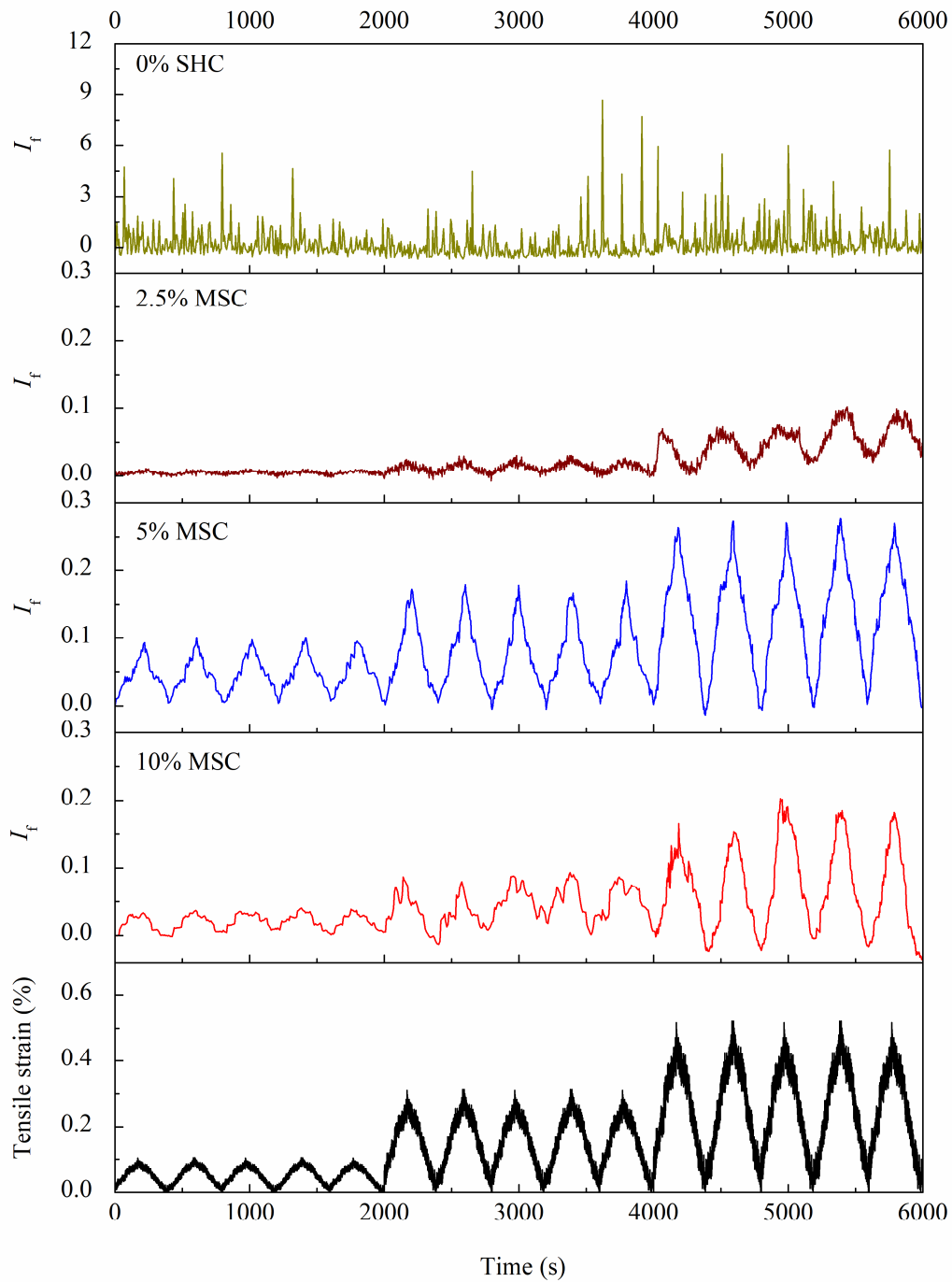


Figure 4.8 Electromechanical behavior of (a) 0% SHC, (b) 2.5% MSC, (c) 5% MSC and (d) 10% MSC under reversed cyclic loading

Although the microcracks were physically closed when the tensile strain was reduced to zero, the electrical interfaces still existed, leading to contact impedance which contributed to the



residual impedance magnitude. The mechanism was predominant when the content of carbon black nanoparticles was low (e.g. 2%) or zero. However, when the content of carbon black nanoparticles was high, such as in 5% and 10% MSCs, the presence of a large number of conductive nanoparticles at cracks' walls diminished the contact impedance of the physically closed cracks.

#### **4.3 Effects of Temperature and Humidity on Electromechanical Behavior of MSC**

Furthermore, the environmental effects on the MSCs were revealed. In this section, there are three aspects studied. Studying the environmental effects allows evaluating the sensing performance of MSCs in different environmental conditions. First, it is critical to study whether the electrical properties of MSCs are stable or not in terms of measurement time. The tests were conducted based on following schemes. The coupon specimens made from 0% SHC, and 2.5%, 5%, and 10% MSCs were cured following the same procedure as described in Section 3.2. The specimens were cured at room temperature of  $25 \pm 2$  °C and relative humidity of  $50 \pm 5\%$ . The impedance analyzer as shown in Figure 2.5 was utilized to measure the impedance of at a fixed frequency of 1500 Hz. The data collection rate is 1 point per 30 minutes and the measurement was continuously performed for 500 hours. For each type of materials, three specimens were tested. The measured impedance magnitudes for three specimens were averaged to form one data point in Figure 4.9, which reports the change of impedance magnitude in terms of measurement time.

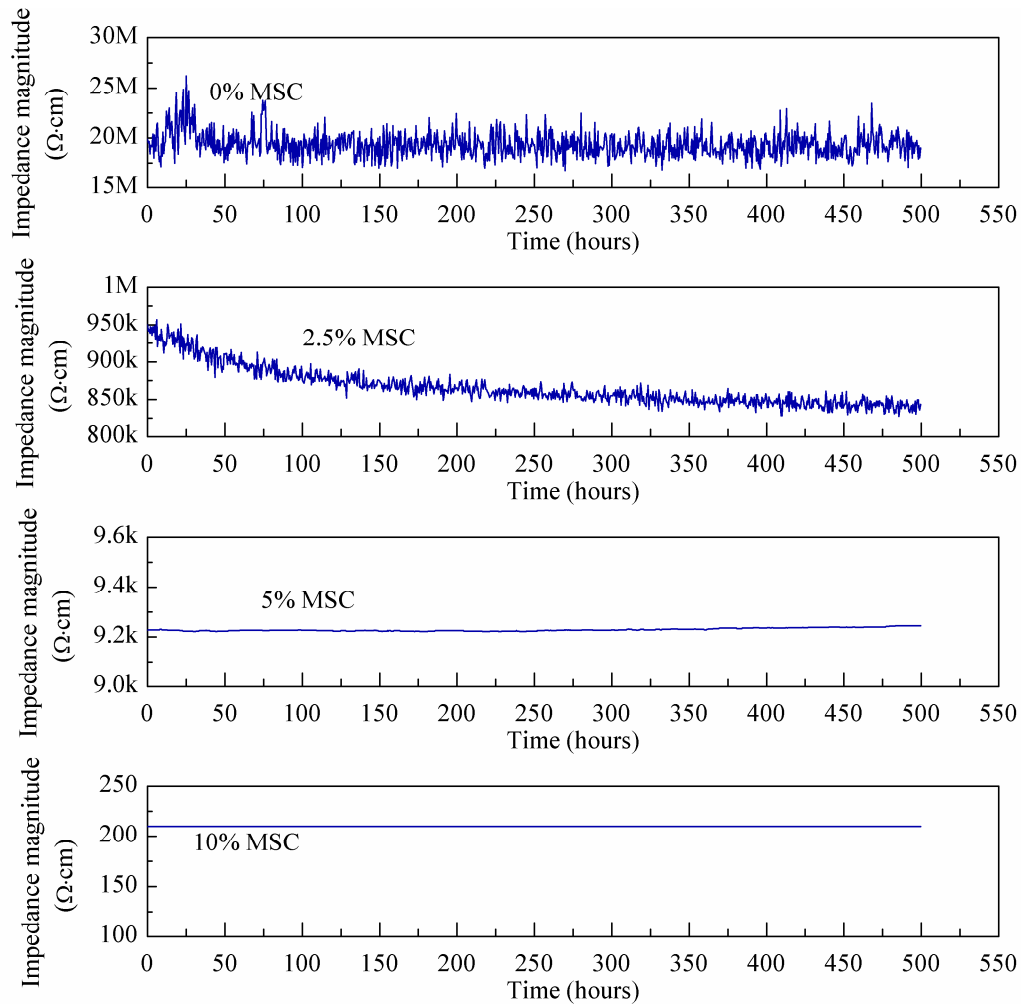


Figure 4.9 The change of average impedance magnitude in terms of measurement time

It is shown that for 0% MSC, the measurement of impedance magnitude varied around a stable value, which was about 20 MΩ·cm. A significant noise level was observed, with the variation of around 5 MΩ·cm. For 2.5% MSC, the noise level was significantly reduced compared with 0% MSC and bulk impedance was 20 times lower, suggesting that adding carbon black nanoparticles into cementitious matrix not only reduced bulk impedance but also improved signal-to-noise ratio significantly. On the contrary, the impedance magnitude of 5% MSC and 10% MSC did not show obvious variation corresponding to increasing measurement time, indicating supremely high signal-to-noise ratio.



Figure 4.10 Desiccator with 6 chambers

Table 4.2 Relative humidity and desiccants

Relative Humidity(percent)	Desiccants	Condition
15	Lithium chloride	Compressed Nitrogen
35	Calcium chloride	Compressed Nitrogen
65	Sodium nitrite	No
75	Sodium nitrite	No
85	Potassium chloride	No
93	di-sodium hydrogen	No

In order to study how different relative humidity level influenced the bulk impedance and sensing behavior, following experimental schemes were performed. One desiccator with six chambers was established, which was made from transparent plexiglass, as shown in Figure 4.10. Each chamber was a sealable enclosure with one relative humidity and temperature meter placed inside. One nitrogen tank was connected to two of the chambers so that relative humidity can be lowered below room humidity. The desiccator was located in the lab with constant temperature

controlled as 25 °C and stable relative humidity controlled as  $50 \pm 5\%$ . Six different humidity conditions, i.e., 15%, 35%, 65%, 75%, 85%, and 93%, were achieved via different desiccants and compressed nitrogen. The humidity conditions and corresponding desiccants were listed in Table 4.2.

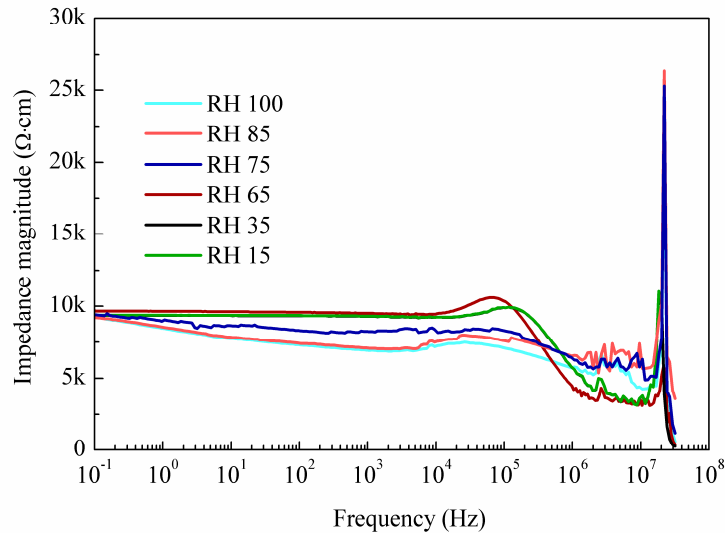


Figure 4.11 Impedance magnitude of 5% MSC under different relative humidity conditions

Upon established desiccator, a series of tests was performed. Before coupon specimens were placed into a desiccator, they were first put into temperature chamber to be heated for 48 hours for 80 °C, allowing internal moisture in cementitious matrix evaporated but not resulting into damage in specimens. Thereafter, specimens were put into desiccator chambers with 15% RH for 72 hours. Afterward, specimens were taken out of the desiccator and scanned using impedance analyzer with a frequency ranging from 0.1 Hz to 32 MHz. The data collection rate was 35 points per frequency decade. Then the specimens were put into the desiccator chamber with 35% RH for another 72 hours. Same EIS scan was conducted thereafter. A similar procedure was performed for 6 times with relative humidity increased from 15% to 93%. The frequency-dependent impedance of 5% MSC was plotted in Figure 4.11. The x-axis is the

frequency ranging from 0.1 Hz to 32 MHz in logarithmic scale. The y-axis is the impedance magnitude. It can be observed that increasing relative humidity resulted into a decrease in impedance magnitude at different frequencies. At 100% RH, 0% MSC showed the lowest impedance magnitude. For 10%, 35%, and 65% RH, impedance magnitude did not change obviously. The results suggest that increasing relative humidity leads to an increase in internal moisture content within the cementitious matrix, involving more ion conductivity into bulk materials.

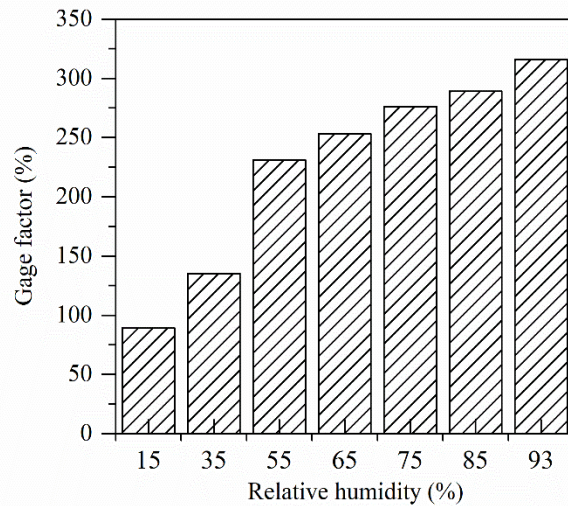


Figure 4.12 Gage factor corresponding to different relative humidity levels

Simultaneously, after each EIS scan, one cyclic tensile sensing test was performed following the same procedure as shown in Section 4.2. The test was performed only on 5% MSC materials. The gage factor comparisons in terms of different humidity condition were plotted in Figure 4.12. It can be found that gage factor increased significantly in correspondence to increasing relative humidity. 5% MSC shows the lowest gage factor (89) at 15% RH and the highest gage factor (312) at 93% RH. It suggests that moisture content of cementitious matrix influenced the sensing performance. Increasing moisture content leads to more ion conductivity

in cementitious matrix, leading to lower bulk impedance. Based on Eq. (3.2), gage factor was hence reduced due to high bulk impedance magnitude.



Figure 4.13 Instron temperature chamber

In order to study the temperature effect on 5% MSC, the coupon specimens made from 5% MSC were put into the environmental chamber, as shown in Figure 4.13. Instron 3119-600 series temperature controlled chamber was used. It has an interlock switch, which operates when the door is opened and cuts power to the heating elements or cooling valve and fan. The temperature can be controlled ranging from  $-150\text{ }^{\circ}\text{C}$  to  $+600\text{ }^{\circ}\text{C}$ . A solartron impedance analyzer was used to measure impedance change during the change in temperature. In this study, the temperature was first gradually increased to  $200\text{ }^{\circ}\text{C}$  with an increment of  $10\text{ }^{\circ}\text{C}$ . At each increment, EIS scan was conducted. Then the temperature was then cooled to  $25\text{ }^{\circ}\text{C}$ . The surface of the specimen was wrapped with epoxy to prevent loss of internal moisture within the cementitious matrix. Figure 4.14 shows the impedance change in terms of the temperature. It is shown that increasing temperature gradually decreased the impedance magnitude of 5% MSC, indicating that, upon an increase in temperature, the atoms within the composites vibrate with more energy and therefore

more vigorously, hence making the electrons flowing through the electric circuit more likely to pass from one carbon black particles to another, so decreasing impedance magnitude.

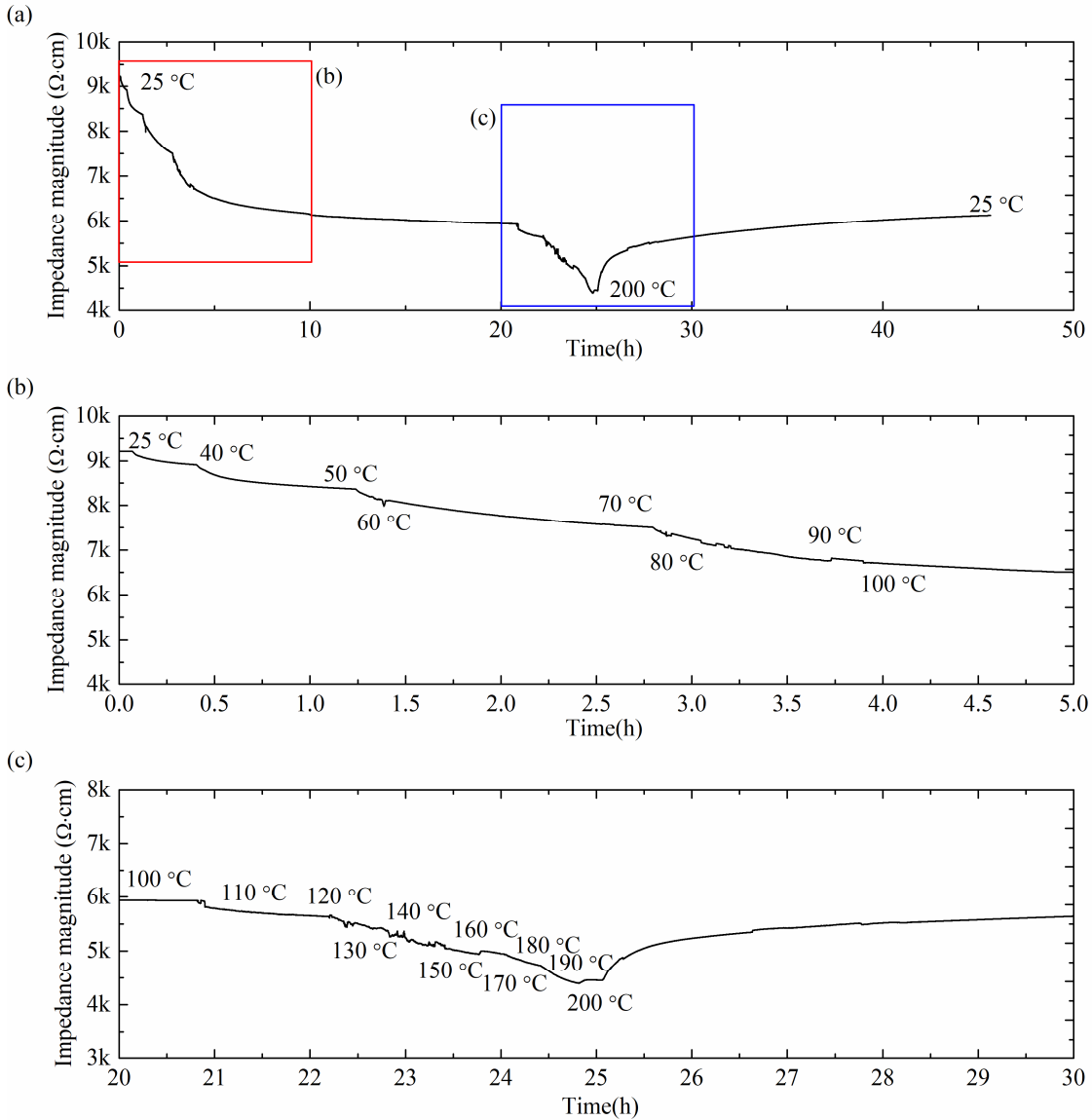


Figure 4.14 Change in impedance magnitude corresponding to varying temperature

#### 4.4 Conclusions

The following conclusions are drawn from this chapter:

1. The 2.5%, 5%, and 10% MSCs exhibit elastic strain sensing capacity, with a linear relation between impedance magnitude and strain (tension and compression). Such linear relation

is not found in 0% SHC, for which the impedance magnitude exhibits significant noise. 5% MSC shows the highest gage factor (254 in tension and 323 in compression) among the four mix designs, due to the optimal combination of partially conductive paths and conductive paths in the cementitious matrix. The gage factor achieved here is 100 higher than common metallic strain gages.

2. The strain sensing capacity of MSCs extends from elastic strain stage to tensile strain-hardening stage and tension softening stage. The nonlinear relation between impedance (impedance magnitude, imaginary part of impedance, and real part of impedance) change and increasing strain is mainly attributed to the multiple cracking process during the strain-hardening stage, and the localized cracking opening during the tension softening stage. In contrast, the relation is linear for 0% SHC. The difference between MSCs and SHC is due to the electrical modification of fiber surface and fiber/matrix interface, which consequently alters the crack impedance behavior.

3. The crack impedance response can be represented by an equivalent circuit which contains a capacitor and a resistor connected in parallel. When the SHC does not contain any carbon black nanoparticles, the capacitor effect is more predominant during crack opening and propagation. For MSCs which include carbon black nanoparticles, both the crack capacitor and crack resistor lead to the nonlinear increase in impedance magnitude, imaginary and real parts with increasing strain.

4. The tensile strain-hardening stage and tension softening stage can be differentiated based on the change in the increasing trend of the imaginary part of the impedance for MSCs. The faster increase of the impedance in the tension softening stage is attributed to the evolution of the localized final failure crack. SHC, however, does not possess this capacity.



5. The imaginary part of the impedance is around 10 times more sensitive to the cracking, compared with the real part and the impedance magnitude. The high sensitivity of imaginary part of the impedance to the cracking is attributed to the capacitor effect of the crack.

6. The reversible strain sensing capacity can be extended to 0.5% for 5% and 10% MSCs. Compared with the normal self-sensing concrete, the robust reversible tensile strain sensing capacity is increased by 50 times. For 5% and 10% MSCs, the presence of a large amount of carbon black leads to a reduction of the cracking effect and provides a reversible cyclic sensing capacity without much residual impedance.

## CHAPTER 5: EFFECTS OF DAMAGE AND HEALING ON THE IMPEDANCE OF MSCS - A MULTI-SCALE MODEL

### 5.1 Introduction

Electromechanical behavior of MSCs is discussed in Chapter 4. Strain sensing after initial cracking of the cementitious materials was attributed to cracking evolution. Also, autogenous self-healing has been observed in MSCs. Therefore, this chapter focuses on the impedance change due to cracking and autogenous self-healing. In particular, the mechanisms underneath the electromechanical behaviors of MSCs were revealed experimentally and theoretically.

For MSCs, as discussed in Chapter 4, impedance change is linearly or pseudo-linearly related to tension or compression elastic strain change, which is called piezoresistivity. The piezoresistivity is normally measured using a gage factor ( $GF$ ), defined in Eq. (3.2). The mechanism of piezoresistivity within the elastic range was interpreted by several researchers. Taya et al. and Xiao et al. proposed that piezoresistivity is attributed to the degeneration of initially percolating networks formed via tunneling effect between conductive fillers [128, 202]. Chung believed that the slight pullout of conductive fibers within the cementitious matrix changes fiber-matrix contact resistivity, resulting in piezoresistivity phenomena [206].

Until now only a few investigations regarding the electromechanical behavior of cementitious materials after cracking have been performed. Chung et al.[100] demonstrated that the fracture of the bridging fibers across microcracks results in the increase in resistivity which indicated the damage occurrence. Peled et al.[207] reported AC electrical impedance spectroscopy characterization of carbon and steel fiber reinforced cementitious composites featuring a tension softening post-cracking behavior. Le et al.[208] quantified the damage extent

(artificial notch) using an electric potential measurement based on a mathematical analogy between the electrostatic field and the elastostatic field under anti-plane shear loading. Due to the uncontrolled crack pattern, it is difficult to directly establish robust relations between the post-cracking mechanical behavior of normal cementitious materials with an electrical response. Hou et al.[209, 210] observed the electrical resistance change of SHC at strain-hardening and tension softening stages under the case of 100% Relative Humidity (RH) curing environment. It was found that at the elastic stage, the resistance change follows a linear relation in accordance with the mechanical strain. However, a nonlinear relation can be observed once the specimen cracks. Li et al.[130, 132] found that the similar nonlinear relation between electrical resistance and mechanical strain exists for SHC with carbon black, cured at normal air conditions. The above studies mainly focused on experimental observations and did not further explain the nonlinear electromechanical behavior of SHC. Ranade et al.[211] investigated the tension induced resistivity change of SHC at the age of 28 days cured at room temperature and humidity. The series resistance analytical model was utilized to describe the influence of microcracking on the composite resistivity of SHC, successfully predicting the composite electrical response based on single cracking behavior. This study mainly focused on the multi-scale framework from a single crack to multiple cracks, and did not further explain the physics underneath the cracking-induced electromechanical response.

This chapter aims to Elucidate the electromechanical behavior and mechanisms of MSC through experiments and modeling. The model involves the fiber pull-out procedure and matrix cracking during the development of flat steady-state cracks. For each crack, the electromechanical response is directly dependent on the crack opening and mechanical stage of fibers bridging the crack. Subsequently, the composite electromechanical response of multiple

cracks is attained via considering cracks connected in series circuits. The experimental results obtained in uniaxial monotonic tension tests on MSCs and SHCs serve as a general support for the proposed physical mechanisms and multi-scale modeling approach. Also, the model is able to interpret the impedance change due to autogenous self-healing occurred in MSCs.

## **5.2 The Multi-Scale Model**

The multiple-scale model is established from single fiber behavior to single crack opening and multiple cracking. Unlike the series resistance analytical model, this model considers different types of equivalent circuit elements to capture different electrical behavior, such as the dielectric behavior of cracking, the electrical conduction behavior of bridging fibers with matrix particles, etc. In this part, there are four sections. Section 5.2.1 discusses the model establishment. Section 5.2.2 focuses on the bulk impedance part in the model. Section 5.2.3 describes the proposed electromechanical model in detail. Lastly, in Section 5.2.4, the model is depicted in three scales: single fiber pull-out, single cracking, and multiple cracking.

### *5.2.1 Model establishment*

One MSC specimen with the geometry of  $L \times W \times T$  is considered, where  $L$  is the gauge length,  $W$  is the width, and  $T$  is the thickness. Assume that four electrodes are attached to the specimen, as shown in Figure 5.1(a). Electrodes were parallel to each other. There is an alternating current  $I$  injected into the specimen and passing through the middle part of the specimen. The voltage  $V$  is measured via two inner electrodes. Voltage measurement and injected alternating current results into bulk impedance ( $Z_b$ ) of the specimen between two inner electrodes (Figure 5.1(a)).

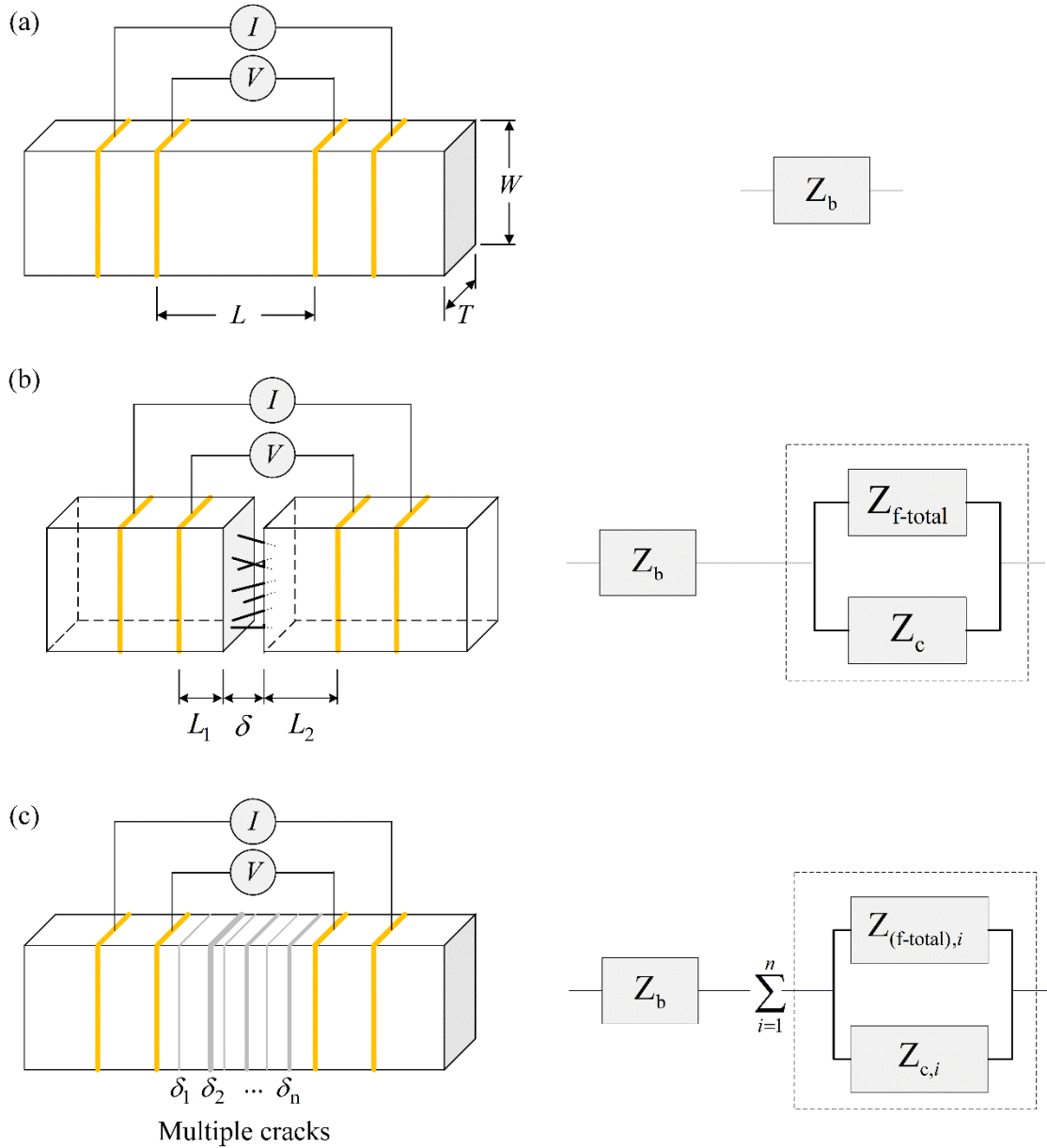


Figure 5.1 Overview of the model: (a) specimen before crack; (b) a single crack; (c) multiple cracks

Assume that the specimen is under uniform tension force, and hence one single crack is running through the transverse cross-section of the specimen with short fibers reinforcing the crack, shown in Figure 5.1(b). The crack is parallel to the cross-section, with the crack width of  $\delta$ . The crack locates between two inner electrodes, separating the gauge length  $L$  into  $L_1$  and  $L_2$ .

The short fibers bridge the crack in both random length and random angle. The bulk impedance becomes two parts separated by the crack. At this scenario, the measured total impedance  $Z_{\text{total-s}}$  is the sum of bulk impedance  $Z_b$  and single crack impedance  $Z_{\text{crack-s}}$  as shown in Eq. (5.1).

$$Z_{\text{total-s}} = Z_b + Z_{\text{crack-s}} = Z_b + \frac{1}{\frac{1}{Z_{f\text{-total}}} + \frac{1}{Z_c}} \quad (5.1)$$

where single crack impedance  $Z_{\text{crack-s}}$  is formed by an equivalent circuit with two impedance elements  $Z_{f\text{-total}}$  and  $Z_c$  in parallel.  $Z_{f\text{-total}}$  represents the change of contact impedance between fibers and matrix;  $Z_c$  represents the impedance of crack capacitance. Determination of  $Z_c$  and  $Z_{f\text{-total}}$  are discussed in Section 5.2.3 in detail. Via Eq. (5.1), the scale linking from the single fiber to the single crack is built.

Figure 5.1(c) illustrates the scenario of multiple cracks. There are  $n$  cracks distributed between two inner electrodes. Following assumptions are made: 1. Cracks run through the transverse cross-section of the specimen and are not inclined. 2. Cracks do not interact with each other. 3. Cracks are flat steady-state cracks and have constant crack width through crack cross-section; 4. There is one crack which opens gradually at the tension softening stage; 5. The initial number of fibers within each crack is a constant  $N_0$ .

The width of each crack is denoted by  $\delta_i$ , where  $i$  is the number of crack from 1 to  $n$ . Thus, the gauge length  $L$  is divided into  $n+1$  parts by cracks. The total impedance  $Z_{\text{total-m}}$  is written as the sum of bulk impedance  $Z_b$  and crack impedance  $Z_{\text{crack-m}}$ , where  $Z_{\text{crack-m}}$  is the total impedance of all cracks.

$$Z_{\text{total-m}} = Z_b + Z_{\text{crack-m}} = Z_b + \sum_{i=1}^n Z_{\text{crack-s}, i} = Z_b + \sum_{i=1}^n \frac{1}{\frac{1}{Z_{(f\text{-total}), i}} + \frac{1}{Z_{c, i}}} \quad (5.2)$$

where  $Z_{(f\text{-total}), i}$  represents  $Z_{f\text{-total}}$  of  $i^{\text{th}}$  crack;  $Z_{c, i}$  represents  $Z_c$  of  $i^{\text{th}}$  crack, which is described in detail in Section 5.2.3. Eq. (5.2) links the single cracking scale to the multiple cracking scale.

### 5.2.2 Bulk impedance

The bulk impedance  $Z_b$  of above sample is as same as described in Figure 2.25. But in this section, the imperfect capacitor is considered as the constant phase element. The bulk impedance is represented by an equivalent circuit model containing an imperfect capacitor (Constant Phase Element  $Q_{b1}$ ) and a resistor ( $R_{b1}$ ) connected in series, in parallel with a Constant Phase Element ( $Q_{b2}$ ), and a resistor ( $R_{b2}$ ) (Figure 5.2). It is modeled that there are three parallel current paths within the cementitious matrix: dielectric paths, conductive paths, and discontinuous conductive paths. Conductive paths are formed by connected pore solutions or conductive fillers, represented by a resistor ( $R_{b2}$ ). Discontinuous conductive paths are conductive paths, but with continuity blocked by “insulated” matrix parts, modeled by a resistor ( $R_{b1}$ ) and a Constant Phase Element ( $Q_{b1}$ ) in series.  $Q_{b2}$  represents the overall dielectric behavior of the cementitious matrix. The bulk impedance is written in Eq. (5.3).

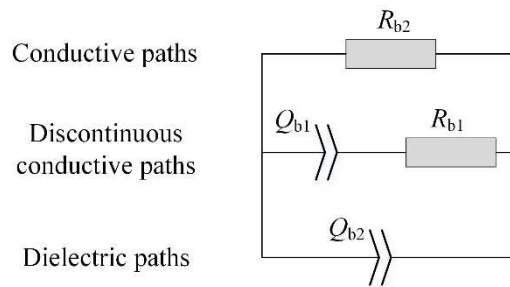


Figure 5.2 Equivalent circuit model of the bulk material

$$Z_b = \frac{1}{(j\omega)^{\lambda_{b2}} Q_{b2} + \frac{1}{R_{b2}} + \frac{1}{R_{b1} + \frac{1}{(j\omega)^{\lambda_{b1}} Q_{b1}}}} \quad (5.3)$$

where  $j$  is the imaginary unit,  $\omega$  is the angular frequency of the sinusoidal signal,  $\lambda_{b1}$  is the exponent parameter of  $Q_{b1}$ , and  $\lambda_{b2}$  is the exponent parameter of  $Q_{b1}$ . It should be noted that the bulk impedance after cracking is equal to uncracked bulk impedance  $Z_b$ .

### 5.2.3 Model details

#### *Single fiber scale*

First, a single crack occurs on the specimen, resulting in the electromechanical response attributed to a single fiber pullout. Second, the single crack model is established by statically calculating the electromechanical responses of all fibers and considering the dielectric effect of the crack. The third step involves linking the single cracking electromechanical behavior to the multiple cracking electromechanical behaviors. It should be mentioned that the impedance change due to elastic deformation before cracking is considered in the multiple cracking scale.

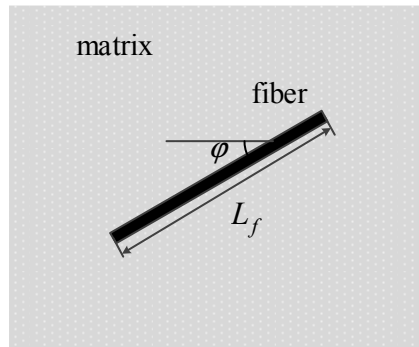


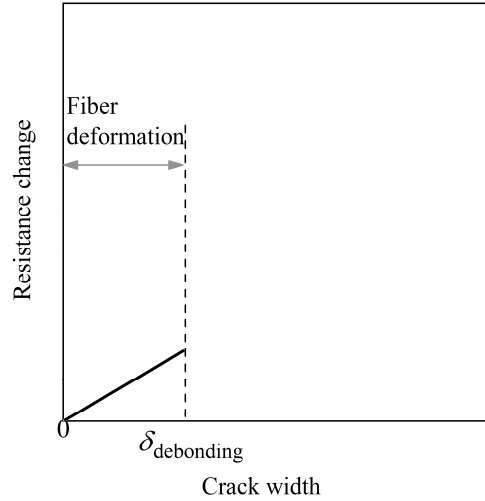
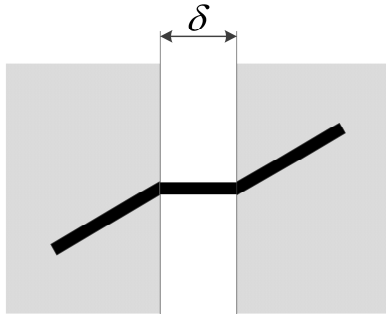
Figure 5.3 A short fiber embedded in the MSC material

As shown in Figure 5.3, there is one fiber embedded in the MSC matrix, with the fiber length of  $L_f$ . Before cracking, the matrix and the fiber contribute to the bulk impedance  $Z_b$ , following the equivalent circuit model in Figure 5.2. The contact impedance of the fiber-matrix interface is simplified as contact resistance ( $R_{f\text{-contact}}$ ). It should be noted that  $R_{f\text{-contact}}$  is part of the



bulk impedance  $Z_b$ , while the change of  $R_{f\text{-contact}}$  due to cracking is part of the crack impedance  $Z_{\text{crack-s}}$ .

(a) Fiber debonding



(b) Fiber pull-out

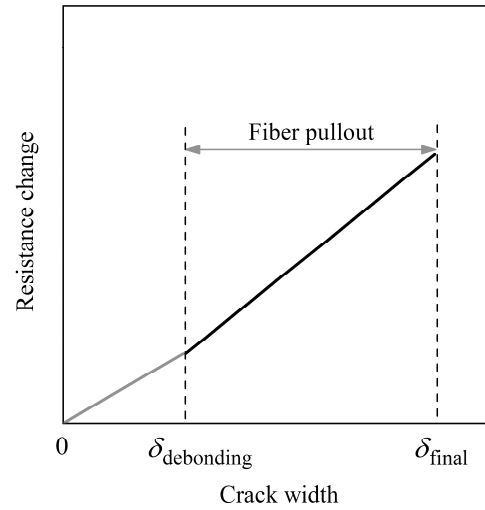
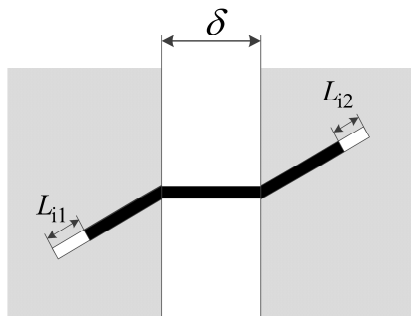


Figure 5.4 Determination of contact resistance  $R_{f\text{-contact}}$  between the fiber and matrix

As shown in Figure 5.4, once there is a crack with opening  $\delta$ , the fiber bridges the crack and hence the fiber is under tensile strain  $\varepsilon_f$ . First, the fiber deforms with the contact area between fiber and matrix not changing. Thereafter, the fiber undergoes the pullout procedure, resulting in the void tunnels at two ends of the fiber. Thus, the contact area between the fiber and

matrix is lessened due to fiber pull-out.  $L_{i1}$  and  $L_{i2}$  denote the length of the two void tunnels, respectively.

While the alternating current is injected into the specimen, there are two types of paths that current passing through the crack. The first path involves the fibers with matrix particles which connect both ends of the crack, behaving as a resistor. For this path, the alternating current passes following medias in sequence: (1) matrix, (2) fiber and matrix interface, (3) fiber, (4) fiber and matrix interface, and (5) matrix. The second path is the double layer capacitance formed by crack edges, with fibers, matrix particles, air, discontinuous humidity, etc. in the crack as dielectric materials. The second current path is considered in the single cracking scale.

In the first current path, the cracking-induced impedance ( $Z_f$ ) for a single fiber is expressed as:

$$Z_f = Z_{int1} + Z_{int2} + Z_{df} \quad (5.4)$$

where  $Z_{int1}$  and  $Z_{int2}$  are changes in the contact impedance, and  $Z_{df}$  is the impedance change due to fiber deformation. In this study,  $Z_{int1}$  and  $Z_{int2}$  are simplified as the change of contact resistance, denoted by  $R_{int1}$  and  $R_{int2}$ .  $Z_{df}$  is considered as the resistance change due to fiber deformation ( $R_{df}$ ).

At the fiber debonding stage,  $Z_f$  is given as a linear relation (Eq.(5.5)) illustrated in Figure 5.4(a).

$$Z_f = R_{df} = \frac{4 \times \rho_f \times L_f \times \varepsilon_f}{\pi \times d_f^2} = \frac{4 \times \rho_f \times \delta}{\pi \times d_f^2} \quad (0 \leq \delta \leq \delta_{debonding}) \quad (5.5)$$

where  $\rho_f$  is the fiber resistivity,  $\varepsilon_f$  is the tensile strain of the fiber,  $d_f$  is the fiber diameter, and  $\delta_{debonding}$  is the crack width at which fiber is fully debonded.

Right after fiber debonding stage is the fiber pull-out stage (Figure 5.4(b)). Assuming tensile strain of fiber does not drop due to pull-out of the fiber. The total length of the pull-out void tunnels ( $L_{i1}$  and  $L_{i2}$ ) is directly related to crack opening  $\delta$ :

$$L_{i1} + L_{i2} = \delta - \delta_{\text{debonding}} \quad (5.6)$$

$R_{\text{int1}}$  and  $R_{\text{int2}}$  are considered as linearly dependent on  $L_{i1}$  and  $L_{i2}$ , respectively. Eq.(5.7) gives  $R_{\text{int1}}$  and  $R_{\text{int2}}$ :

$$R_{\text{int1}} = \rho_c \times (\pi \times d_f) \times L_{i1} \quad \text{and} \quad R_{\text{int2}} = \rho_c \times (\pi \times d_f) \times L_{i2} \quad (5.7)$$

where  $\rho_c$  is the fiber-matrix contact resistivity.

Then  $Z_f$  at fiber pull-out stage is derived from Eq.(5.4), (5.5), (5.6), and (5.7):

$$Z_f = \rho_c \times (\pi \times d_f) \times (\delta - \delta_{\text{debonding}}) + \frac{4 \times \rho_f \times \delta_{\text{debonding}}}{\pi \times d_f^2} \quad (\delta_{\text{debonding}} < \delta \leq \delta_{\text{final}}) \quad (5.8)$$

where  $\delta_{\text{final}}$  is the crack width where fiber ruptures or is fully pulled out.

Eq.(5.9) summaries  $Z_f$ :

$$Z_f = \begin{cases} \frac{4 \times \rho_f \times \delta}{\pi \times d_f^2} & 0 \leq \delta \leq \delta_{\text{debonding}} \\ \frac{4 \times \rho_f \times \delta_{\text{debonding}}}{\pi \times d_f^2} + \rho_c \times \pi \times d_f \times (\delta - \delta_{\text{debonding}}) & \delta_{\text{debonding}} < \delta \leq \delta_{\text{final}} \end{cases} \quad (5.9)$$

Figure 5.4 illustrates Eq.(5.9), displaying two linear relations through debonding and pull-out stage. Considering the deformation of fiber can be ignored, Eq.(5.9) can be simplified into one linear relation from debonding to the pull-out stage (Eq.(5.10)).

$$Z_f = \rho \times \pi \times d_f \times \delta \quad (0 \leq \delta \leq \delta_{\text{final}}) \quad (5.10)$$

where  $\rho$  is the defined resistivity parameter considering both fiber deformation and contact resistivity.

Simultaneously, the theoretical single fiber load vs crack width relation ( $P$ - $\delta$ ) is given as [212]:

$$P = \begin{cases} \pi \sqrt{(\tau_0 \delta + G_d) \frac{E_f d_f^2 (1 + \eta)}{2}} & 0 \leq \delta \leq \delta_{\text{debonding}} \\ \pi \tau_0 (L_f - \delta + \delta_{\text{debonding}}) (d_f + \beta (\delta - \delta_{\text{debonding}})) & \delta_{\text{debonding}} \leq \delta \leq \delta_{\text{final}} \end{cases} \quad (5.11)$$

where  $\tau_0$  is the frictional bond strength,  $E_f$  is the fiber elastic modulus,  $G_d$  is the chemical bond energy, and  $L_f$  is the fiber length.

$\delta_{\text{debonding}}$  corresponds to the displacement at which fully debonding is completed, which is given by:

$$\delta_{\text{debonding}} = \frac{2\pi L_f^2 (1 + \eta)}{E_f d_f} + \sqrt{\frac{8G_d L_f^2 (1 + \eta)}{E_f d_f}} \quad (5.12)$$

The effect of fiber alignment on the pullout load, so-called ‘‘snubbing effect’’, was considered. An empirical relation is given by:

$$P(\varphi) = P(0)e^{f\varphi} \quad (5.13)$$

### *Single cracking scale*

Electromechanical model at the single cracking scale is derived. In this study, the crack is not traction free but bridged by numerous fibers with random orientation and embedment lengths, as displayed in Figure 5.5. The single crack model involves two impedance elements  $Z_{f\text{-total}}$  and  $Z_c$  in a parallel circuit (Figure 5.1). This section first concentrates on the determination of  $Z_{f\text{-total}}$  and then discusses  $Z_c$ .

As illustrated in Figure 5.5, the fibers bridge a crack in parallel, and hence the impedance (here it is simplified as resistance, as explained above) of all fibers (fiber number is  $N$ ) can be determined by the parallel circuit in Figure 5.5. Thus, the total fiber impedance  $Z_{f\text{-total}}$  is written in Eq.(5.14).

$$Z_{f\text{-total}} = R_{f\text{-total}} = \frac{1}{\sum_{h=1}^N \frac{1}{R_{f,h}}} \quad (5.14)$$

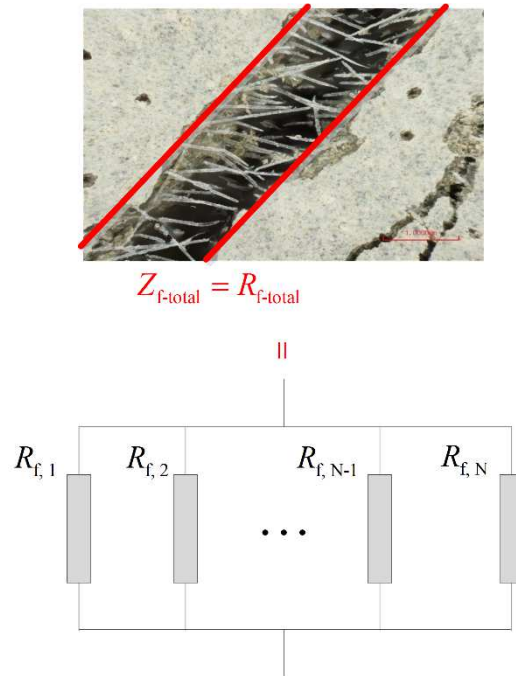


Figure 5.5 Determination of  $Z_{f\text{-total}}$

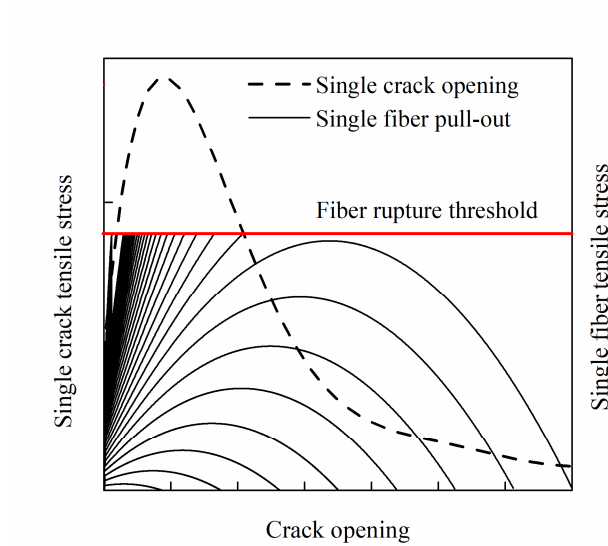


Figure 5.6 Plot of single crack opening v.s. single crack tensile stress, and corresponding single fiber pull-out stress-strain relations

The contact resistance change of each fiber is directly determined by its mechanical stage (Figure 5.4). Figure 5.6 shows the link between the single crack behavior and single fiber behavior, schematically. Under tensile force, the single crack opening and stress relation is illustrated as the dashed lines. With a crack, all fibers undergo single fiber debonding and pull-out process. the solid lines represent single fiber debonding and pull-out curves for all fibers. The fiber rupture strength is plotted as the red line to limit fibers' pull-out behavior. It is observed that, for a given crack opening, there are a certain amount of fibers bridging the crack, with some of them under debonding stage and others at the pull-out stage. Once a fiber reaches rupture strength or fully pulled out, it does not connect two crack edges. With changing crack opening, the proportion of fibers at debonding stage and fibers at pull-out stage varies. In this study, it is considered that merely the fibers at debonding and pull-out stages contribute as the resistor current path ( $R_{f\text{-total}}$ ). In order to quantify  $R_{f\text{-total}}$ , it is necessary to first determine the relation between the number of fibers bridging the crack ( $N$ ) and crack opening ( $\delta$ ).

At a given crack width, for fibers which bridge the crack, orientation probability density function ( $p(\varphi)$ ) and the probability density function of the centroidal distance ( $p(z)$ ) is given in Eq.(5.15) and Eq.(5.16).

$$p(\varphi) = \sin \varphi \quad (0 \leq \varphi < \frac{\pi}{2}) \quad (5.15)$$

$$p(z) = \frac{2}{L_f} \quad 0 \leq z \leq \frac{L_f}{2} \quad (5.16)$$

Thus, an initial number of fibers ( $N_0$ ) is given in Eq.(5.17).  $N_t$  is the total number of fibers in the matrix.

$$dN_0 = N_t p(\varphi) d\varphi p(z) dz \quad \text{for } 0 \leq \varphi \leq \arccos\left(\frac{2z}{L_f}\right) \text{ and } 0 \leq z \leq \frac{L_f}{2} \quad (5.17)$$

where  $N_t = \frac{A}{A_f} V_f$ ,  $A_f$  is fiber cross-section area, and  $V_f$  is the fiber volume fraction.

Original fiber number ( $N_0$ ) indicates how many fibers have the potential to bridge the crack. As the crack opens, the number of fibers ( $N$ ) bridging the crack decreases gradually, due to fiber rupture and fully pull-out. The procedure to determine the status of the fiber is shown below. Based on the  $P \sim \delta$  relation of a single fiber pullout, the composite crack bridging law can be obtained by averaging over the contributions of only those individual fibers that cross the matrix crack plane as the crack opens up.

Averaging  $\sigma \sim \delta$  relation across a crack:

$$\sigma(\delta) = \frac{V_f}{A_f} \int_{\phi_0}^{\phi_1} \int_{z=0}^{(L_f/2)/\cos\phi} P(\delta, L_e) g(\phi) p(\phi) p(z) dz d\phi \quad (5.18)$$

The ratio ( $F(\delta)$ ) of fibers fully pulled out or ruptured can be determined by algorithm in Figure 5.7.

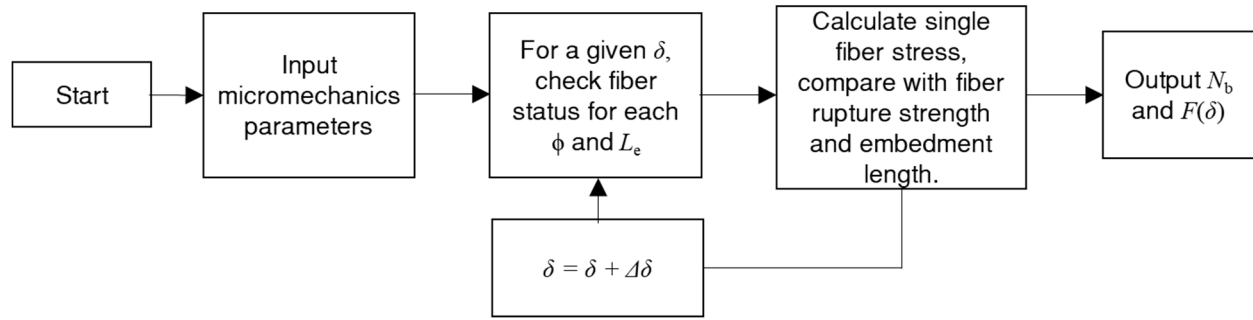


Figure 5.7 Algorithm to determine the ratio of fibers fully pulled out or ruptured

Therefore, the number of fibers ( $N$ ) in terms of crack width is calculated:

$$N = N_0(1 - F(\delta)) \quad (5.19)$$

Combining Eq.(5.13) and Eq.(5.19) comes out  $R_{f-total}$ , shown in Eq.(5.20).

$$R_c = R_{f\text{-total}} = \frac{1}{\sum_{h=1}^{N_0(1-F(\delta))} \frac{1}{R_{f,h}}} \quad (5.20)$$

Then we focus on  $Z_c$ , the impedance of parallel crack edges. Within crack, fibers, matrix particles, discontinuous humidity, etc. are considered as dielectric materials. Under DC current, crack edges are insulated. However, the cracking area can be penetrated by an AC current by capacitive charging and discharging effect of the dielectric materials.

The  $Z_c$  is determined as follows:

$$Z_c = \frac{1}{(j\omega)^\lambda Q_c} = \frac{\delta}{(j\omega)^\lambda \varepsilon_r \varepsilon_0 A} \quad (5.21)$$

where  $Q_c$  is the constant phase element,  $\varepsilon_r$  is the relative static permittivity,  $\varepsilon_0$  is the electric constant,  $A$  is the crack area, and  $\lambda$  is an exponent from 0 to 1.

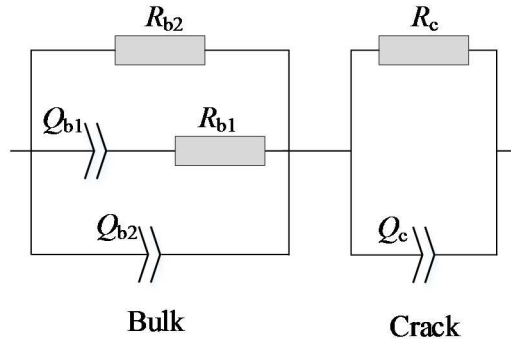


Figure 5.8 Single cracking equivalent circuit model

The single cracking equivalent circuit model is plotted in Figure 5.8. The total impedance of above circuit is as follows:

$$Z_{\text{total-s}} = \frac{1}{\frac{1}{Z_c} + \frac{1}{Z_{f\text{-total}}}} + Z_b = \frac{1}{\frac{(j\omega)^\lambda \varepsilon_r \varepsilon_0 A}{\delta} + \sum_{h=1}^{N_0(1-F(\delta))} \frac{1}{R_{f,h}}} + \frac{1}{(j\omega)^{\lambda_{b2}} Q_{b2} + \frac{1}{R_{b2}} + \frac{1}{R_{b1} + \frac{1}{(j\omega)^{\lambda_{b1}} Q_{b1}}}} \quad (5.22)$$

*Multiple cracking scale*



The multiple microcracking is the key feature of MSCs. During the elastic stage, there are no cracks occurred. Once specimen undergoes the tension softening stage, there is one crack in the specimen which opens gradually with increasing strain. Therefore, the total impedance  $Z_{\text{total-m}}$  is written as the sum of bulk impedance  $Z_b$ , the elastic impedance  $Z_{\text{elastic}}$ , the total impedance of multiple cracks at strain-hardening stage  $Z_{\text{strain-hardening}}$ , and total impedance of multiple cracks at tension softening stage  $Z_{\text{tension softening}}$ .

In the elastic stage,  $Z_{\text{elastic}}$  is assumed to be linearly related to strain level, given in Eq.(5.23).

$$Z_{\text{elastic}} = GF \times \varepsilon \times Z_b \quad (5.23)$$

where,  $GF$  is the elastic gauge factor, and  $\varepsilon$  is the tensile strain.

At the strain-hardening stage, there are  $n$  single crack circuits (one  $Z_{f\text{-total}}$  and one  $Z_c$  in parallel) connected in series. Eq.(5.24) is derived:

$$Z_{\text{strain-hardening}} = \sum_{i=1}^n \frac{1}{\frac{1}{Z_{(f\text{-total}),i}} + \frac{1}{Z_{c,i}}} = \sum_{i=1}^n \frac{1}{\frac{(j\omega)^{\lambda_i} \varepsilon_r \varepsilon_0 A}{\delta_i} + \left( \sum_{h=1}^{N_0(1-F(\delta))} \frac{1}{R_{f,h}} \right)_i} \quad (5.24)$$

Above equation shows that strain-hardening impedance can be expressed as the function of the crack width of each crack  $\delta_i$ , constant phase element exponent  $\lambda_i$ , and the crack number  $n$ .

The tension softening impedance is shown in Eq.(5.25), considering the failure crack as the  $n^{\text{th}}$  crack.

$$Z_{\text{tension-softening}} = \frac{1}{\frac{(j\omega)^{\lambda_n} \varepsilon_r \varepsilon_0 A}{\delta_n} + \left( \sum_{h=1}^{N_0(1-F(\delta))} \frac{1}{R_{f,h}} \right)_n} \quad (5.25)$$

So total impedance of multiple cracking is expressed in Eq.(5.26):

$$Z_{\text{total-m}} = \begin{cases} Z_b + Z_{\text{elastic}} & 0 \leq \varepsilon \leq \varepsilon_{\text{crack}} \\ Z_b + Z_{\text{elastic}} + Z_{\text{strain-hardening}} & \varepsilon_{\text{crack}} \leq \varepsilon \leq \varepsilon_{\text{peak}} \\ Z_b + Z_{\text{elastic}} + Z_{\text{strain-hardening}} + Z_{\text{tension-softening}} & \varepsilon_{\text{peak}} \leq \varepsilon \leq \varepsilon_{\text{ultimate}} \end{cases} \quad (5.26)$$

where  $\varepsilon_{\text{crack}}$  is the initial crack strain,  $\varepsilon_{\text{peak}}$  is the strain corresponding to the peak strain, and  $\varepsilon_{\text{ultimate}}$  is the ultimate strain.

## 5.3 Experimental Validations

### 5.3.1 Validation test 1

First validation test regards about the single crack opening test and uniaxial tension test of 0% SHC and 5% MSC. The mix proportions of the materials are reported in Table 3.1. Same single crack opening test was conducted but the continuous measurement of impedance at a fixed frequency of 1500 Hz was performed. Also, similar uniaxial tension test was conducted but the gage length was different, and the continuous measurement of impedance was performed. The single crack opening test was performed on double-notched specimens (Figure 5.9(a)). The 152.4 mm × 50.8 mm × 12.5 mm specimen was notched on both sides by 10 mm each so that under tension, a single crack formed along the notched cross-section. This test was conducted with displacement control at a rate of 0.0005 mm/s. During testing, a high-resolution digital image correlation system was adopted for accurate measurement of the crack opening (Figure 5.9(b)). The specimen surface was painted with black speckles to track the movement of the speckles during loading. The region measured by digital image correlation system is highlighted using blue color. The crack opening values were obtained by measuring the relative vertical displacement between two red lines through the digital image correlation system. Four copper electrodes were attached to the surfaces of the specimen. Two outer electrodes were used to

inject AC current, and two inner electrodes were used for measuring voltage. Impedance measurement was performed at a frequency of 1500 Hz through the tensile test.

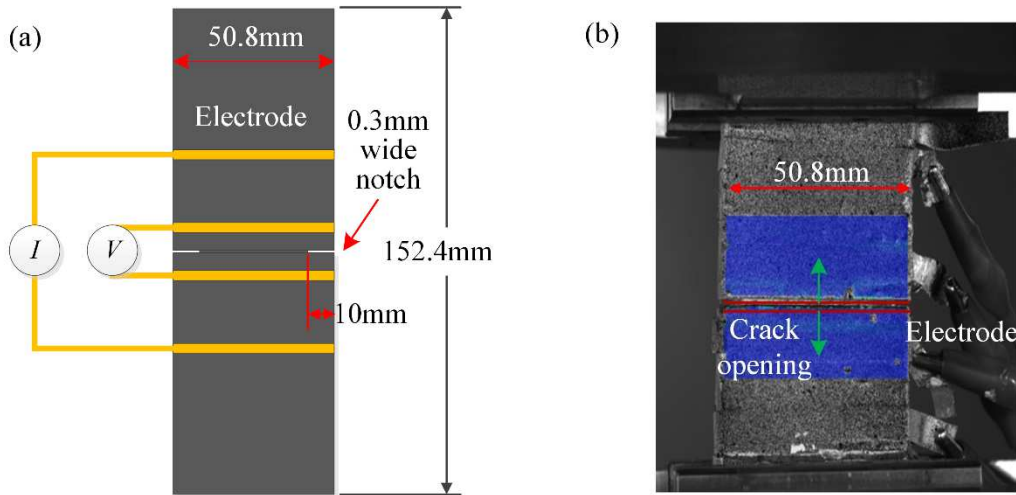


Figure 5.9 Single crack opening test: (a) specimen geometry, and (b) test setup

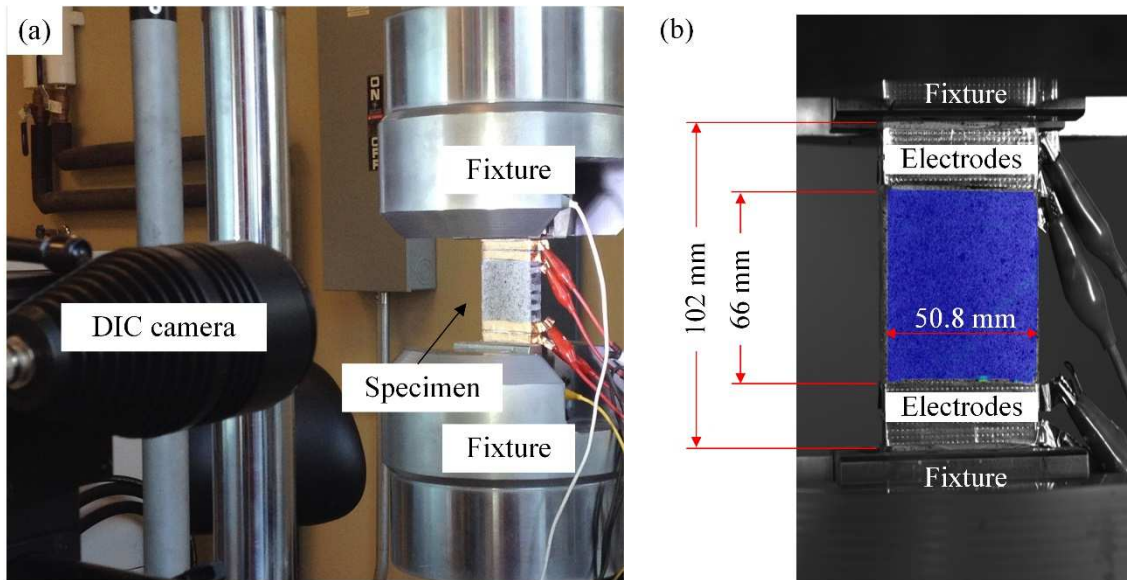


Figure 5.10 Uniaxial tension test: (a) test setup; (b) specimen details

The uniaxial tension test was performed on the unnotched MSC coupon specimens. The test setup is shown in Figure 5.10. The outer two electrodes had a spacing of 102 mm, which is

used to inject AC current. The inner two electrodes had a spacing of 66 mm, for measuring voltage change during loading. The uniaxial tension test was conducted with the same test rate as the single crack opening test. Similar impedance measurement protocols as the single crack opening test were performed during the tensile test. Digital Image Correlation technology (DIC) was utilized to accurately capture the single crack opening and tension strain. DIC is an optical non-contact 2D and 3D deformation measurement technique. It captures sets of high-resolution images before and after deformation of an object to represent different non-deformed and deformed stages.

This test validated the model from single fiber scale to single crack scale, and multiple cracks scale. In terms of single fiber scale, the two parameters which cannot be determined by test was inversely computed based on the single cracking impedance  $\square$  opening relation. The parameters derived from 0% SHC and 5% MSC can be compared to validate the physical assumption in this model. Furthermore, varying the parameters will allow understanding the electromechanical behavior of MSCs deeply. Also, the link from single crack to multiple cracks was verified based on experimental observations.

### *5.3.2 Validation test 2*

The second validation test was mainly focused on the link from single crack scale to multiple cracks. Also, the validation test revealed the self-healing phenomena occurred in the strain-hardening cementitious materials. It should be noted the cementitious materials used in this validation test is slightly different from 0% SHC mentioned in Chapter 3, which also validates the applicability of this model to common strain-hardening cementitious composites. Table 5.1 shows the mix proportion of SHC in this validation test.

An experimental program was devised for preloading the specimens under uniaxial tension to different damage levels, and then subjecting the specimens to different numbers of wet/dry cycles for self-healing to occur. Each complete cycle contained a 24-h dry cycle followed a 24-h wet cycle. Under uniaxial tension, 0% SHC exhibits a multiple microcracking behavior at macro-scale. The increasing level of applied tensile strain leads to an increasing number of microcracks formed in the material. Each microcrack, at the mesoscale, follows the fiber-bridging “spring law” describing the relationship between the tensile stress across the crack and crack opening. Therefore, in terms of damage level, the tests in this study were performed at (1) single crack opening scale (mesoscale), to investigate the effect of single crack opening on material complex impedance, and (2) multiple cracking scale (macro-scale), to investigate the combined effects of crack opening and crack number increase on material complex impedance. Electrical impedance spectroscopy was conducted on undamaged specimens before loading, after different levels of damage, and after different cycles of self-healing.

Table 5.1 Mixing proportion of SHC in Validation test 2

Cement	Water	Sand	Fly ash	Superplasticizer	PVA Fiber
kg/m <sup>3</sup>	kg/m <sup>3</sup>	kg/m <sup>3</sup>	kg/m <sup>3</sup>	kg/m <sup>3</sup>	Vol-%
266	309	456	956	2.7	2

Figure 5.11 shows the  $\sigma \sim \delta$  curve of SHC. The test was paused at different crack opening levels, i.e., 10, 20, 50, 100, 200, 400  $\mu\text{m}$ , denoted as a, b, c, d, e, f, respectively. At each crack opening level, one EIS scan was conducted. Also, the uniaxial tensile test was conducted to measure the tensile stress-strain curve of SHC (Figure 5.12). Similarly, the tension test was paused at six strain levels, i.e., 0.5%, 1%, 1.5%, 2%, 2.5%, and 3%, so that EIS measurements were performed. At measurements, healing cycles were applied to the damaged specimens.

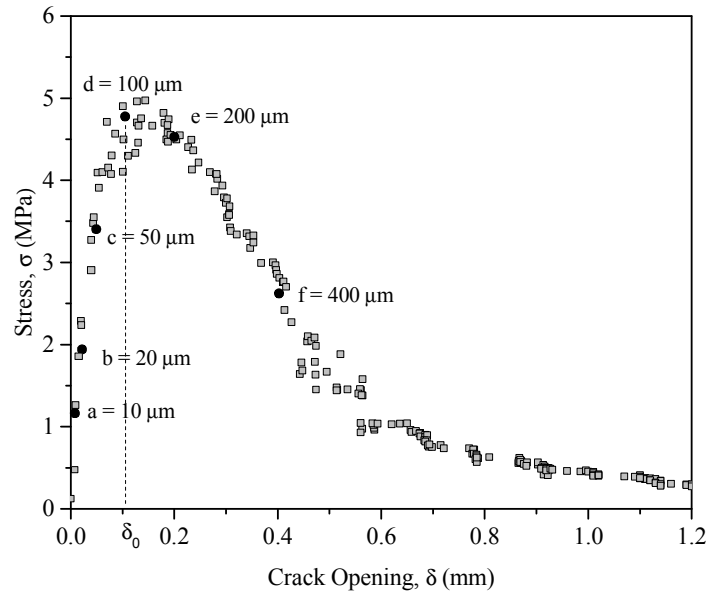


Figure 5.11 Single crack opening behavior ( $\sigma \sim \delta$  relation) of SHC. EIS was performed at different crack opening values as marked on the curve

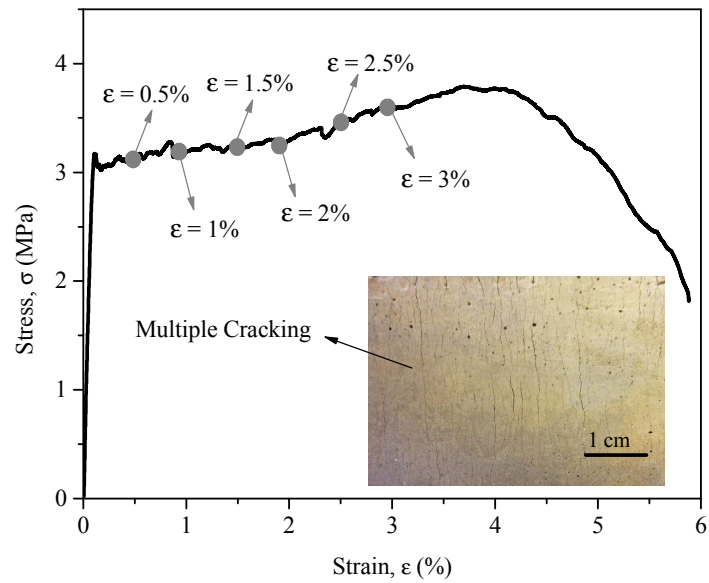


Figure 5.12 Tensile stress-strain curve ( $\sigma \sim \epsilon$  relation) and multiple microcracking behavior of SHC. EIS was performed at different strain values as marked, corresponding to different damage levels within SHC

## 5.4 Results and Discussions: Validation Test 1

### 5.4.1 Single crack opening test results

The fiber bridging tensile stress v.s. crack opening ( $\sigma\sim\delta$ ) relation, aka the fiber bridging “spring law”, is shown in Figure 5.13. For both material designs, the values of complementary energy calculated from  $\sigma\sim\delta$  curves were larger than crack tip energy of the matrices, thus leading to multiple cracking behavior and strain-hardening in both materials. The peak fiber bridging capacity of 0% SHC is higher than 5% MSC, with a lower critical crack opening corresponding to the peak fiber bridging stress. This is because 5% MSC has a weaker interfacial bond between fibers and the cementitious matrix.

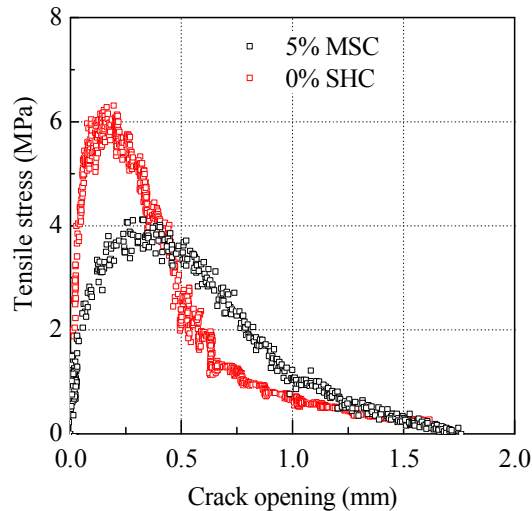


Figure 5.13 Single crack stress v.s. crack opening relations

Based on Eq.(5.11) ~ (23), the proportion of fibers at different stages were calculated. As shown in Figure 5.14, the ratios of debonding fibers, pull-out fibers, rupture fibers, and fully pulled-out fibers were plotted with lines and underneath shaded areas. The total area of debonding and pull-out denotes the fibers bridging the crack. The dashed black line reflects the proportion of working fibers in terms of crack opening. For 0% SHC, it can be found that before

75  $\mu\text{m}$ , there are few fibers fully pulled out or ruptured. After 75  $\mu\text{m}$  wide crack opening, there exists significant drop in the total proportion of debonding and pull-out fibers. For 5% MSC, the whole trend is similar to 0% SHC but the details of the curve are different. The significant drop in the proportion of debonding and pull-out fibers happens at the crack opening of 100  $\mu\text{m}$ .

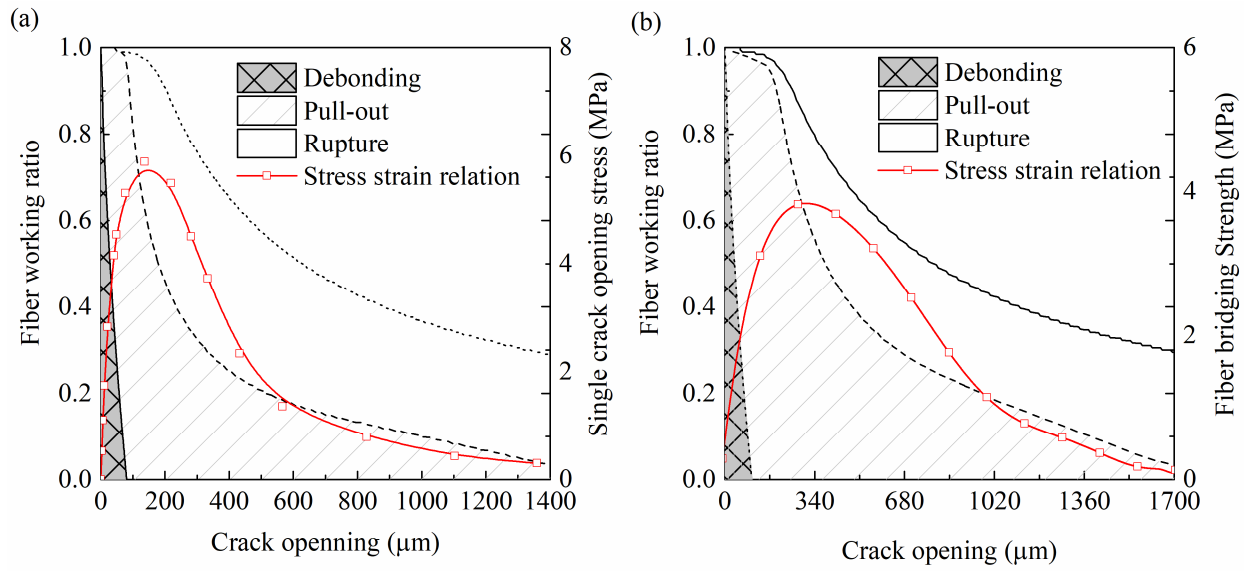


Figure 5.14 The ratio of bridging fibers calculated based on single crack opening test results. (a) 0% SHC. (b) 5% MSC

#### 5.4.2 Impedance ~ crack opening relation at single cracking scale

Figure 5.15 plots the relation of impedance magnitude and phase angle v.s. crack opening for 0% SHC. It should be noted that measured data at 1500 Hz is continuous all through the crack opening procedure. In order to unveil the physics underneath experimental phenomena, the model mentioned above was utilized to fit the test results. The model results were plotted as dashed lines in Figure 5.15. The parameters for the fitting are:  $\epsilon_r = 7.42$ , and  $\rho = 1.6 \times 10^{16}$   $\Omega \cdot \text{m/m}$ .  $\epsilon_r$  is as same scale as concrete (4.5), rubber (7), etc.  $\rho$  is an extremely high value which matches the insulation property of PVA fibers with coated oil. The parameters obtained validated the feasibility of the model.



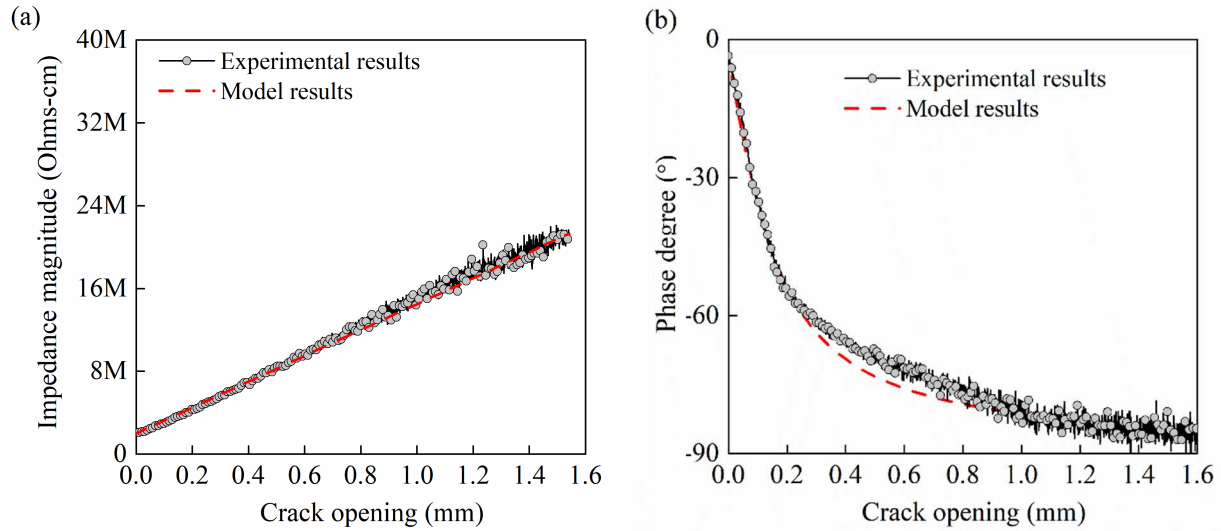


Figure 5.15 Relations of impedance change v.s. crack opening of 0% SHC: (a) Impedance magnitude; (b) Phase degree

Strong linear correlations were observed between impedance magnitude change and crack opening for all frequencies (Figure 5.15(a)). This linearly increasing trend is becoming more obvious with decreasing frequency level. That is because the constant phase element  $Q_c$  in the model (Figure 5.7) exhibits less impedance to high-frequency AC current. Due to insulated PVA fibers, constant phase element  $Q_c$  dominates the cracking impedance  $Z_{total}$ . Therefore, linear relation between impedance magnitude and crack opening can be derived based on Eq.(5.22), which is matching to experimental observations.

It is found that the constant phase element  $Q_c$  dominates the impedance behavior of cracking for 0% MSC, instead of  $R_{f-total}$ . That is because the PVA fibers with matrix particles have extreme high resistivity and thus AC current is more easily to pass the crack edge via dielectric behavior.

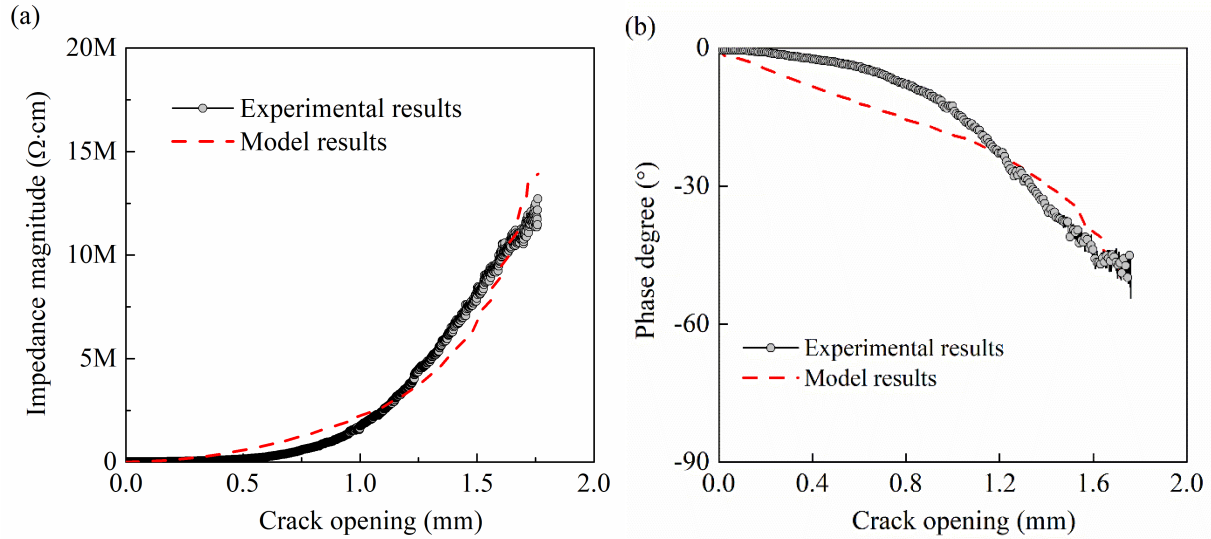


Figure 5.16 Relations of impedance change v.s. crack opening of 5% MSC: (a) Impedance magnitude; (b) phase degree

Figure 5.16 plots the electromechanical responses of 5% MSC at different frequencies. It is observed that nonlinear relations exist between the crack opening and the impedance magnitude. The increase in impedance magnitude is relatively slow when the crack opening is below 0.4 mm, and becomes faster afterward (Fig. 16(a)). The relation between the crack opening and the phase degree are plotted in Fig. 16(b). The trend is different from that of 0% SHC, suggesting that carbon black particles modified the capacitor and resistor effect of cracking.

Table 5.2 Exponent parameter  $\lambda$  in terms of crack opening

Crack opening range	$\lambda$
0 $\square$ 0.127	0.76
0.127 $\square$ 0.248	0.84
0.248 $\square$ 0.452	0.9
0.452 $\square$ 1.76	0.96

The model results are plotted correspondingly. The model parameters are:  $\epsilon_r = 140$ , and  $\rho = 4 \times 10^{10} \Omega \cdot \text{m/m}$ .  $\epsilon_r$  is 20 times higher than that of 0% SHC.  $\rho$  is 6 orders lower than that of 0% SHC. It is presented in Table 5.2 that the exponent parameter  $\lambda$  is increasing with the crack opening, indicating the crack behaves more and more like a perfect capacitor with increasing crack opening. Based on parameters derivation, it is found that the presence of conductive carbon black particles led to a significant change of contact impedance at the fiber/matrix interfaces. Therefore, an increase of impedance magnitude during crack opening was due to the combined effects of change in resistance which depends on statistical fiber debonding, pull out and rupture behavior as the crack opens, and the change in capacitance which depends on the crack opening; this combined effect led to nonlinear relations between crack opening and impedance magnitude change. The comparisons of parameters validated the model.

#### *5.4.3 Impedance ~ strain relation at multiple cracking scale*

The tensile test stress-strain relation and average crack width in terms of strain are plotted in Figure 5.17. It can be found that for 0% SHC material, under tensile force, strain-hardening behavior can be observed with strain-hardening capacity as high as around 5%. The average crack width increases from zero to around  $50 \mu\text{m}$  before 1%. Afterward, the average crack width is nearly constant to  $56 \mu\text{m}$ . That means, during the strain-hardening stage, in the model calculation, average crack width can be fixed as  $56 \mu\text{m}$ .

Figure 5.18 shows the electrical-mechanical response of 0% SHC during the tensile test. The model results are compared with test results. It can be concluded that under tensile test, the impedance magnitude is changing in a nearly linear way. However, the phase degree is too noisy to be reported. Simultaneously, the model results validate the linear relation. Good matching can

be observed between model results and test results. The model indeed provides reasonable physical interpretation for the electromechanical response of 0% SHC cracking under tensile test.

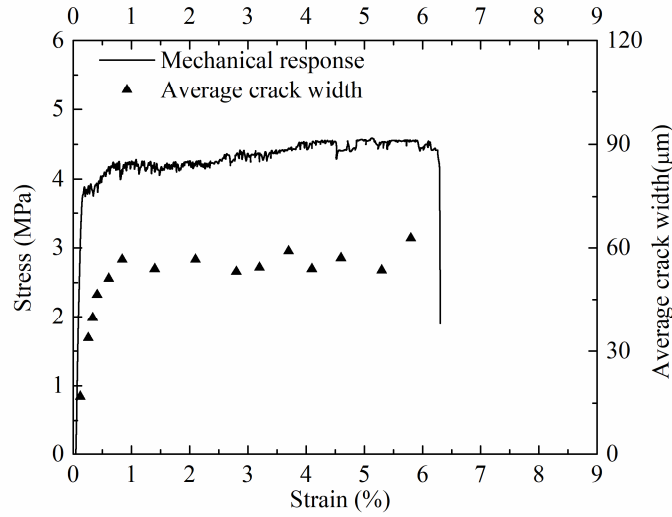


Figure 5.17 Tensile stress-strain relation and average crack width of 0% SHC

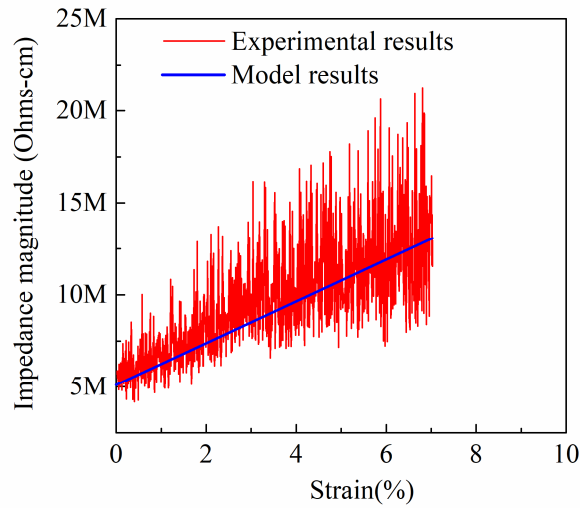


Figure 5.18 Relation of tensile strain vs. impedance magnitude

Similarly, the mechanical responses of 5% MSC are also plotted in Figure 5.19. The 5% MSC shows high ductile and unique multiple cracking behavior, which is characterized as strain-

hardening property. The average crack width of 5% MSC in terms of strain level follows the same trend as that of 0% SHC material. However, the average crack width is relatively smaller than that of 0% SHC material. That is due to the matrix toughness and fiber-matrix interface change caused by carbon black dosing.

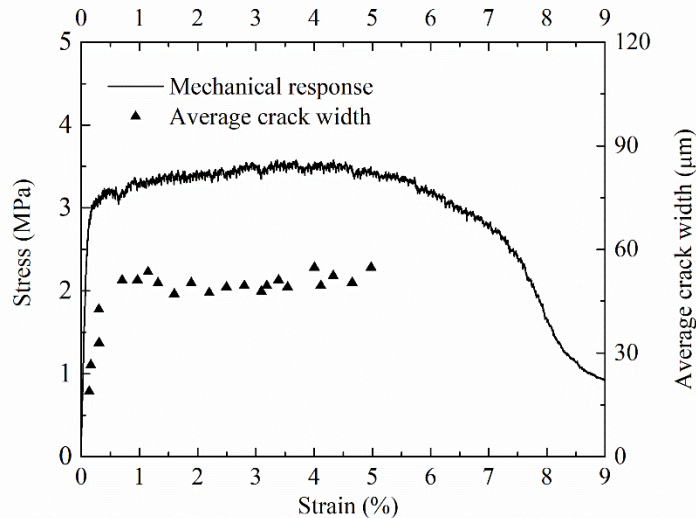


Figure 5.19 Relation of tensile strain v.s. impedance magnitude

Figure 5.20 shows the electrical-mechanical response of 5% MSC during a tensile test. The model results are compared with test results. It can be found that impedance magnitude follows a nonlinear relation corresponding to tensile strain, and similarly, the model results showed the nonlinear behavior, suggesting that the model is able to link single cracking to multiple cracking scale. Slight difference between experimental results and model results are caused by the assumption made during calculations. 1. Average crack width was adopted for calculation. However, the crack width distribution should be considered for model calculation. 2. During the strain-hardening stage, there was large crack occurring, which induced large impedance magnitude and phase angle change. But in this model, it is assumed that there is no large crack occurring during the strain-hardening stage.

For 0% SHC material, the average crack width is enough to simulate the real test results. However, for 5% MSC material, because of nonlinear impedance response of single crack opening, it is hard to interpret the results merely using the average crack width, and hence the maximum crack width was taken into consideration.

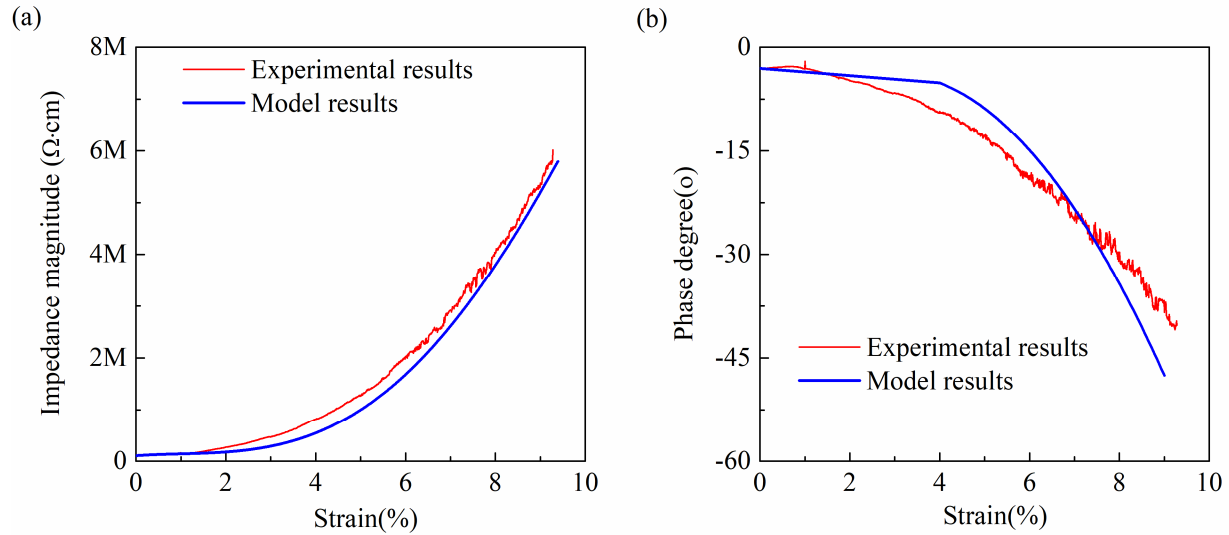


Figure 5.20 Relation of tensile strain vs. impedance: (a) impedance magnitude; (b) phase degree

#### 5.4.4 Parameter study

In order to further understand the nonlinear relations of 5% MSC at the single crack scale, the parameter study was conducted based on this model with parameters verified in above sections. In this section, three parameters are analyzed: the fiber-matrix contact resistivity  $\rho$ , the cracking relative permittivity  $\varepsilon_r$ , and the initial fiber number  $N_0$ .

Figure 5.21(a) shows the change of impedance magnitude-crack opening relations in terms of relative permittivity  $\varepsilon_r$ . Assuming merely relative permittivity changes, the bulk impedance and the other parameters are constant. Figure 5.21(b) shows the influence of fiber-matrix contact resistivity  $\rho$  on the impedance magnitude-crack opening relations. Figure 5.21(c)

shows the change of impedance magnitude-crack opening relations due to the change of initial number of fibers.

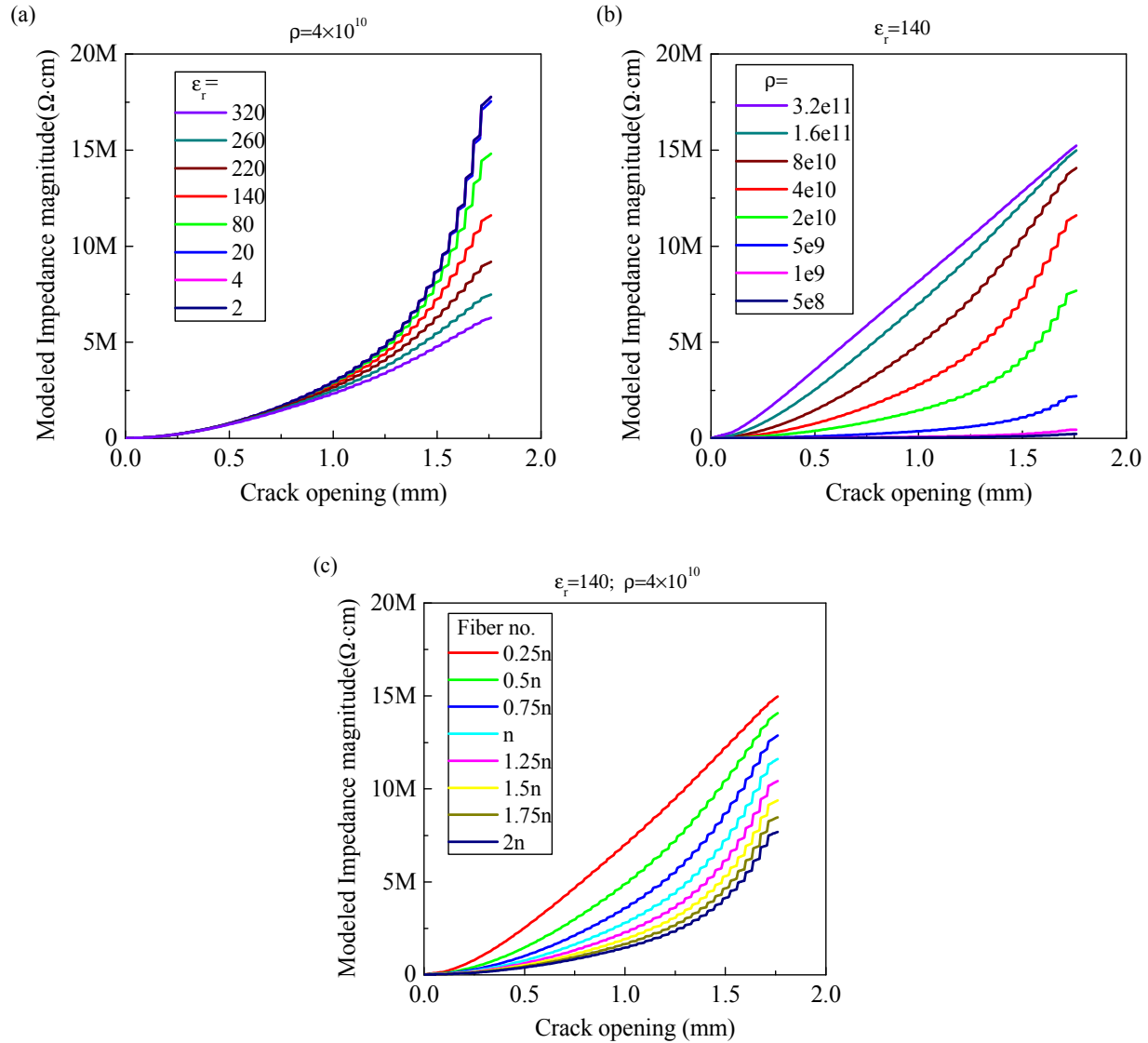


Figure 5.21 Parameter study of the model (a) cracking relative permittivity; (b) fiber-matrix contact resistivity; (c) initial fiber number

As shown in Figure 5.21(a), the increasing relative permittivity decreases the impedance magnitude and vice versa. However, increasing fiber-matrix contact resistivity increases the impedance magnitude (Figure 5.21(b)). More initial fibers in the bulk material induce higher impedance magnitude, see Figure 5.21(c). It should be noted that in this model, the initial bulk

impedance magnitude change due to change of fiber number is not considered. It can be observed that the nonlinear behavior of 5% MSC is due to low fiber-matrix contact resistivity  $\rho$ , high fiber number  $n$ , and high  $\epsilon_r$ .

## 5.5 Results and Discussions: Validation Test 2

### 5.5.1 Impedance ~ crack opening relation at single cracking scale

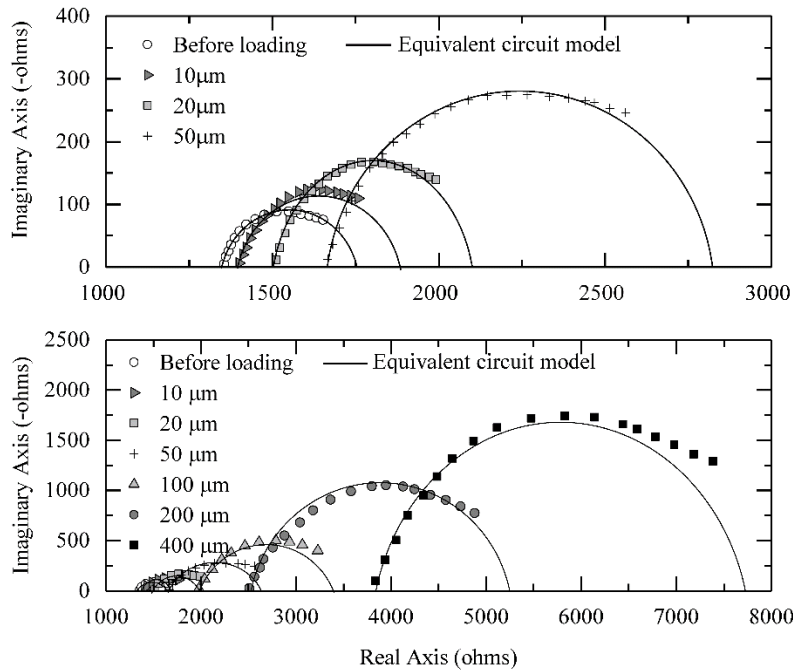


Figure 5.22 EIS Nyquist plots of 0% SHC at different crack openings

Figure 5.22 shows the evolution of Nyquist plot in correspondence with increasing crack opening levels in the complex plane. As shown in Chapter 4, the rightmost arc due to the electrode-specimen interface was removed so that this study mainly focused on the material response. At each crack opening, the experimental data yield a depressed semicircular arc in the complex plane. The center of the arc is displaced below the real axis because the material-crack system contains distributed elements, leading to a relaxation time that is not single-valued but



continuously distributed. The angle by which the semicircular arc is depressed below the real axis is related to the width of the relaxation time distribution.

Figure 5.22 reveals that the impedance arc shifts from left to right and the diameter of impedance arc increases corresponding to increasing crack opening, suggesting that frequency dependent impedance of SHC increases due to cracking evolution. At a low-frequency (e.g. 0.5 kHz), such increase is dominated by increasing  $R_c$ , the circuit element that represents the resistor effect of the crack; at higher frequencies, this increase is due to the combined effects of increasing  $R_c$  and decreasing  $C_c$ . In order to validate the model in Figure 5.7, the experimental data in Figure 5.22 was fitted. It is shown that the model results were matching the experimental results reasonably. It should be noted that, in this study (validation test 2), only the link from single cracking scale to multiple cracking scale was concentrated. So, the parameters analyzed in this study were  $R_c$  and  $Q_c$  shown in Figure 5.7, not the relative permittivity  $\epsilon_r$  and fiber-matrix contact resistivity  $\rho$ . The electrical parameters  $R_c$  and  $Q_c$  were derived from data fitting and are plotted corresponding to crack opening  $\delta$  in Figure 5.23. The linear relation between  $Q_c$  and  $\delta$  was observed. This supports the hypothesis that a crack in SHC exhibits capacitor behavior as shown in Eq.(5.21).

The relation between  $R_c$  and  $\delta$  is nonlinear, following a second order polynomial relation. nonlinearity is attributed to the combined effects of the loss of moisture content during testing, and the reduction of the number of fibers bridging the crack resulting from fibers debonding, pullout or rupture during increasing crack opening (Eq.(5.22)). This study validates the single cracking equivalent circuit model.

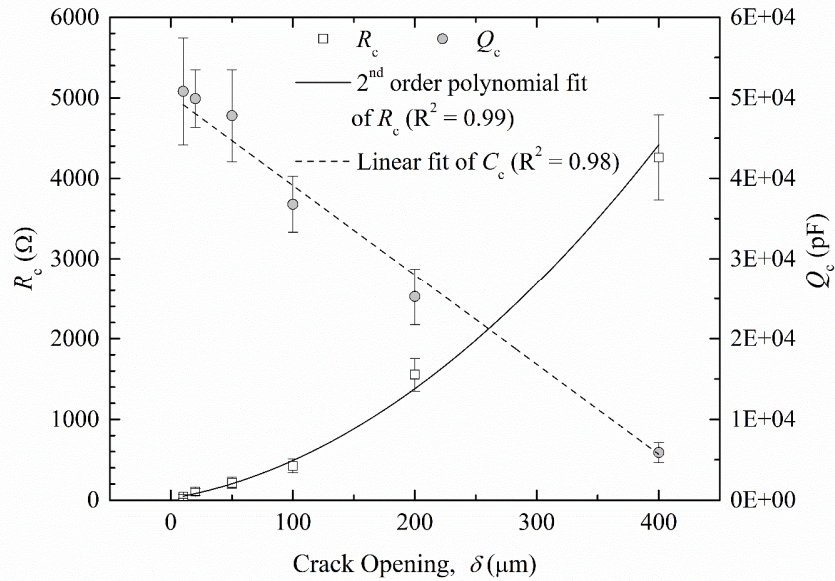


Figure 5.23 Effects of single crack opening on  $R_c$  and  $Q_c$

### 5.5.2 Impedance ~ strain relation at multiple cracking scale

The equivalent circuit model describing the multiple cracking behavior in SHC and MSC was used to predict the effect of multiple cracking on the complex impedance of material system. During uniaxial tension test, the crack opening of each crack at different strain levels was experimentally measured and input into the model for prediction. The complex impedance at different strain levels was collected and plotted in Figure 5.24. In this figure, the interface responses have been removed.

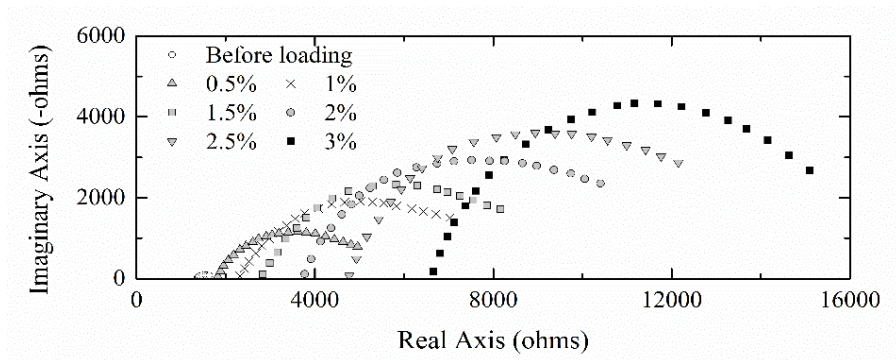


Figure 5.24 EIS Nyquist plots of SHC at different tensile strain levels

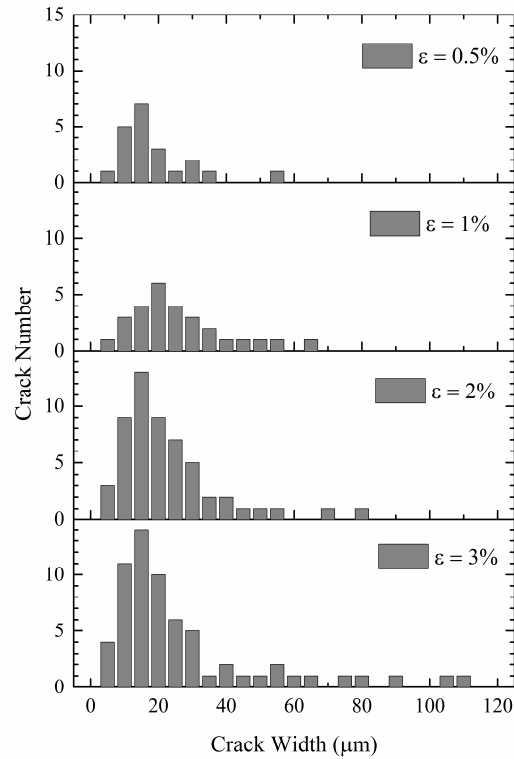


Figure 5.25 Effect of tensile strain on statistical distribution of crack width

It can be observed that the increase in tensile strain, which is accompanied by multiple cracking process, led to a shift of Nyquist plot arc from left to right along the real axis and an increase in the diameter of impedance arc. The crack width distribution at different tensile strain levels is shown in Figure 5.25. It can be observed that the number of cracks increased, and the mean crack width slightly increased, corresponding to increasing tensile strain levels.

Figure 5.26 plots the comparisons between predicted impedance change (impedance magnitude and phase degree) in terms of tensile strain at three different AC frequencies. It is shown that despite the variation in experimental data among specimens, the model predicted results closely matching the experimental measurement at different frequencies for both impedance magnitude and phase angle. The increase in impedance magnitude and phase angle with increasing tensile strain is attributed to an increase in crack number and the change in crack

width distribution. The comparisons between model results and experimental results validated the proposed model.

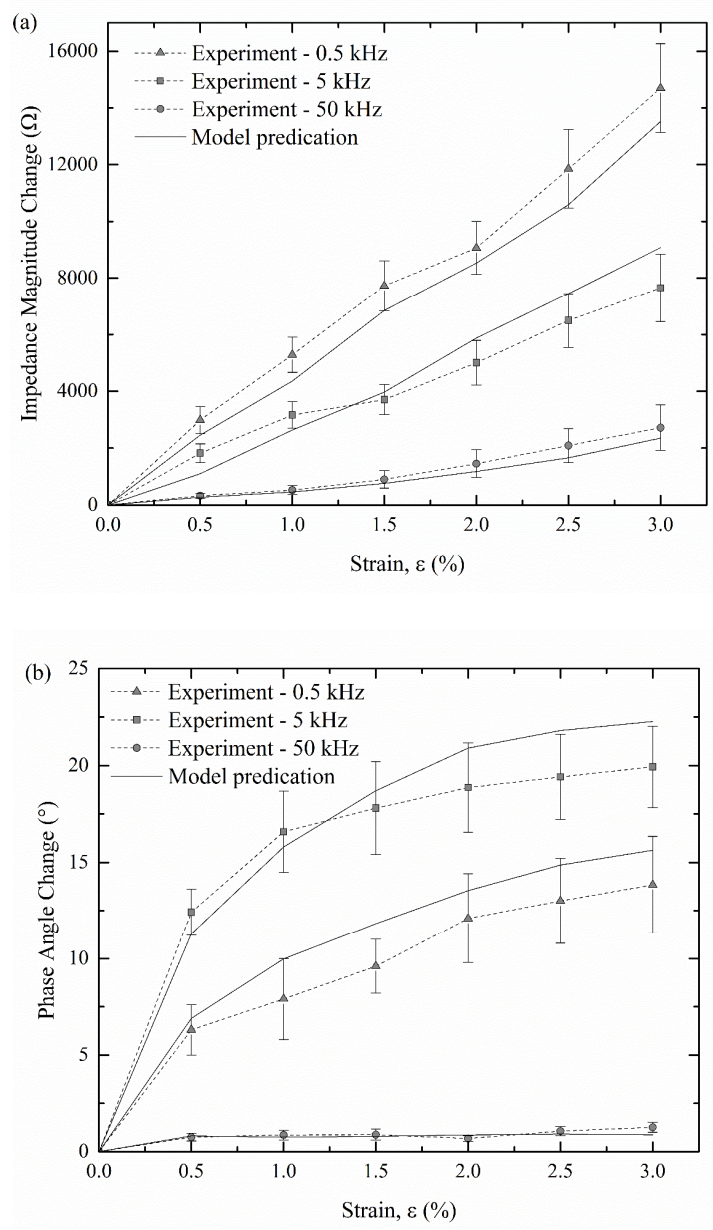


Figure 5.26 Effects of tensile strain on (a) impedance magnitude and (b) phase angle at different AC frequencies

### 5.5.3 Effect of crack self-healing

Specimens with multiple cracking damage (2% strain) were applied with wet and dry healing cycles. Self-healing of the microcracks in SHC can be deemed as a reversed damage process. This model was thus utilized to predict the impedance change during healing process. Figure 5.27 shows the microscope image of one crack in the coupon specimen. It can be observed that after tension, the crack width was obvious with an average crack width of 34  $\mu\text{m}$ . After 2 days healing, average crack width was 21  $\mu\text{m}$  and the crack became less significant, suggesting that part of the crack width was healed. After 14 days healing, the crack became invisible based on surface observation



Figure 5.27 Optical microscopy and SEM images of self-healing phenomenon in SHC

. The material complex impedance before cracking, after multiple cracking when loaded to a 2% tensile strain, and after different self-healing cycles were measured using EIS. It is observed that multiple cracking in SHC at 2% tensile strain leads to a significant shift of the impedance spectrum to the right along the real axis, and a significant increase in arc diameter along the imaginary axis (Figure 5.28). Self-healing causes an opposite effect. With increasing healing time, the impedance spectrum moves backward to the left along the real axis, and the arc diameter decreases. This indicates that self-healing of the microcracks leads to a reduction in

resistance at high and low frequencies, due to the decrease in the damage level reflected as the decrease in crack number and average crack width. Furthermore, the decrease in arc diameter indicates a reduction in the capacitor effects of the microcracks.

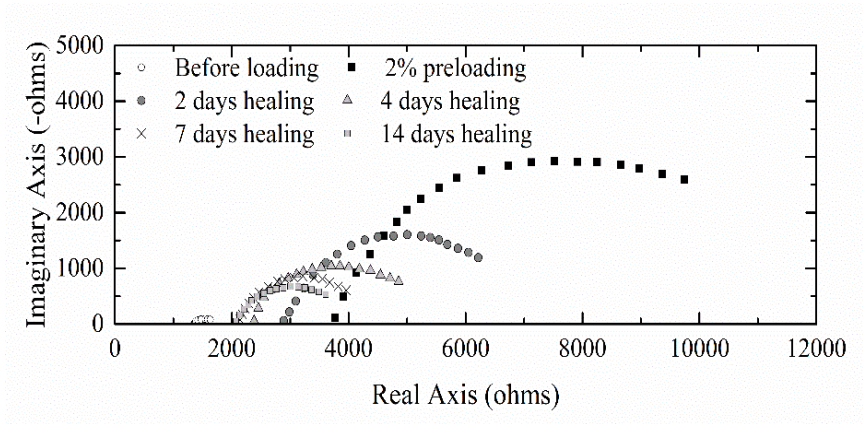


Figure 5.28 EIS Nyquist plots of SHC before loading, after preloading to 2% tensile strain, during self-healing.

Figure 5.29 shows the change in the statistical distribution of crack width in SHC specimens due to self-healing, characterized by microscopy from the sample surface. With increasing wet/dry exposure cycles, both the crack number and mean crack width decreased in the SHC specimens. With the information on crack width distribution in Figure 5.29, the capacitance  $Q_{c,i}$  and resistance  $R_{c,i}$  of the  $i^{\text{th}}$  crack with known crack width were determined and were inputted into the equivalent circuit model to predict the frequency-dependent complex impedance of the material at different self-healing cycles. The results are plotted in Figure 5.30 in terms of the relation between impedance magnitude, or phase degree change, and healing time, at three different AC frequencies.

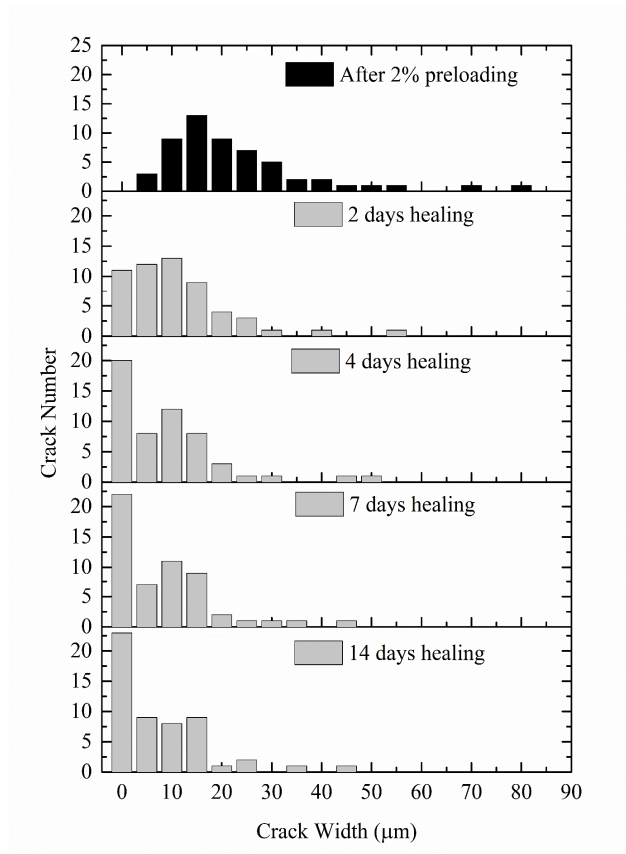


Figure 5.29 Effect of self-healing on statistical distribution of crack width

Figure 5.30 shows that the proposed model was able to predict the decreasing trend of impedance magnitude and phase degree with different healing time, indicating that the model captures the important mechanisms underlying the relation between damage level and complex impedance. The test results in Validation test 2 support the applicability of this multi-scale model from single cracking scale to multiple cracking scale and also reveals the relations between self-healing process and complex impedance of cementitious materials.

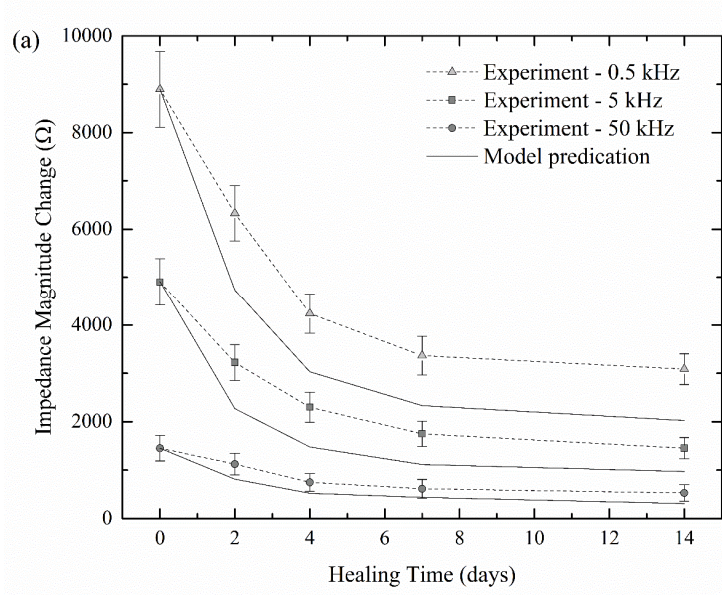
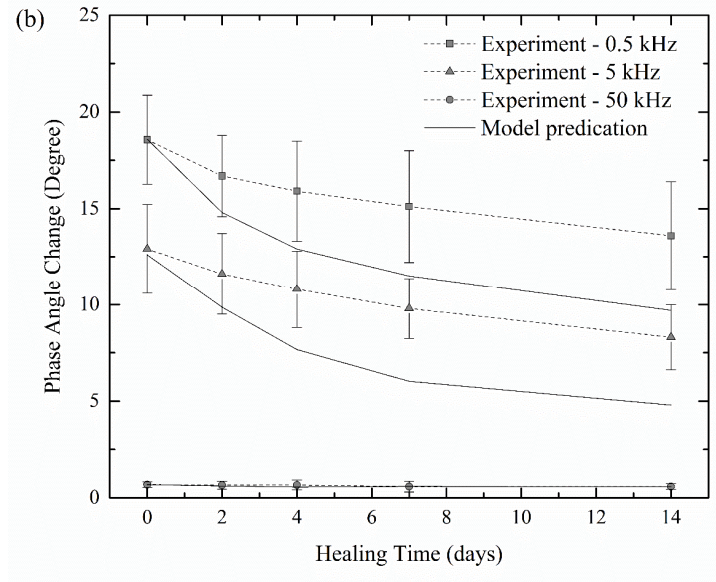


Figure 5.30 Effects of self-healing on (a) impedance magnitude and (b) phase angle at different AC frequencies

## 5.6 Conclusions

In this chapter, the effect of cracking and healing on SHCs and MSCs are studied. A theoretical model is proposed, combining micromechanics theory with equivalent circuit analysis. The following conclusions are drawn:



1. The electromechanical behavior of MSC and SHC is explained by a model framework combining micromechanics with equivalent circuit model. The model links length scale from single fiber debonding and pullout, to single cracking opening, and to multiple cracking.

2. The model reveals the capacitance effect and resistance effect of cracks in the cementitious matrix. The resistance effect is attributed to change of fiber-matrix contact resistance. The capacitance effect is contributed by two crack walls with fibers, particles, etc. as dielectric materials. During single fiber debonding and pullout, the electromechanical response is due to the fiber deformation and the change of contact area between the fiber and the matrix. During single crack opening, the fiber/matrix contact impedance of all fibers which bridge the crack, as well as crack capacitor, contributes to electromechanical responses. Thereafter, multiple cracking electromechanical responses are modeled as multiple “single cracking circuits” in series. Comparisons between experimental results and model results validated the proposed model.

3. Single crack electromechanical results validate the model. The relation of impedance magnitude and crack opening is linear for 0% SHC. On the other hand, the relation of impedance magnitude and crack opening for 5% MSC is nonlinear. For 0% SHC, the influence of fibers can be neglected due to the high fiber impedance and fiber/matrix contact impedance. Therefore, the impedance change is dominated by the change of the crack capacitor formed by two crack walls, which is linearly dependent on crack opening. On the other hand, for 5% MSC, carbon black modifies fiber/matrix contact impedance and relative permittivity of the crack capacitor, and thus the influence of fibers cannot be ignored. Since the number of bridging fibers in terms of crack opening follows a nonlinear relation, the impedance ~ crack opening relation becomes nonlinear.

4. The frequency-dependent effect of multiple cracking on the complex impedance of SHC material is well predicted by the proposed model, which accounts for the statistical distribution of crack width as well as crack resistance and crack capacitance contribution of each individual crack.

5. The transition from a slower increase in impedance magnitude to faster increase occurs at approximately 100  $\mu\text{m}$  crack opening, which is consistent with the transition from steady-state crack propagation to Griffith-type crack propagation. This phenomenon is frequency-dependent.

6. The frequency-dependent effect of self-healing on the complex impedance of SHC material is reasonably explained by the proposed model. Self-healing leads to the change in crack number and crack width distribution, which is captured by the changes in crack resistance and crack capacitance in the model. In order to more accurately predict the self-healing effect, the present model needs to be refined to take into account nonhomogeneous crack healing phenomena and the chemical composition of the self-healing products.

## **CHAPTER 6: SPATIAL DAMAGE SENSING IN MSCS THROUGH TIME-DIFFERENCE ELECTRICAL IMPEDANCE TOMOGRAPHY**

### **6.1 Introduction**

In practice, common two-probe or four-probe resistance or impedance measurements reveal the presence and formation of cracks, but hardly provide details regarding the spatial structure of the cracks. Electrical Impedance Tomography (EIT) based on alternating current (AC) or Electrical Resistance Tomography (ERT) based on direct current (DC) makes it possible to reconstruct spatial distribution and structure of the cracks on the basis of a set of electrical measurements from the boundary [213]. Based on boundary measurements, an approximation of the spatial distribution of the impedance or resistance within the object are reconstructed. The spatial distribution of resistance or impedance shows the contrast between damage with extremely low conductivity and non-damaged part with relatively higher conductivity.

As a diffusive tomography method, EIT or ERT has been a focus of medical and geophysical research for decades [213-216]. To date, there are still limited studies about EIT or ERT on cementitious materials. Buettner et al. [217, 218] applied ERT to monitor moisture infiltration into concrete pillars and pavement sections. Hou et al. [209, 210, 219] utilized single frequency EIT to image fiber-reinforced cementitious composites (100% RH cured) loaded by axial tension and three-point bending. It is shown that the geometric propagation of dense fields of microcracks, strain-hardening, and crack localization in cementitious composites were all captured by EIT conductivity maps. Karhunen et al. [220, 221] performed a feasibility study of ERT for imaging concrete samples (saturated with  $\text{CuSO}_4$  solution). The results showed that the conductivity map provided reliable estimates for the size and location of the cracks, the steel

rebar, and the nonconductive inclusions. Hallaji and Pour-Ghaz [222, 223] utilized ERT to successfully detect and locate cracks by applying sensing skins on the surface of the concrete. Also, Hallaji et al. showed that EIT is able to show the shape and position of the waterfront of nonuniform flow in the cementitious materials [224, 225]. Gupta et al. utilized EIT to detect the location and severity of damage in self-sensing concrete with CNT-based thin films to modify the cement-sand particles interface [147].

Despite the recent advances, knowledge gaps are evident. First, although promising results of ERT were reported in previous literature, EIT is more suitable for cementitious materials than ERT. Cementitious materials possess highly heterogeneous electrical microstructure formed by different phases (conductive or nonconductive). Thus, a cementitious material is not an ideal resistor whose resistance is time and frequency independent. Once under DC, cementitious materials are susceptible to the polarization effect, resulting in an unstable resistance measurement from time to time. Consequently, it is difficult to achieve simultaneous boundary measurements on the cementitious materials, which are critical for image reconstructions. In contrast, alternating current (AC) is able to diminish the polarization effect of cementitious materials due to the periodically reversed direction of the current. Second, previous successes of directly utilizing EIT to the cementitious materials depended heavily on the moisture content of the material. The conductivity of the cementitious materials is dominantly determined by the moisture phase within the matrix. The moisture content, however, is strongly time-dependent and become extremely low after the age of 42 days. Therefore, resistance or impedance measurements are prone to low signal-to-noise ratios due to the low conductivity of cementitious materials. Besides, high impedance of the cementitious materials leads to low contrast between non-damaged part and cracks. Also, the impedance of cementitious materials is

known as a rough range, which means that the electrical properties of cementitious materials is highly nonuniform. Third, sensing skin applied on the surface of the cementitious materials is only able to detect surface emerged cracks, despite high sensitivity [222, 223, 226]. Also, the sensing skin provides merely the 2D information of damage on the surface of the concrete element without capturing the damage depth within cementitious materials. Fourth, in most of the current studies, image reconstructions were performed based on resistance part of the impedance, neglecting the capacitance effect. However, as discussed above, a cementitious material is not an idea resistor and thus capacitor effect cannot be neglected. Capacitor effect is further evident when cracks are present in cementitious materials. In this sense, impedance is a more accurate measure than resistance for cementitious materials. Unlike resistance, impedance is a complex number which is composed of impedance magnitude and phase shift. The real part of the complex impedance reflects the resistance effects, while the imaginary part of the complex impedance relates to the capacitance effects. The differences of image reconstructions between different types of impedance measurements (impedance magnitude, real part, and imaginary part) are still unknown. Furthermore, the impedance of cementitious materials is highly frequency-dependent. As most of the previous studies on the cementitious materials merely focused on one selected single frequency, it is hence necessary to understand whether and how frequencies can lead to changes in the damage detection using EIT technology.

This study aims to address above issues. First, a FEM model, considering the electrical properties of MSCs, was established. Difference imaging scheme was adopted for image reconstructions. Parameter studies based on MSCs provided strategies to tailor the electrical microstructures of cementitious materials for electrical impedance tomography. Second, one multi-frequency EIT measurement system was established for the cementitious materials. The

cementitious materials were tailored with damage sensing capacity via dosing carbon black nanoparticles so that electrical conductivity of the cementitious materials does not rely on the moisture content within the cementitious matrix. A set of EIT measurements were performed on the cementitious materials with three parameters: specimen type (coupon specimen and beam specimen), frequency (1 Hz  $\square$  1 MHz), and damage pattern (distributed cracks and a single localized crack). Image reconstructions were performed based on impedance magnitude, real part, and imaginary part of the impedance separately at different frequencies. By doing so, all of the factors which might influence the EIT results on cementitious materials were considered. The image reconstruction problems of EIT in this study were solved using the Time-difference imaging scheme, which attempted to recover an estimate of the change in conductivity within the cementitious materials based on data frames measured before and after the damage. Compared with the absolute imaging scheme, Time-difference imaging scheme requires less computational efforts and is more tolerant to the measurement noise and modeling errors [222, 223]. The image reconstructions in terms of the parameters mentioned above allow to elucidate the fundamental factors that influence the application of EIT on cementitious materials for the damage sensing purpose.

## **6.2 Electrical Impedance Tomography**

The process of estimating the impedance from the measured data is known as an inverse problem. The inverse problem can be solved using a reconstruction algorithm. There are two primary types of image reconstruction algorithms. One is difference imaging, and the other is absolute imaging. Difference imaging aims to recover an estimate of the change in conductivity based on data frames measured at two times. Absolute imaging is about recovering an estimate of the absolute conductivity of the medium from which the boundary data was acquired.

Compared with absolute imaging, difference imaging is more robust and tolerant to model errors and noise. Also, the nonuniform electrical property of cementitious materials makes it hard to apply absolute imaging. Therefore, in this study, difference imaging was adopted. In order to solve the inverse problem, a forward problem is necessary to predict observations.

Based on Maxwell's equations, the electric potential ( $\mu(\vec{x})$ ) within a medium ( $\Omega$ ) can be expressed as Laplace's equation:

$$\nabla \cdot (\gamma \nabla \mu) = 0 \quad \text{in } \Omega \quad (6.1)$$

where  $\gamma$  is the conductivity distribution.

Then the complete electrode boundary conditions are:

$$V_k = \mu + z_k \gamma \frac{\partial \mu}{\partial n} \quad (6.2)$$

$$I_k = \int_{E_k} \gamma \frac{\partial \mu}{\partial n} dS \quad (6.3)$$

where  $I_k$  is the current injected from the  $k^{\text{th}}$  electrode  $E_k$  which has a contact impedance  $z_k$ ,  $V_k$  is the constant voltage on electrode  $E_k$ ,  $n$  is the outward unit normal vector and

$$\gamma \frac{\partial \mu}{\partial n} = 0 \quad (6.4)$$

Besides, the complete electrode model consists of following two equations together with the conditions for conservation of charge:

$$\sum_{k=1}^K I_k = 0 \quad (6.5)$$

And an arbitrary choice of a ground:

$$\sum_{k=1}^K V_k = 0 \quad (6.6)$$

Based on complete electrode model, the forward model can be established using finite element method. The difference between two measurements are considered.

$$\delta\gamma = \gamma_2 - \gamma_1 \quad (6.7)$$

$\delta\gamma$  is the conductivity contrast based on two EIT voltage measurements  $V_1$  and  $V_2$  taken at two measurements.

Considering forward computations using finite element method,  $V_1$  and  $V_2$  become

$$V_1 = U(\gamma_1) + e_1; \quad V_2 = U(\gamma_2) + e_2 \quad (6.8)$$

where  $U$  is the forward operator,  $e_1$  and  $e_2$  is the Gaussian distributed measurement noise.

In this study, the image reconstructions were based on a linear approach for computational efficiency and high tolerance to modeling error. Eq.(6.7) was further approximated by the first order Taylor approximations as:

$$V_i \approx U(\gamma_0) + J(\gamma_i - \gamma_0) + e_i, \quad i=1, 2 \quad (6.9)$$

where  $\gamma_0$  is the linearization point, and  $J = \frac{\partial U}{\partial \gamma}(\gamma_0)$  is the Jacobian matrix evaluated at  $\gamma_0$ .

Eq.(6.7) can be further written as

$$\delta V = V_2 - V_1 \approx J(\gamma_2 - \gamma_1) + (e_2 - e_1) = J\delta\gamma + \delta e \quad (6.10)$$

Therefore, the objective is to estimate the conductivity change  $\delta\gamma$ . The least squares solution is necessary to find to minimize  $\|J\delta\gamma - \delta V\|$ . A Tikhonov regularization method was applied to reduce the effects of solving an ill-conditioned system by restoring continuity of the solution of the data. Therefore, rather than minimize  $\|J\delta\gamma - \delta V\|$ , one needs to minimize an expression of form:

$$\delta\gamma = \arg \min_{\delta\gamma} = \left\{ \|J\delta\gamma - \delta V\|^2 + \psi^2 \|R\delta\gamma\|^2 \right\} \quad (6.11)$$



where  $R$  is a regularization matrix and  $\psi$  is a regularization parameter that controls the amount of regularization.

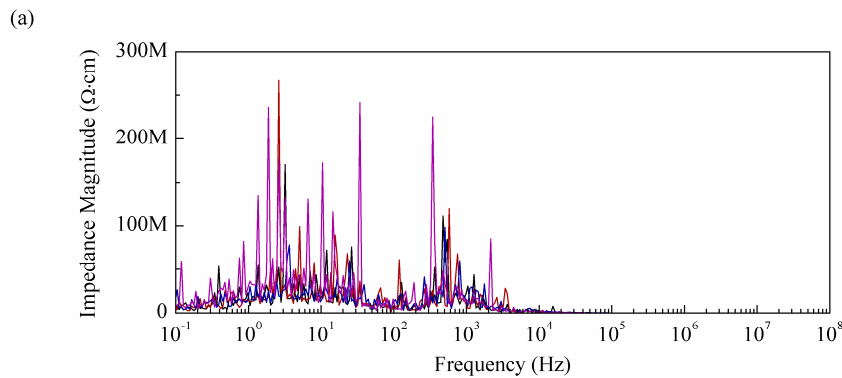
The solution to Eq.(6.11) is

$$\delta\gamma = (J^T J + \psi^2 R^T R)^{-1} J^T \delta V \quad (6.12)$$

Then the equation can be substitute into Newton-Raphson formula to solve. In following studies, Tikhonov regularization was utilized. In this study, a Matlab toolkit (Eidors) was utilized to perform image reconstructions.

### 6.3 Electrical Properties Characterization of Cementitious Materials

In order to unveil the parameters which determine the feasibility of applying electrical impedance tomography on cementitious materials, the electrical property of MSCs and the normal cementitious materials needs to be characterized. In this section, electrical impedance spectroscopy was adopted for material characterization on coupon specimen with the dimension of 165 mm × 51 mm × 12.5 mm. The same test setup was adopted as shown in Figure 3.2.



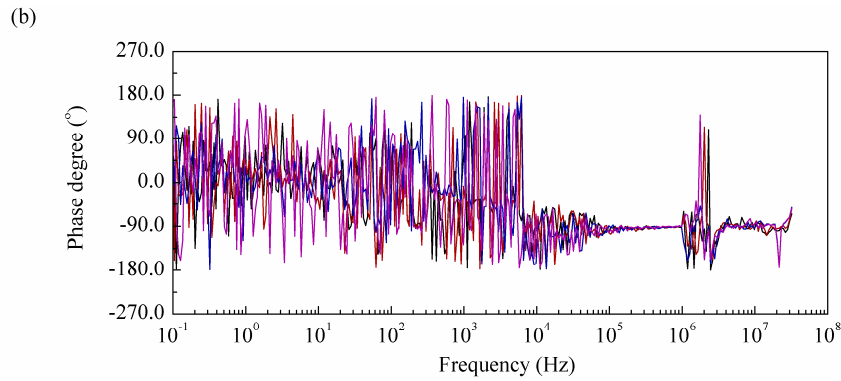


Figure 6.1 Electrical Impedance response of the normal cementitious material. (a) impedance magnitude; (b) phase degree

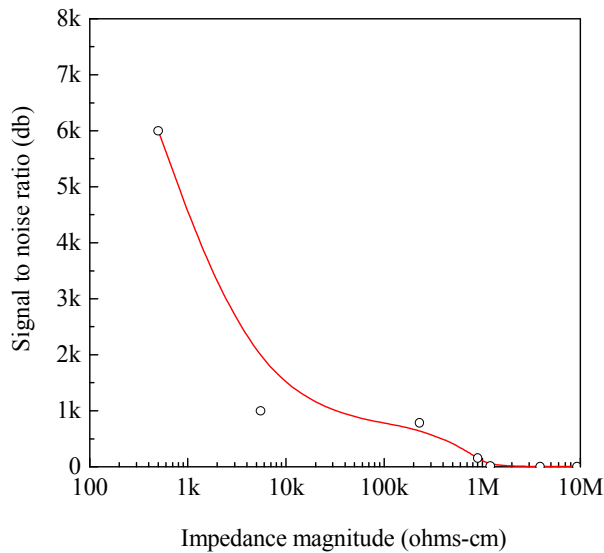


Figure 6.2 Relationship between signal-to-noise ratio and impedance magnitude

Here, typical test results are plotted in Figure 6.1, which shows the impedance magnitude and phase degree with respect to frequency. The x-axis in Figure 6.1 is frequency in a logarithmic scale from 0.1 Hz to  $1 \times 10^8$  Hz. The y-axis shows the impedance magnitude and phase degree. Based on the measurement data, there were three parameters extracted: signal-to-noise ratio, average impedance magnitude, and standard variation of impedance magnitude representing the uniformity of electrical property. The relation between impedance magnitude

and the signal-to-noise ratio was established and plotted in Figure 6.2. It was observed that a decrease in signal-to-noise ratio led to an increase in impedance magnitude.

#### 6.4 Parameter Study

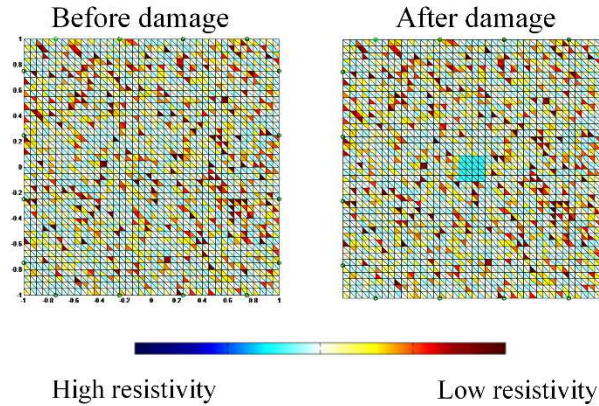


Figure 6.3 Finite element mesh

One FEA model was established [227, 228]. As shown in Figure 6.3, one square specimen was used for EIT parameter analysis. The nonuniformity of the electrical resistivity was input based on the measurement to simulate a real material. Damage was simulated via defining part of the specimen with zero conductivity. Table 6.1 summarizes all the parameters considered in this study. There are three types of parameters: measurement parameters, material property parameters, and finite element model parameters.

Table 6.1 Parameters considered in this study

Parameter type	Parameters	Values or options
Measurement	Signal-to-noise ratio (dB)	1000, 100, 10, 1
	Current injection and voltage measurement pattern	1. (Adjacent, Adjacent); 2. (Opposite, Opposite); 3. (Adjacent, Opposite); 4. (Opposite, Adjacent)
Material property	Impedance magnitude (Ohms)	10M, 1M, 0.1M, 0.01M, 1000
	Electrical property distribution (variation)	5%; 15%; 30%; 45%

Finite Element Model	Electrode number	4; 8; 16; 40
	Meshing size (element number)	1024; 3200; 12800

The signal-to-noise ratio is considered as the parameter due to the measurement procedure and instruments. It should be noted that the noise cannot be avoided but can be reduced by improving measurement facility. If the measurement condition is same, it is commonly believed that the signal-to-noise ratio is directly related to impedance magnitude, as shown in Figure 6.2. Since supreme high impedance and low impedance induces significant loss of accuracy and thus measurement involves more noise, it is necessary to control the impedance magnitude in a certain range.

In this study, there were four current injection and voltage measurement patterns considered. The description of the different current injection and voltage measurement pattern can be found from the literature [229]. The finite element model parameters include the meshing size and the electrode number. In following sections, the parameter study was conducted.

It should be mentioned that merely the typical results are reported. Firstly, the parameter study was conducted on the finite element number, as shown in Figure 6.4. The simulation scenario can be shown here: measurement pattern (adjacent, adjacent); impedance magnitude(0.01M); electrical property distribution: 15%; electrode number: 16; Signal-to-noise ratio: 1, 10, 100, 1000. It can be found that signal-to-noise ratio determines whether the damage can be captured or not. But small mesh size helps to localize damage.

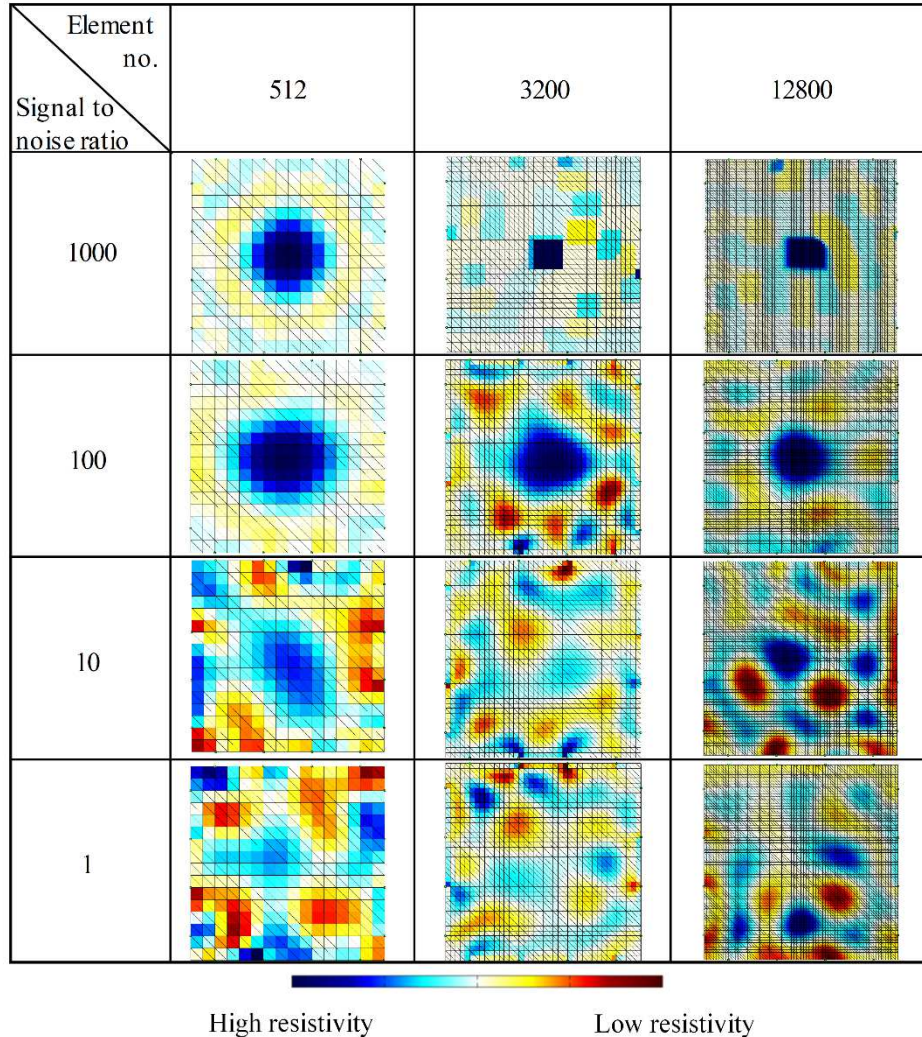


Figure 6.4 Comparisons of image reconstructions in terms of signal-to-noise ratio and element number

Figure 6.5 shows the image reconstruction results comparison in terms of the signal-to-noise ratio and the electrode number. It can be shown that the higher the signal-to-noise ratio, the higher the image quality. The damage can be characterized by image reconstructions with the signal-to-noise ratio of 100 and 1000. Simultaneously, increasing electrode number could increase the quality of image reconstruction. The measurement with 4 electrodes could only detect the existence of the damage but not provide the damage details.

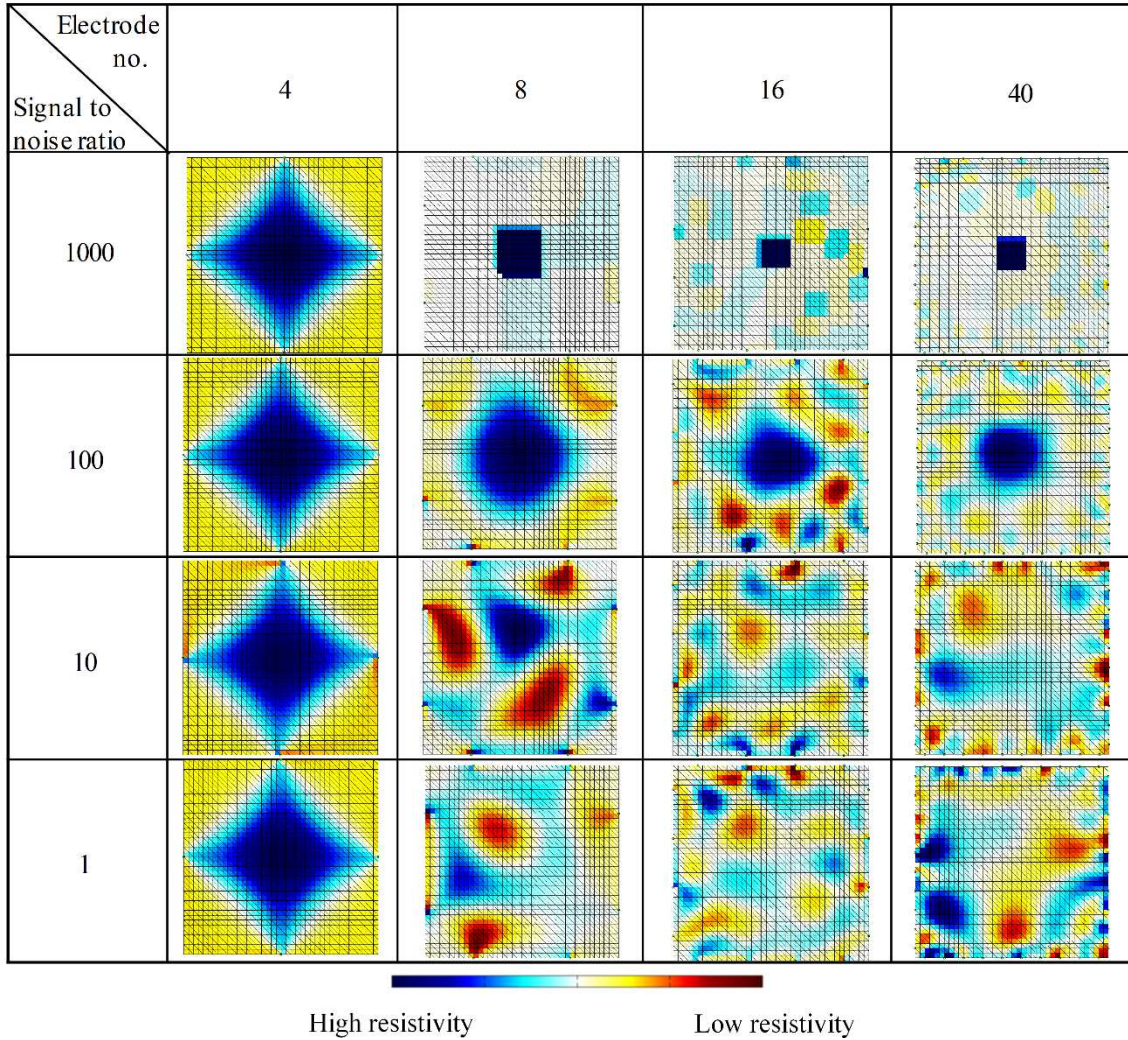


Figure 6.5 Comparisons of image reconstructions in terms of the signal-to-noise ratio and the electrode number

It can be found that impedance magnitude does not influence the image reconstruction. However, the signal-to-noise ratio dominates the image reconstruction quality. As shown in Figure 6.6, the signal-to-noise ratio should be higher than 100 for damage detection.

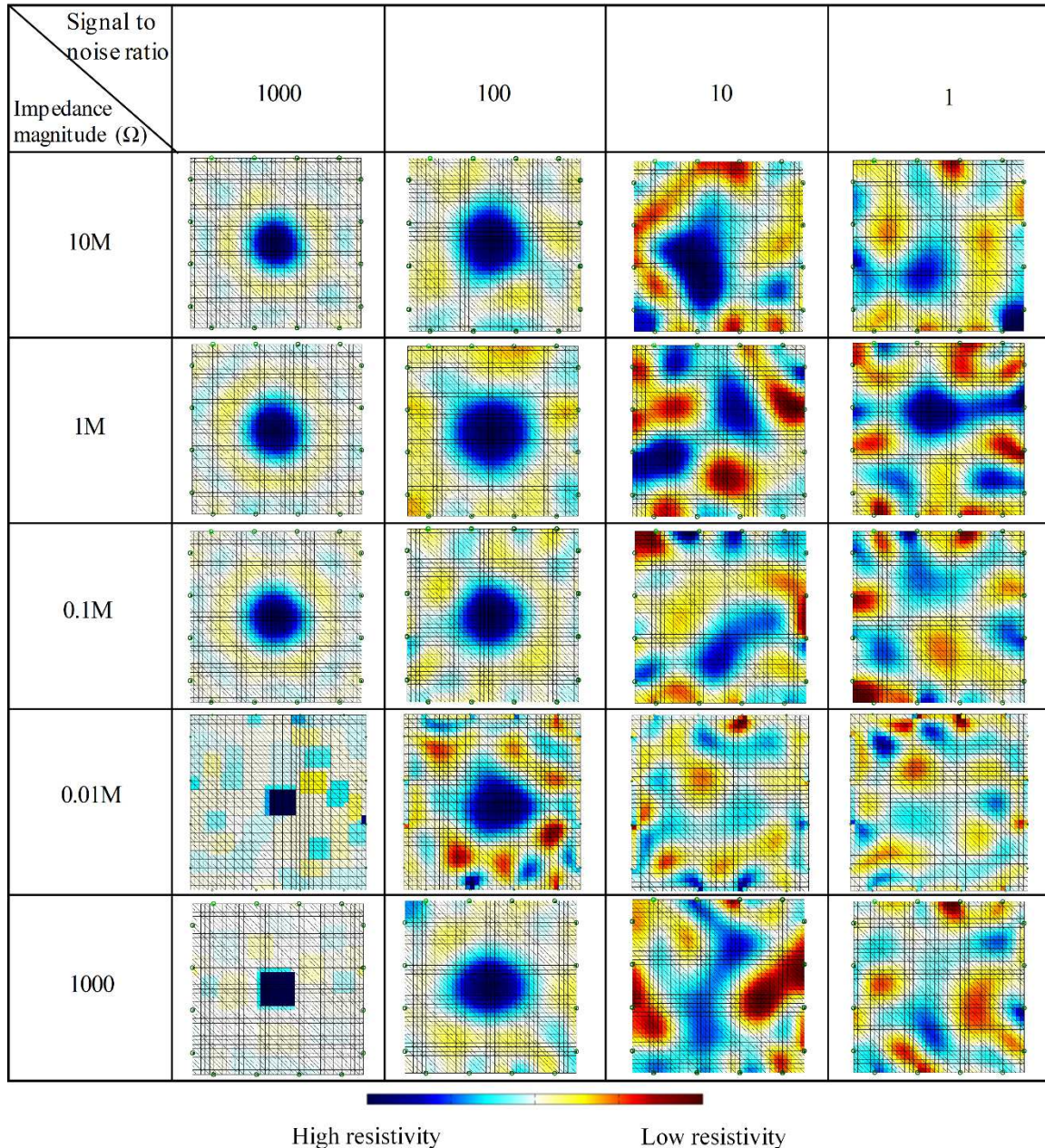


Figure 6.6 Comparisons of image reconstructions in terms of the signal-to-noise ratio and the impedance magnitude level

Figure 6.7 shows the image reconstruction results in terms of the signal-to-noise ratio and the uniformity variation. It can be found that the uniformity variation of the background electrical property does not influence the image reconstruction quality. However, for the cementitious materials, cracks and air voids, moisture gradients and the chloride distribution in

the matrix create the uniformity variation in the cementitious materials. Therefore, for the cementitious materials, the difference imaging is more robust compared with absolute imaging scheme for cementitious materials.

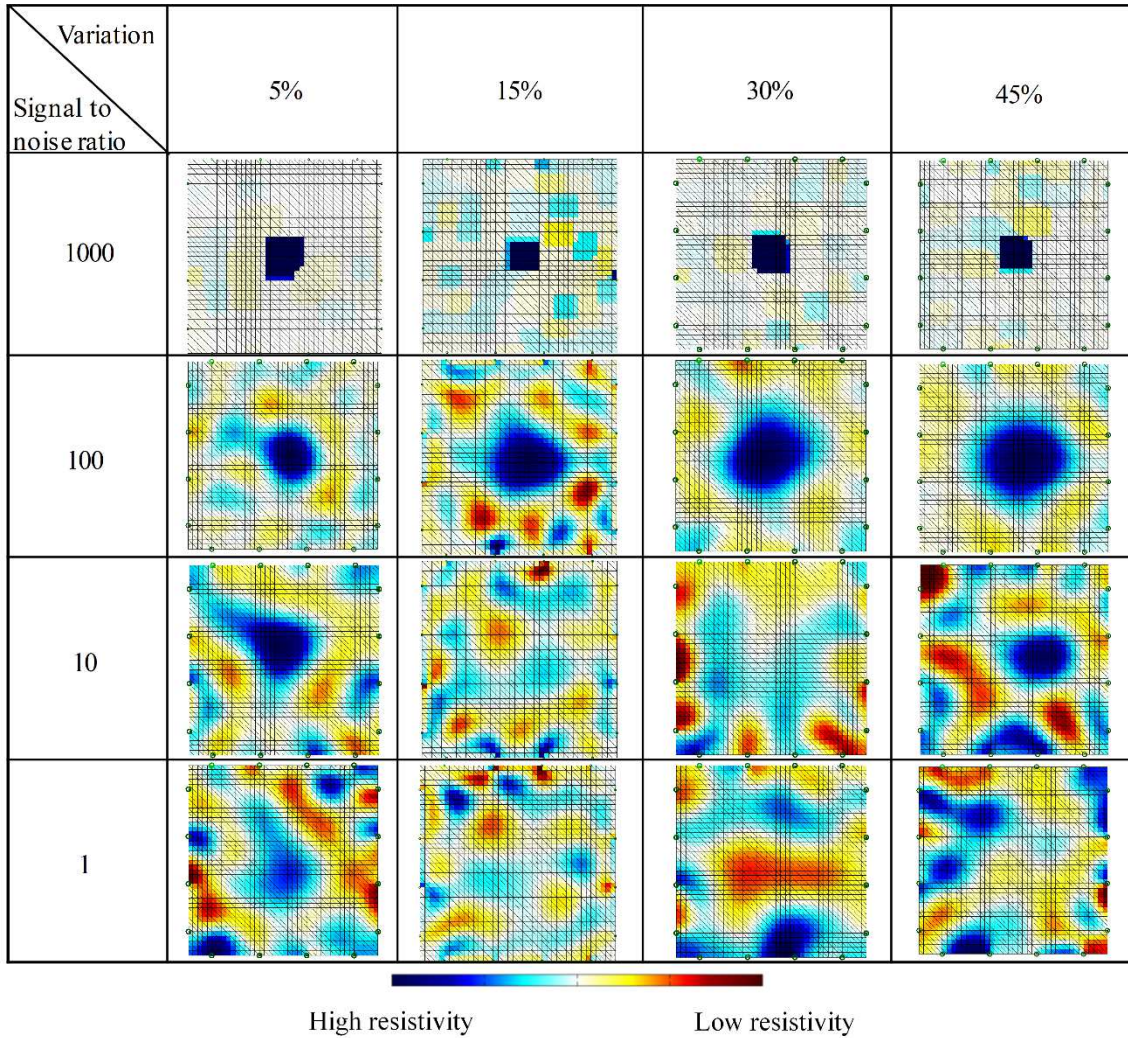


Figure 6.7 Comparisons of image reconstructions in terms of the signal-to-noise ratio and the uniformity variation



## 6.5 Experimental Methodology

### 6.5.1 Materials and specimens

Cementitious materials were deliberately designed with different electrical conductivities and cracking patterns. Four types of cementitious materials were designed and prepared as shown in Table 6.2. Cementitious material N1 was designed with a distributed damage pattern under tension, while N2 demonstrated a localized crack under tension. The distributed damage pattern of N1 was achieved by integrating micromechanics theory [193], rheology control [149], and microstructure tailoring. Details of material design are described in Chapter 3. The binder systems of N1 and N2 contained water, a polycarboxylate-based high range water reducer, Type I Portland cement, ASTM standard type F fly ash ( $\text{CaO} < 7\%$ ), and fine silica sand (average particle size =  $250\mu\text{m}$ ). Polyvinyl alcohol (PVA) fibers were incorporated into the cementitious material N1 at a volume fraction of 2% and N2 at a reduced volume fraction of 0.5%, respectively. Via doing so, N2 showed a typical normal fiber-reinforced concrete behavior with one crack opening gradually under tension. Based on cementitious materials N1 and N2, the electrical conductivity was further modified via introducing carbon black nanoparticles at a volume percentage of 5%, resulting in cementitious materials C1 and C2. After design, C1 demonstrated the distributed damage as N1, and C2 had the same damage pattern as N1 (localized cracking). As carbon black modified the electrical property of the cementitious materials, the 42-day resistivity of the materials is also reported in Table 6.2. The resistivity of N1 and N2 is three orders higher than that of C1 and C2 at the age of 42 days, suggesting the conductive paths and partially conductive paths formed within C1 and C2. It should be mentioned that the resistivity was measured on coupon specimens ( $165.1\text{ mm} \times 51\text{ mm} \times 12.7\text{ mm}$ ) with the four-point probing method (gauge length = 65 mm) to avoid contact resistance.

Table 6.2 Material design in this chapter

Cementitious material (water binder ratio)	Water kg/m <sup>3</sup>	Cement kg/m <sup>3</sup>	Sand kg/m <sup>3</sup>	Fly ash kg/m <sup>3</sup>	Superplasticizer kg/m <sup>3</sup>	Fiber Vol %	Carbon black kg/m <sup>3</sup>	42-day Average resistivity Ω·cm
N1(0.26)	312	292	456	935	2.7	2	0	5.1×10 <sup>6</sup>
N2(0.26)	312	292	456	935	2.7	0.5	0	9.8×10 <sup>6</sup>
C1 (0.27)	312	292	456	836	2.7	2	25	9.4×10 <sup>3</sup>
C2 (0.27)	312	292	456	836	2.7	0.5	25	9.4×10 <sup>3</sup>

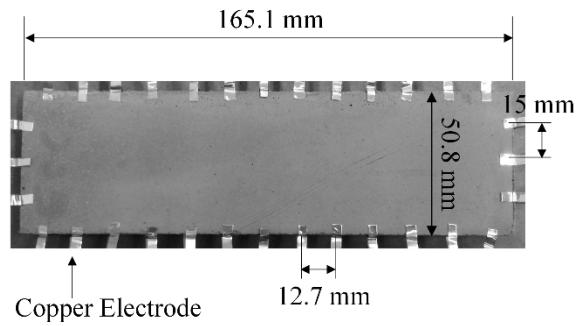


Figure 6.8 Coupon specimen with 32 electrodes

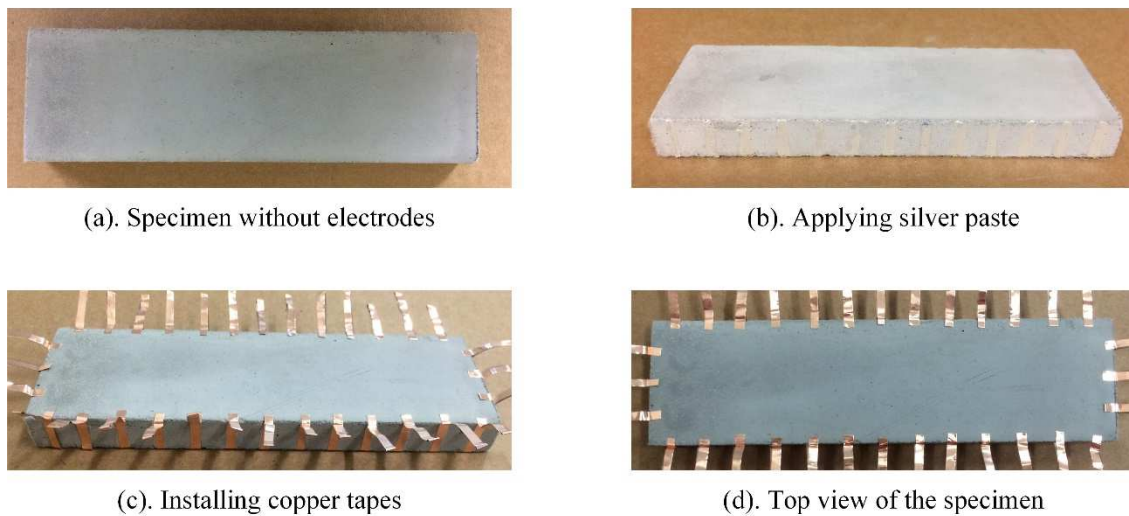


Figure 6.9 Procedures to apply silver paste and copper electrodes

Two types of specimens were prepared: (a) coupon specimens with a dimension of 165.1 mm × 51 mm × 12.7 mm for the uniaxial tension test (Figure 6.8), and (b) beam specimens with

a dimension of 406 mm × 102 mm × 102 mm for the flexure test (Figure 6.10). Afterward, the specimens were exposed to the outdoor environment until the age of 42 days for testing.

In order to facilitate EIT measurements on the coupon specimens, electrodes were placed on the perimeter surface of the specimens, as shown in Figure 6.9. The electrodes were made via applying a thin layer of colloidal silver paste directly to the side surface of the specimen after sanding the surface, then attaching a layer of copper tape (width = 3.2 mm) on the top of the silver paint. The silver paint layer was intended to smooth the specimen surface and to minimize the contact impedance. The copper tape is the copper foil (thickness = 0.038 mm) with an acrylic conductive adhesive (thickness = 0.032 mm). There was a total of 32 electrodes for one specimen, with a distance between two adjacent electrodes of 12.7 mm. Afterward, the insulated tape was applied on the top of the electrodes and the specimen to avoid loss of contact between the electrodes and the specimen.

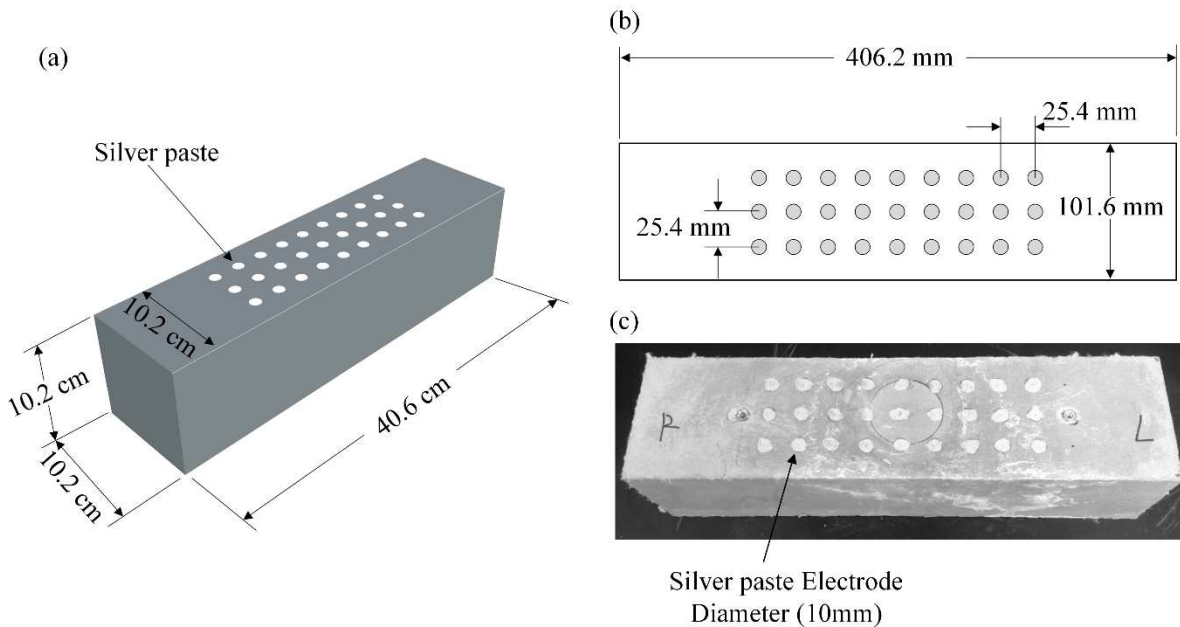


Figure 6.10 Beam specimen with 24 electrodes on one single side: (a) beam specimen illustration; (b) electrode setup; (c) one beam specimen

Figure 6.10 shows the electrode details of the beam specimens. 27 electrodes were installed on one side of the specimen in 3 rows and 9 columns. This is to simulate the structural member with a single access surface available (Figure 6.10(b)). The silver paste was applied as circle electrodes on the surface of the specimen with a diameter of 10 mm. Copper electrodes with acrylic conductive adhesive were then attached to the silver paste layer. Thereafter, insulated tapes were applied to fix copper electrodes on the surface of the specimens. The distance between adjacent electrodes was 25.4 mm.

### 6.5.2 EIT measurement system

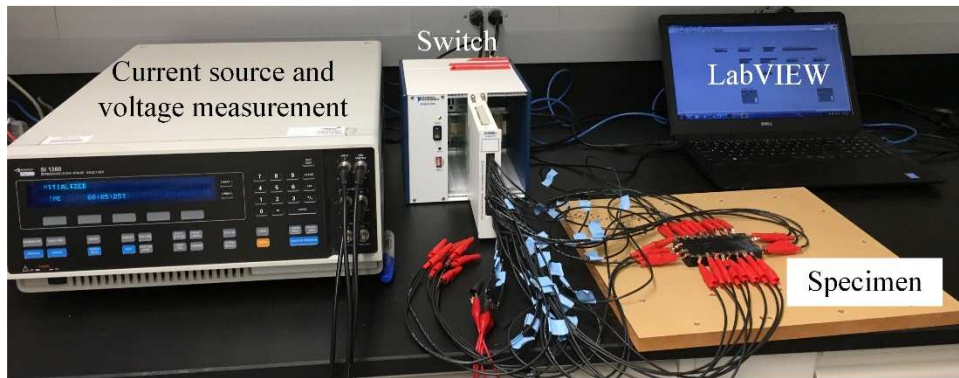


Figure 6.11 Electrical Impedance Tomography test setup



Figure 6.12 Design of switch matrix

One EIT test system was established to perform frequency-dependent EIT measurements before and after mechanical tests described in the above sections (Figure 6.11). Boundary

voltage measurements and current injection were performed using an impedance analyzer. The current source, voltage measurement, and switch matrix were controlled via LabView code (Laptop). Using the LabView software, the switch was commanded to interrogate the specimens by injecting alternating currents across a pair of boundary electrodes, while the boundary voltages were measured at all other remaining boundary electrodes. Figure 6.12 shows the design of the switch matrix. There were 64 output channels connected with the alligators to collect boundary voltage measurements. Four input channels were connected with the current source and voltage measurement, respectively.

The procedure was repeated following adjacent driven pattern, which is the most common pair drive protocol. The current is applied through two electrodes numbered as 1 and 2, and the voltage measured from pairs of electrodes 3 and 4, 4 and 5, etc. Current is then applied through the next pair of electrodes and the voltage measurements repeated. The procedure is repeated until each possible pair of electrodes has been used to inject current. Above measurement protocol produces  $M \times (M-3)$  measurements, where  $M$  is the electrode number. Thus, there were a total of 928 measurements for the coupon specimen and 504 measurements for the beam specimen.

Before damage was introduced to a specimen, an EIT reference measurement of the specimen was obtained using the aforementioned EIT system. Next, the specimens were subjected to the mechanical testing to generate certain damage patterns. Thereafter, the EIT system was employed for performing the other EIT boundary voltage measurements. It should be noted that both impedance magnitude and phase difference were collected for one measurement. In this study, alternating current with seven frequencies was injected into the specimen (1 Hz, 10 Hz, 100 Hz, 1 kHz, 10 kHz, 100 kHz, and 1 MHz). One set of measurements took from 8

minutes (1 Hz) to 1 minutes (1 MHz) for the coupon specimen, and 6 minutes (1 Hz) to 45 seconds (1 MHz) for the beam specimen.

### 6.5.3 Mechanical test methodology

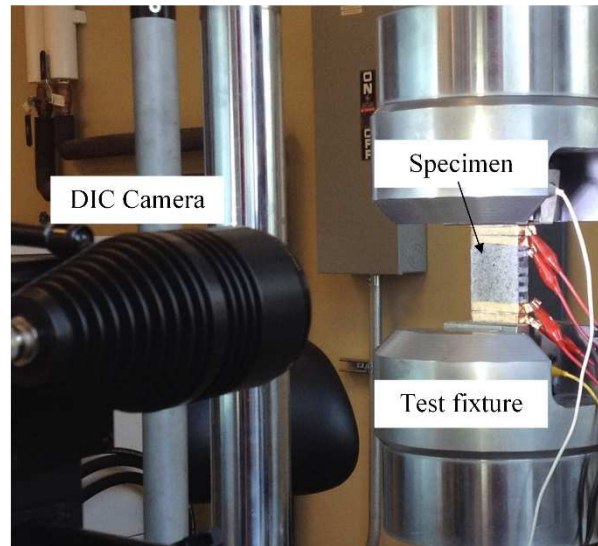


Figure 6.13 Uniaxial tensile test setup

Two types of mechanical tests were performed on the prepared specimens to induce different damage patterns: uniaxial tension test on the coupon specimens and four-point bending test on the beam specimens. The uniaxial tension test was conducted as shown in Figure 6.13. Both ends of the coupon specimen were gripped by the hydraulic steel grip attached to an 11 kips Shorewestern testing system. The testing gauge length was 100 mm and the deformation of specimens was measured with a Digital Image Correlation (DIC) system set up in front of the hydraulic testing frame. The tensile test was performed under displacement control at the rate of 0.0025 mm/s. The test was stopped once certain damage patterns (distributed damage or localized damage) were attained.

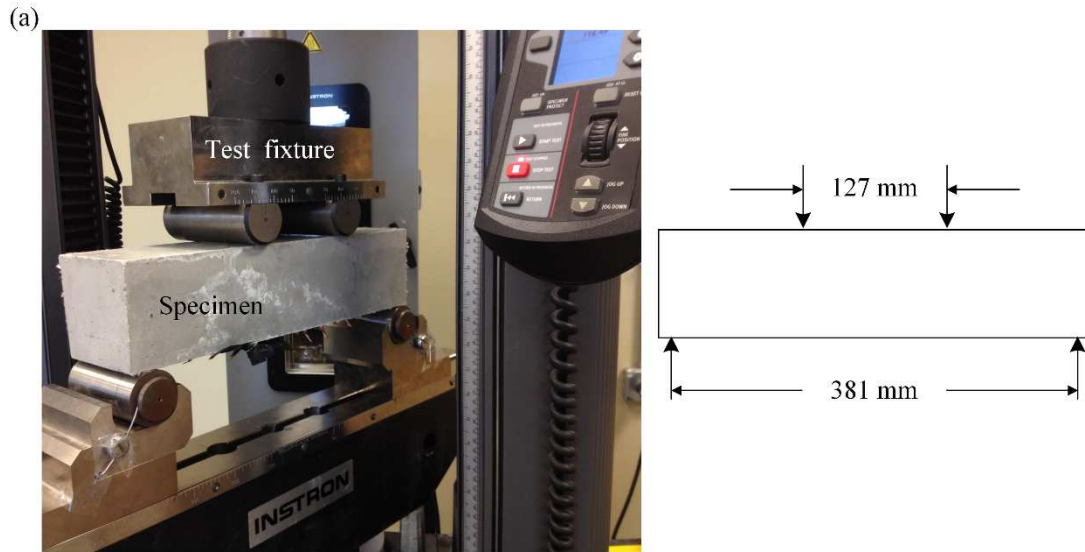


Figure 6.14 Beam specimen under four-point bending test: (a) test setup and dimension; (b) crack in the mid-span of the beam

Displacement-controlled four-point bending tests (0.003 mm/s) were performed on the N2 and C2 beam specimens using Instron electromechanical testing frame, as shown in Figure 6.14(a). The upper span to the bottom span ratio was 3, ensuring maximum moment occurring at the midspan. The test was stopped as soon as the force dropped to 85% of the maximum force value. Figure 6.14(b) shows the induced single crack in the midspan of N2 beam.

#### 6.5.4 Finite element modeling

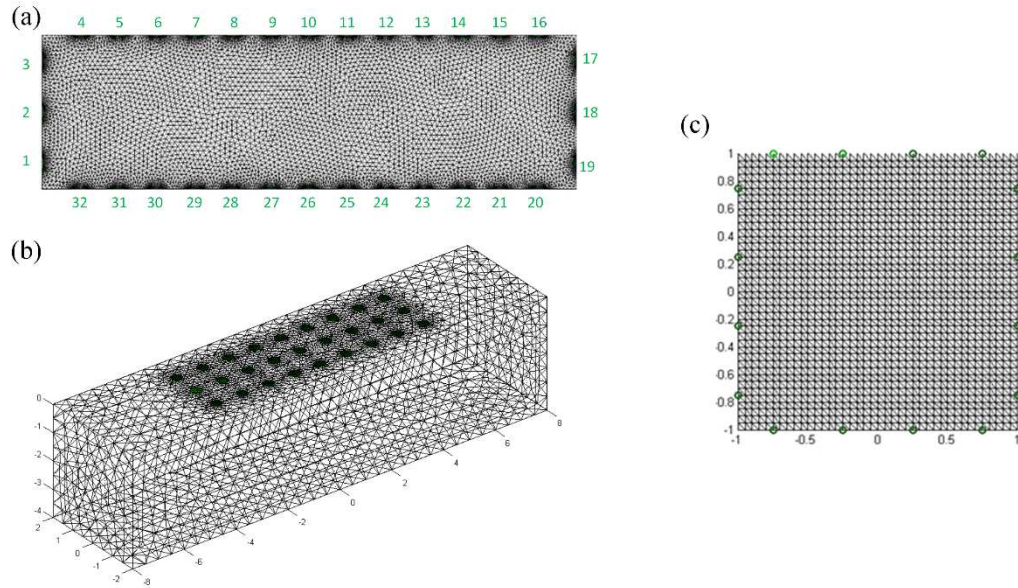


Figure 6.15 Finite element model of (a) coupon specimen with 32 electrodes; (b) beam specimen with 24 electrodes; (c) panel specimen with 16 electrodes

For the coupon specimen, the electrodes covered the entire thickness of the specimen, and hence image reconstruction averages the electrical resistivity in the direction perpendicular to the large surfaces of the specimen, which is sufficient to reflect the damage pattern of the coupon specimen. Therefore, 2D image reconstruction was performed with a finite element model shown in Figure 6.15(a). For the beam specimen, 3D finite element model was established based on the specimen dimension and location of electrodes, as shown in Figure 6.15(b). It should be noted that the meshing size is fine enough for accurate calculation, and further increasing meshing number does not increase the accuracy. The finite element model simulated exactly the measurement scenarios in above sections. For the panel specimen used for EIT system validation, two-dimensional model was established as shown in Figure 6.15(c). There were 16 electrodes around the specimen.



## 6.6 Results and Discussion

This section presents the results of the experimental studies. The EIT system collected both impedance magnitude ( $|Z|$ ) and phase shift ( $\phi$ ), via which complex impedances (real part ( $Z_r$ ) and imaginary part ( $Z_m$ )) were calculated following Eq.(6.12). As for the cementitious composites, the phase degree below 1 MHz is normally ranging from  $0^\circ$  to  $-90^\circ$ , the imaginary part of the impedance is thus negative. Therefore, in the image reconstructions based on imaginary part, the change of the resistivity has a negative sign, showing the opposite color compared with image reconstructions based on impedance magnitude and real part. This phenomenon might not be true if high-frequency inductance phenomena occurred. But in this study, test results did not show the occurrence of high-frequency inductance.

$$Z_r = |Z| \cos \phi, \quad Z_m = |Z| \sin \phi \quad (6.13)$$

In section 6.6.1, image reconstruction results of panel specimen and coupon specimen with controlled damage pattern were presented to validate the applicability of EIT system. In sections 6.6.2, 6.6.3, and 6.6.4, not only the impedance magnitude but also real and imaginary part were used for image reconstructions. The 2D frequency-dependent EIT results are reported in sections 6.6.2 and 6.6.3 for coupon specimens. The damage sensing on the beam specimen is discussed in section 6.6.4.

There is one assumption for image reconstruction in this study. Before applying damage, the reference data was collected, and then damage data was collected after applying damage. In this study, it is assumed that the differences between reference data and the damage data are only resulted from applied damage, and the electrical property of the cementitious material did not vary from time to time. In this study, the test was conducted in the room with stable humidity,

and the time interval between reference data and damage data was less than 1 hour. So, the assumption is reasonable.

### 6.6.1 Validation of the EIS system

#### Validation 1: square panel specimen with a middle hole

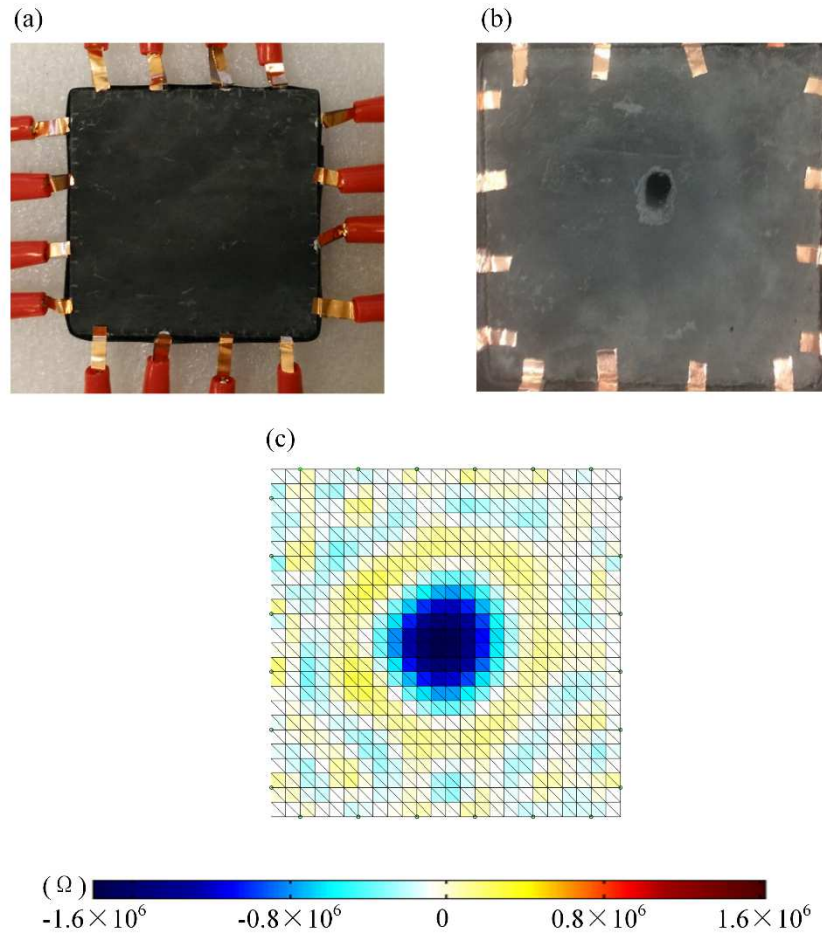


Figure 6.16 Image reconstructions of square panel specimen (a) square specimen with 16 electrodes; (b) damage in the middle of the specimen; (c) image reconstruction

First, a panel made from 5% MSC was prepared for EIT system validation (Figure 6.16). Based on above parameter studies, measurements on 5% MSC possessed high signal-to-noise ratio for EIT image reconstructions. Same electrode setup as shown in Figure 6.9 was adopted for the panel specimen. EIT data collection was conducted on the specimen, with 208 data points ( $16 \times 13$ ). In this validation study, a current was injected at a single frequency of 1500 Hz. The

adjacent current pattern was utilized. The same procedure was repeated for three times, and hence the average of all three scans was utilized as the reference measurement. Then a center hole was drilled in the middle of the specimen with a diameter of 5 mm. Thereafter, another three repeated EIT scans were conducted on the specimen. With the collected data, image reconstruction was performed.

Figure 6.16 shows the image reconstruction results. It is clearly demonstrated that the image reconstruction was able to accurately identify the middle hole within the specimen, validating the applicability of EIT system on 5% MSC. The deep blue color distribution in the 2D finite element model indicates that there was a significant increase of impedance in the middle of the specimen. Although damage size was overestimated, the damage location and geometry were clearly reflected.

*Validation 2: Coupon specimen with a middle hole*

Another experiment was conducted to further validate the applicability of EIT test system and the damage sensing behaviors of MSCs. In this study, there were two types of specimens prepared for the test, i.e., N1 (0% MSC) and C1 (5% MSC). Figure 6.17 shows the damage with a specimen of N1. EIT scan was conducted at a fixed frequency of 1500 Hz. Impedance magnitude was utilized for image reconstructions.

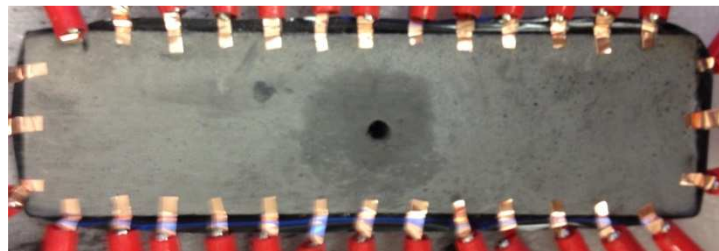


Figure 6.17 Damage within a specimen of N1

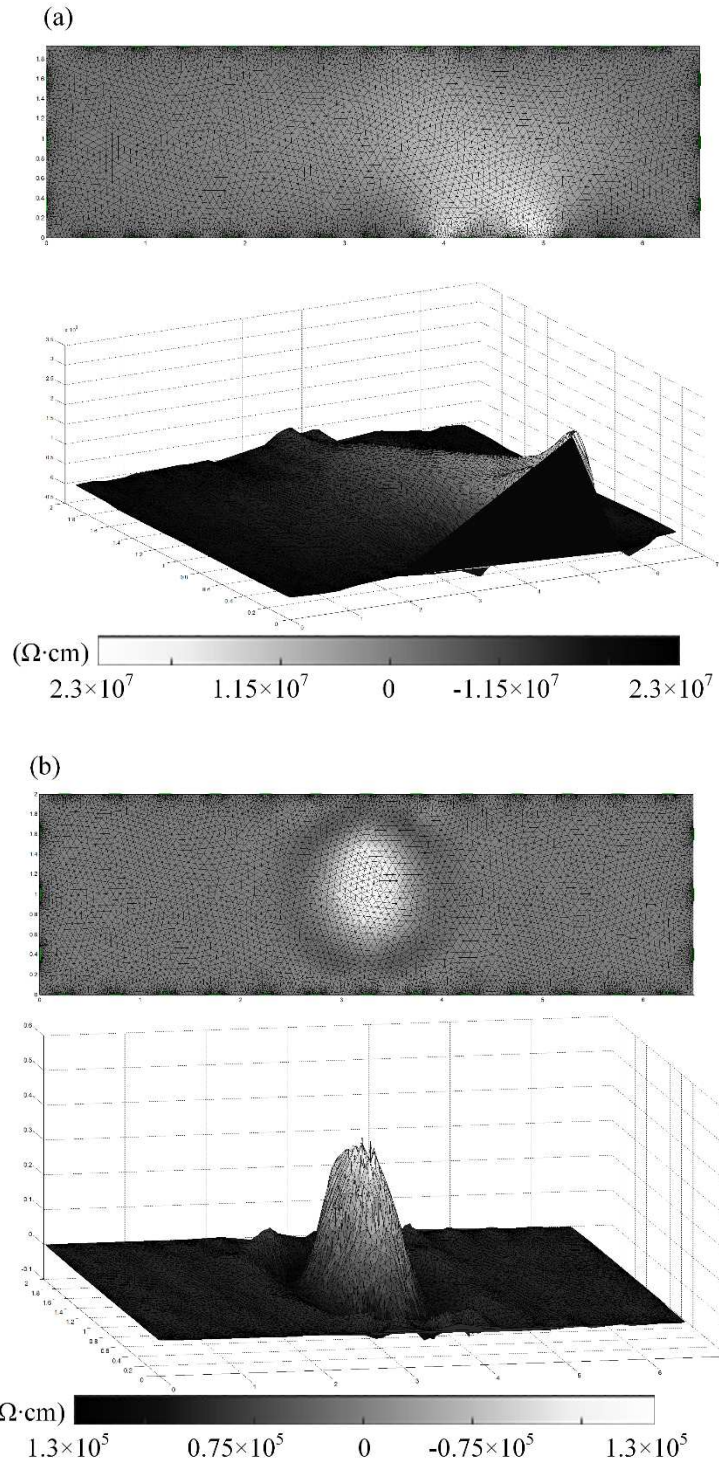


Figure 6.18 Electrical impedance tomography image reconstructions of (a) N1 and (b) C1

Figure 6.18(a) shows image reconstructions of N1. It can be found that the image reconstruction was not able to capture the exact location and the damage geometry, although the appearance of the damage was detected. That is consistent with the conclusion drawn from parameter study part, which means low signal-to-noise ratio led to poor quality of image reconstructions.

Figure 6.18(b) shows the image reconstruction for C1. The location of the circular damage can be correctly detected by EIT. The size of the damage was overestimated due to the smoothing effect of the regularization. The three-dimensional view of image reconstructions shows that there exists one single high resistivity peak all over the specimen surface, indicating the localized damage.

Above two tests validated the applicability of EIT system for cementitious materials and the damage sensing properties of MSCs. Following tests further reveal the critical parameters of EIT on cementitious materials.

#### *6.6.2 Damage sensing of 2D localized cracks*

Damage sensing of localized cracks involves coupon specimens C2 and N2. Uniaxial tension tests were performed to induce single localized damage in coupon specimens. Figure 6.19 and 6.20 exhibit the results of C2 and N2. Both figures show photographs of the specimen and image reconstructions corresponding to three different measurement parameters (impedance magnitude, real part, and imaginary part) at seven frequencies (1 Hz, 10 Hz, 100 Hz, 1 kHz, 10 kHz, 100 kHz, and 1 Mhz). Uniaxial tension tests generated the similar crack pattern in C2 and N2. There was one large crack (average crack width = 2.4 mm) in the middle region of coupon specimen N2. A similar large crack was observed on the right side of coupon specimen C2 (average crack width = 2.3 mm). The large crack separated the coupon specimens into two parts

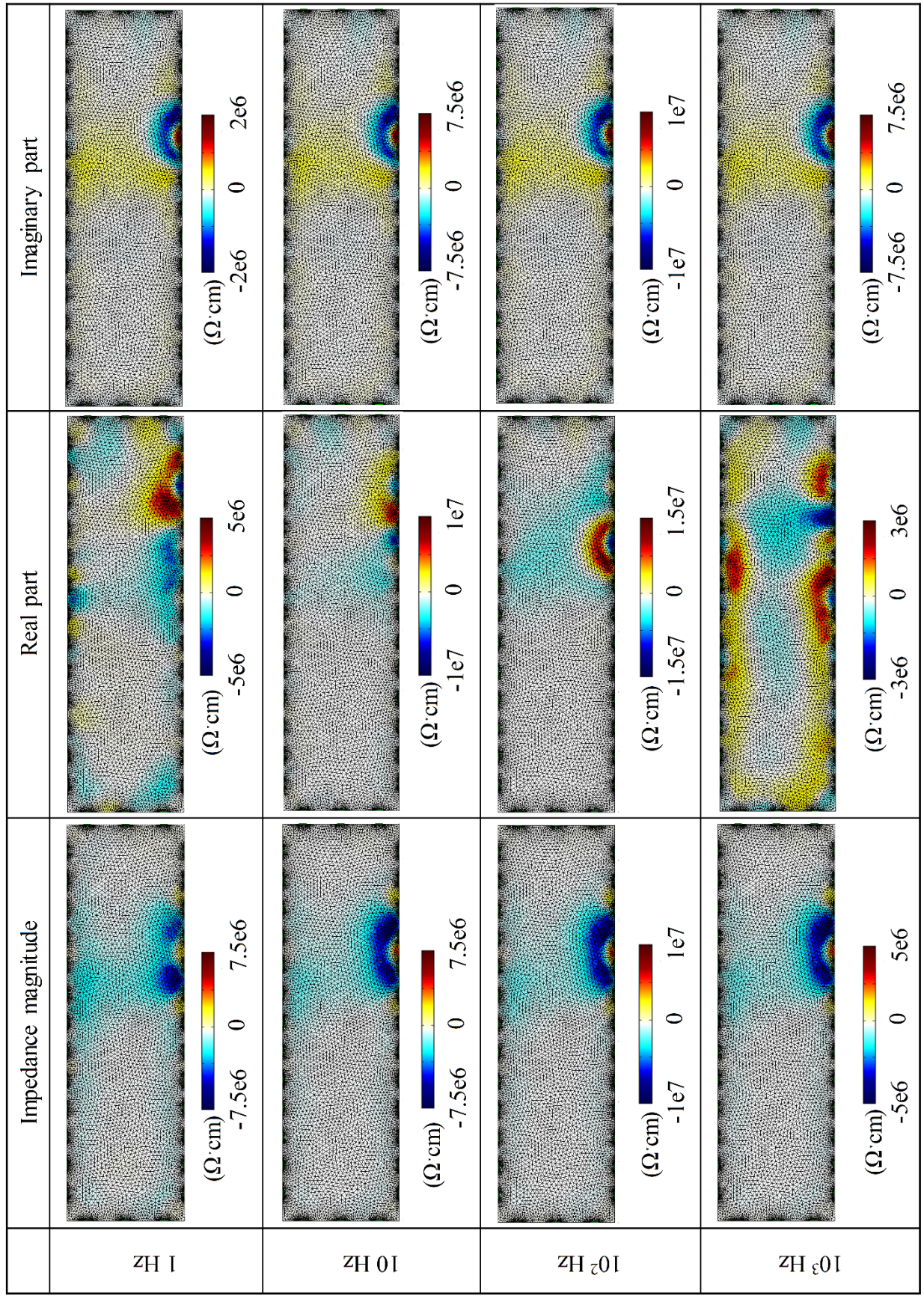
with some PVA fibers bridging the crack. It should be noted that the contrast and color of the photographs were adjusted to highlight the cracks.

Figure 6.19 shows image reconstruction results of coupon specimen N2. As the impedance of the cementitious material is frequency-dependent, image reconstructions at different frequencies are significantly different. Compared with damage pattern observed from the surface, a rather large area of conductivity change is observed in the reconstructions based on impedance magnitudes from 1 Hz to 1 kHz, imaginary part from 1 Hz to 1 kHz, and real part from 1 Hz to 100 Hz. Although the occurrence of the damage and rough region were reflected, it is impossible to exactly assess the locations, extents, and shapes of the damage based on those images. After 10 kHz, reconstructions (impedance magnitude, real part, and imaginary part) merely reflected meaningless noise without any damage information. Just as described above, in the reconstructions of impedance magnitude and real part of impedance, the increase of resistivity (blue) represented the damage. However, in the image reconstructions based on imaginary part of the impedance, the decrease of resistivity (yellow or red) reflected the damage.

Figure 6.20 shows image reconstruction results of coupon specimen C2. The features of the damage are clearly reflected by the image reconstructions at a frequency range from 1 Hz to 100 kHz. The quality of the image reconstructions based on impedance magnitude, imaginary part, and real part is almost same before 1 kHz. At 10 kHz, despite noisy, the image reconstructions based on impedance magnitude and imaginary part still display the single crack clearly. At a frequency of 100 kHz, the image reconstructions based on impedance magnitude and imaginary part also capture damage information, but with deformed damage shape and much more noise. However, image reconstructions based on real part is not able to capture damage details at a high-frequency range (above 1 kHz). At the highest frequency (1 MHz), merely noise

is reflected in all image reconstructions. It should be noted that there is a slight difference in crack shape as shown in image reconstructions compared with the real damage pattern. One possible reason is that the crack was not exactly same throughout the specimen depth, but 2D image reconstruction captured the average resistivity change along the depth of the specimen. The damage extent captured in image reconstructions was relatively larger than the real case, which was resulted from the use of Tikhonov regularization in the calculation.

The comparisons between Figure 6.19 and Figure 6.20 validate that the EIT is able to capture details of a localized crack in the cementitious materials, and the cementitious material C2 showed more sensitivity compared with the cementitious material N2, although same EIT setup, measurement protocol, and image reconstruction algorithms were adopted. The frequency range for high-quality image reconstructions of a single crack is from 1 Hz to 1 kHz for real part, but 1 Hz to 10 kHz for impedance magnitude and imaginary part of impedance. Within the above frequency range, image reconstructions exactly reflect the detailed damage information (location, shape, and severity). Image reconstructions based on impedance magnitude and imaginary part at the frequency range from 10 kHz to 100 kHz were also able to capture the contrast between the damage and unchanged parts, while real part image reconstructions at above frequency range merely display noise without showing any damage information.





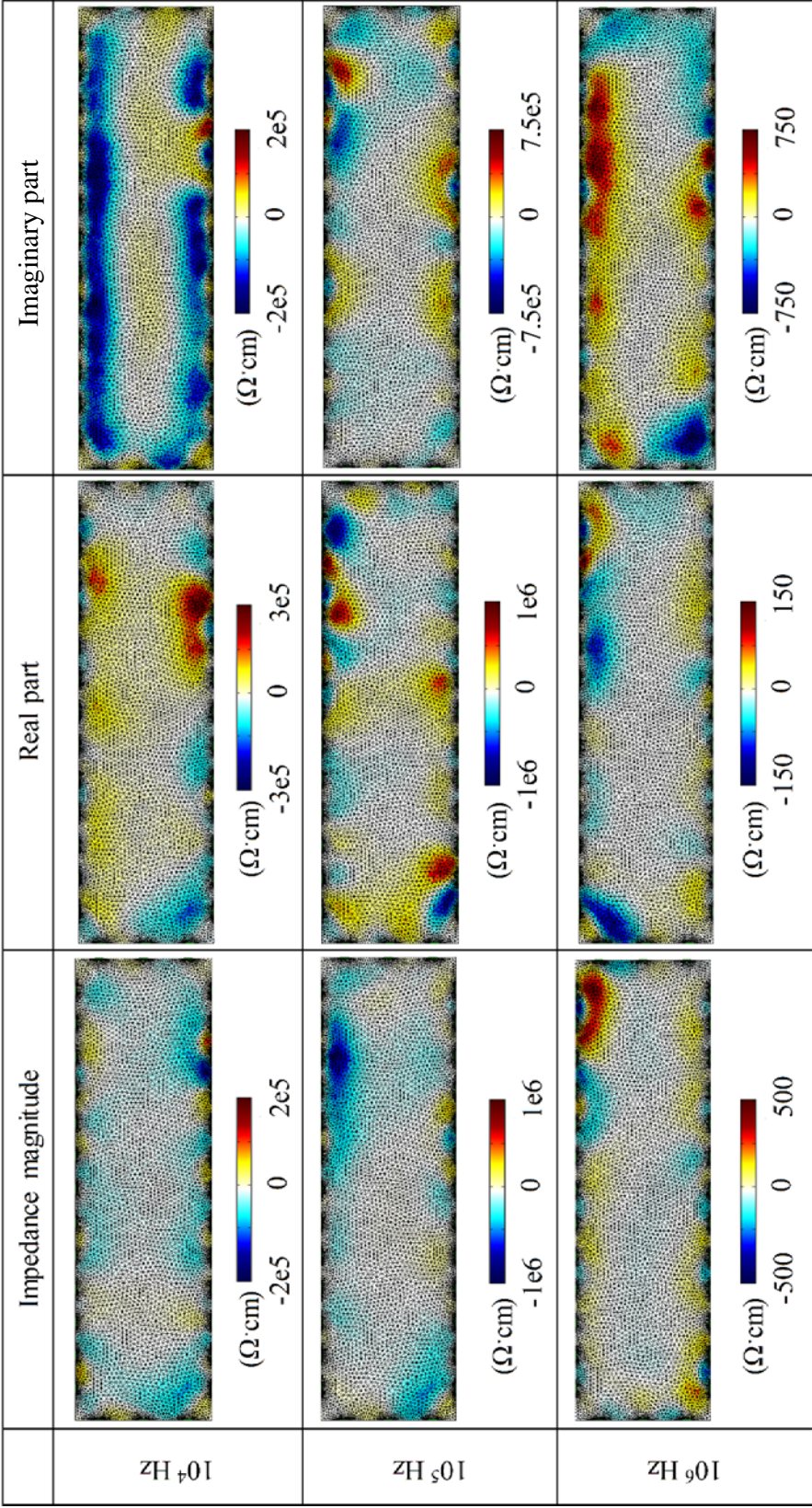
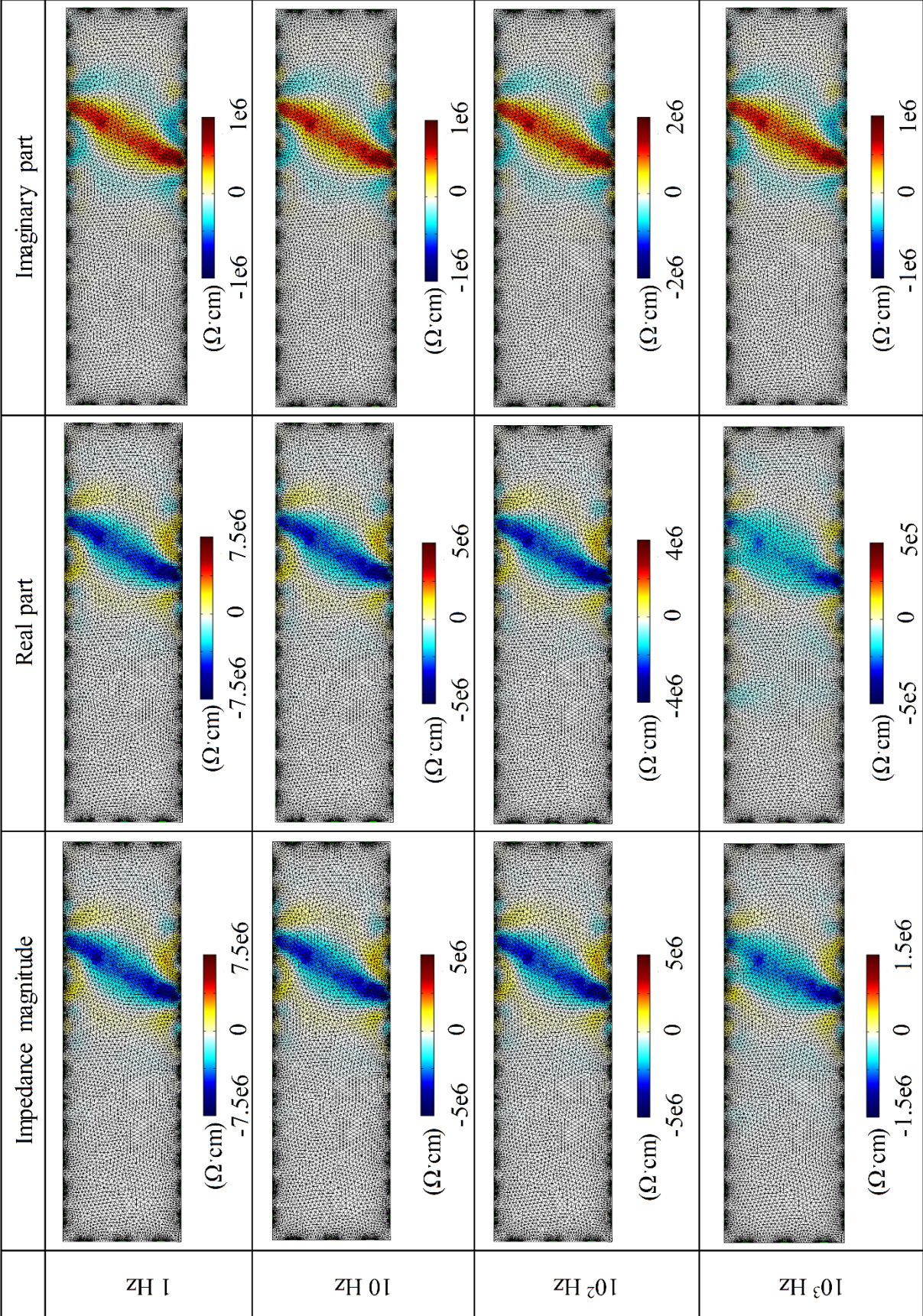


Figure 6.19 Image reconstructions of coupon specimen N2 with a localized crack



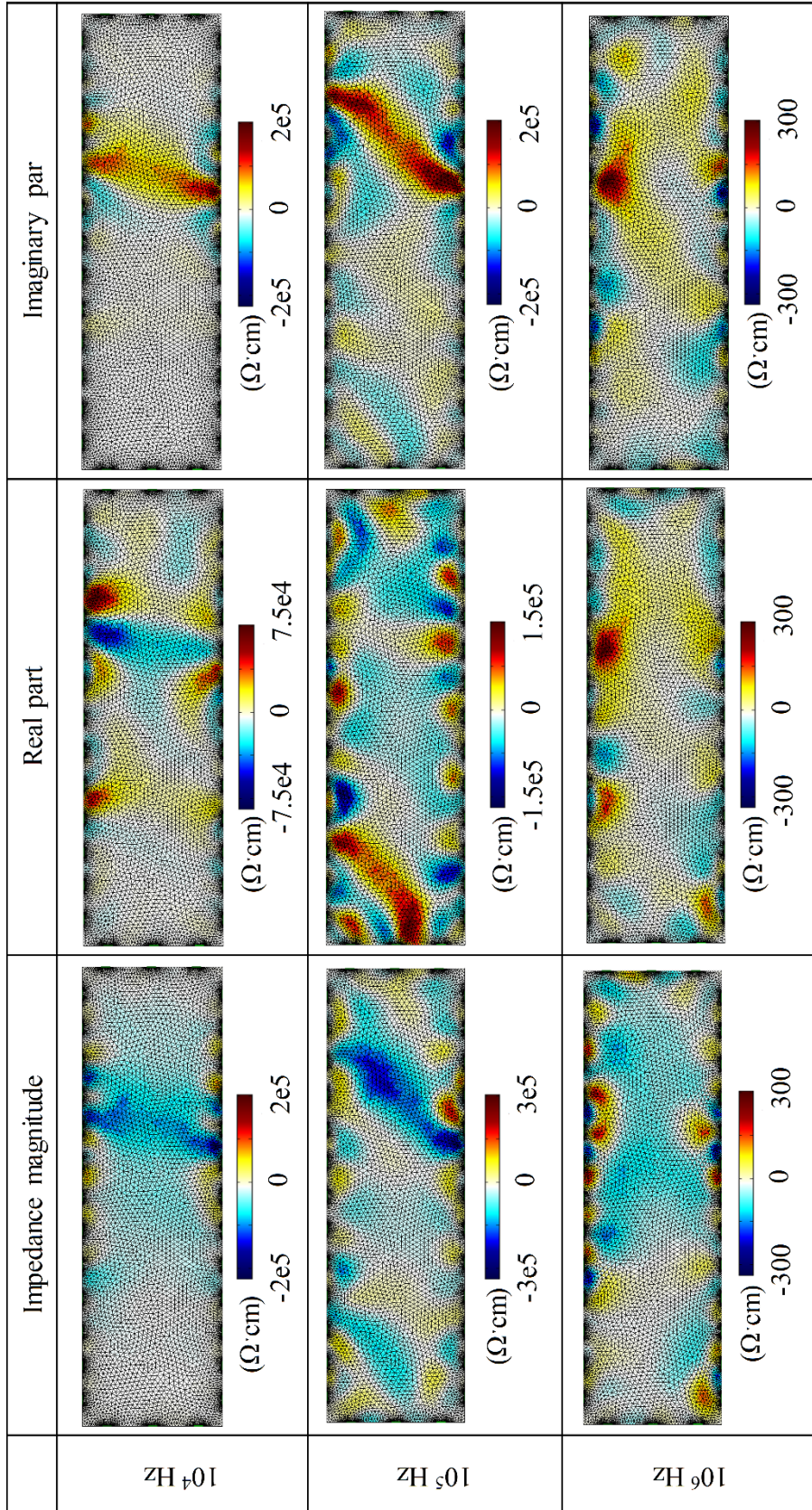


Figure 6.20 Image reconstructions of coupon specimen C2 with a localized crack

### *6.6.3 Damage sensing of 2D distributed cracks*

The distributed cracking pattern and the corresponding image reconstructions of C1 and N1 are plotted in Figure 6.22, and 6.23. As it is difficult to directly visualize the microcracks, the cracks were highlighted in white. Figure 6.21(a) shows the distributed cracks (average crack width = 54  $\mu\text{m}$ ) on the surface of the N1 specimen, with one final failure crack (maximum crack width = 1.1 mm) in the middle region. Figure 6.21(b) illustrates the microcracks distribution (average crack width = 53  $\mu\text{m}$ ) in coupon specimen C1 with one single crack on the left side of the specimen (maximum crack width = 0.8 mm).

As shown in Figure 6.22, the damage state is not discernable from the image noise. The change of impedance type (impedance magnitude, real part, and imaginary part) and the change of frequencies result into different reconstructions. On the contrary, Figure 6.23 clearly shows the location and extent of distributed cracks in the form of a change in electrical impedance with the frequency ranging from 1 Hz to 10 kHz. While every single crack was not able to be identified, image reconstructions exactly revealed the spatial distribution of the cracks. The damage severity was fully captured. The final failure crack on the left side shows the most significant contrast compared with other cracks. Also, the multiple microcracks with an average crack width of 36  $\mu\text{m}$  on the right side of the specimen were illustrated clearly, even though the cracks were invisible via direct observation. Before 10 kHz, image reconstructions based on impedance magnitude, real part, and imaginary part do not show apparent differences. With the frequency ranging from 1 Hz to 1 kHz, the image noise can be ignored. At 10 kHz, the damage distribution appears less prominent and much noise was observed for image reconstructions based on real part. However, the image reconstructions based on imaginary part and the impedance magnitude still showed the image reconstructions without much noise. The image

reconstructions at high frequencies (100 kHz and 1 MHz), however, are not able to reflect damage information.

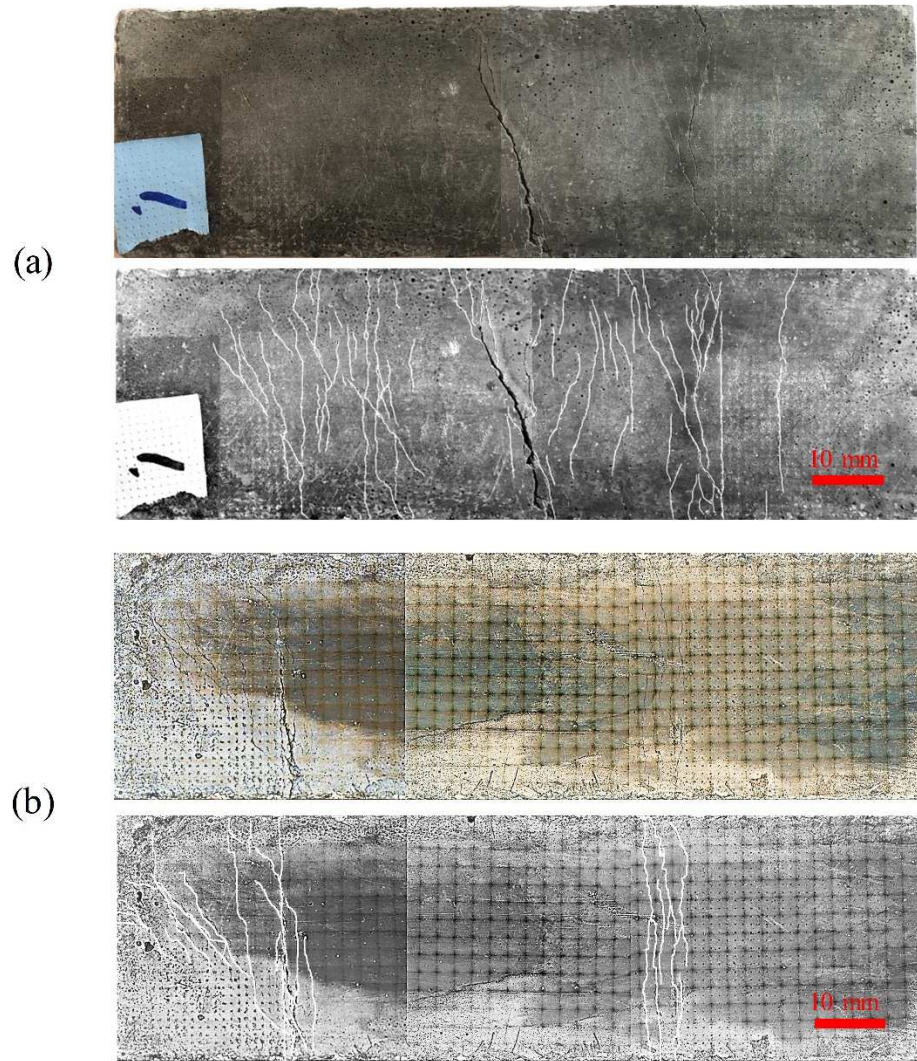
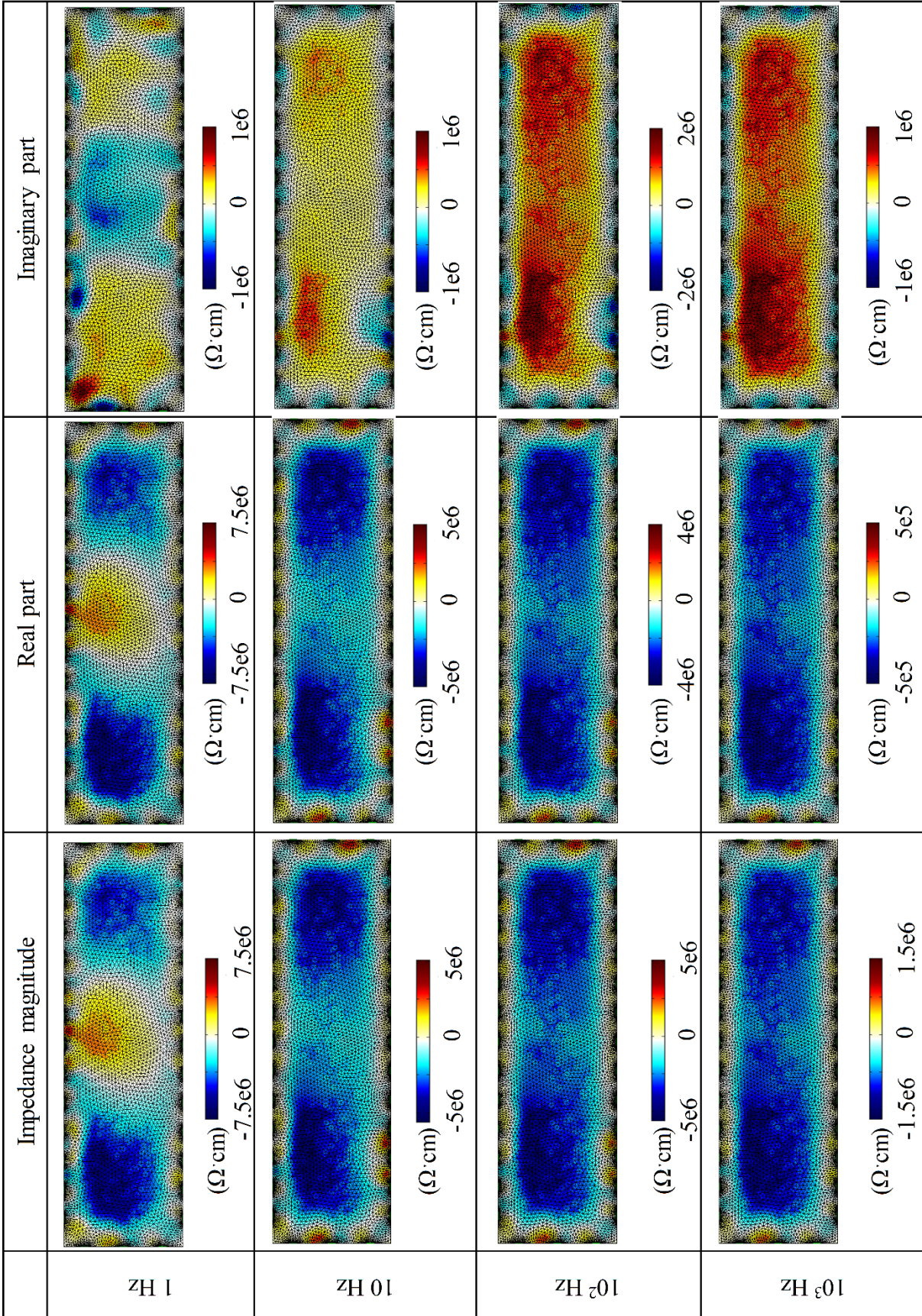


Figure 6.21 Specimens with distributed cracks and processed images: (a) N1; (b) C1



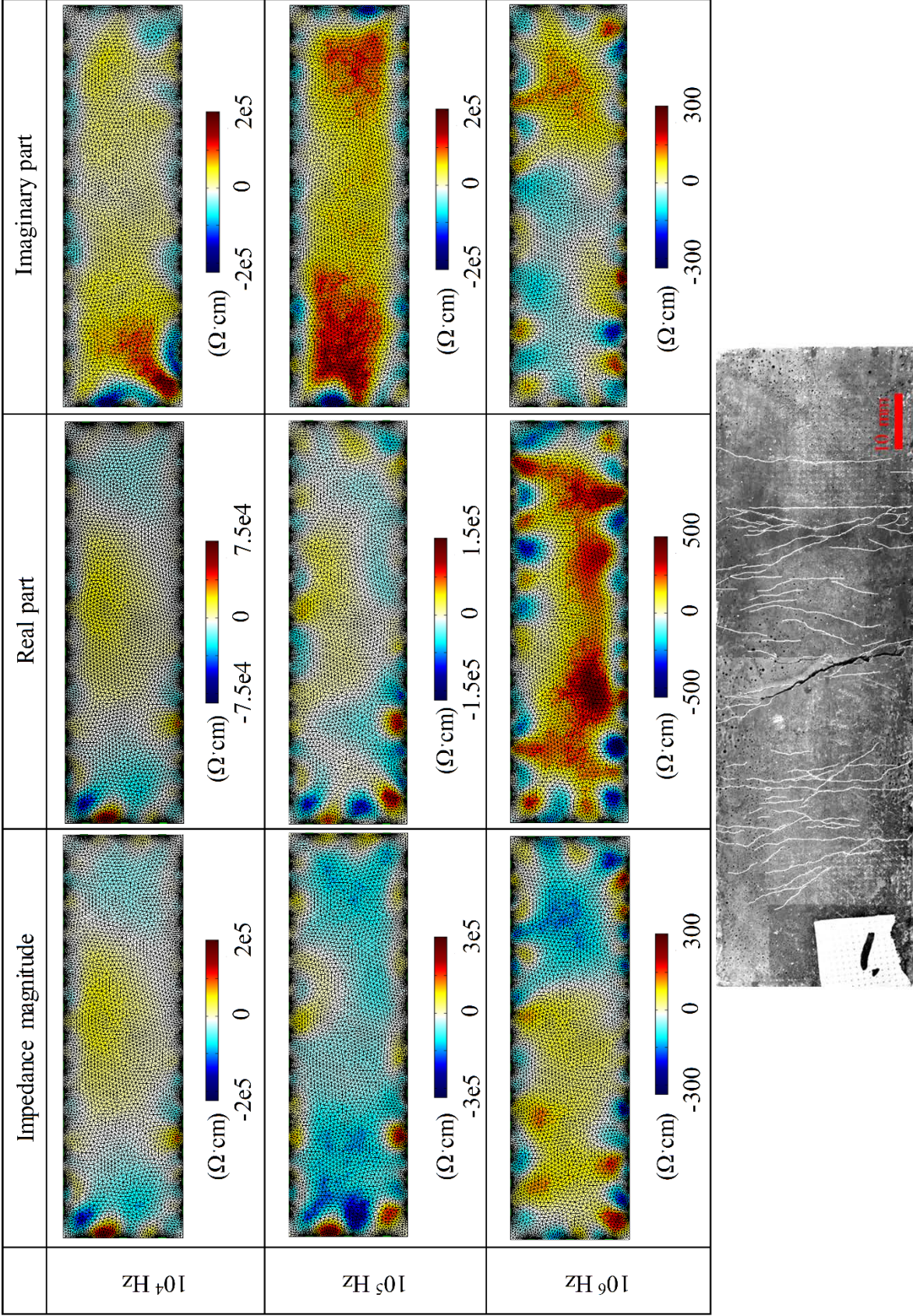
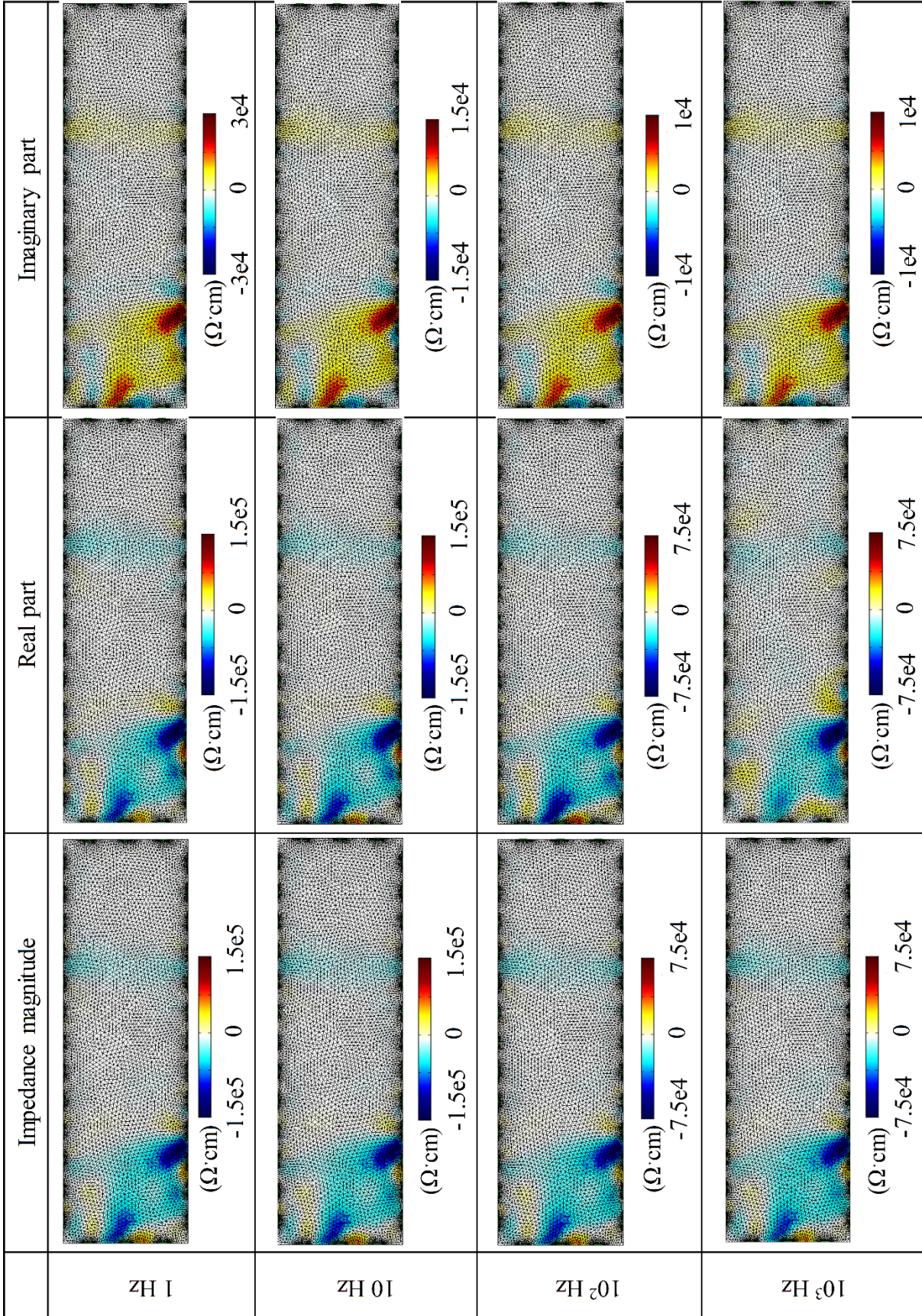


Figure 6.22 Image reconstructions of coupon specimen N1 with distributed cracks





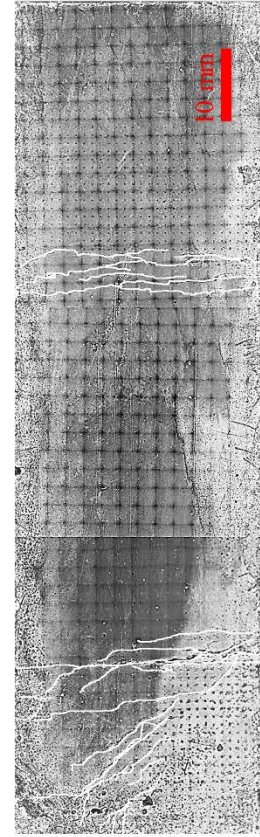
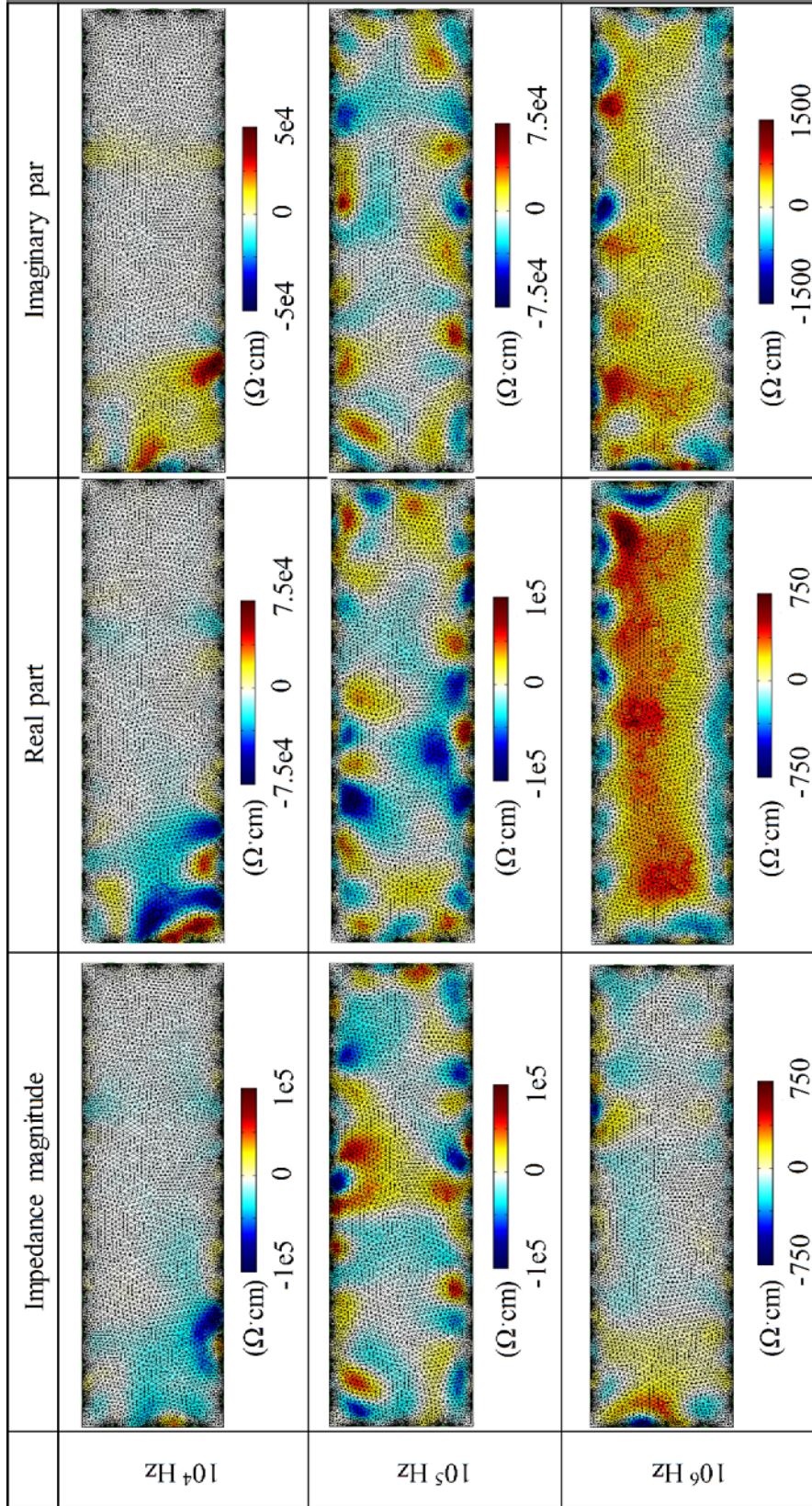


Figure 6.23 Image reconstructions of coupon specimen C1 with distributed cracks

Comparing the results of N1 and C1 in Figure 6.22 and Figure 6.23 shows that, in the case of distributed damage detection, C1 clearly outperformed N1. Despite the fact that distributed multiple microcracks are more difficult to detect than localized cracks, EIT image reconstructions still showed high-resolution damage detection on coupon specimens C1. For distributed damage sensing, the optimized frequency is the same as that for localized damage sensing, which is from 1 Hz to 1 kHz.

#### *6.6.4 Damage sensing of 3D crack in the beam specimen*

The final phase of this study is the three-dimensional damage sensing on the beam specimen. As localized cracks dominate the health condition of structural members, this study focuses on a single localized crack in beam specimens prepared with C2 and N2. As discussed in section 6.5, a four-point bending test was performed on the beam specimen. The relation of load versus the stroke of the testing frame is plotted in Figure 6.24. The test was terminated once the loads dropped to 85% of the peak load. Figure 6.24 shows that the loading capacity of beam C2 is around 12.5% lower than that of the beam N2. As preparation of C2 involved carbon black, which absorbed a large amount of water, resulting in more voids within the beam, the loading capacity correspondingly decreased. An evolution of a single crack at the mid-span of the beam was observed as a consequence of the flexure test. The beam was removed from the testing frame and a photo was taken to report the crack pattern. It should be mentioned that in this study, the electrodes were installed on the tension side of the beam. As shown in Figure 6.25 and Figure 6.28, one single crack with an average crack width of around 0.36 mm and a depth of around 6.2 cm was induced on the N2 beam specimen, while the single crack on the C2 beam was 0.3 mm wide and 6.3 mm deep. Due to the difficulty in directly visualizing single crack on the beam C2, the crack was marked with a blue marker as shown in Figure 6.25(a) and Figure 6.28(a).

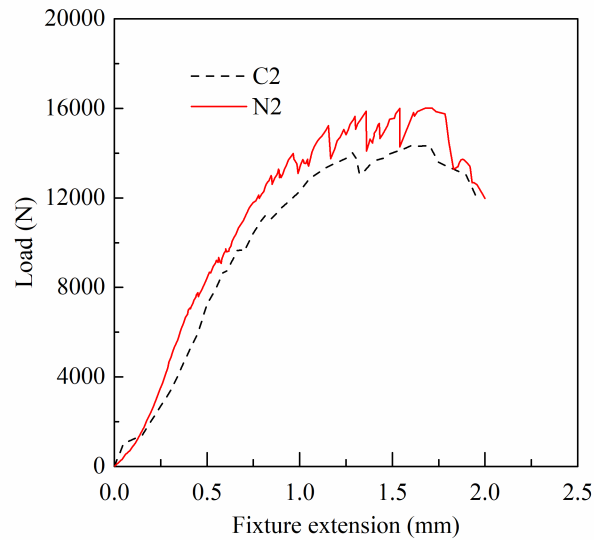


Figure 6.24 Relation of fixture extension and load

Figure 6.25 illustrates that the single crack located in the mid-span of the N2 beam, on the right side of electrodes at the 5<sup>th</sup> column. The crack was nearly perpendicular to the longitudinal direction of the beam. Figure 6.26 organizes all the image reconstruction results. It can be seen that most of the image reconstructions did not apparently reflect the damage information. However, some of the image reconstructions did capture the damage occurrence, despite poor accuracy and much noise. The image reconstructions based on impedance magnitude and imaginary part at 1 Hz roughly reflected the damage location without much noise. However, the depth could not be assessed at all and the damage extent was overestimated compared with the real crack. Figure 6.27 plots the three-dimensional slice of the N2 beam. Based on the impedance change (blue part), the depth was measured all through the cross-section of the N2 beam (102 mm). Although the difference imaging scheme was utilized and hence measurement noise was minimized, the quality of the image reconstruction was still poor due to the low signal-to-noise ratio. Since the resistivity of the N2 beam is too high for current to sufficiently propagate through the entire material, the measured boundary voltage responses were

not sensitive to damage features, i.e. damage depth. It can also be concluded that, compared with the real part of the impedance, imaginary part and impedance magnitude are more suitable for image reconstructions of high impedance objects.

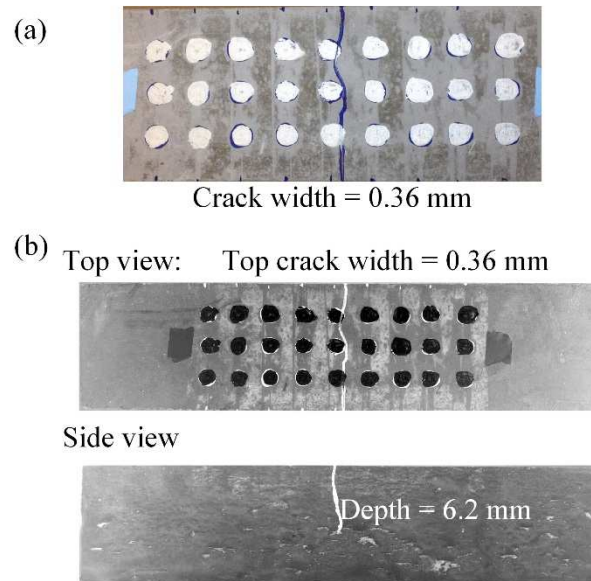
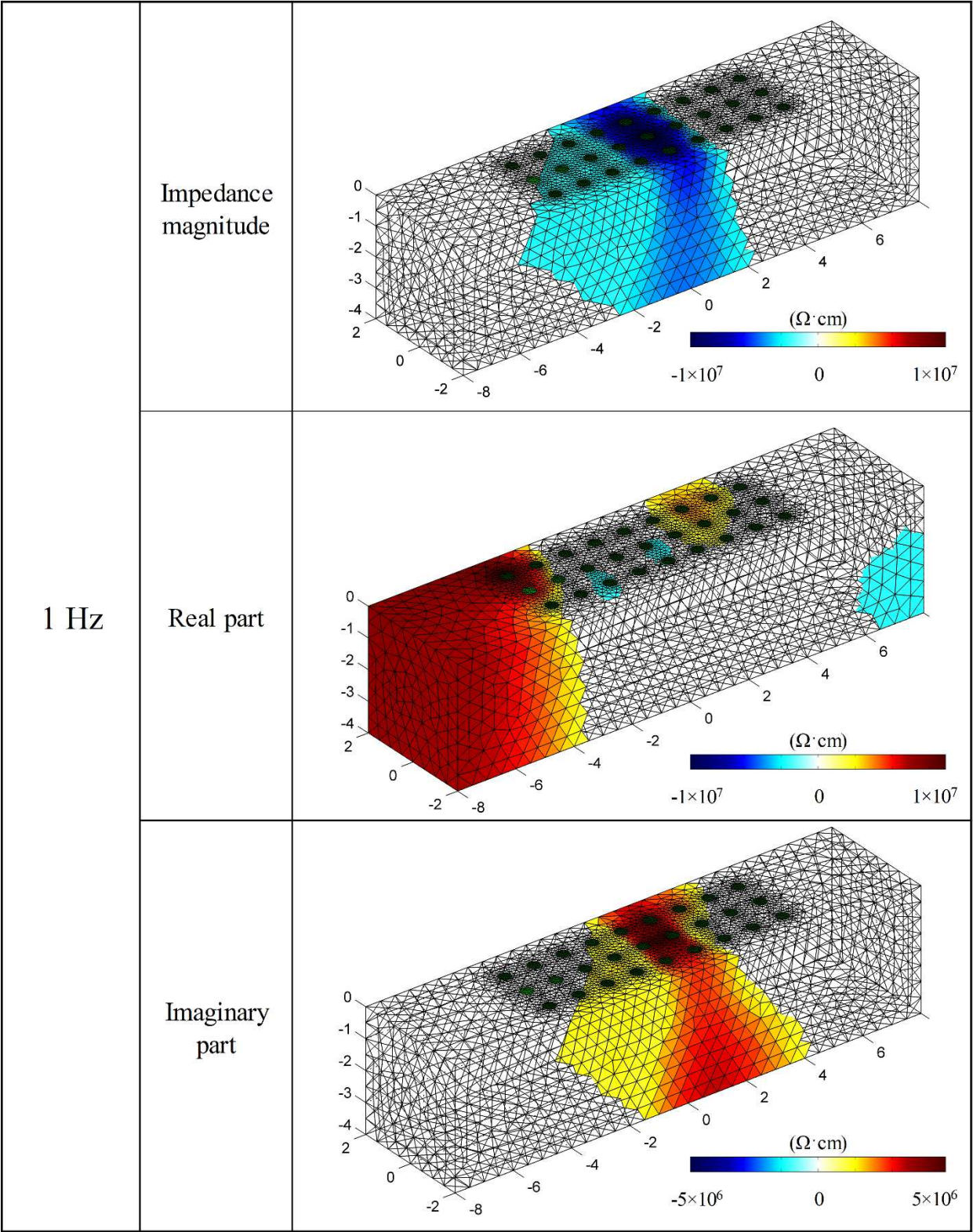


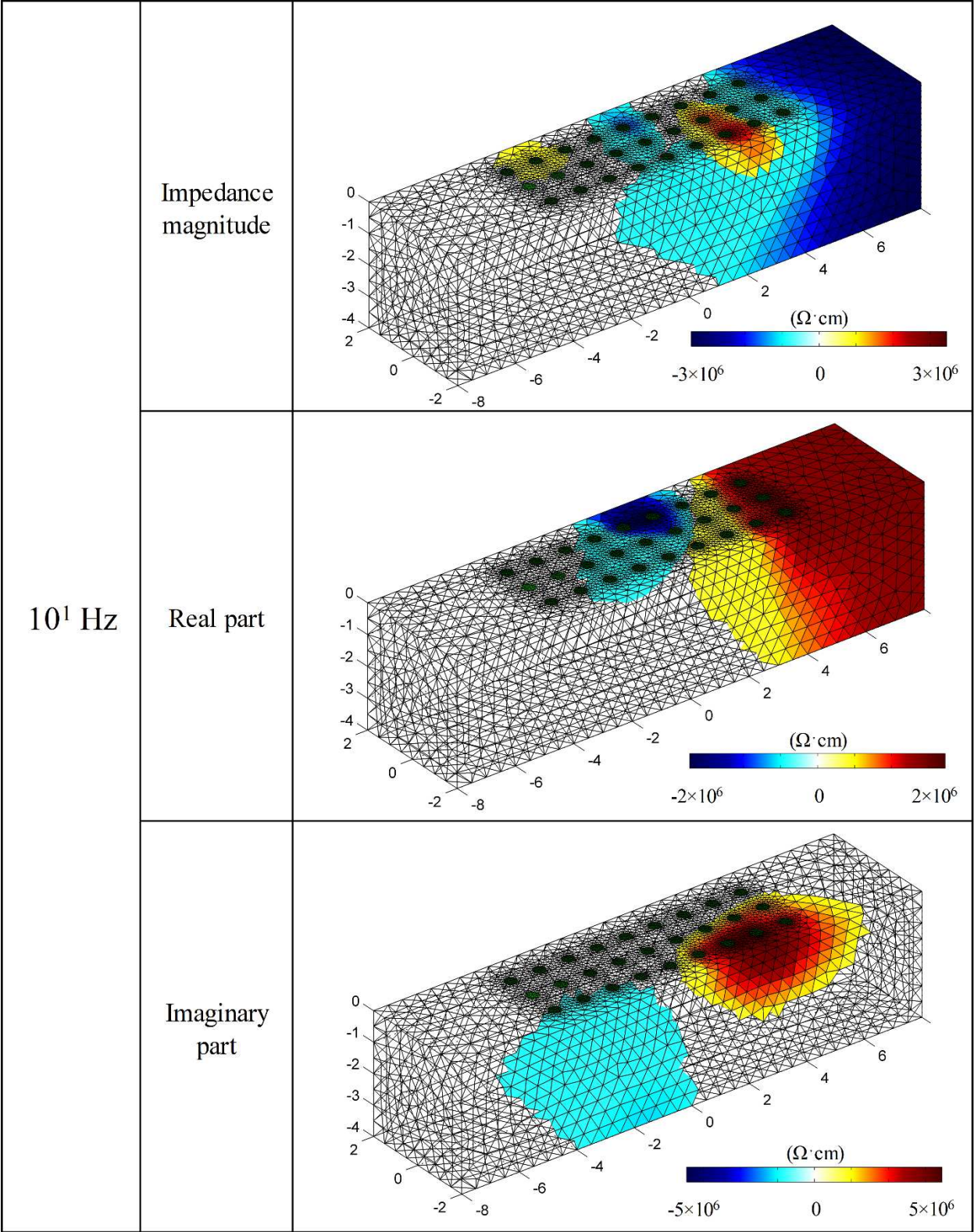
Figure 6.25 Crack details of N2 beam

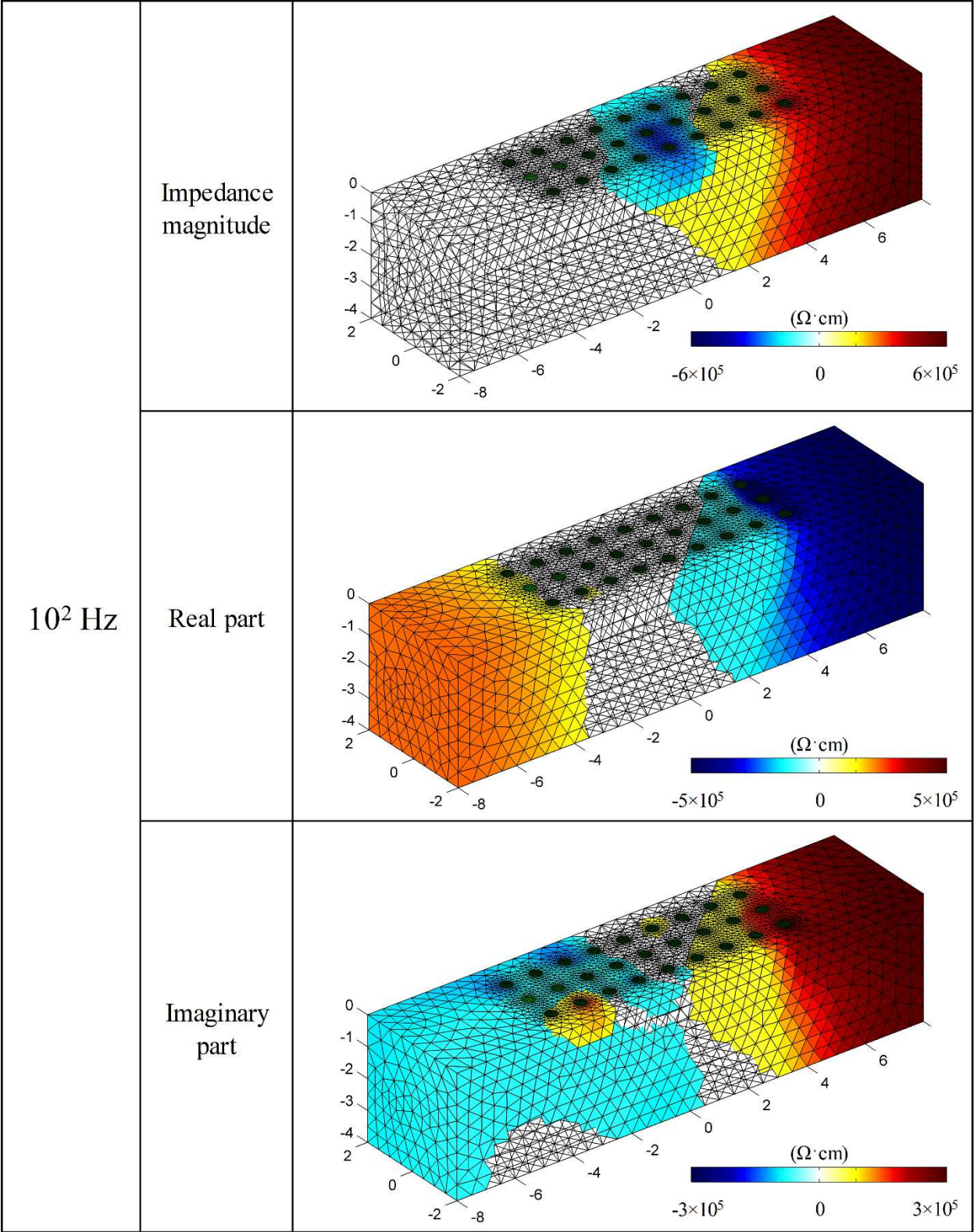
On the contrary, the image reconstructions of the C2 beam yielded drastically different results. Figure 6.28 shows that the crack pattern of the C2 beam is similar to that of the N2 beam, except that crack located between electrodes at the 4<sup>th</sup> column and the 5<sup>th</sup> column. The crack depth was 6.3 mm, which was around half the depth of the C2 beam. The image reconstruction results are summarized in Figure 6.29. Compared with results in Figure 6.27, the results are less noisy when the frequency is below 10 kHz. The results show that the image reconstructions based on all types of impedance (impedance magnitude, real part, and imaginary part) clearly show the impedance increase (blue part for impedance magnitude and real part; red part for imaginary part). The impedance change is located in the same position as the crack, suggesting that the crack location can be captured.

Especially for real part image reconstructions, the surface extent of the resistivity change was very narrow, which is similar to the damage. However, the real part image reconstructions (from 1 Hz to 10 kHz) underestimated the crack depth significantly. At 100 kHz, although the crack depth was better estimated, the shape of the damage was deformed. However, image reconstructions based on imaginary part show an accurate estimation of damage depth. At 1 Hz and 10 Hz, the damage size was overestimated. From 100 Hz to 100 kHz, the image reconstructions based on imaginary part of impedance estimated the damage depth more accurately, but the surface extent of the crack was overestimated compared with the image reconstructions based on real part of impedance.

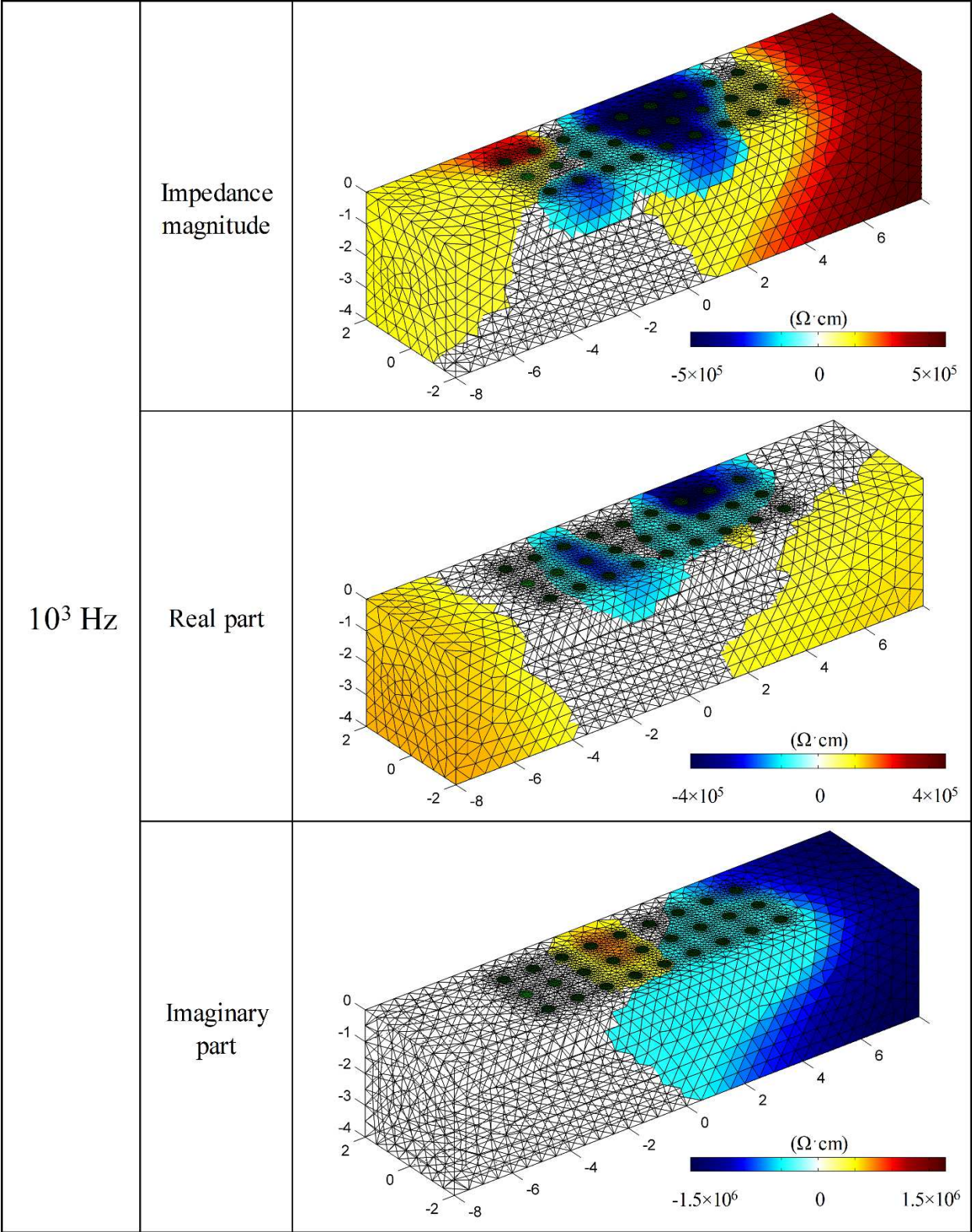
On the contrary, the image reconstructions based on impedance magnitude exactly reflected the damage information. It should be noted that, with increasing frequency, the estimated crack depth decreased correspondingly. Figure 6.30 illustrates the three-dimensional slice of the beam at different frequencies (1 Hz, 10 Hz, 1 kHz, and 10 kHz). The red line represents the real crack depth and location. It is found that the image reconstructions at 1 kHz showed the estimated crack depth as same as the crack. At the lower frequencies, the current was not able to propagate to the deep part of the beam and thus the damage depth was overestimated. Increasing frequency allowed more current to propagate to the deeper part of the beam and thus the image reconstructions indicated the damage depth more accurately. It is shown that the frequency of 1 kHz was the optimal frequency for this test scenario. Further increasing frequency (10 kHz) induced less crack depth, suggesting that the alternating current passed through the narrow part of the crack via capacitor effect. However, at 10 kHz, the damage extent and location were not exactly reflected.

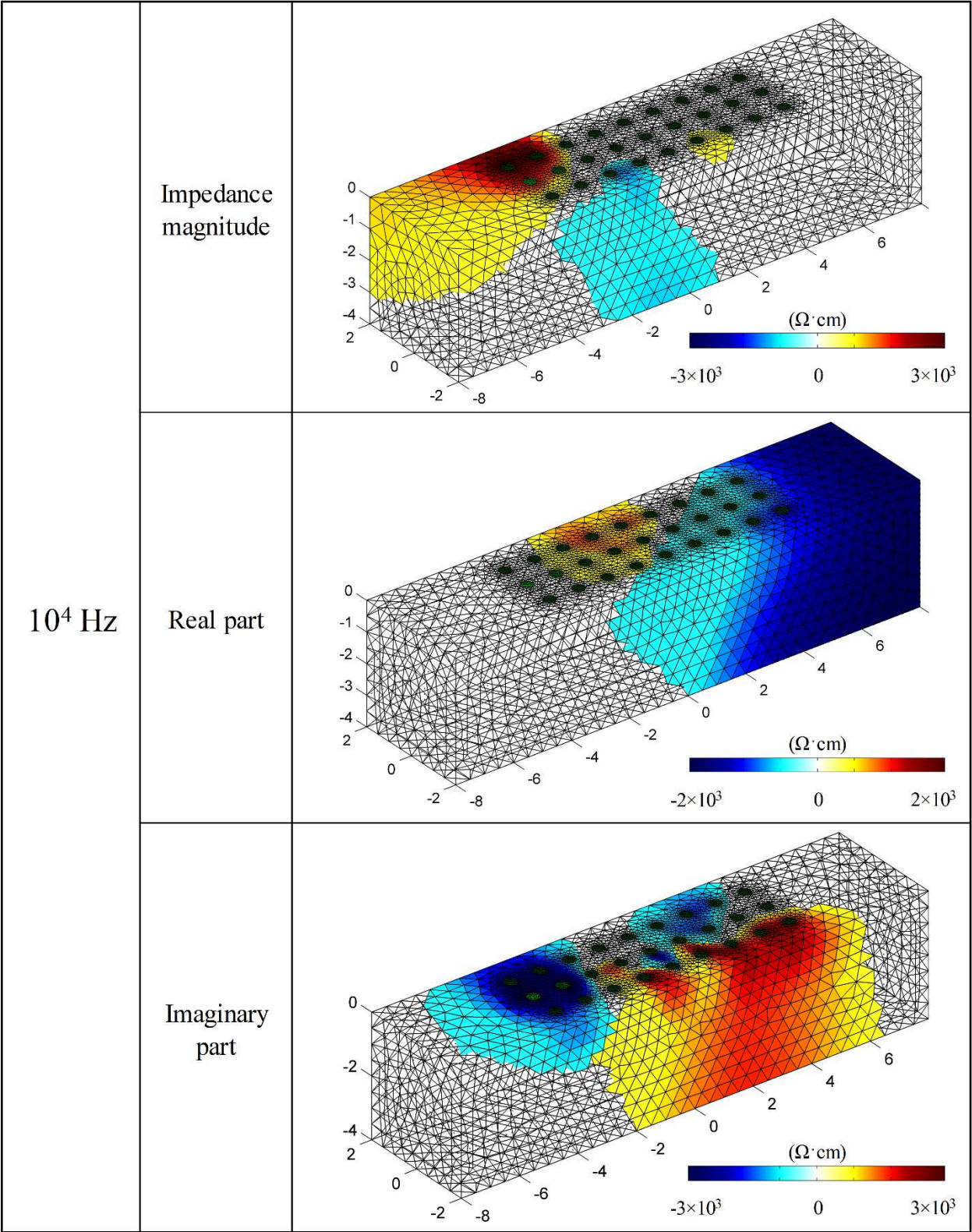


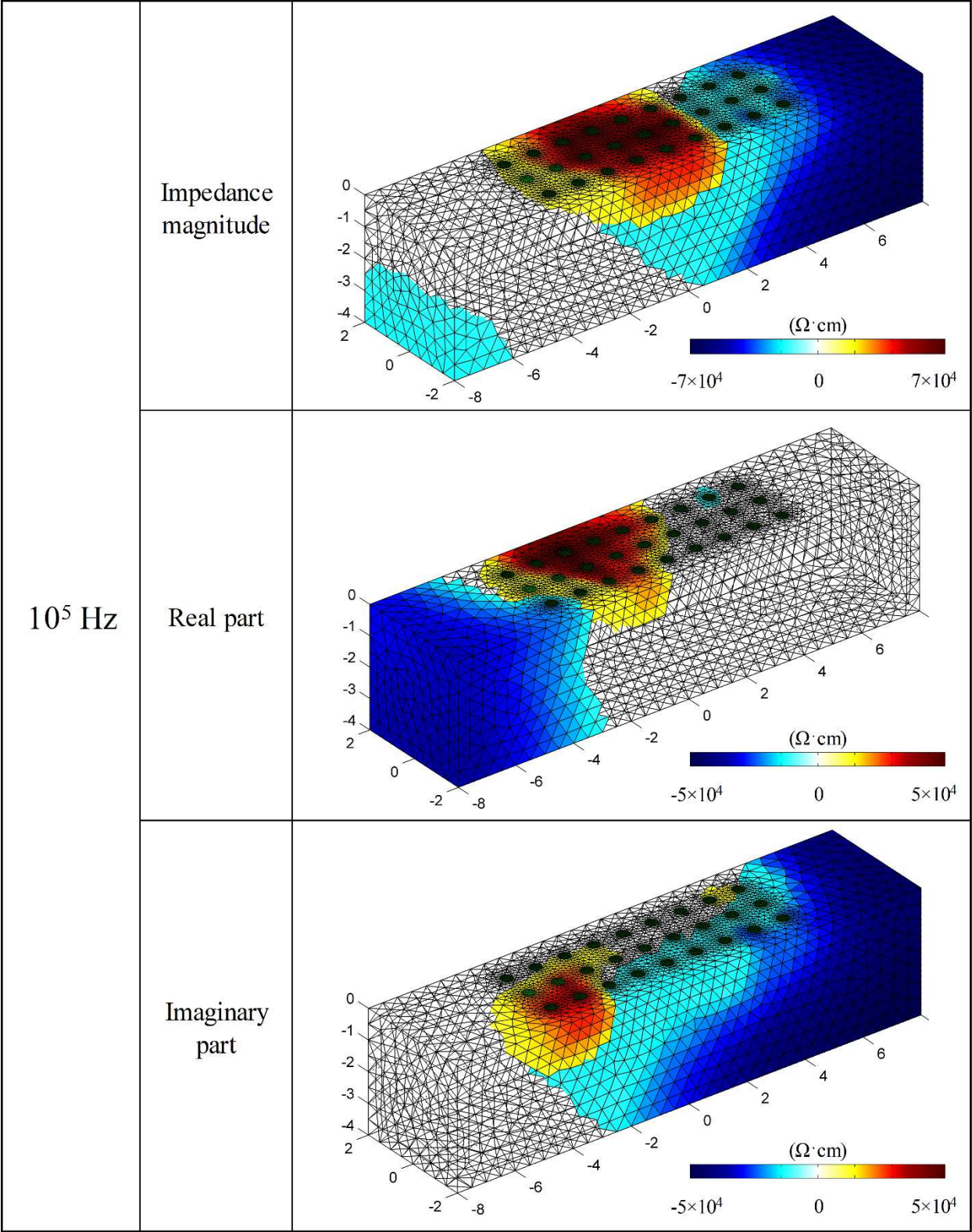












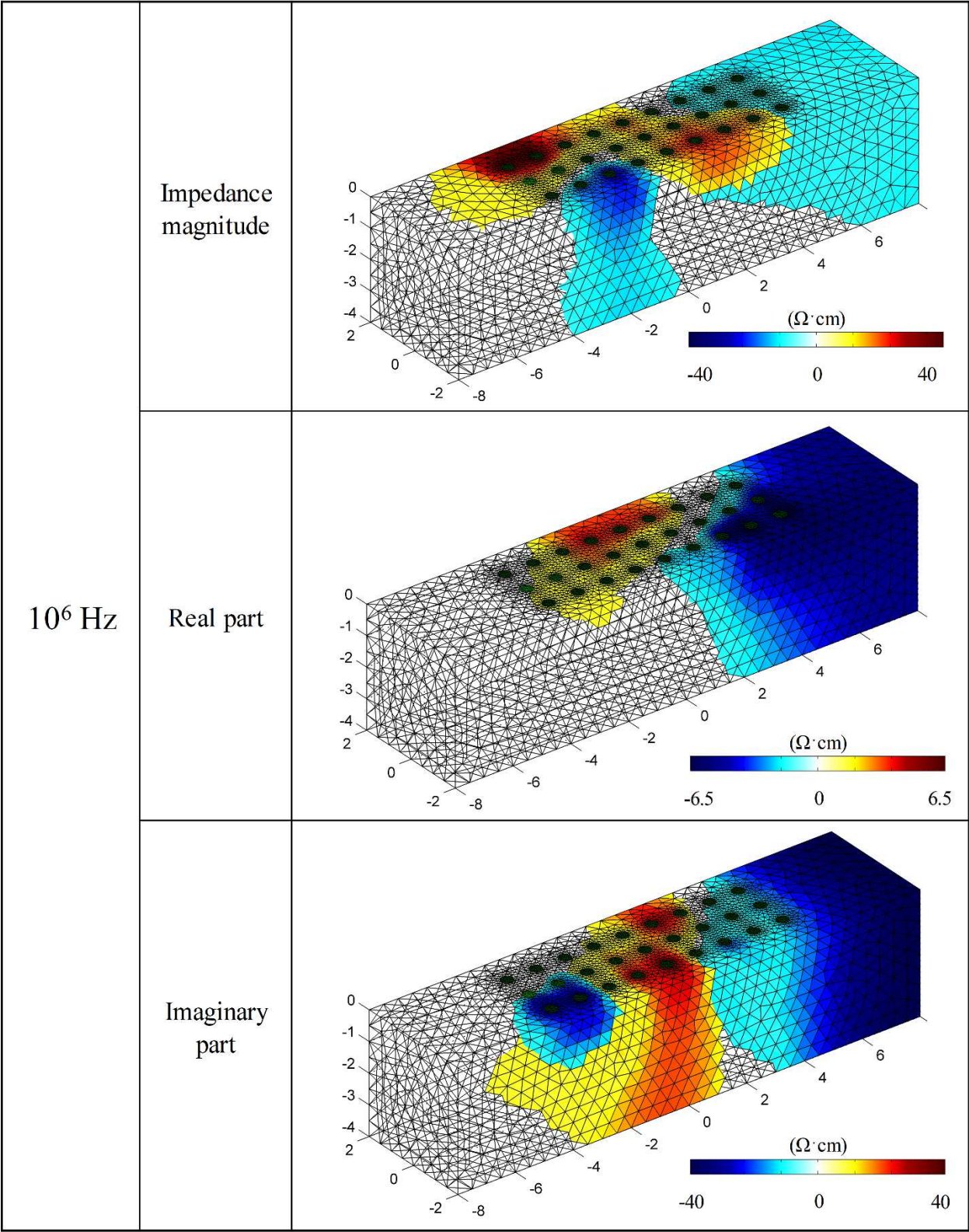


Figure 6.26 Image reconstructions of the coupon specimen (C2) with a single crack

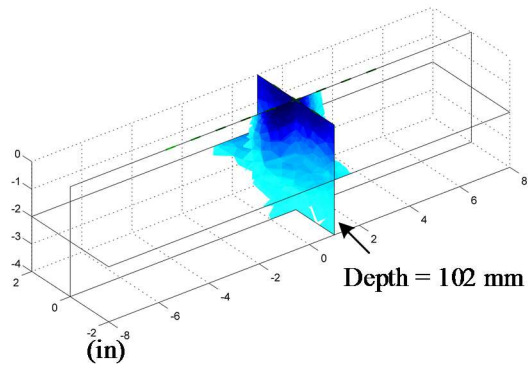


Figure 6.27 3D slice of the beam (Image reconstruction based on impedance magnitude at 1 Hz)

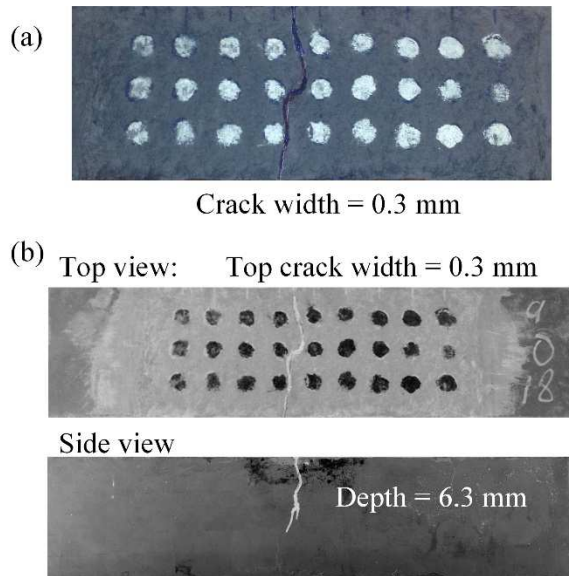
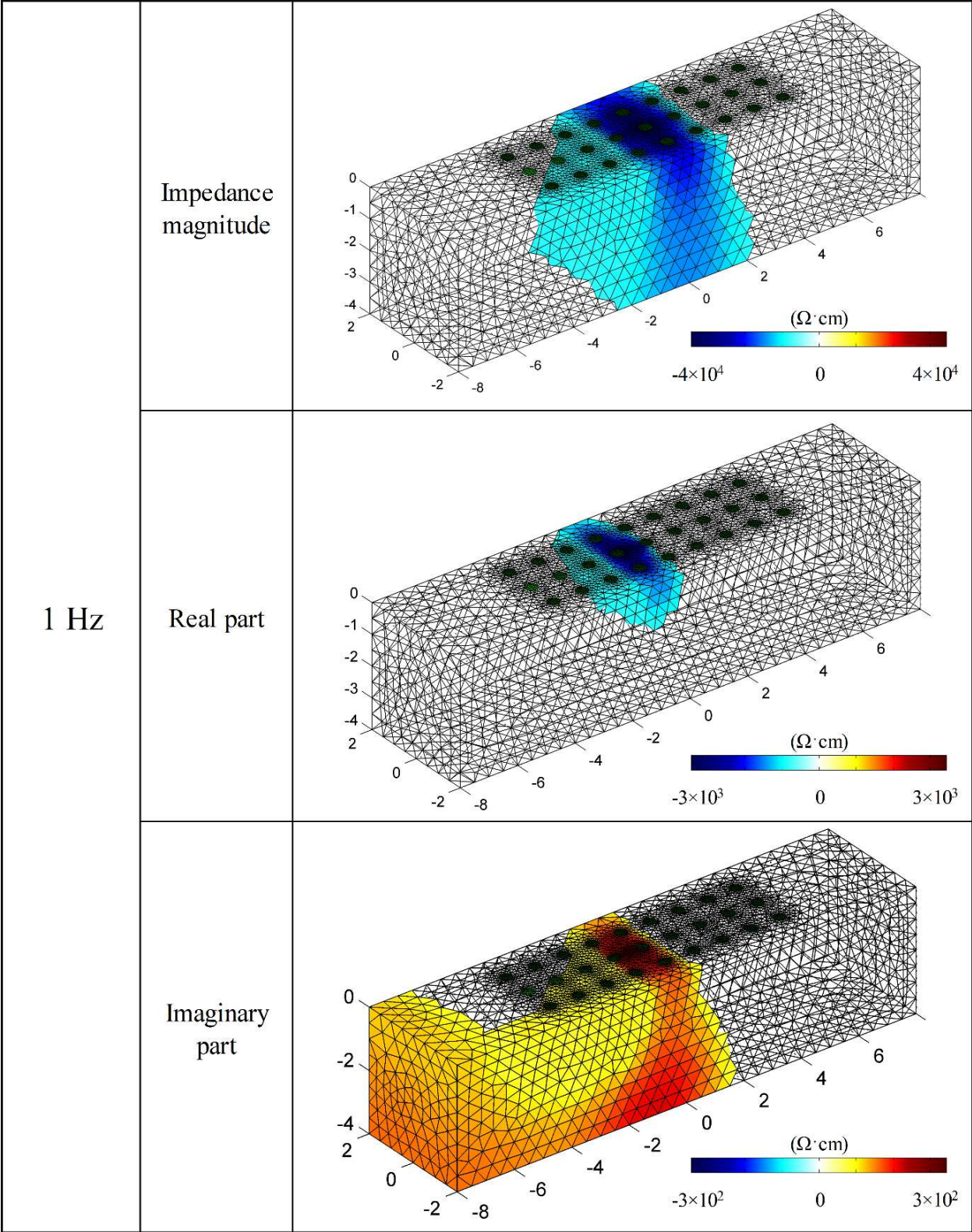
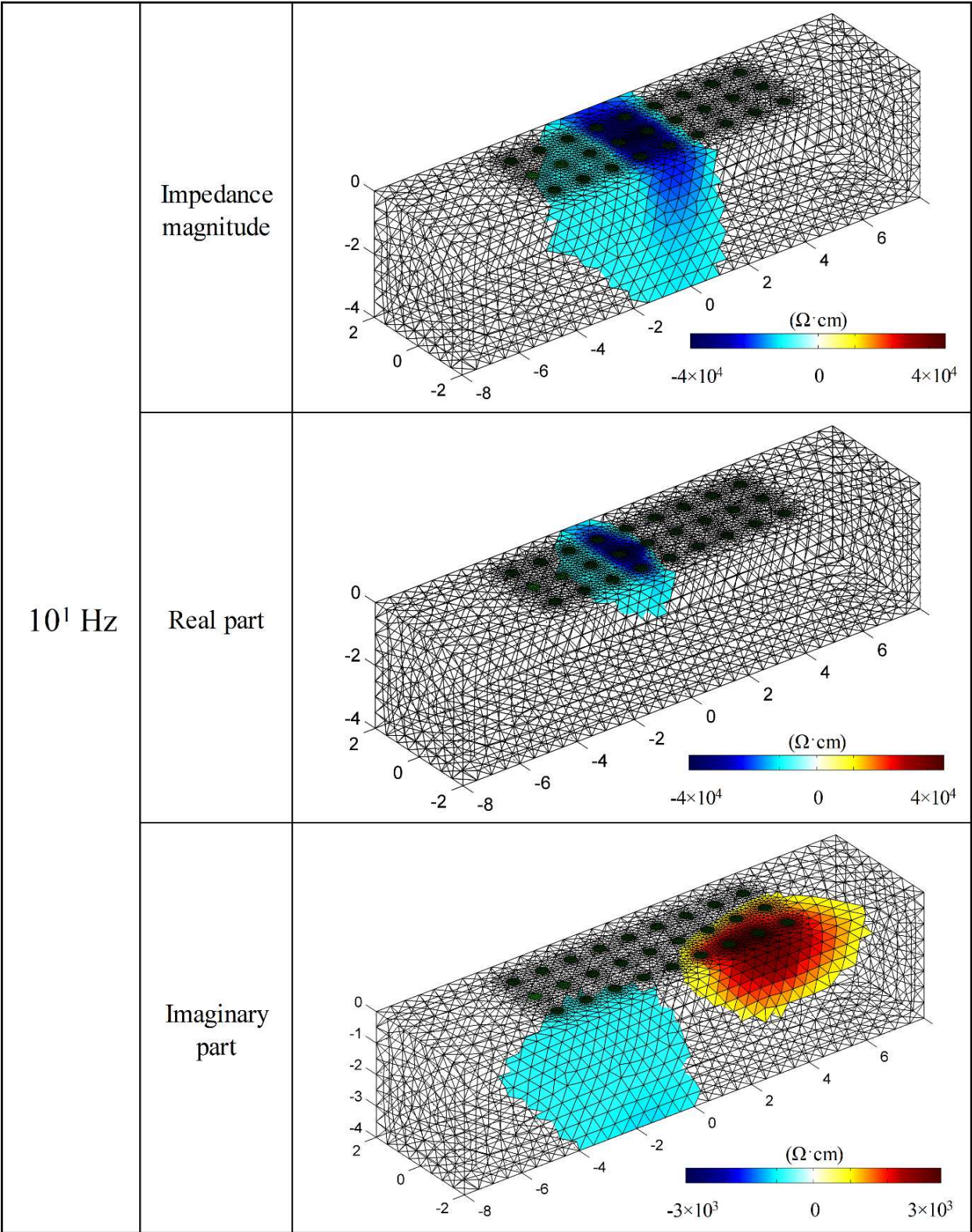
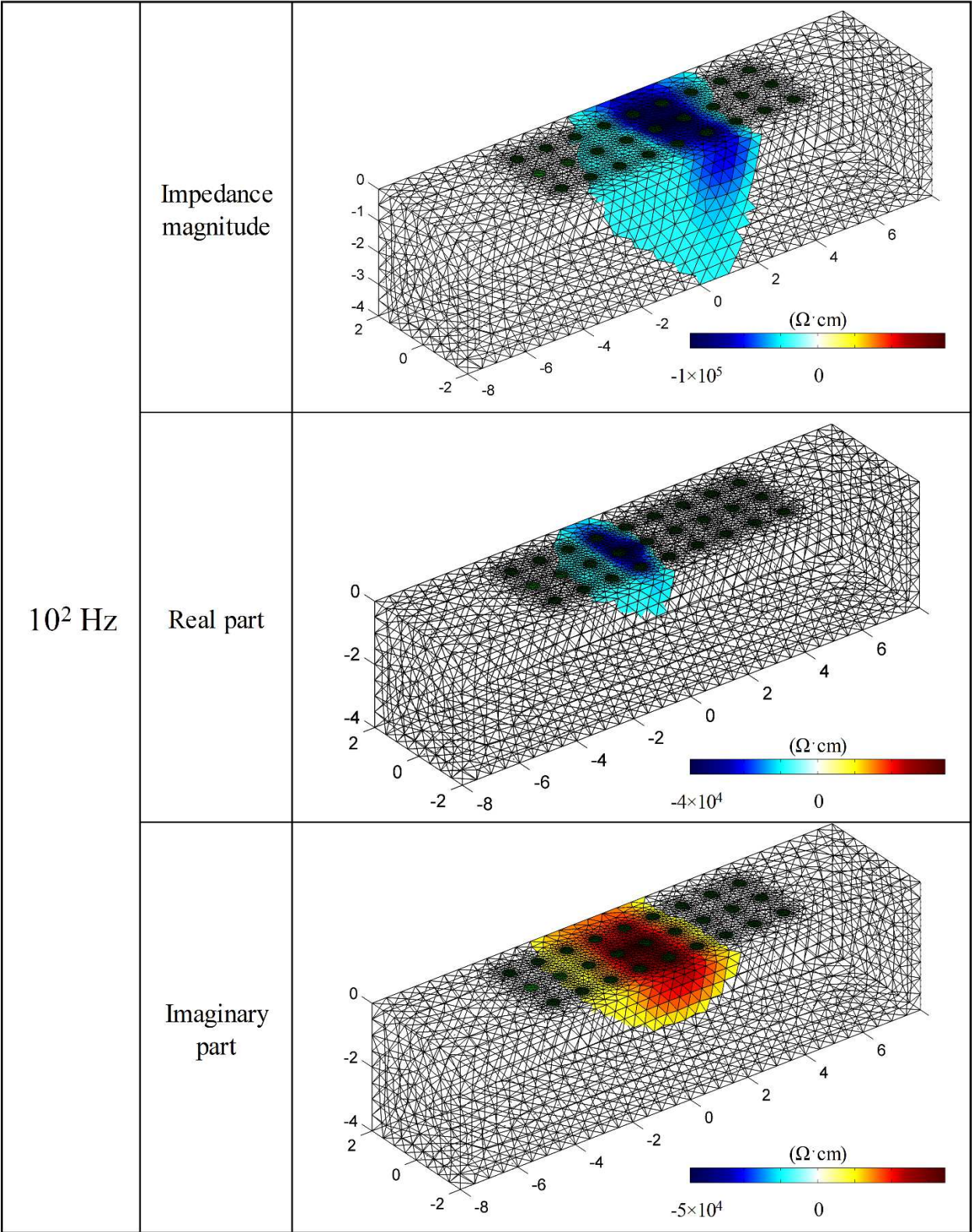


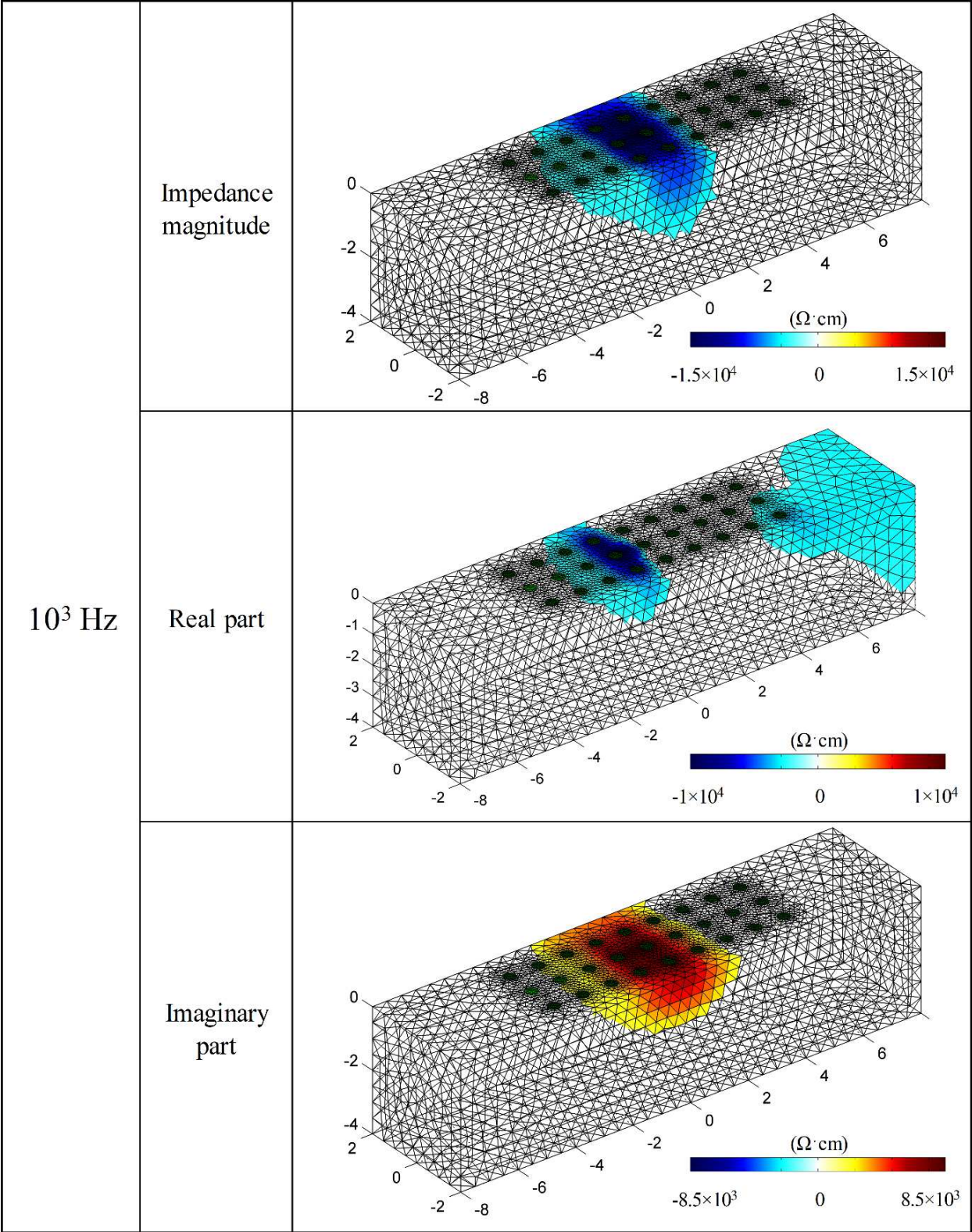
Figure 6.28 Crack details of C2 beam

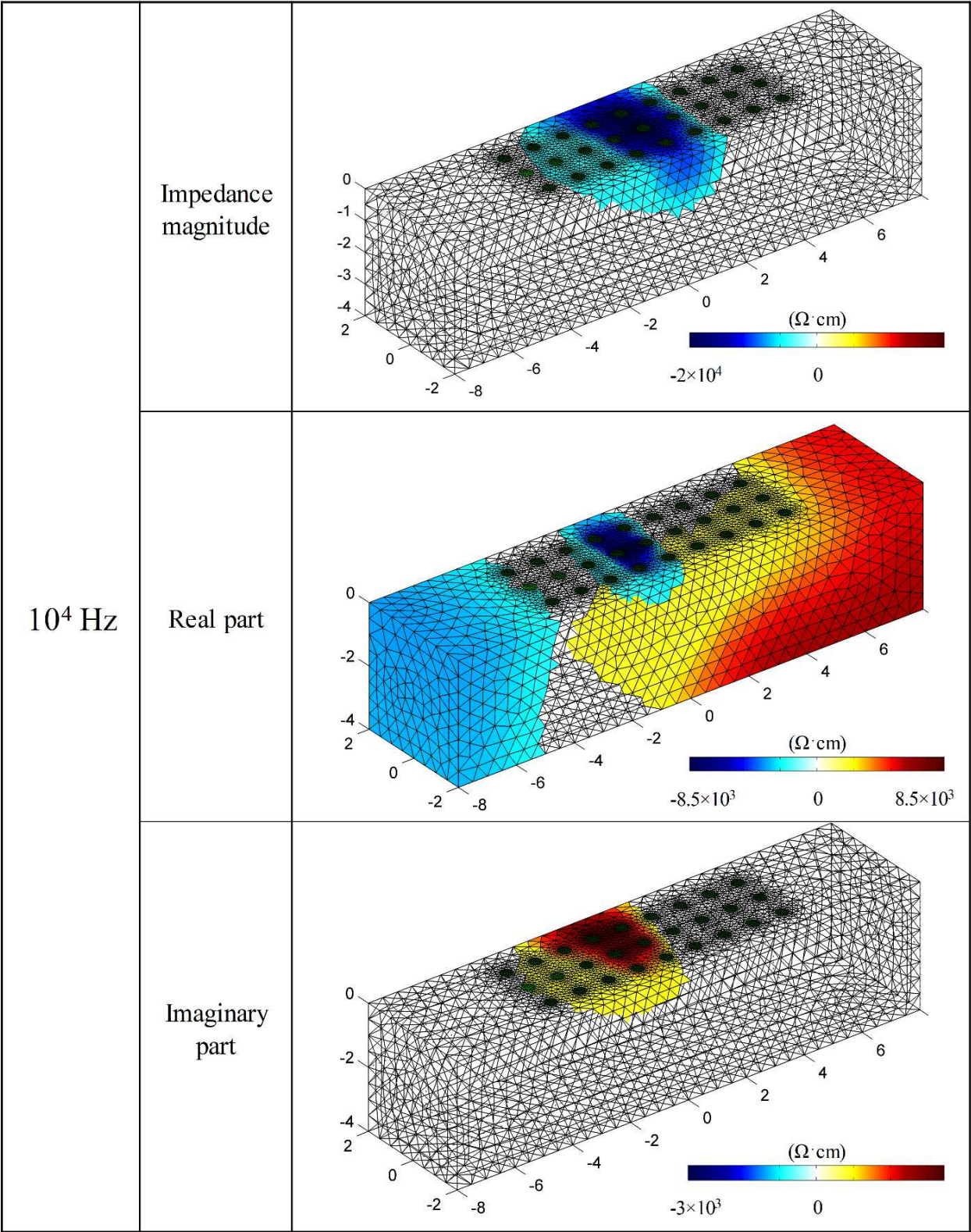


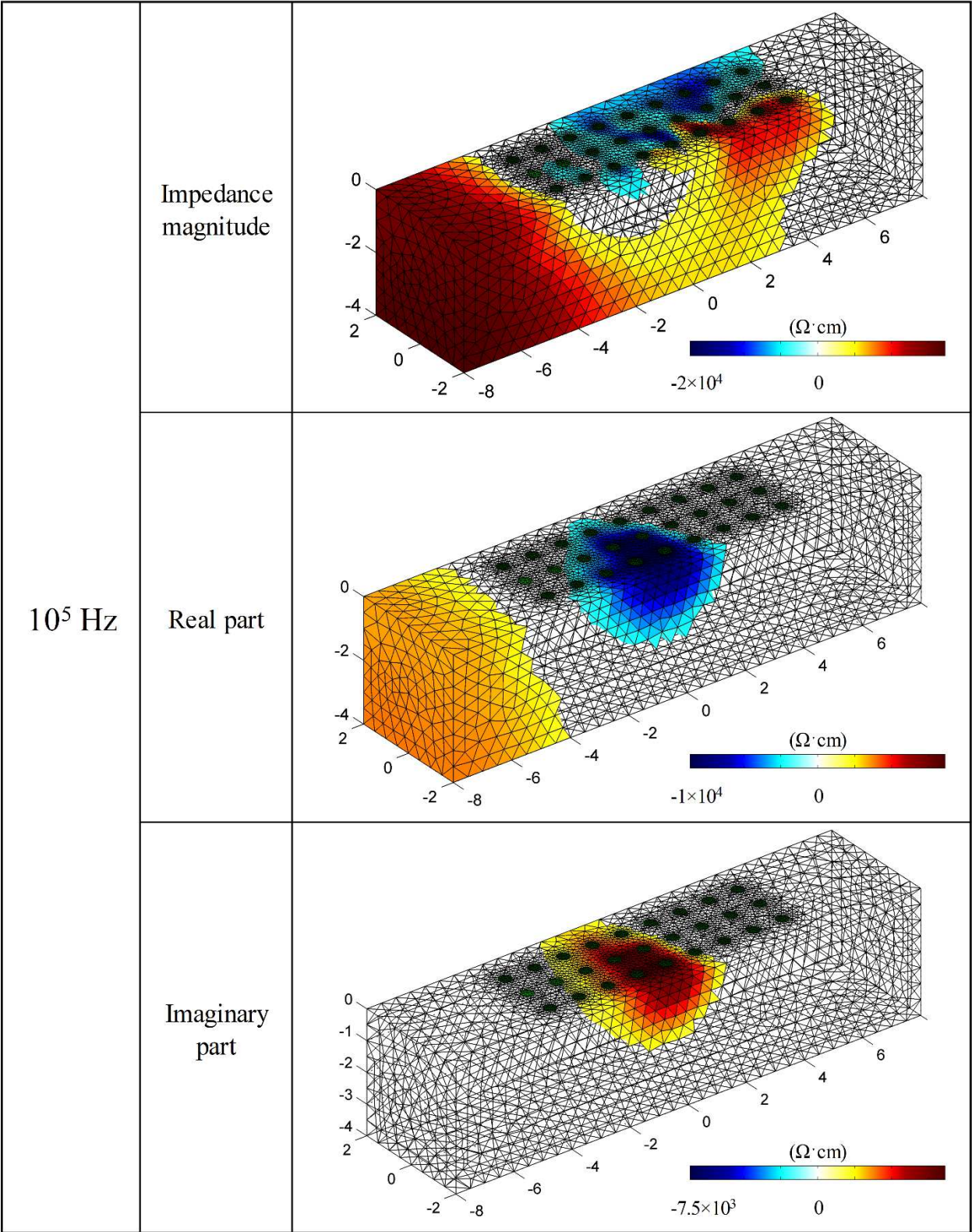












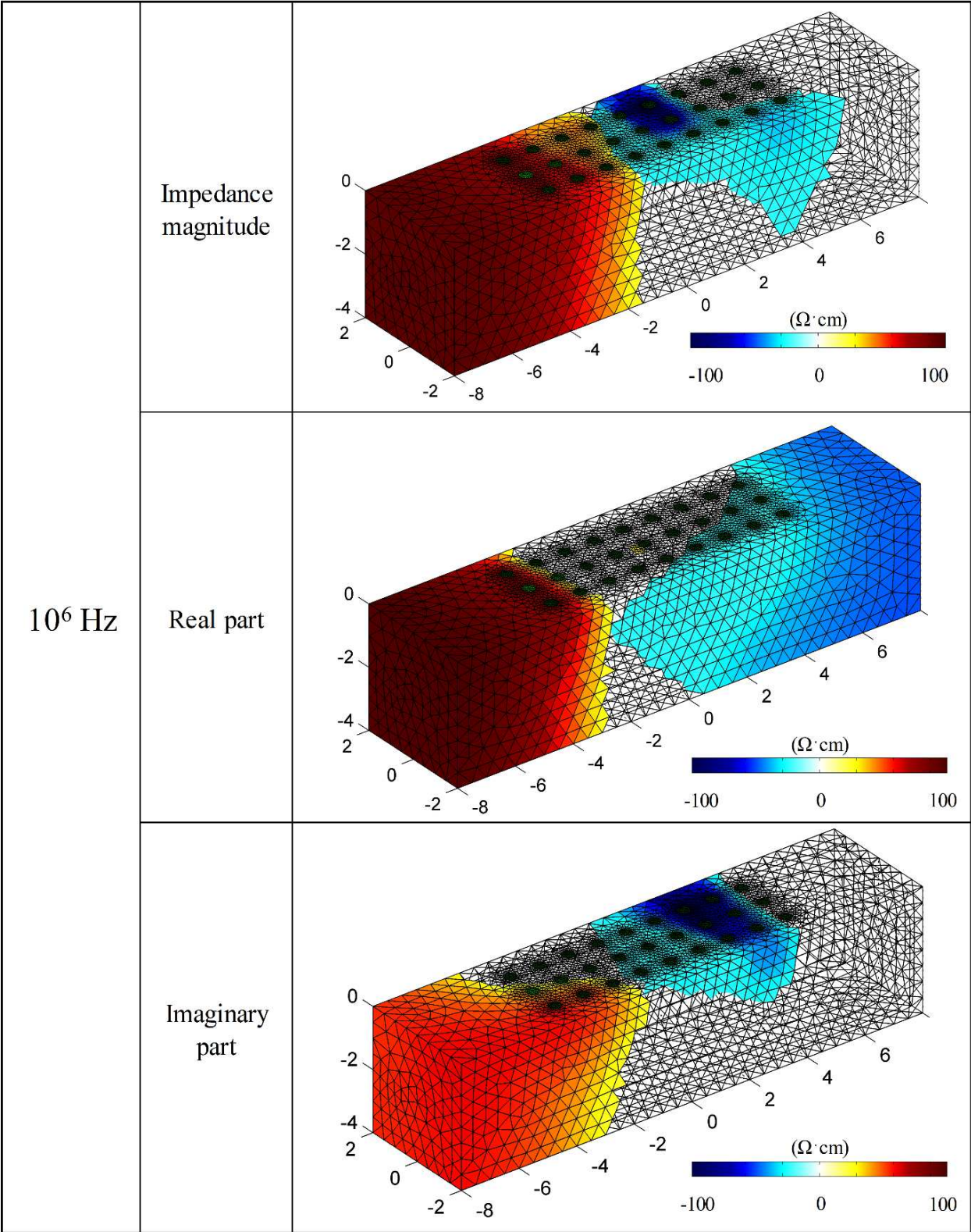


Figure 6.29 Image reconstructions of the coupon specimen (C2) with a single crack

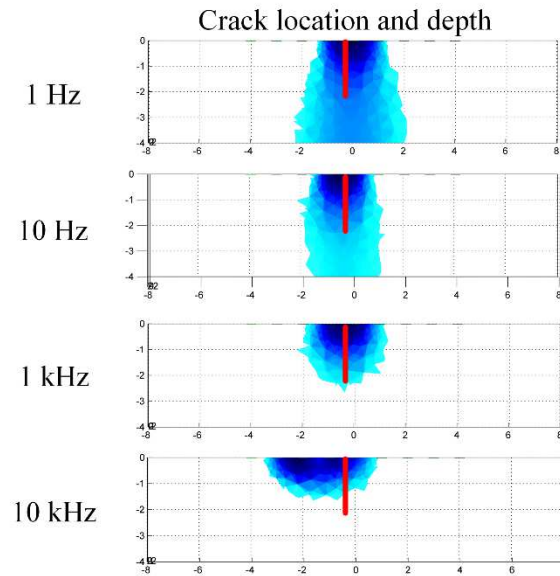


Figure 6.30. 3D slice of the image reconstructions showing crack location and depth

## 6.7 Conclusions

This study evaluates the damage sensing performance of EIT on cementitious materials with several parameters, i.e., frequency (from 1 Hz to 1 MHz), impedance type (impedance magnitude, real part of impedance, and imaginary part of impedance), damage pattern (localized damage and distributed damage), dimension (two-dimensional and three-dimensional), material (SHC and MSC), etc. The following conclusions are reached:

1. A multi-frequency EIT system is established for cementitious materials. A high-frequency range ( $10^{-2}$  Hz  $\sim$   $3.2 \times 10^7$  Hz) can be achieved. Image reconstructions based on EIT system are able to detect spatially distributed damage within cementitious materials.

2. For localized damage, image reconstructions of coupon specimen made from normal cementitious materials show damage occurrence but does not capture damage details. On the other hand, image reconstructions of MSC coupon specimen reflect the damage details. The damage location, extent, and shape are exactly imaged. At a frequency ranging from 1 Hz to 1

kHz, there is no apparent noise shown in the image reconstructions. The image reconstructions based on different impedance types do not show any difference. Increasing frequency induces more noise in the image reconstructions.

3. For distributed damage, two-dimensional image reconstructions on normal cementitious materials do not reflect the damage information at all. However, the image reconstructions of MSC clearly show the damage severity, shape, location, and extent. Despite the fact that every single crack is not identified, the distribution of multiple cracks is shown clearly. The effective frequency range is from 1 Hz to 10 kHz.

4. Three-dimensional image reconstructions of normal cementitious materials show the occurrence of the damage but do not catch the crack depth, extent, location, and severity accurately. However, for MSC, the image reconstructions clearly show the crack details. The effective frequency range is from 1 Hz to 10 kHz.

5. Although the image reconstructions based on different impedance types do not show apparent differences in two-dimensional scenarios, the three-dimensional image reconstructions based on different impedance types yield dramatically different results. Image reconstructions based on real part of impedance estimates the crack extent very accurately, but the damage depth is underestimated. On the other hand, image reconstructions based on impedance magnitude and imaginary part are able to detect the crack depth accurately. Especially, image reconstructions based on impedance magnitude show damage details clearly.

6. The three-dimensional image reconstructions are highly frequency dependent. Low-frequency current is not sensitive to deep part of the damage, while high-frequency current (1 kHz and 10 kHz) is able to propagate to the deep region of the beam and thus the damage depth estimation is more accurate.

# CHAPTER 7: SPATIAL DAMAGE SENSING IN MSCS THROUGH FREQUENCY-DIFFERENCE ELECTRICAL IMPEDANCE TOMOGRAPHY

## 7.1 Introduction

The image reconstruction of EIT or ERT is an ill-posed inverse problem. Directly solving the inverse problem based on merely change-of-state measurements is absolute imaging, which is sensitive to modeling errors and measurement noise. Difference imaging, however, is able to tolerate the modeling error [230], which requires two sets of measurements to be performed: reference state measurement and change-of-state measurement. Commonly, difference imaging is referred to as “Time-difference imaging”, because reference state measurement and change-of-state measurement are performed before and after tests.

The research of EIT or ERT on the cementitious materials started from “Time-difference” EIT or ERT. Buettner et al. [217, 218] applied ERT to monitor moisture infiltration into concrete pillars and pavement sections. Hou et al. [209, 210, 219] utilized ERT to image fiber reinforced cementitious composites (100% RH cured) loaded by axial cyclic loads and three-point bending. It is shown that with the difference imaging, the geometric propagation of dense fields of microcracks, strain-hardening, and crack localization in cementitious composites were all captured by an ERT conductivity map. Hallaji and Pour-Ghaz [222] utilized the difference imaging scheme to successfully detect and locate cracks and damage in concrete by applying sensing skin on the surface of the concrete. Also, Hallaji et al. showed that EIT is able to show the shape and position of the waterfront of nonuniform flow in the cementitious materials [224]. However, it should be noted that the reference state of the existing cementitious structures is not usually available. The electrical properties of cementitious materials are highly dependent on the

moisture content and thus, in practice, the measurements of reference state before test become invalid and unreliable once moisture content changes.

Absolute imaging does not rely on reference state measurements before the test for image reconstructions but is not as robust as difference imaging. Using absolute imaging, Karhunen et al. [220, 221] performed a feasibility study of ERT for imaging concrete samples. The results showed that the conductivity map provided reliable estimates for the size and location of cracks, the steel rebar, and the nonconductive inclusions. Hallaji et al. [223] proposed one new computational method based on absolute imaging for crack detection using the sensing skin applied on the surface of the specimen. It is indicated that the absolute imaging based on the proposed method was more successful in capturing the complex crack patterns. However, the proposed method also relies on the reference state measurements before cracking for error minimization. On the basis of the above method, Smyl [225] also successfully visualized 3D unsaturated moisture flow in the cementitious materials with discrete cracks.

Despite recent advances, knowledge gaps are evident. The current well-accepted imaging schemes are not suitable for cementitious material. For “Time-difference” imaging, the reference state is not always available. Absolute imaging is susceptible to modeling and measurement errors, and is not computationally efficient [230]. Frequency-difference EIT (fdEIT) technology is thus proposed for the cementitious materials in this study. fdEIT is an imaging scheme [231, 232] that combines both the advantages of “Time-difference” imaging and absolute imaging. Unlike “Time-difference” EIT, frequency-difference EIT requires potential measurements at two different frequencies simultaneously so that the reference state before the test is no longer needed. The measurement of one frequency is considered as the reference state, and hence the other measurement is the change-of-state.



There are fundamental questions to apply fdEIT for crack detection in cementitious materials. First, whether the frequency-dependent impedance of cracked part and non-cracked part is different enough for frequency-difference EIT or not needs to be answered. Although the frequency-dependent impedance of cementitious materials was studied in the last decades, there are merely a few studies regarding the frequency-dependent impedance of cracked part of the cementitious materials. Li and Li [233] reported the evolution of impedance (Nyquist plot) in terms of strain level of the HPRCC materials. Further studies are necessary to reveal the differences between cracked part and non-cracked part at different frequencies. Second, since the large difference between cracked materials and non-cracked materials under selected frequencies results in the higher contrast in the reconstructed images, it is necessary to study how to select the optimal frequencies.

To address these issues, four-probe electrical impedance spectroscopy was performed on cementitious materials with a single crack developing. The frequency-dependent impedance of cracked part and noncracked part was revealed for frequency-difference EIT purposes. Then a frequency different Electrical Impedance Tomography (fdEIT) system was established for the cementitious materials to detect the localized and distributed cracks in the cementitious materials. A wide frequency range was selected from 0.1 Hz to 1MHz. Frequency-difference EIT was used on MSCs for imaging the localized and distributed damage in MSCs.

## **7.2 Frequency-dependent Impedance of Cracking**

One series of tests was devised to evaluate the frequency-dependent impedance cementitious materials. As normal cementitious materials possess high resistivity, applied electrical current could not sufficiently propagate through the entire material, which limits the resolution of image reconstructions. Therefore, in this chapter, MSCs were used.

### 7.2.1 Materials and specimens

Cementitious materials C1 and C2 were prepared based on Table 6.2. The material preparation and sample details can be found in Section 6.5.1.

Two types of specimens were used: (1) coupon specimens with dimensions of 161.5 mm  $\times$  51 mm  $\times$  12.5 mm for uniaxial direct tension tests, and (2) beam specimens with a dimension of 406 mm  $\times$  102 mm  $\times$  102 mm for flexure tests. Coupon specimens were made from C1 and C2, while the beam specimen was made from C2.

### 7.2.2. Single crack opening test with impedance measurements

One coupon specimen (161.5 mm  $\times$  51 mm  $\times$  12.5 mm) was notched along its centerline perpendicular to the loading axis for the single crack opening test, as shown in **Figure 7.1**. The notch width is 0.3 mm running continuously all around the specimen with depths of 10 mm on the lateral sides and 2mm on the other two sides. Due to stress concentration, the notch forces the crack to happen in this section.

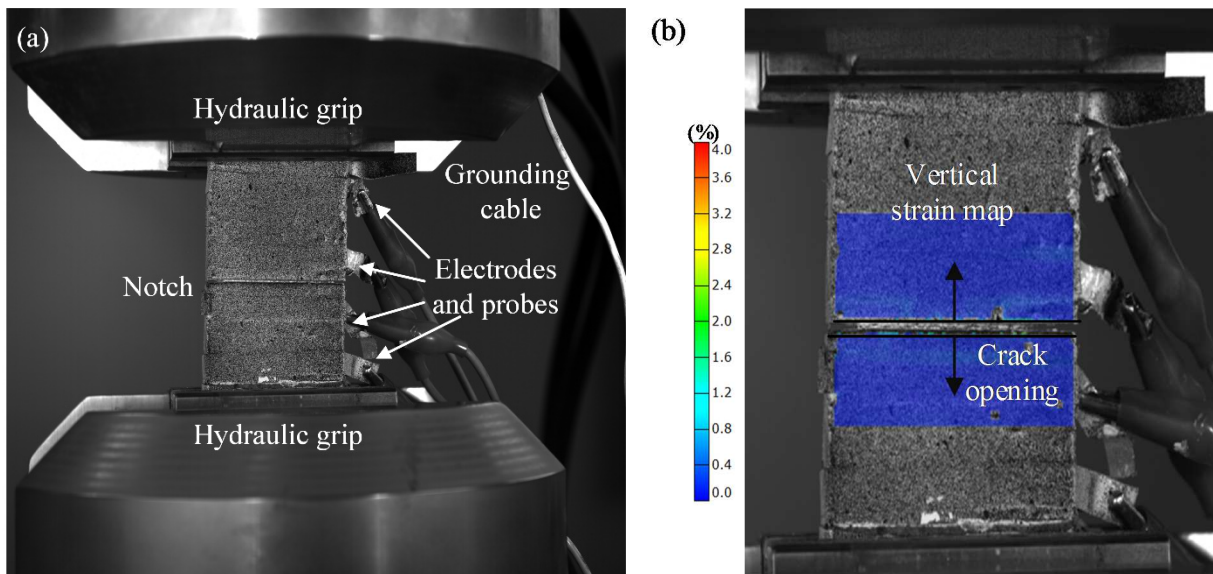


Figure 7.1 Single crack opening test on C1 with four-probe impedance measurement: (a) test setup; (b) DIC results showed crack opening

As shown in Figure 7.1(a), both ends of the specimen were gripped by the hydraulic grip. An ARAMIS Digital Image Correlation (DIC) system was set up in front of the hydraulic material testing frame for accurate single crack opening measurement. DIC system included a pair of non-perpendicular 12-megapixel charge-coupled device (CCD) cameras with 24 mm of focal length lenses. External fluorescent light sources were used to maintain constant optimum illumination of the surface of the specimen. Figure 7.1(a) is the high-resolution image captured by the DIC system. The specimen surface was painted with black speckles so that the movement of the speckles during loading can be tracked by DIC system. Figure 7.1(b) shows a typical processed image of DIC on single crack opening test. The blue area is the vertical strain map on the surface of the specimen. It is shown that when a single crack occurred in the notch, there was no strain concentration (no other colors except blue) on the specimen surface. Via measuring the relative movement of the notch edge highlighted as two black lines in Figure 7.1(b), the crack opening was captured accurately. For one single crack opening test, a total of 250 images were captured.

At different levels of crack opening, four-probe EIS was performed with an impedance analyzer to reveal the frequency-dependent electrical responses of the specimen. Four copper electrodes (Figure 7.1) with an acrylic conductive adhesive were attached to the surfaces of the specimen with conductive silver colloidal paste applied first. The silver colloidal paste was used to smooth the specimen surface and minimize the interfacial impedance. The frequency-dependent alternating current was injected into the specimen via two outer electrodes, and simultaneously in-situ voltages (amplitude and phase difference) were measured via two inner electrodes. The distances between the inner electrodes and the outer electrodes were three times larger than that of the specimen thickness to allow the current to be uniformly distributed within

the specimen between two inner electrodes and perpendicular to the inner electrodes. The EIS measurements were carried out with a 100 mv amplitude excitation, which was slight enough to ensure that the material system was a linear system. Impedance measurements (magnitude and phase shift) were performed with 35 data per decade ranging from 0.1 Hz to 1 MHz. One series of measurements took less than 10 minutes. As two inner electrodes were located close to the notch edge, change of the impedance was due to the crack opening. The impedance (impedance magnitude and phase shift) as a function of frequency was then plotted, yielding the impedance spectrum in terms of a Bode plot. The complex components of the impedance (real part of impedance  $Z_r$  and imaginary part of impedance  $Z_m$ ) were computed on the basis of impedance magnitude  $|Z|$  and phase shift  $\theta$  (Eq.(6.13)).

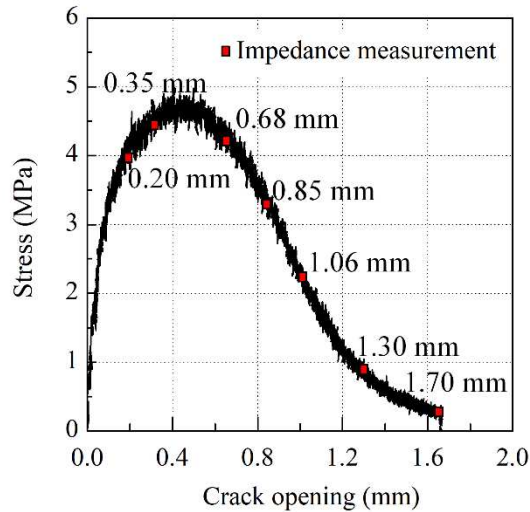


Figure 7.2 Single crack opening behavior ( $\sigma \sim \delta$  relation) of C1. EIS was performed at different crack opening values as marked on the curve

Figure 7.2 shows the  $\sigma \sim \delta$  relation of C1. At different crack openings, the uniaxial tension test was paused to allow the EIS scan. In total, there were eight EIS measurements, including one scan before the test, and seven scans during the test marked by red points on the  $\sigma \sim \delta$  curve.

### 7.2.3 Frequency-dependent impedance

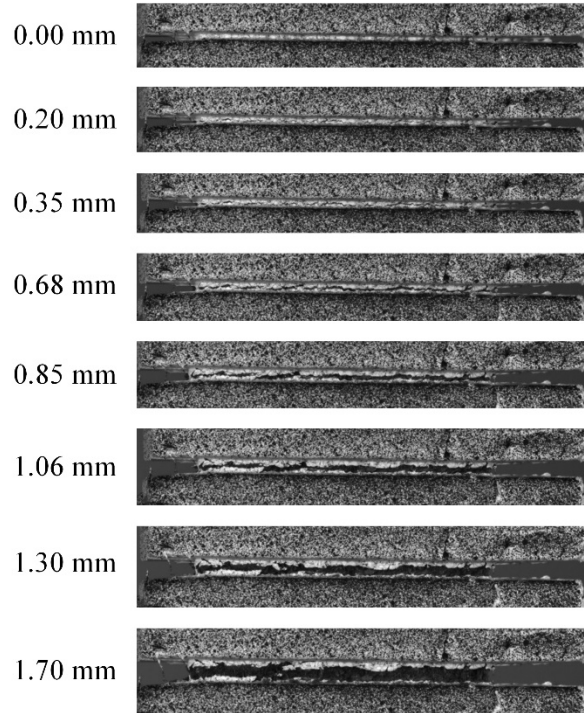


Figure 7.3 High-resolution images of a single crack opening

Figure 7.3 shows the high-resolution images ( $4096 \times 3072$ ) of the single crack opening test described above. The raw images captured via the DIC system were cropped to focus on the notched area of the specimen. There was a total of eight crack opening levels shown in the figure to represent different stages of a single crack opening. At different crack opening levels, the Bode plots of impedance spectra of the material-crack system are shown in Figure 7.4. The impedance magnitude, real part of impedance, and imaginary part of impedance in terms of frequency ranging from 0.1 Hz to 1 MHz are plotted in Figure 7.4 (a), (b), and (c), respectively, with the x axis (frequency) in the logarithmic scale. The Bode plots of the impedance magnitude and the real part of impedance followed same decreasing trend with increasing frequency, except that the real part of impedance is slightly lower than impedance magnitude at each frequency. However, the imaginary part of impedance showed a different trend. As the phase degree for a

cementitious material is from  $0^\circ$  to  $-90^\circ$ , the imaginary part of impedance is negative. At a low-frequency range, the imaginary part of impedance remained at a low level, indicating the absence of capacitance effect. Thereafter, the imaginary part of impedance reached a peak at a high-frequency and decreased afterward, suggesting the matrix-crack system can be represented by capacitance effect with one relaxation time in the high-frequency range.

For the impedance magnitude and the real part of impedance, as the crack opening increases, the impedance value at each frequency increases correspondingly. At the same time, the decreasing trend with increasing frequency becomes more apparent with the increasing crack opening. For the imaginary part, the absolute value at each frequency also increases with increasing crack opening. It should be noted that, for imaginary part at 0.00 mm and 0.20 mm, positive values were observed after  $10^5$  Hz, suggesting the occurrence of high-frequency inductance. It is because of this, for C1 without damage, high-frequency AC ( $>10^5$  Hz) penetrated the specimen and captured the inductance formed by the measurement circuits. With increasing damage level, the high-frequency AC ( $>10^5$  Hz) was not able to penetrate the specimen and thus reflected the matrix-crack system information only without any high-frequency inductance. The significant change of imaginary part of impedance due to increasing crack opening occurs at a frequency range from  $10^3$  Hz to  $10^6$  Hz, suggesting that capacitance effect of C1 was well expressed in the high-frequency range. The peak of the imaginary part of impedance moves from high-frequency to relatively low-frequency as the crack opening increases, indicating that the capacitance effect of the material-crack system becomes more evident as more damage was involved in the system.

To be specific, one typical cracking scenario (real part of impedances with crack openings of 0.00 mm and 0.85 mm) in Figure 7.4 is plotted in Figure 7.5 as one example. It

should be noted that the observations from this figure can be applied to other cracking scenarios. It is observed in Figure 7.5 that cracking in C1 with a crack opening of 0.85 mm leads to a significant increase in the real part of impedance at all frequencies.

This increase is highly dependent on the frequency, and higher frequencies induce lower increase in the real part of impedance. This trend is prominent in the high-frequency range (from 1 kHz to 1 MHz). Two specific frequencies ( $f_1$  and  $f_2$ ) induce two increases in the real part,  $\delta_{t,1}$  and  $\delta_{t,2}$  ( $\delta_{t,1} > \delta_{t,2}$ ). For Time-difference EIT, two measurements were performed before and after cracking at one single frequency. The differences captured by the two measurements are due to the increase of the real part at one frequency, like  $\delta_{t,1}$  or  $\delta_{t,2}$ . Therefore, the image reconstructions based on Time-difference EIT aim to reflect the contrast between cracked part and non-cracked part of the materials, using the differences in the two measurements. On the contrary, frequency-difference EIT is based on the differences between two increases, which is  $\delta_{t,1} - \delta_{t,2}$ . Instead of performing two measurements before and after cracking, EIT scans were conducted on the cracked sample at two different frequencies, say,  $f_1$  and  $f_2$ . At a frequency of  $f_1$ , the impedance of the cracked part is  $|Z|_{0.00,1}$  and the impedance of the bulk material is  $|Z|_{0.85,1}$ . At a frequency of  $f_2$ , the impedance of the cracked part is  $|Z|_{0.00,2}$  and the impedance of the non-cracked part is  $|Z|_{0.85,2}$ . Since the difference between  $|Z|_{0.00,2}$  and  $|Z|_{0.00,1}$  is insignificant, the differences between two measurements mostly result from  $\delta_{t,1} - \delta_{t,2}$ .

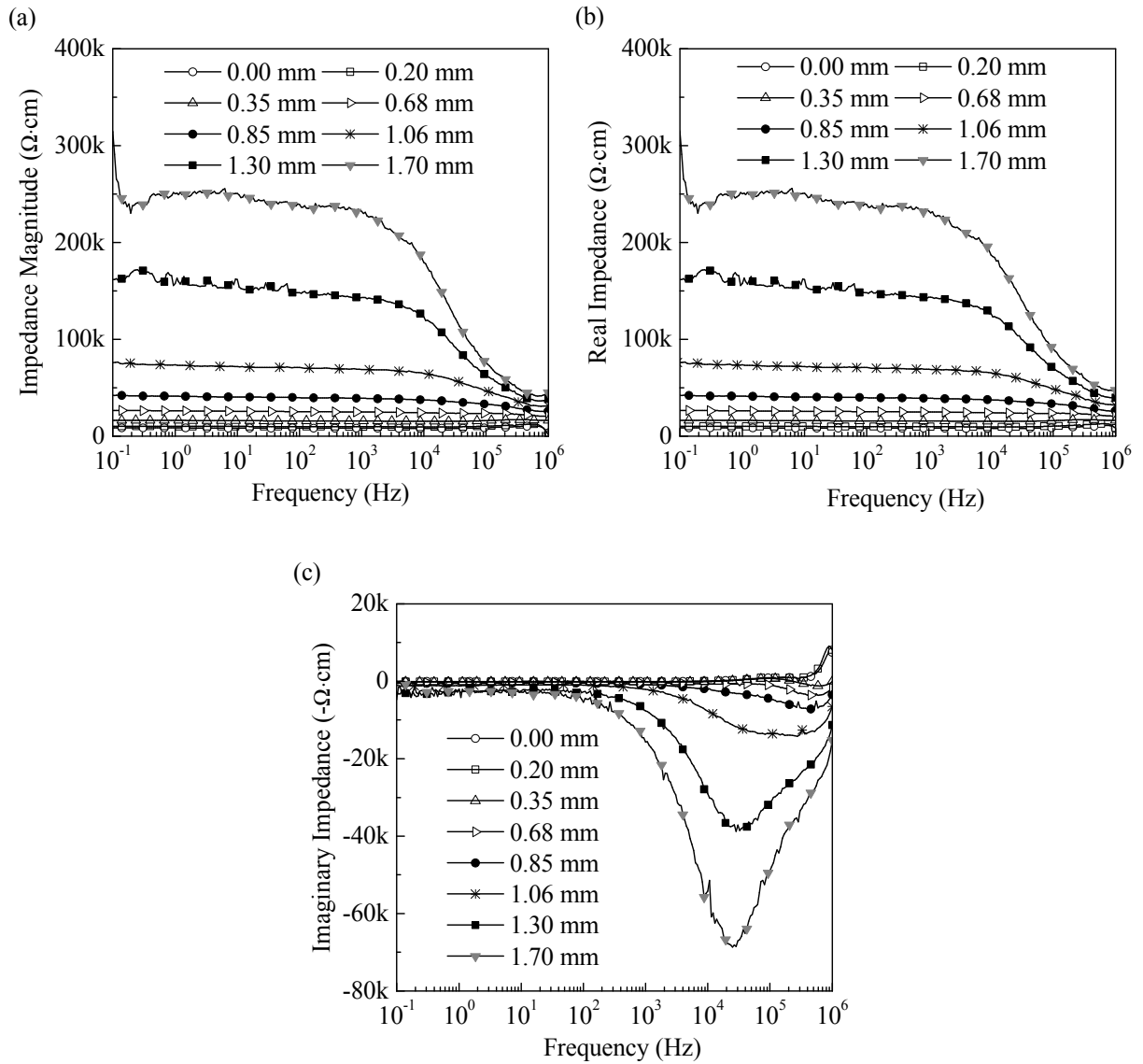


Figure 7.4 Frequency-dependent behaviors of the impedance with crack opening increases: (a) impedance magnitude; (b) real part of impedance; (c) imaginary part of impedance

In order to validate whether frequency-difference EIT can be applied on C1 with different crack openings, a change parameter ( $\xi$ ) was proposed (Eq.(7.1)). In Eq. (7.1),  $Z_{i,f}$  stands for impedance magnitude  $|Z|$ , the real part of impedance  $Z_r$ , or the imaginary part of impedance  $Z_m$  with the crack opening of  $i$  mm at the frequency of  $f$  Hz ( $0.1 \text{ Hz} \leq f < 1 \text{ MHz}$ ).



$$\xi = \frac{Z_{i,f} - Z_{0.00,f}}{Z_{i,0.1} - Z_{0.00,0.1}} \quad (7.1)$$

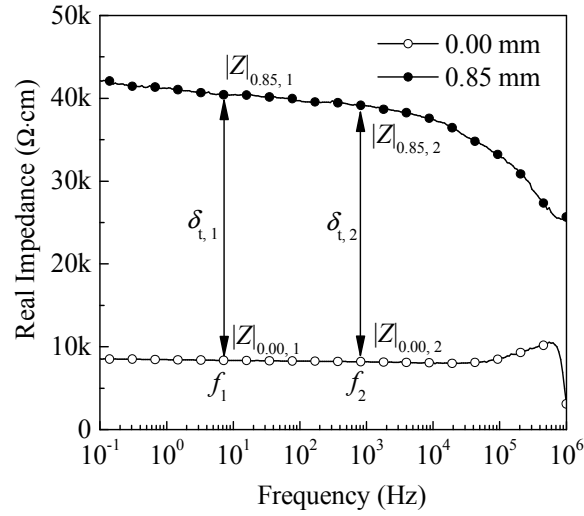
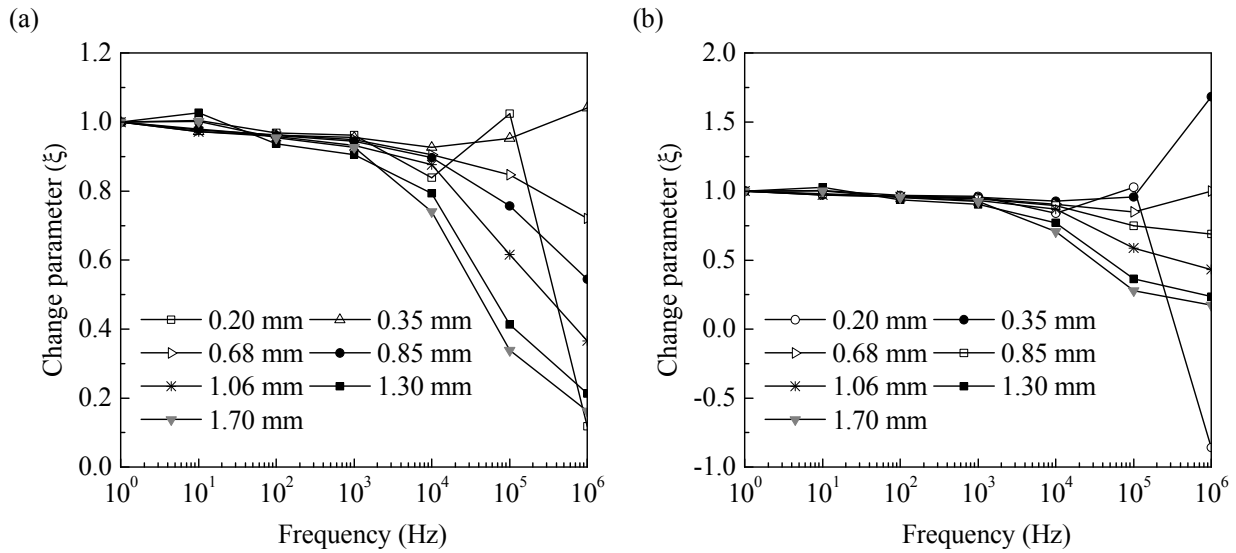


Figure 7.5 Frequency-dependent real part of impedances measured with crack openings of 0.00 mm and 0.85 mm



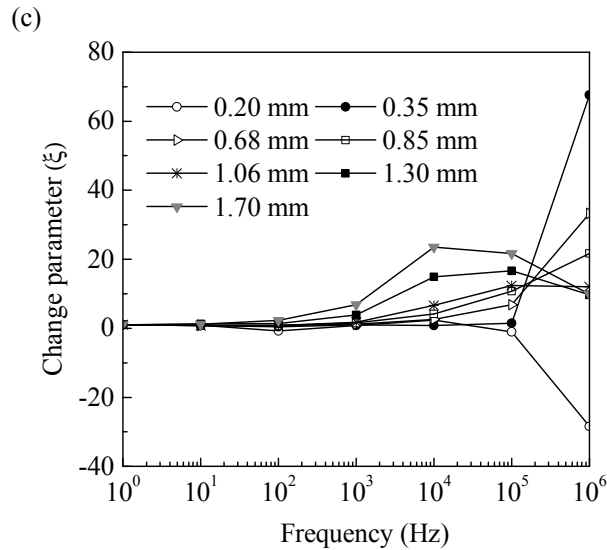


Figure 7.6 The change parameter ( $\zeta$ ) of different crack openings at different frequencies: (a) impedance magnitude; (b) real part; (c) imaginary part

For each frequency at each crack opening, a change parameter ( $\zeta$ ) can be calculated. If two change parameters at two different frequencies are different, the selected two frequencies are able to provide contrast between the cracked part and non-cracked part. Figure 7.6 plots the change parameters calculated for the impedance magnitude, the real part, and the imaginary part at seven frequencies (1 Hz, 10 Hz, 100 Hz, 1 kHz, 10 kHz, 100 kHz, and 1 MHz). Due to long measurement time, 0.1 Hz was not used. The change parameter is frequency-dependent and crack opening-dependent. For any selected two frequencies, the change parameters at one crack opening are different. Especially, a pair of frequencies where one is from the low-frequency range (1 Hz ~ 1 kHz) and one is from the high-frequency range (1 kHz ~ 1 MHz) show the significantly different change parameter. Figure 7.6 also reveals that, at one frequency, the change parameter with the larger crack opening shows a higher value, suggesting that larger crack opening induces more contrast between the cracked part and non-cracked part.

## 7.3 Frequency-difference EIT Test and Image Reconstructions

### 7.3.1 Frequency-difference EIT system for cementitious materials

An experimental frequency-difference EIT system requires a precise current source, a voltage measurement, a matrix switch, and a robust domain-to-electrode contact (Figure 7.7). In this study, an impedance analyzer was adopted to inject alternating current with different frequencies and perform voltage measurements (amplitude and phase difference). A National Instrument matrix switch ( $4 \times 64$ ) was utilized to switch the current injection and voltage measurement channels along the boundary of the measurement domain. The impedance analyzer and the matrix switch were controlled via LabVIEW. The switch was commanded to interrogate the specimens by injecting alternating current across a pair of adjacent boundary electrodes, while the boundary voltages were measured at all other remaining boundary electrodes.

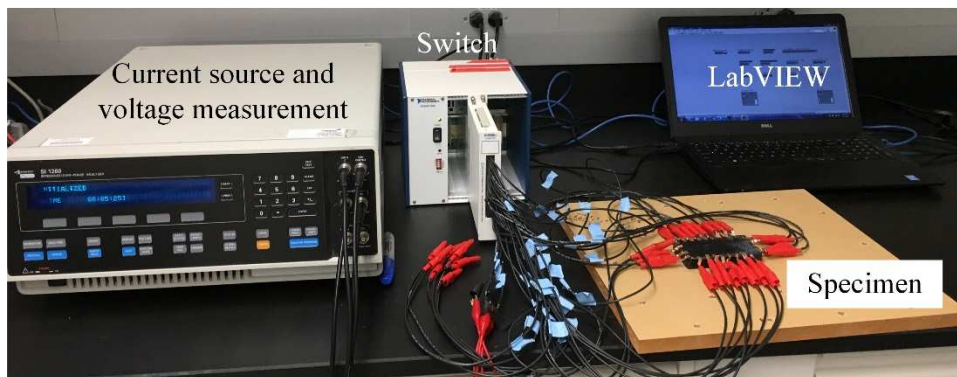


Figure 7.7 Frequency-difference Electrical Impedance Tomography test setup in this study

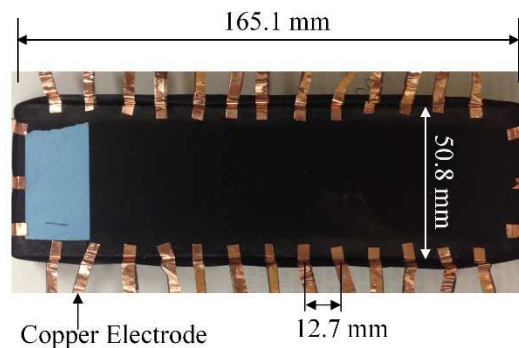


Figure 7.8 Electrode setup on the coupon specimen

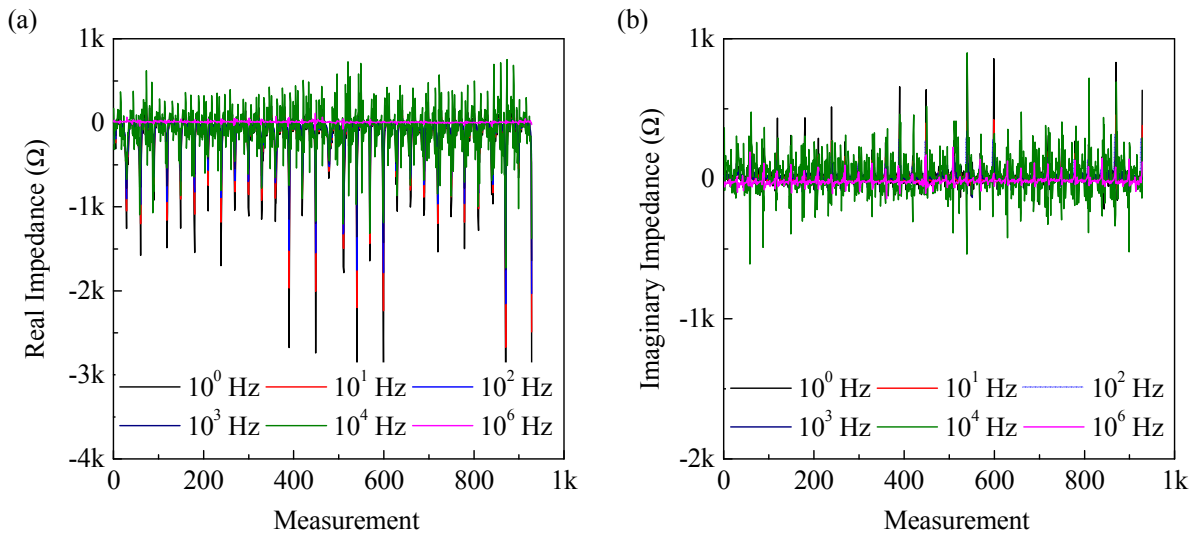


Figure 7.9 Measured frequency-dependent impedance data based on established EIT system: (a) real part of impedance; (b) imaginary part of impedance

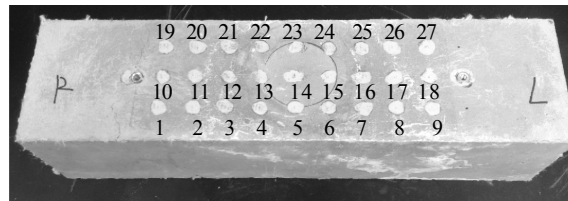


Figure 7.10 Beam specimen with 27 electrodes on one single side

Figure 7.8 shows the electrode setup on the coupon specimen. A total of 32 electrodes were installed on the side edge of the specimen. There were 13 electrodes on the long edge of the specimen, with a distance between two adjacent electrodes of 12.7 mm. For the short edge of the specimen, three electrodes were installed with a distance between two adjacent electrodes of 10 mm. An electrical impedance tomography scan was conducted on the coupon specimen following a traditional adjacent stimulation and measurement pattern, where current was injected via two adjacent electrodes, and the voltage was measured via adjacent pairs of the other electrodes. Therefore, there was a total of  $32 \times 30 = 928$  measurements. Figure 7.9 plots the

typical EIT measurements on a coupon specimen without any cracks. The frequency-dependent real part of impedance and imaginary part of impedance were shown at different frequencies (1 Hz, 10 Hz, 100 Hz, 1 kHz, 10 kHz, 1 MHz). It should be mentioned that the measurements at 100 kHz were not plotted due to presence of large amount of noise. for too much noise. The measurement data showed lower magnitude with increasing frequency for both real part and imaginary part of impedance. Especially, at a frequency of 1 MHz, the amplitude is as low as a constant line compared with the other frequencies.

Figure 7.10 shows the electrode setup on a beam specimen. 27 electrodes were placed in the middle part of the beam in 3 rows and 9 columns. The diameter of the electrode is 1 cm and the distance between adjacent rows and columns is 25.4 mm. It should be noted that the electrodes were installed on the tension side of the beam for the purpose of detecting the damage depth within the beam. The stimulation and measurement pattern follow the same trend as the adjacent pattern: when current injected through one pair of two adjacent electrodes, like, 1~2, the voltage measurement was performed via the other electrodes, i.e., 3~4, 4~5, 5~6, etc. With current injected through all electrodes, there was a total of 648 measurements.

### *7.3.2 Test methodology*

#### *Validation tests*

The following tests were conducted to validate the applicability of the established frequency-difference EIT system. One coupon specimen with 24 electrodes around the specimen was selected. The specimen was cut into two pieces and then frequency-difference EIT measurement was performed to collect the data. Image reconstructions were conducted to detect damage. Afterward, water was dropped into the crack and then the frequency-difference EIT system collected the data for the purpose of reflecting water occurrence in the crack.

*Mechanical tests*

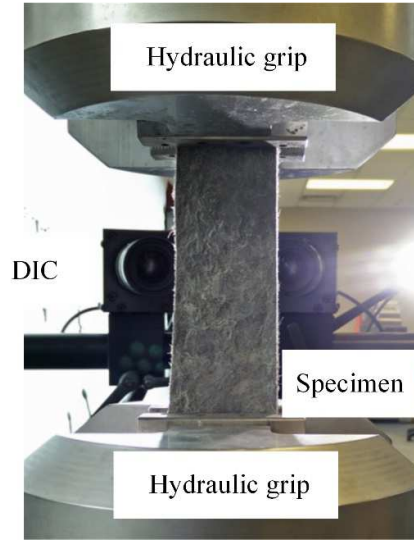


Figure 7.11 Uniaxial tensile test setup

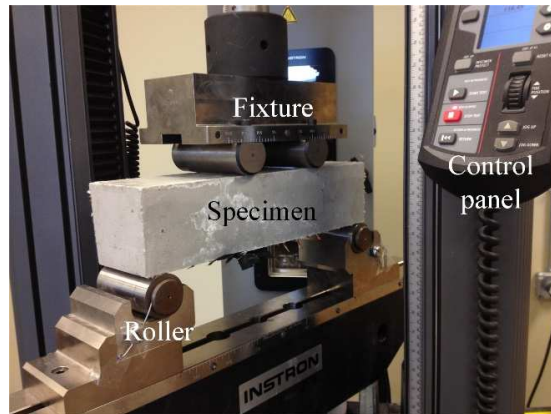


Figure 7.12 Flexure test setup

Two types of mechanical tests were conducted to induce damage in cementitious materials. The first type of test was uniaxial tension test, as shown in Figure 7.11. In order to validate the performance of frequency-difference EIT on the cementitious materials, the following test protocols were determined. As soon as the tension test was terminated, A series of EIT measurements were performed at various frequencies. The frequency-difference EIT image reconstructions were implemented with EIT measurements after tests. The second type of test was a four-point bending test. Figure 7.12 shows the test setup in this study.

## 7.4 Frequency-difference EIT Test and Image Reconstructions

Similar algorithm in Chapter 6 was utilized for image reconstructions of frequency-difference EIT. Frequency-difference imaging is aimed at recovering the conductivity differences that existed at two frequencies and hence reflecting the contrast ( $\delta\gamma_f$ ) between the cracked part and the non-cracked part.

$$\delta\gamma_f = \gamma_{f2} - \gamma_{f1} \quad (7.2)$$

$\delta\gamma_f$  is the conductivity contrast based on two EIT voltage measurements  $V_{f1}$  and  $V_{f2}$  at two frequencies  $f_1$  and  $f_2$ . As shown in Figure 7.4, the conductivity contrast between two frequencies is merely due to the crack occurrence, because the impedance of the non-cracked material is almost constant with increasing frequency.

Considering forward computations using finite element method,  $V_{f1}$  and  $V_{f2}$  become

$$V_{f1} = U(\gamma_{f1}) + e_{f1}; \quad V_{f2} = U(\gamma_{f2}) + e_{f2} \quad (7.3)$$

where  $U$  is the forward operator,  $e_{f1}$  and  $e_{f2}$  is the Gaussian distributed measurement noise.

Eq.(7.3) was further approximated by the first order Taylor approximations as:

$$V_{fi} \approx U(\gamma_{f0}) + J(\gamma_{fi} - \gamma_{f0}) + e_{fi}, \quad i = 1, 2 \quad (7.4)$$

where  $\gamma_{f0}$  is the linearization point, and  $J = \frac{\partial U}{\partial \gamma}(\gamma_{f0})$  is the Jacobian matrix evaluated at  $\gamma_{f0}$ .

Eq.(7.3) can be further written as

$$\delta V = V_{f2} - V_{f1} \approx J(\gamma_{f2} - \gamma_{f1}) + (e_{f2} - e_{f1}) = J\delta\gamma_f + \delta e_f \quad (7.5)$$

A Tikhonov regularization method was applied to reduce the effects of solving an ill-conditioned system by restoring continuity of the solution of the data. Therefore, rather than minimize  $\|J\delta\gamma_f - \delta V_f\|$ , one needs to minimize an expression of form:

$$\delta\gamma_f = \arg \min_{\delta\gamma_f} \left\{ \|J\delta\gamma_f - \delta V_f\|^2 + \psi^2 \|R\delta\gamma_f\|^2 \right\} \quad (7.6)$$

where  $R$  is a regularization matrix and  $\psi$  is a regularization parameter that controls the amount of regularization.

The solution to Eq.(7.6) is

$$\delta V_f = (J^T J + \psi^2 R^T R)^{-1} J^T \delta V_f \quad (7.7)$$

In this study, a Matlab toolkit (Eidors) was utilized to perform image reconstructions.

## 7.5 Results and Discussions

This section presents image reconstructions based on measurements in Section 7.3. For comparisons, Time-difference EIT image reconstructions can be found in Chapter 6. The regularization parameter in image reconstructions was adjusted so that best quality was achieved.

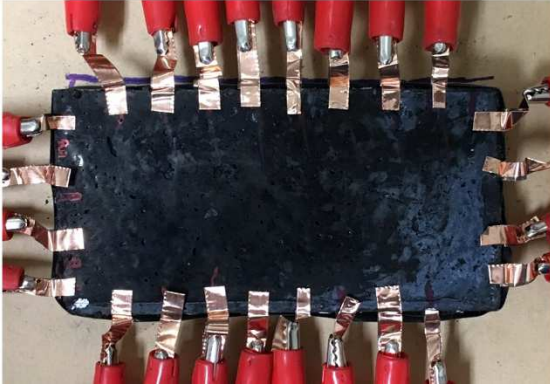
### 7.5.1 Validation test

Figure 7.13 shows frequency-difference EIT image reconstructions. It is illustrated that a vertical crack appeared in the middle cross section of the specimen. The crack passed through the specimen and divided the specimen into two pieces. Image reconstructions based on two different frequencies captured the damage occurrence. The damage details, i.e., location, geometry, and severity, were clearly reflected. The image reconstructions based on different pairs of frequencies showed slight differences. There was a noise distribution on the right side of the specimen, which can be used as reference to differentiate differences caused by water presence. Figure 7.14 shows that image reconstructions were able to reflect the water presence, as the high impedance region in the middle became less obvious. The water drops were placed along the crack in the specimen.

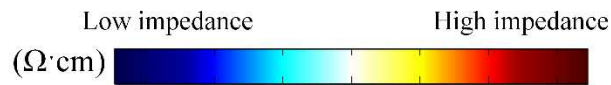


(a)

Before damage



After damage



(b)

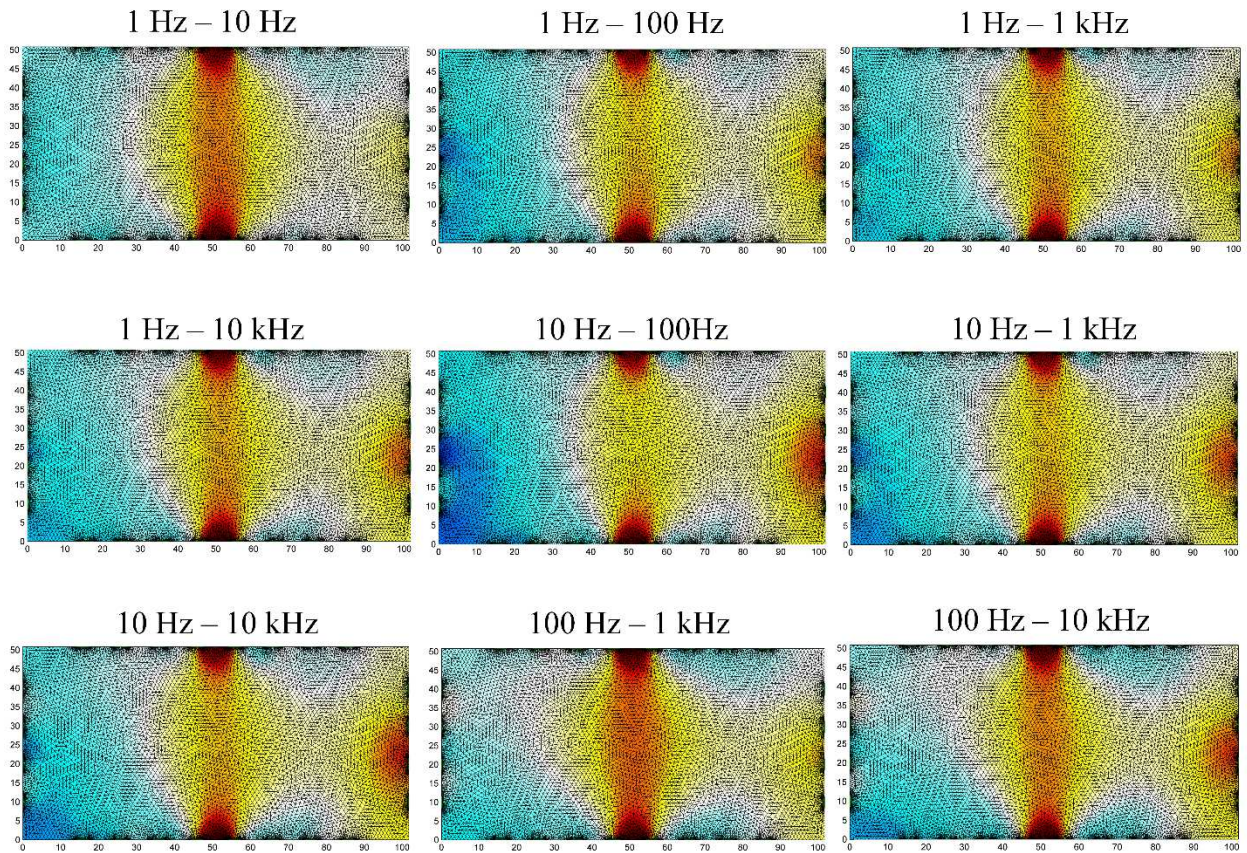


Figure 7.13 Image reconstructions reflected damage in the middle of the specimen

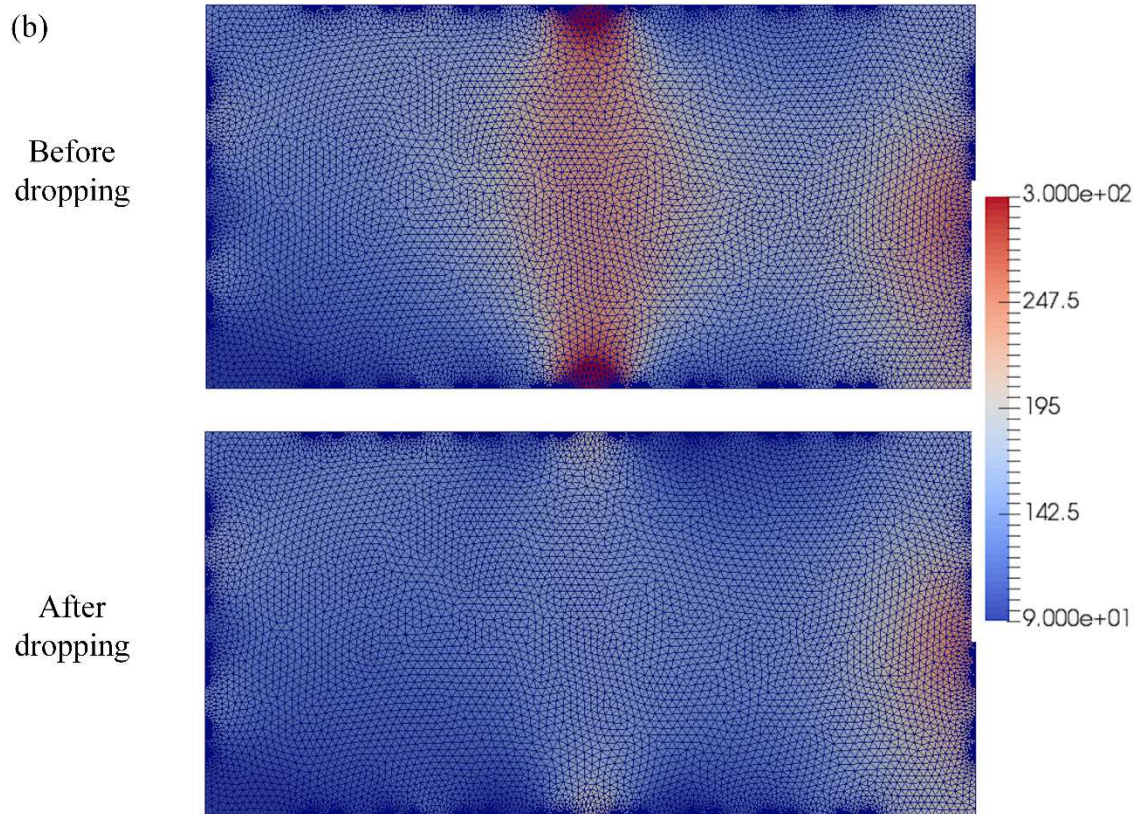
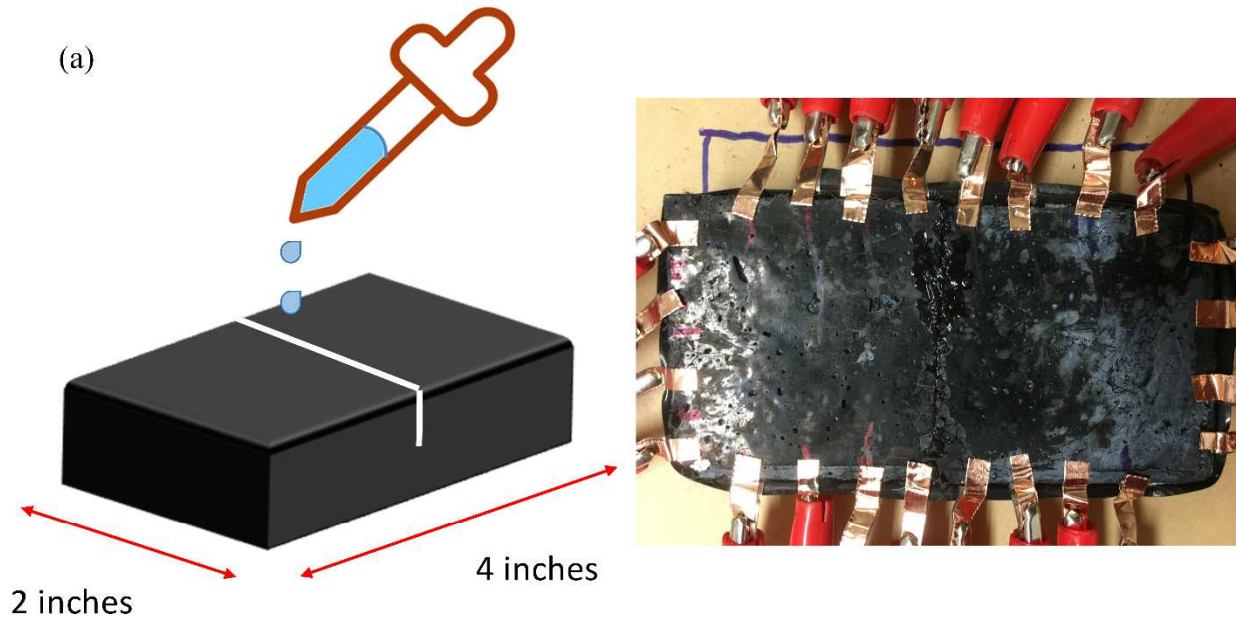


Figure 7.14 Image reconstructions reflected water presence

### 7.5.2 Damage sensing of the localized damage

Under uniaxial tension, the coupon specimen made from C2 showed a localized single crack (average crack width = 2.3 mm) on the right side of the specimen (Figure 7.15). The crack separated the specimen into two parts, merely connected by some PVA fibers. The image reconstructions were performed with Time-difference and frequency-difference schemes. In this study, a range of different regularization parameters were tested and one which produced the best quality image was selected by comparing the images. Since the impedance of the cementitious material is frequency dependent, Time-difference EIT image reconstructions at different frequencies vary significantly, as shown in Figure 6.20. Time-difference EIT worked well in this scenario.

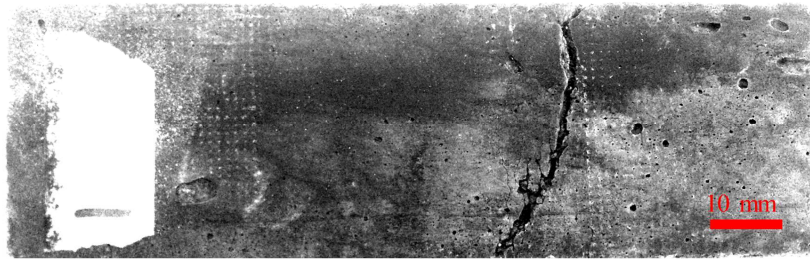
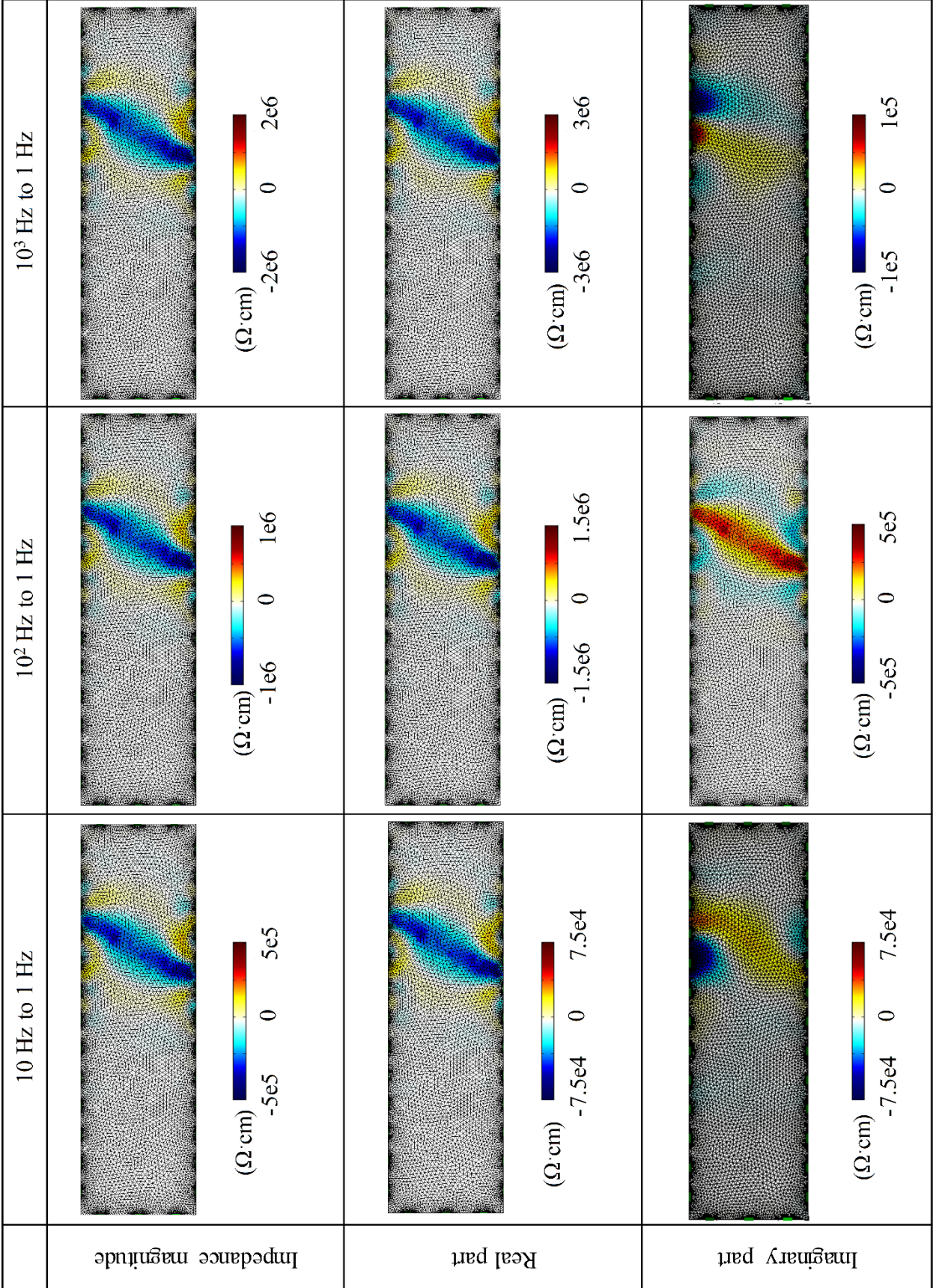
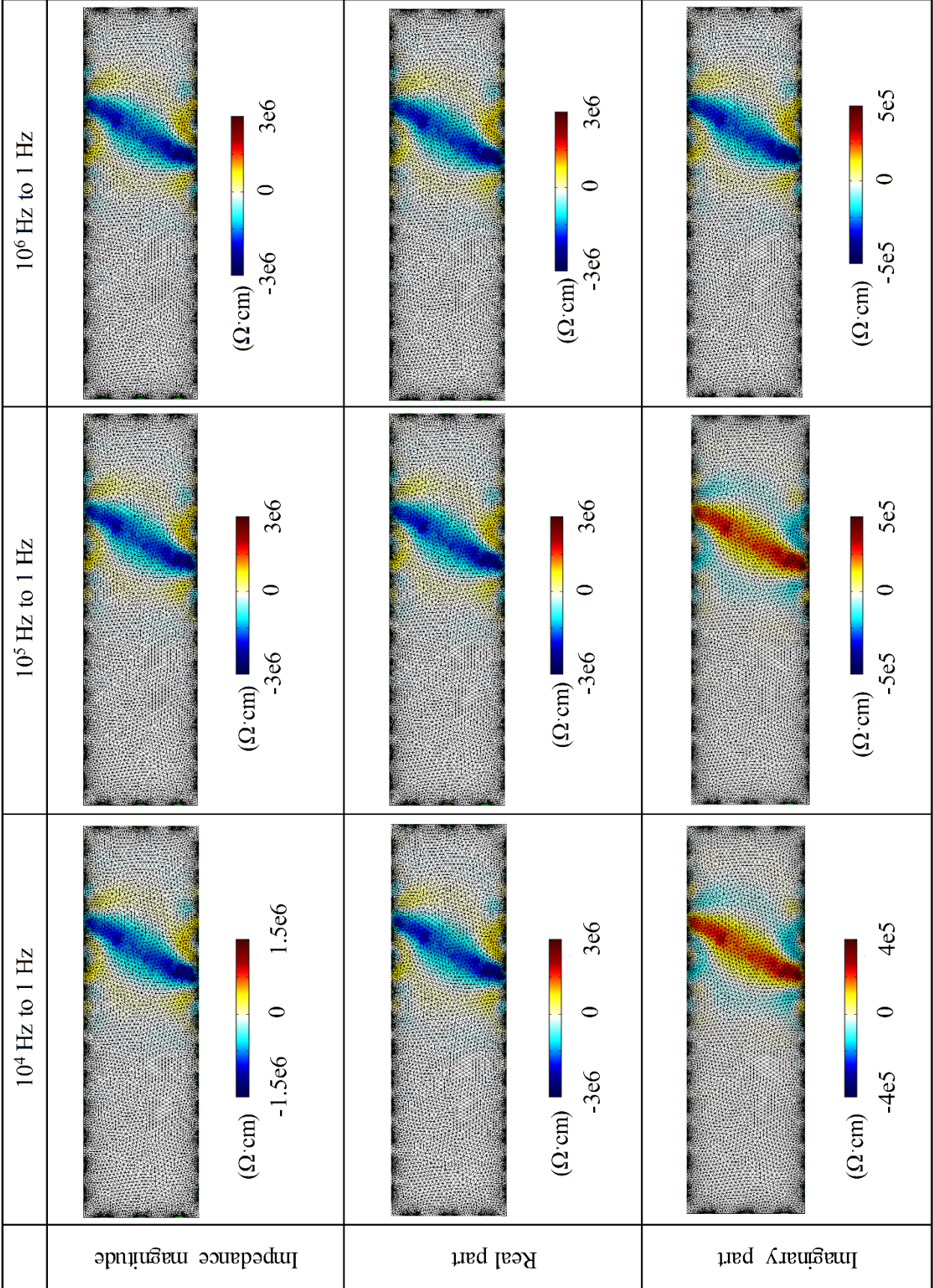
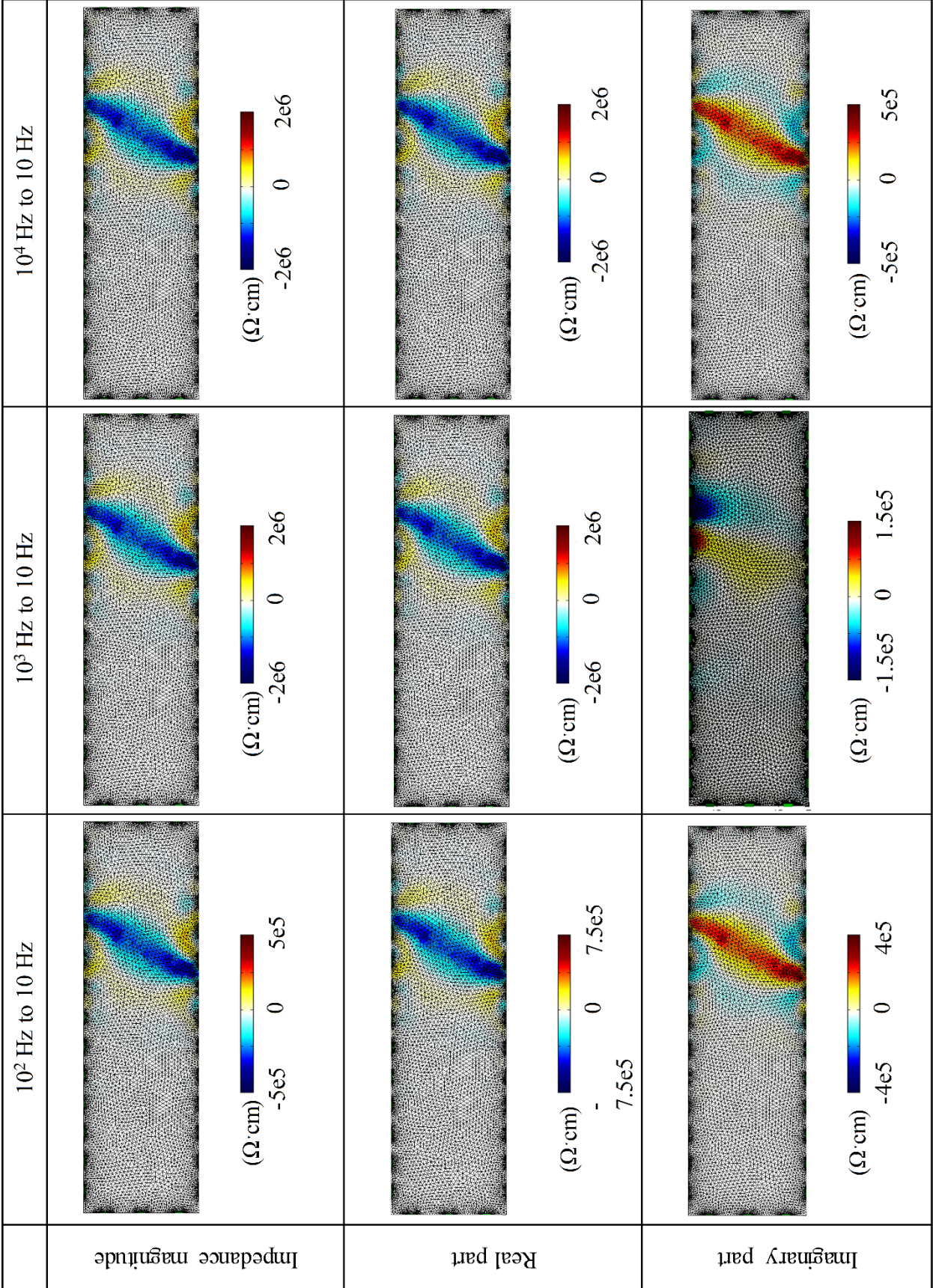


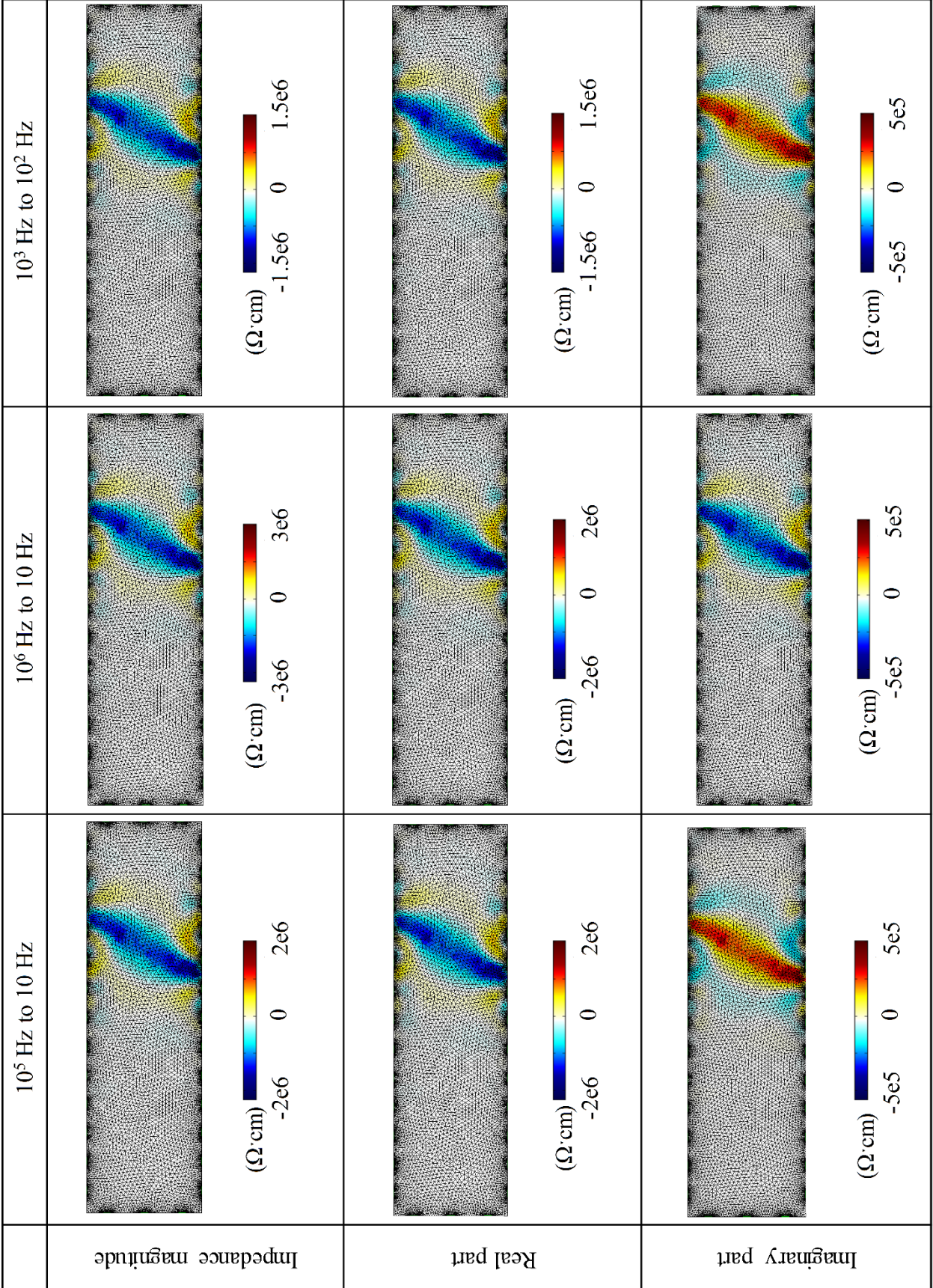
Figure 7.15 Localized damage in the coupon specimen

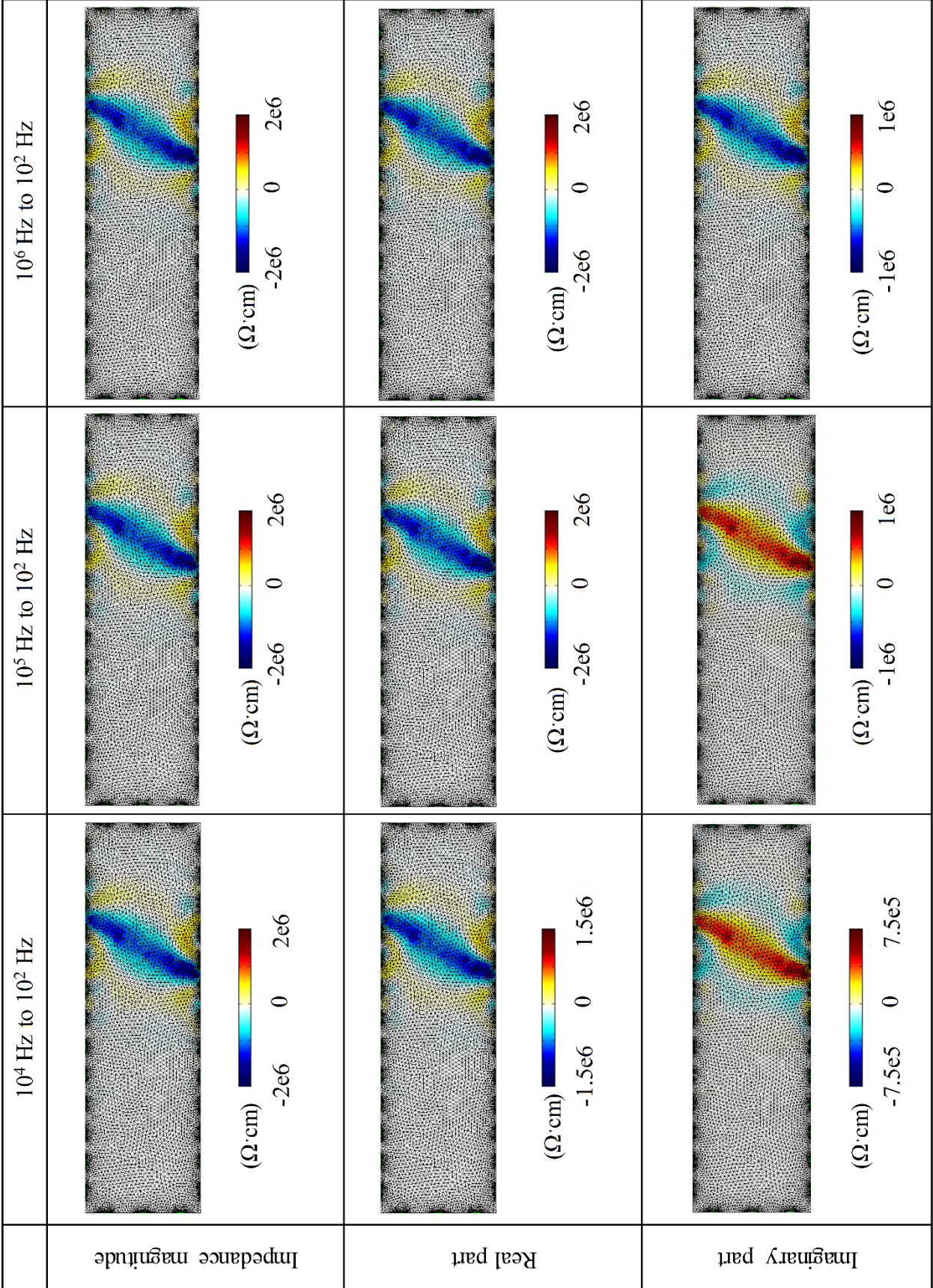
The frequency-difference image reconstructions are illustrated in Figure 7.16. One image reconstruction based on a reference measurement and a change-of-state measurement is located in a corresponding row and column. For example, the image reconstruction based on the difference of measurement at 1 Hz and the measurement at 10 Hz is in the 1<sup>st</sup> row and 1<sup>st</sup> column.



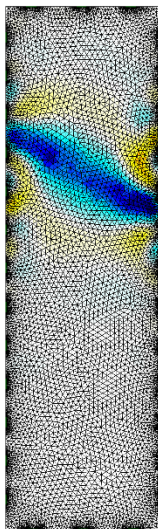
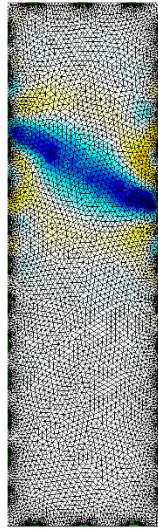
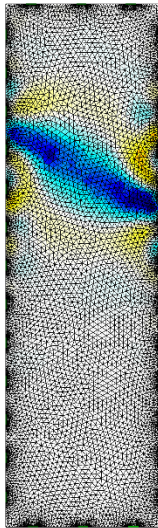
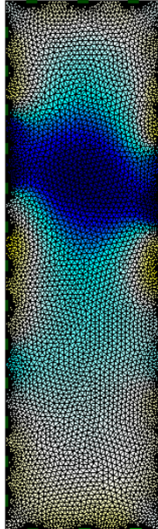
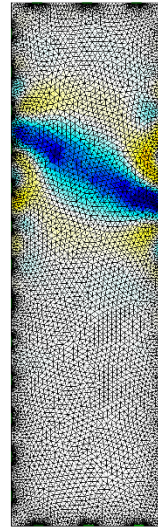
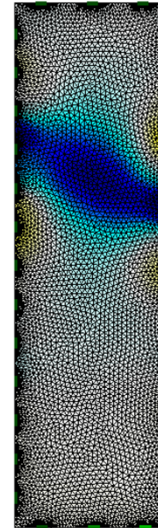
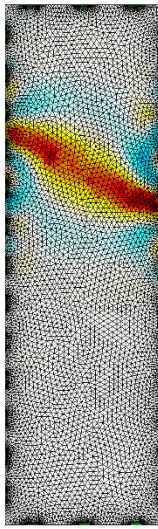
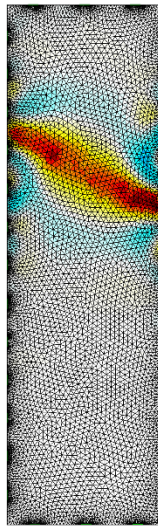
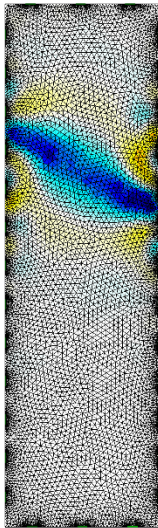










	10 <sup>4</sup> Hz to 10 <sup>3</sup> Hz	10 <sup>5</sup> Hz to 10 <sup>3</sup> Hz	10 <sup>6</sup> Hz to 10 <sup>3</sup> Hz
Impedance magnitude	 <p>(Ω·cm) -5e5 0 5e5</p>	 <p>(Ω·cm) -5e5 0 5e5</p>	 <p>(Ω·cm) -5e5 0 5e5</p>
Real part	 <p>(Ω·cm) -2e5 0 2e5</p>	 <p>(Ω·cm) -3e5 0 3e5</p>	 <p>(Ω·cm) -3e5 0 3e5</p>
Imaginary part	 <p>(Ω·cm) -2e5 0 2e5</p>	 <p>(Ω·cm) -5e5 0 5e5</p>	 <p>(Ω·cm) -5e5 0 5e5</p>

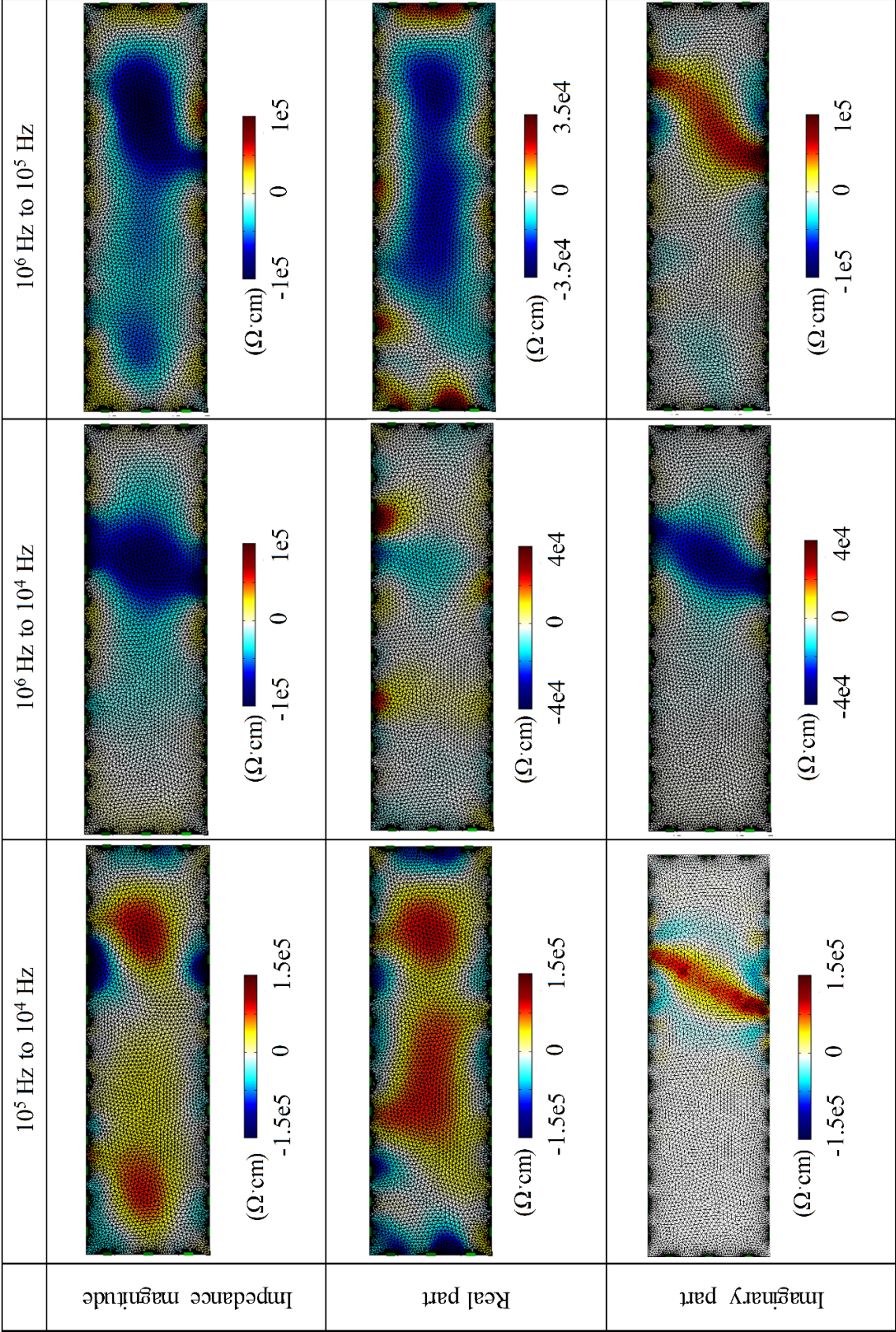


Figure 7.16 Image reconstructions for damage detection of localized damage

Figure 7.16 shows image reconstructions based on impedance magnitudes, real part and imaginary part. It is shown that for image reconstructions with reference frequency ranging from 1 Hz to 1 kHz, the damage details were captured clearly, i.e., location, extent, shape, etc., without much noise. The extent of the damage was somewhat overestimated, which was due to the use of Tikhonov regularization. Image reconstructions with reference frequency of 10 kHz and 100 kHz show much noise. Although image reconstructions based on 1 MHz and 100 kHz detected occurrence of damage at the right side of the specimen, the presence of noise makes it hard to identify the exact details of the crack. Furthermore, image reconstructions based on pairs of frequencies, 100 kHz and 10 kHz, 1 MHz and 100 kHz, displayed only noise.

Image reconstructions based on the real part of the impedance show similar quality as the impedance magnitude. Image reconstructions with the reference frequency of 10 kHz and 100 kHz depict meaningless noise. The similarity between EIT based impedance magnitude and EIT based on real part of impedance can be explained by Figure 7.4 and Figure 7.6. The frequency dependent behaviors of the impedance magnitude and the real part were identical except for the value (Figure 7.4). It was also mentioned that the measured signal at a frequency of  $10^5$  Hz was too noisy. Therefore, the image reconstructions with measurements at  $10^5$  Hz as the reference measurement or change of state measurement were susceptible to modeling errors.

Figure 7.16 also shows image reconstructions based on the imaginary part of the impedance. Unlike impedance magnitude and real part, image reconstructions showed damage details clearly in the high-frequency range. Even for image reconstructions based on 1 MHz and 100 kHz, the damage location and shape were clearly reflected without much noise, although the shape of the damage was deformed a little bit. Also, it was observed that the image reconstructions based on low frequencies, i.e., 1 Hz and 10 Hz, 1 Hz and 1kHz, and 10 Hz and 1

kHz, did not fully capture the damage information. This can be explained by Figure 7.4 and Figure 7.6. In the low-frequency range, the differences of imaginary part of impedances between different frequencies were not apparently observed, suggesting that it is difficult to achieve image reconstructions with clear damage information at a low-frequency range.

### 7.5.3 Damage sensing of distributed damage

The distributed cracking pattern and the corresponding image reconstructions of C2 are plotted in Figure 7.17. As it is difficult to directly visualize the microcracks, the cracks were highlighted in white color in figures. Figure 7.17 shows the distributed cracks (average crack width = 65  $\mu\text{m}$ ) on the surface of the coupon specimen, with one final failure crack (maximum crack width = 1.8 mm) in the middle region. Figure 6.23 shows the image reconstructions based on Time-difference EIT.

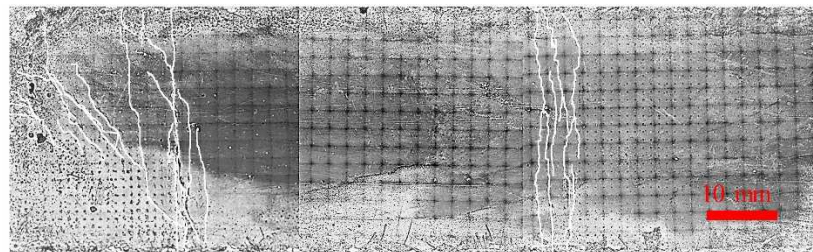


Figure 7.17 Distributed damage in the coupon specimen

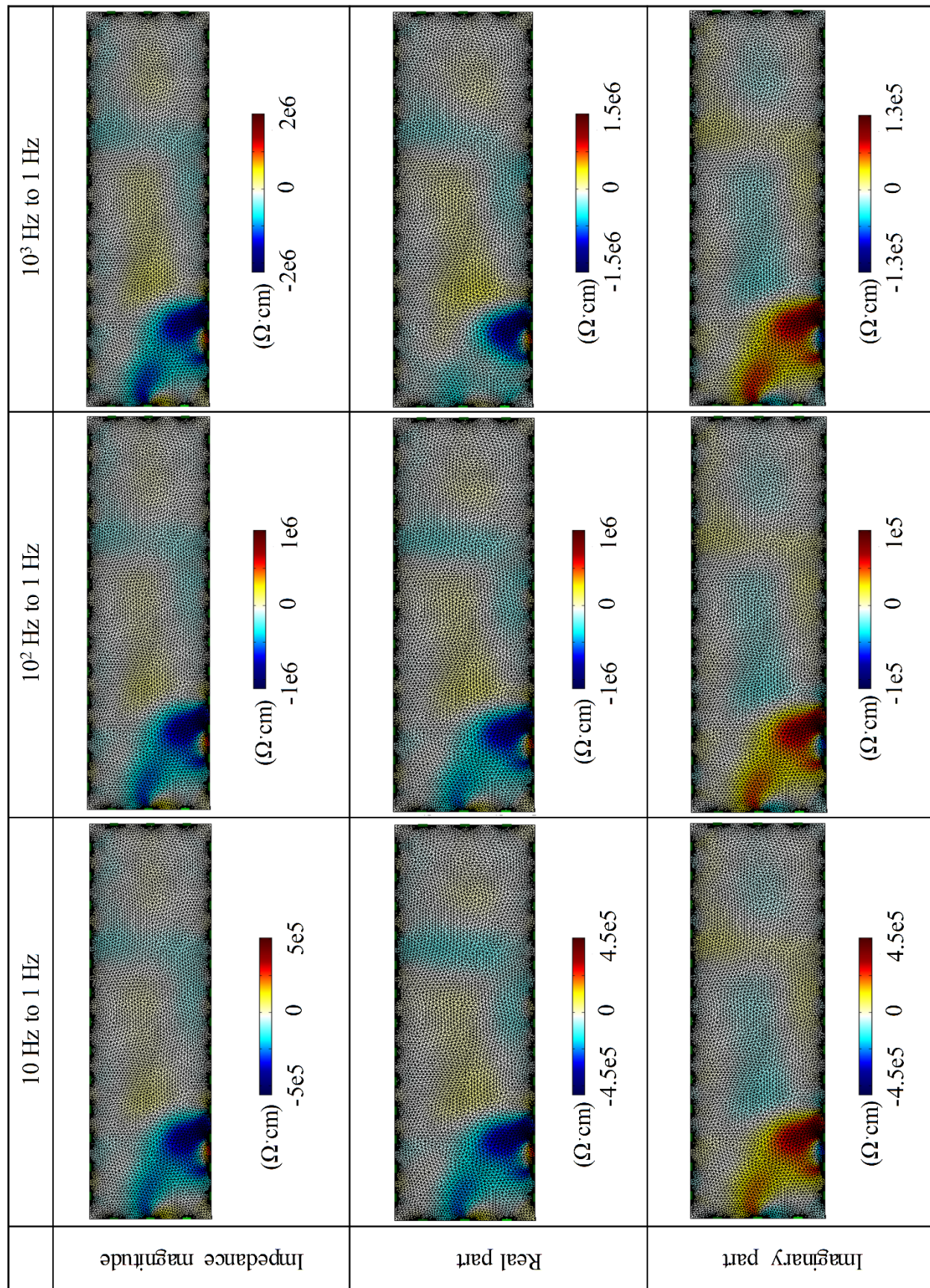
Figure 7.18 shows image reconstructions. It is shown that for image reconstructions with reference frequency ranging from 1 Hz to 1 kHz, the damage details were captured clearly, i.e., location, extent, shape, etc, without much noise. Same as image reconstructions for localized damage, the extent of the damage was overestimated. The image reconstructions with the reference frequency of 10 kHz also showed low level of noise, which is different from localized damage image reconstructions. However, image reconstructions with reference frequency and

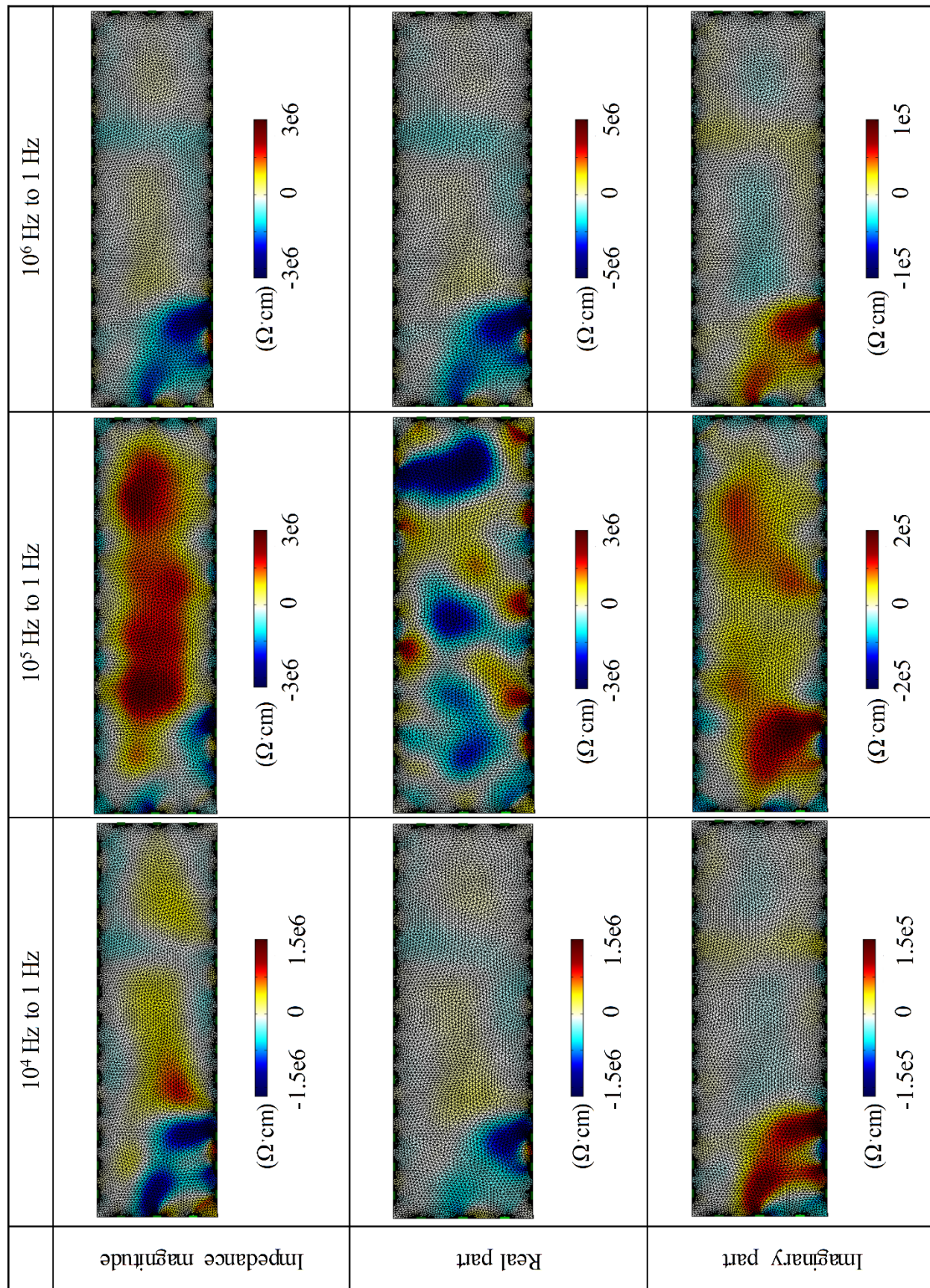
change-of-state frequency of 100 kHz showed noise only, suggesting impedance measurements at 100 kHz exhibited high amount of noise.

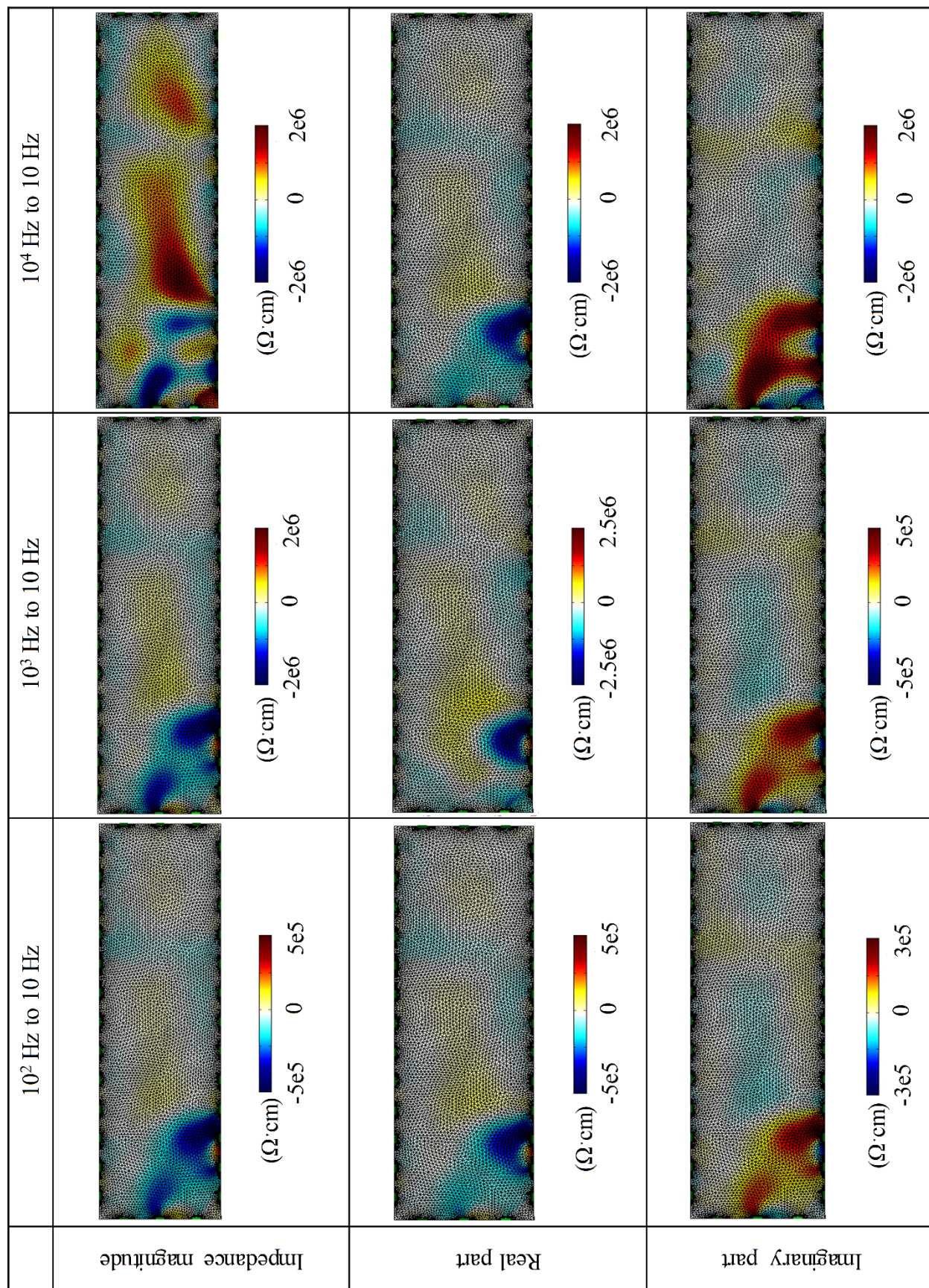
Image reconstructions based on the real part of the impedance show similar quality as the impedance magnitude. Image reconstructions with the reference frequency or change-of-state frequency of 100 kHz depict meaningless noise. The similarity between EIT based impedance magnitude and EIT based on real part of impedance can be explained by Figure 7.4 and Figure 7.6. The frequency dependent behaviors of the impedance magnitude and the real part were identical except for the value (Figure 7.4).

Image reconstructions based on the imaginary part of impedance are also plotted in Figure 7.18. Compared with image reconstructions based on impedance magnitude and real part of impedance, image reconstructions based on imaginary part of impedance showed similar quality but there were more pairs of frequencies showing low level of noise. For example, image reconstructions based on 10 kHz and 100 Hz showed a damage state more clearly for imaginary part of impedance than impedance magnitude and real part.

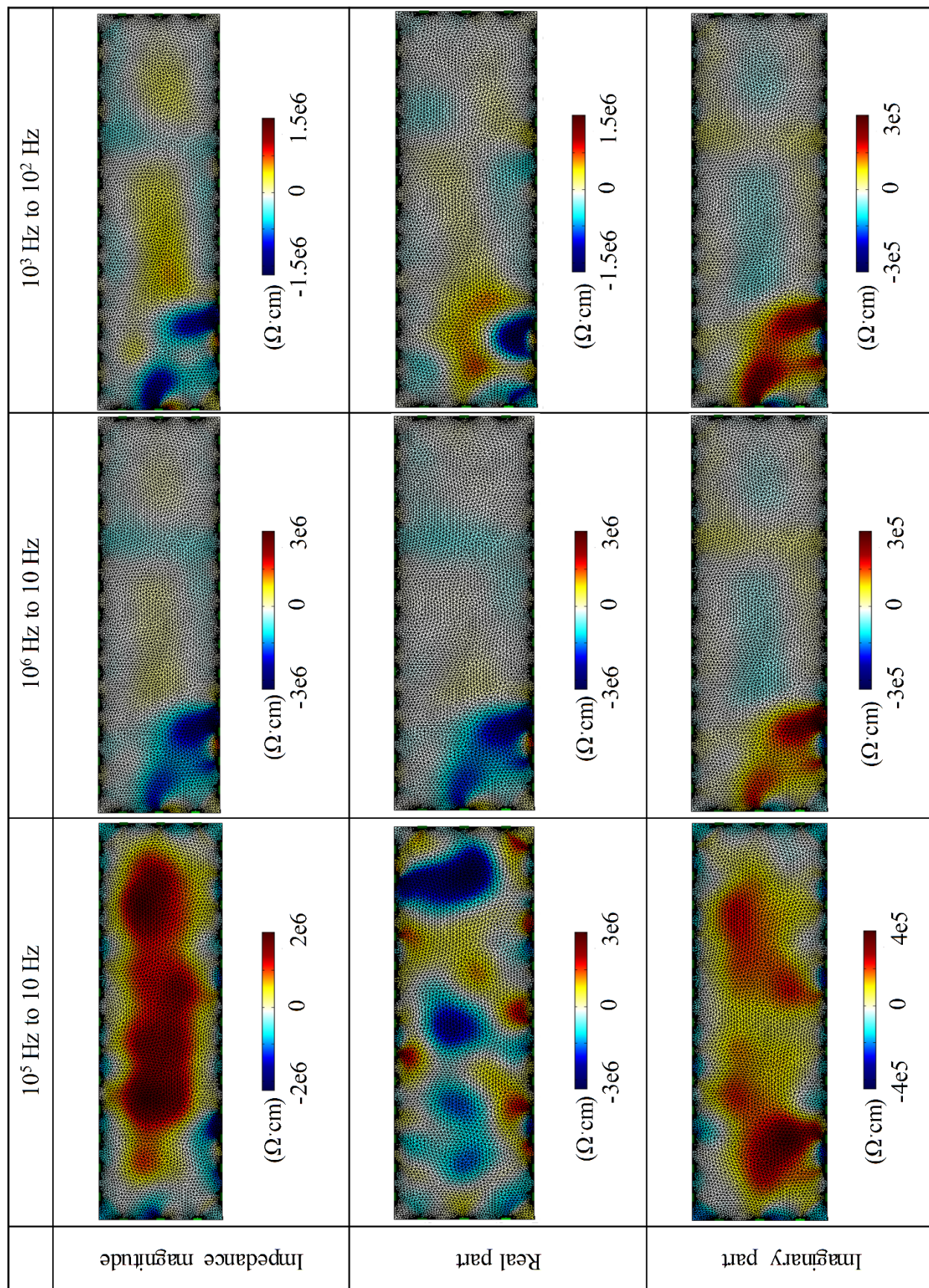
All of the image reconstructions were able to identify the severity of damage within cementitious materials. It can be observed that the darker blue color for impedance magnitude and real part occurred on the left side of the specimen, darker red color for imaginary part located on the left side of the specimen appeared, and lighter blue or red color located on the right side of the specimen also occurred. This color suggests that the damage on the left of specimen was more severe than that on the right side.

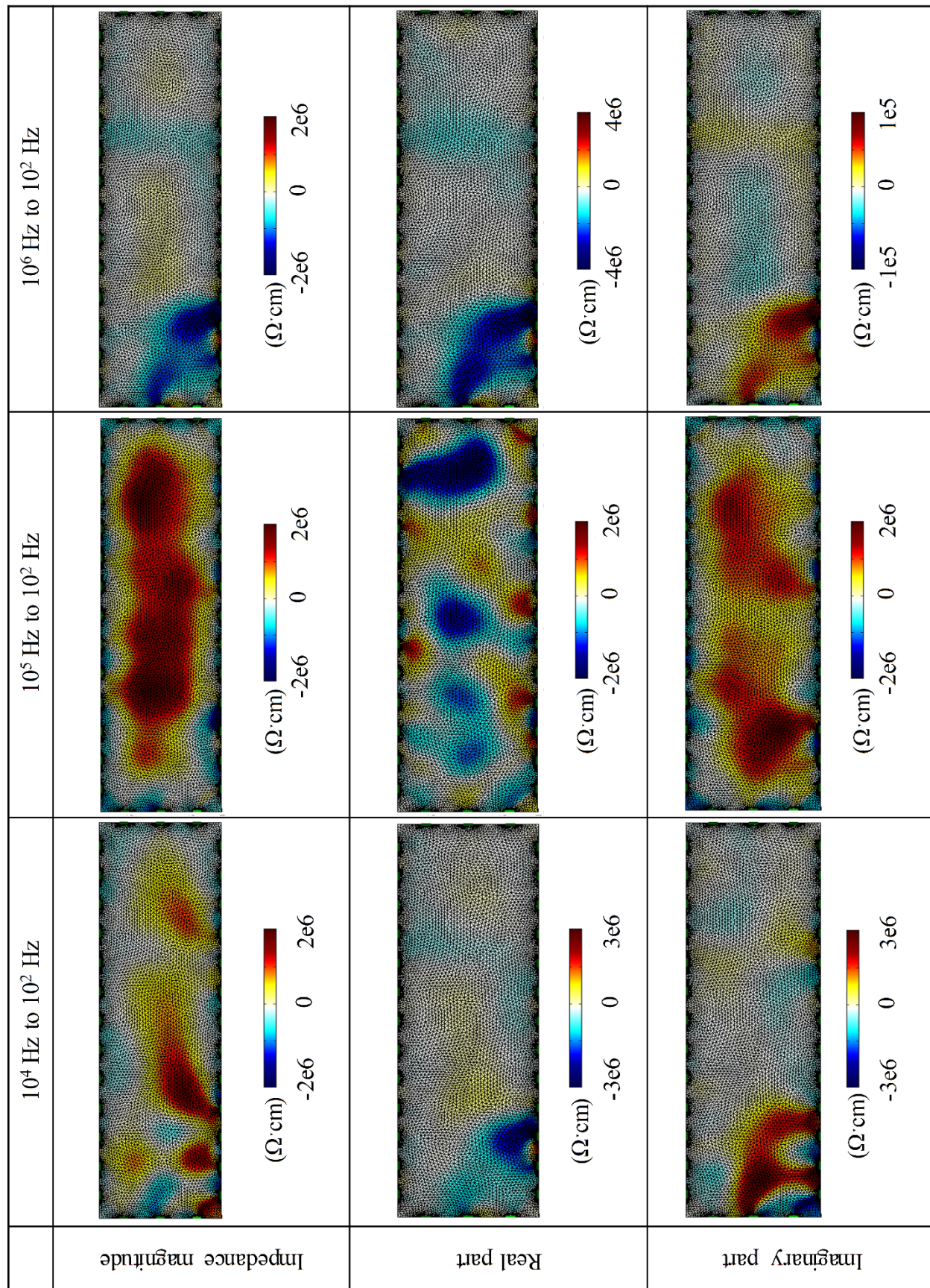


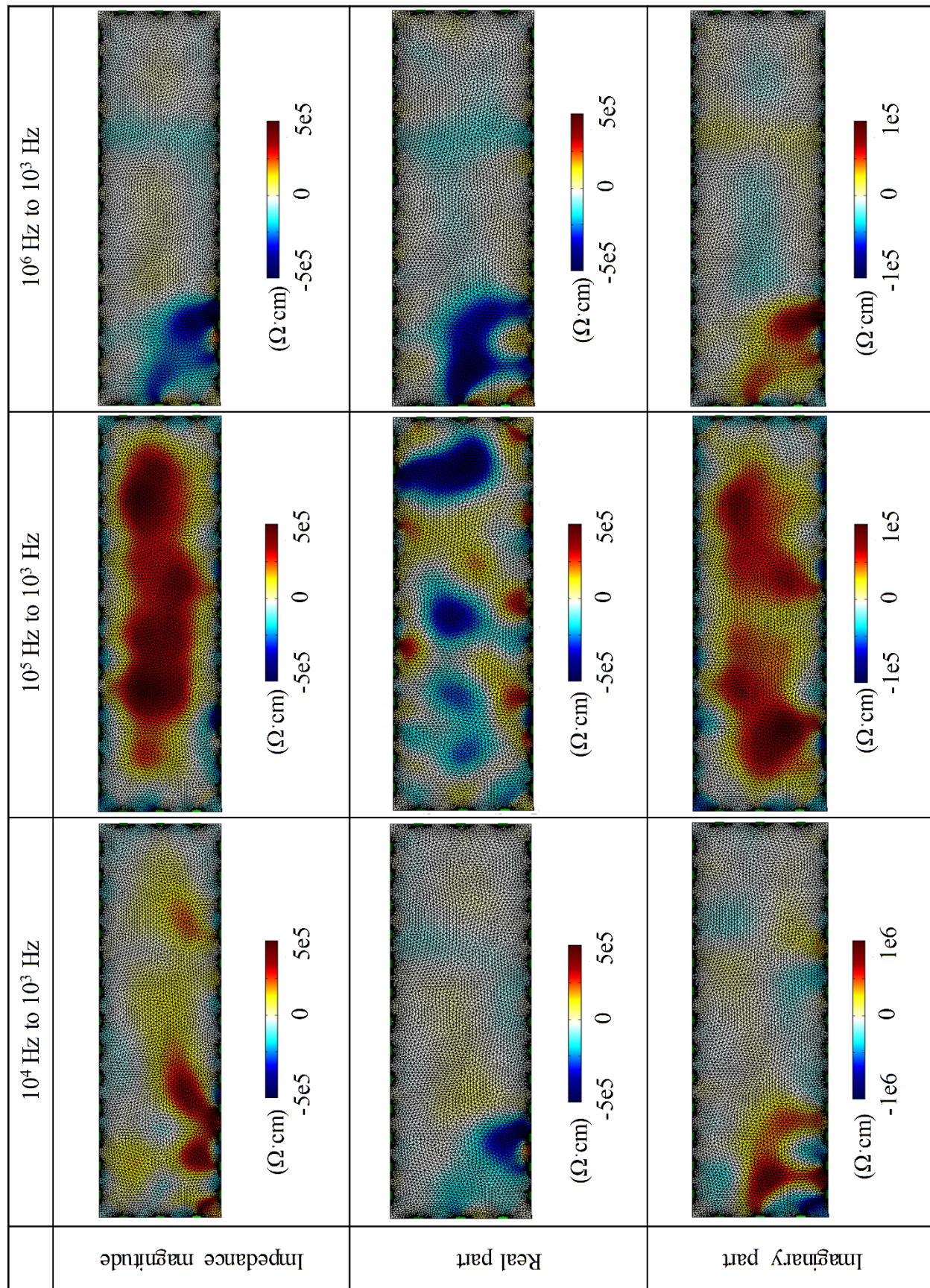












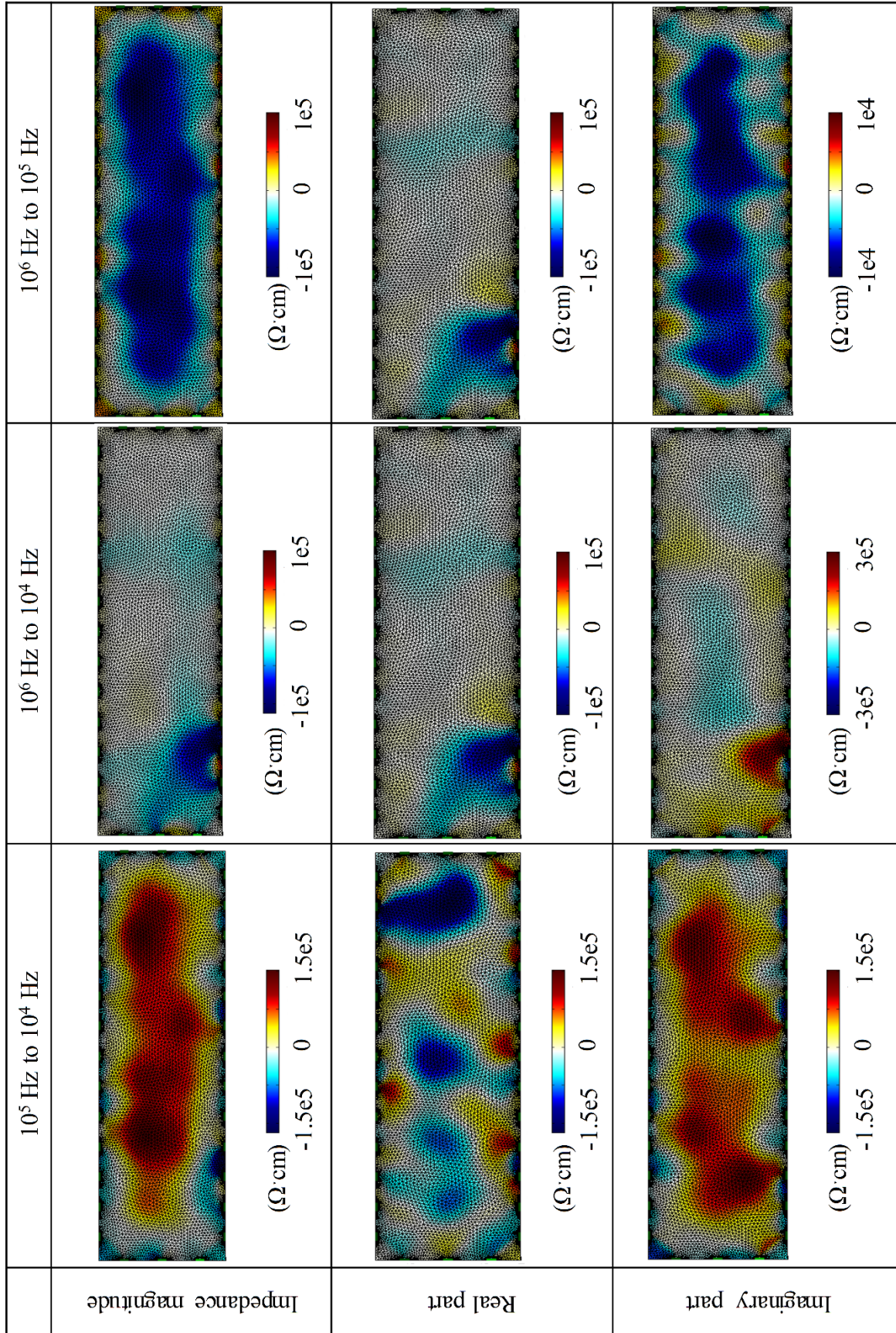


Figure 7.18 Image reconstructions for detection of distributed damage

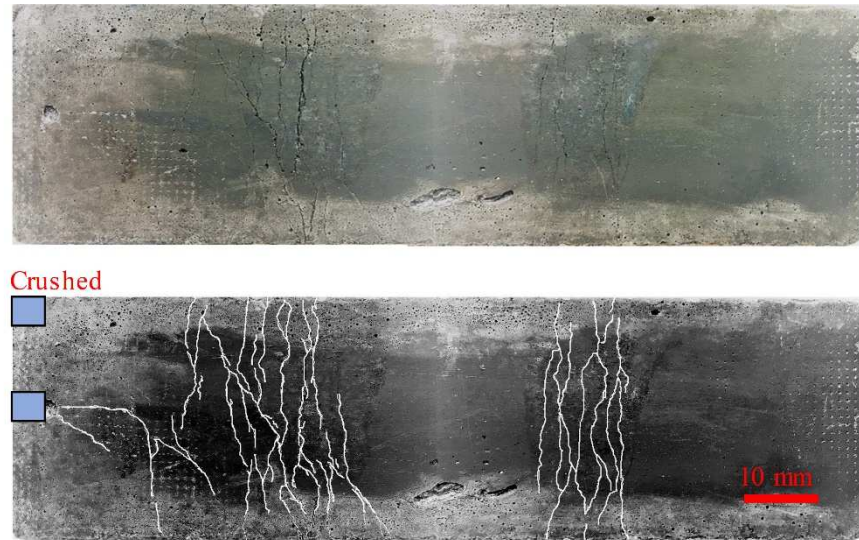
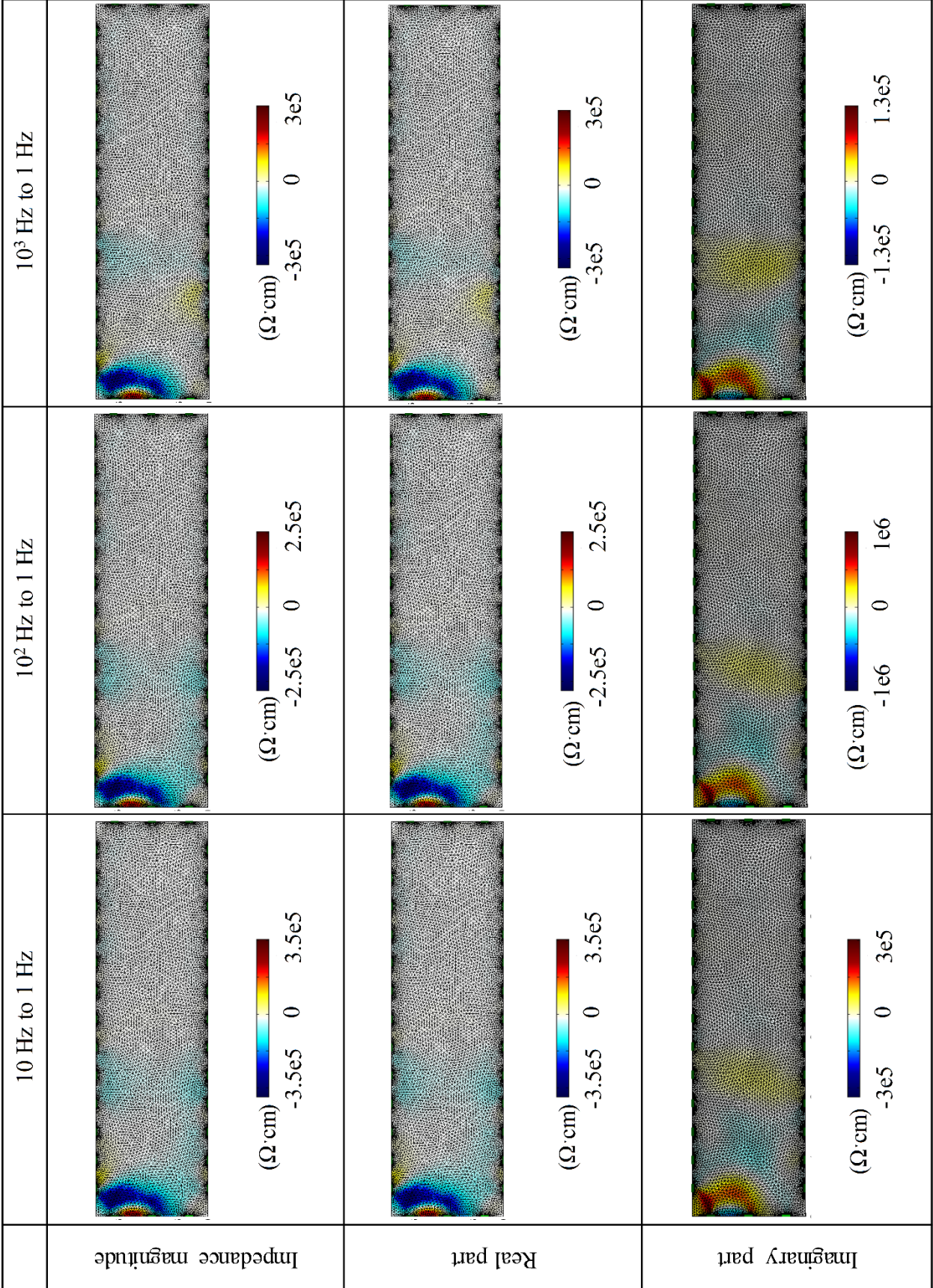
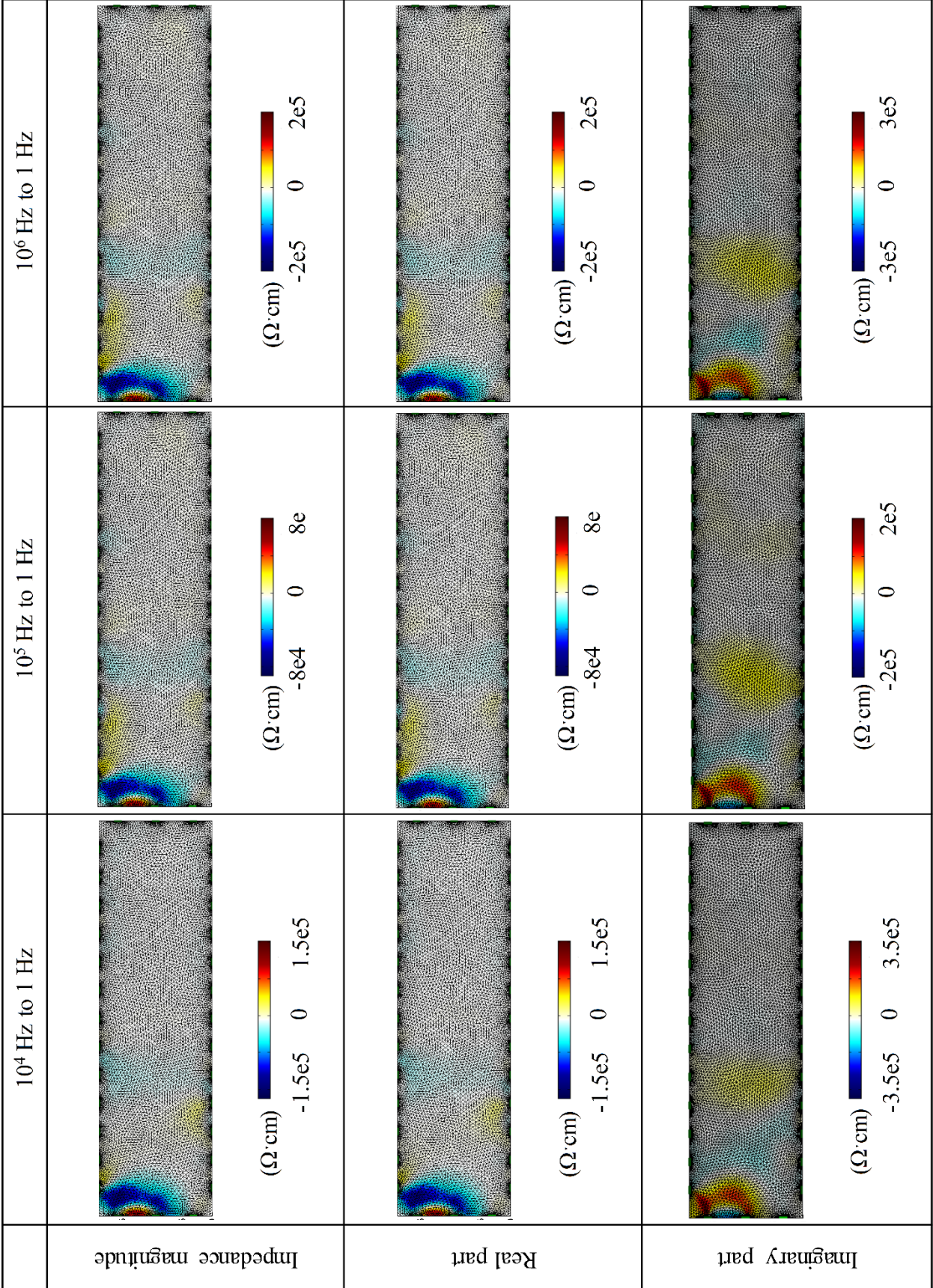


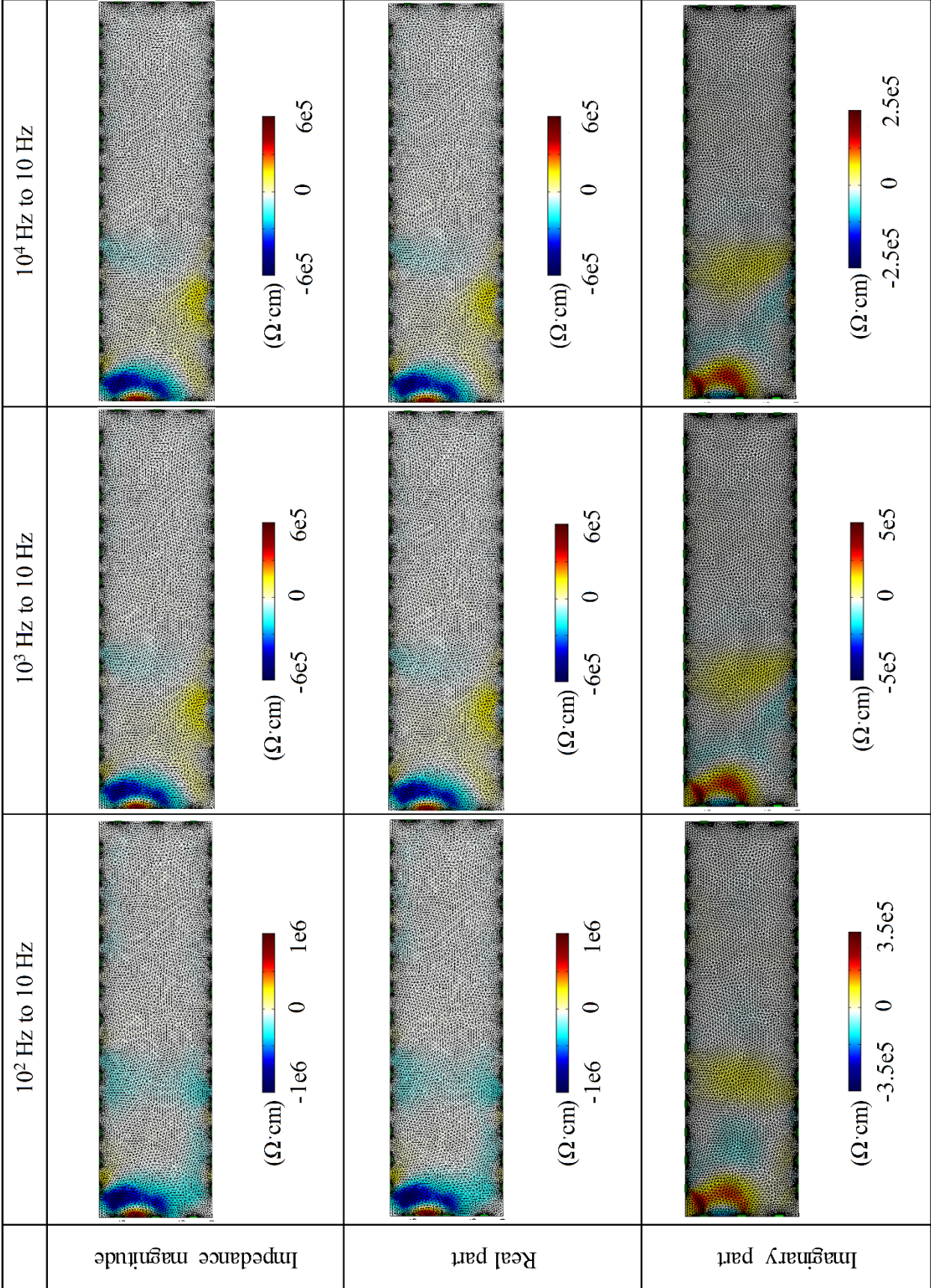
Figure 7.19 Distributed damage in the coupon specimen

Figure 7.19 shows the damage pattern for the other distributed cracking scenario. As the cracks are difficult to be observed, the color of the figure was changed, and the cracks or damage were highlighted and marked. It is seen that the left edge of the sample was crushed due to nonuniform surface of the specimen. As this study focused on the image reconstructions for different patterns, this specimen can be used. There were distributed cracks on the right side and left side of the specimen. The significant damage was on the left side of the specimen.

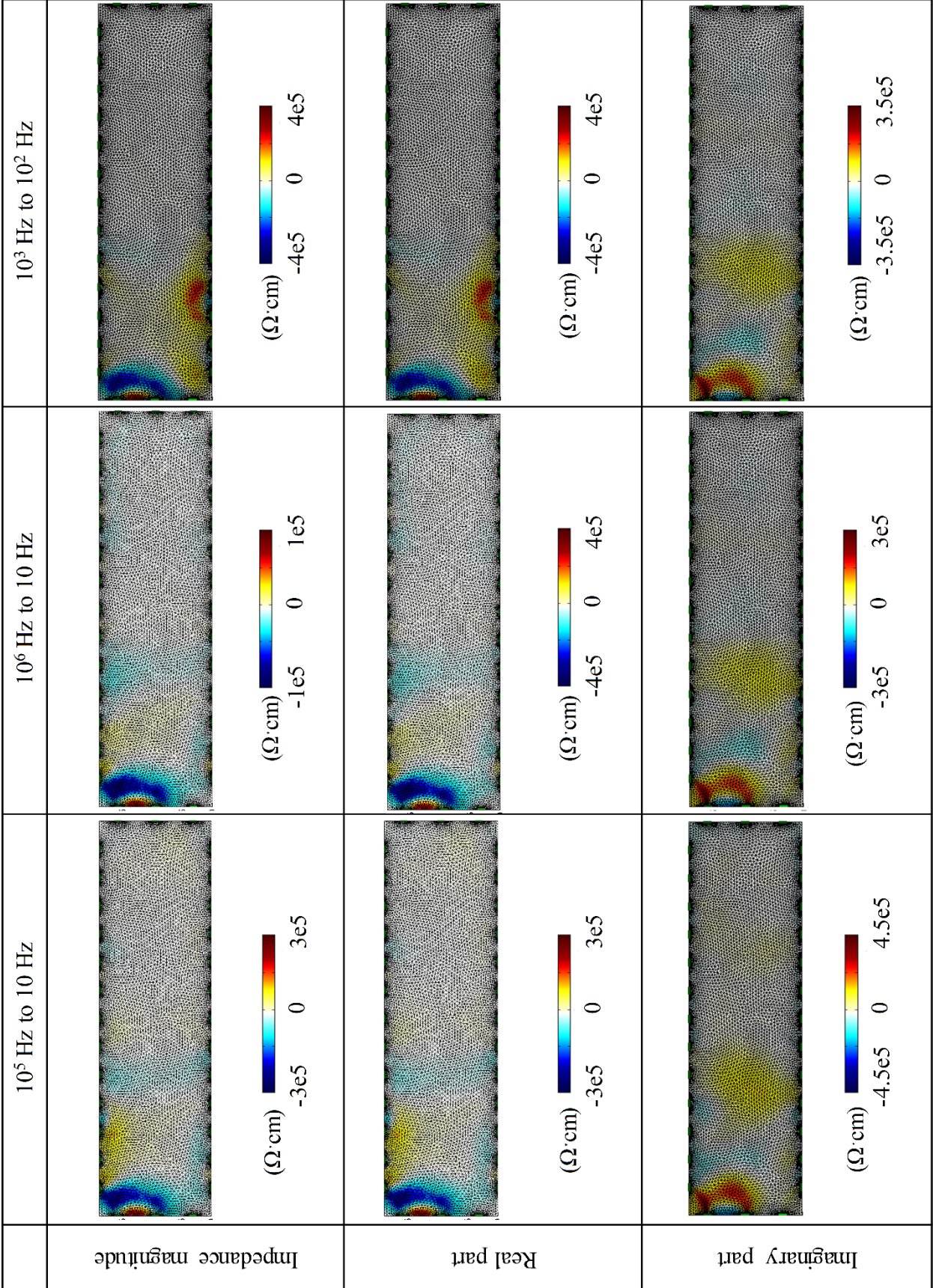
Figure 7.20 shows image reconstructions for above damaged specimen. It can be observed that for most of the image reconstructions, the crush damage and the distributed cracks on the left were clearly captured without much noise. Not only the damage location, extent, shape was able to be reflected but also the damage severity was differentiated between the crush damage and distributed cracks. The optimum frequency range is from 1 Hz to 100 kHz. Image reconstructions based on impedance magnitude and real part did not reflect the distributed damage on the right side, which was less severe than other damage. However, imaginary reconstructions based on imaginary part capture the distributed damage on the right hand.

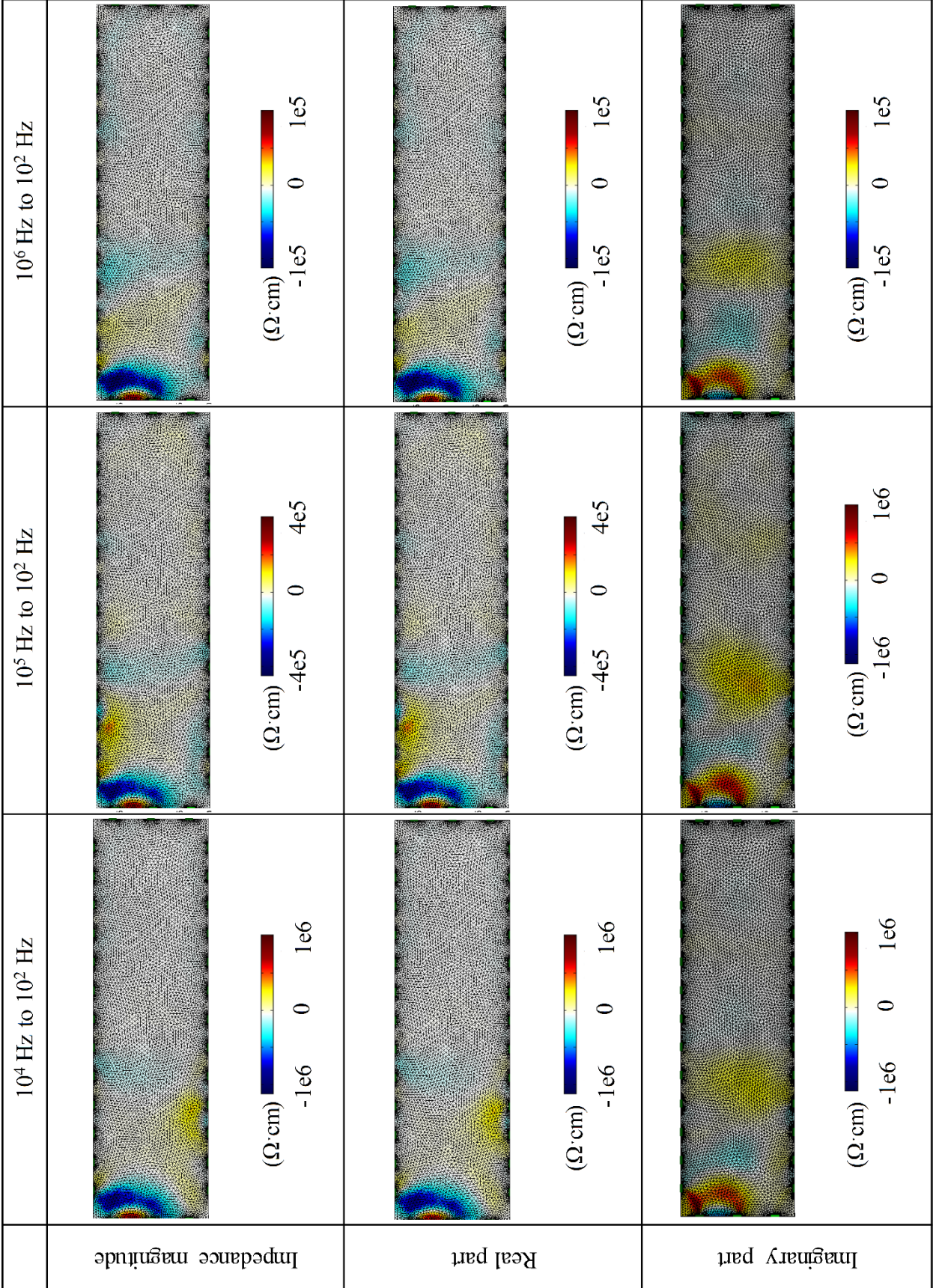


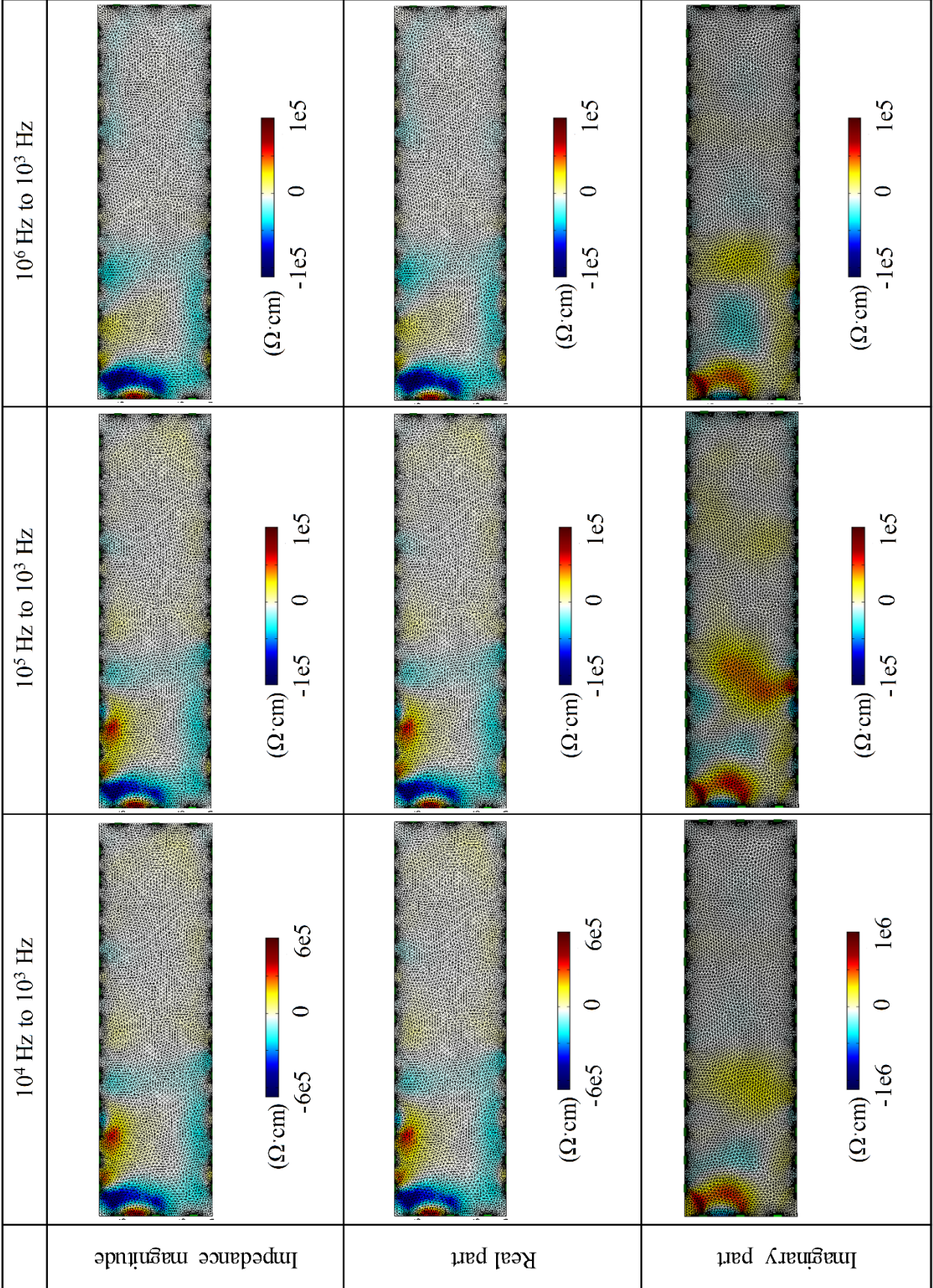












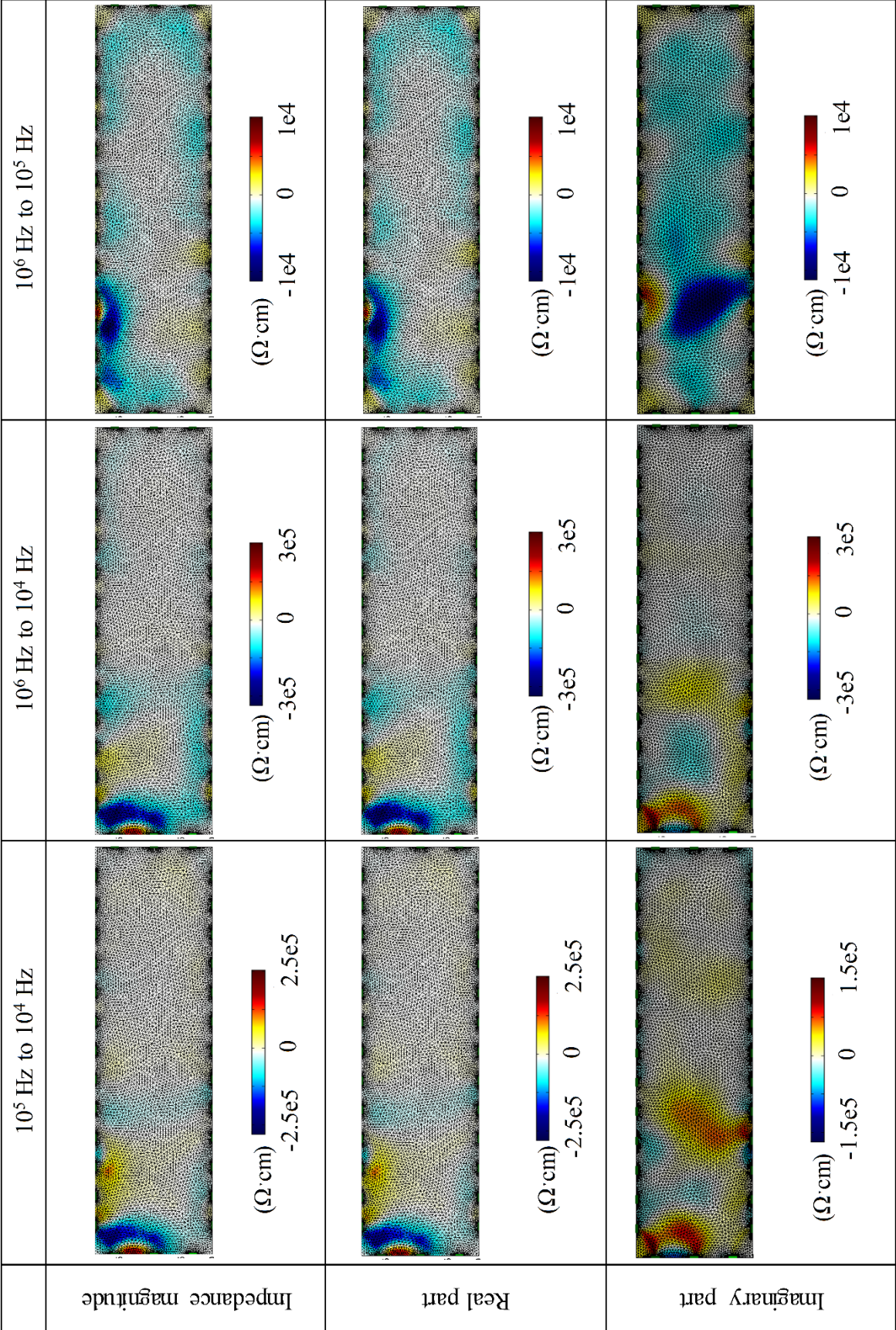


Figure 7.20 Image reconstructions for detection of distributed damage

#### 7.5.4 Damage sensing of beam specimen

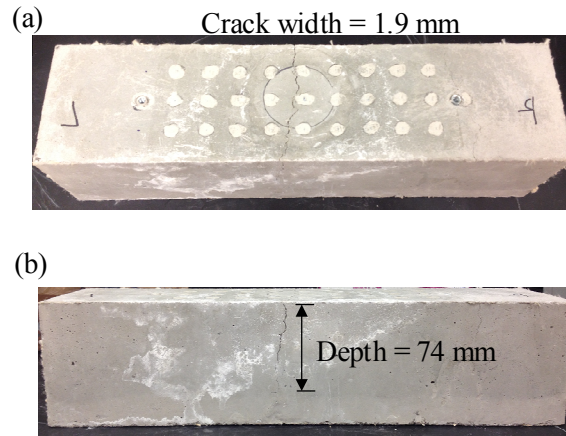
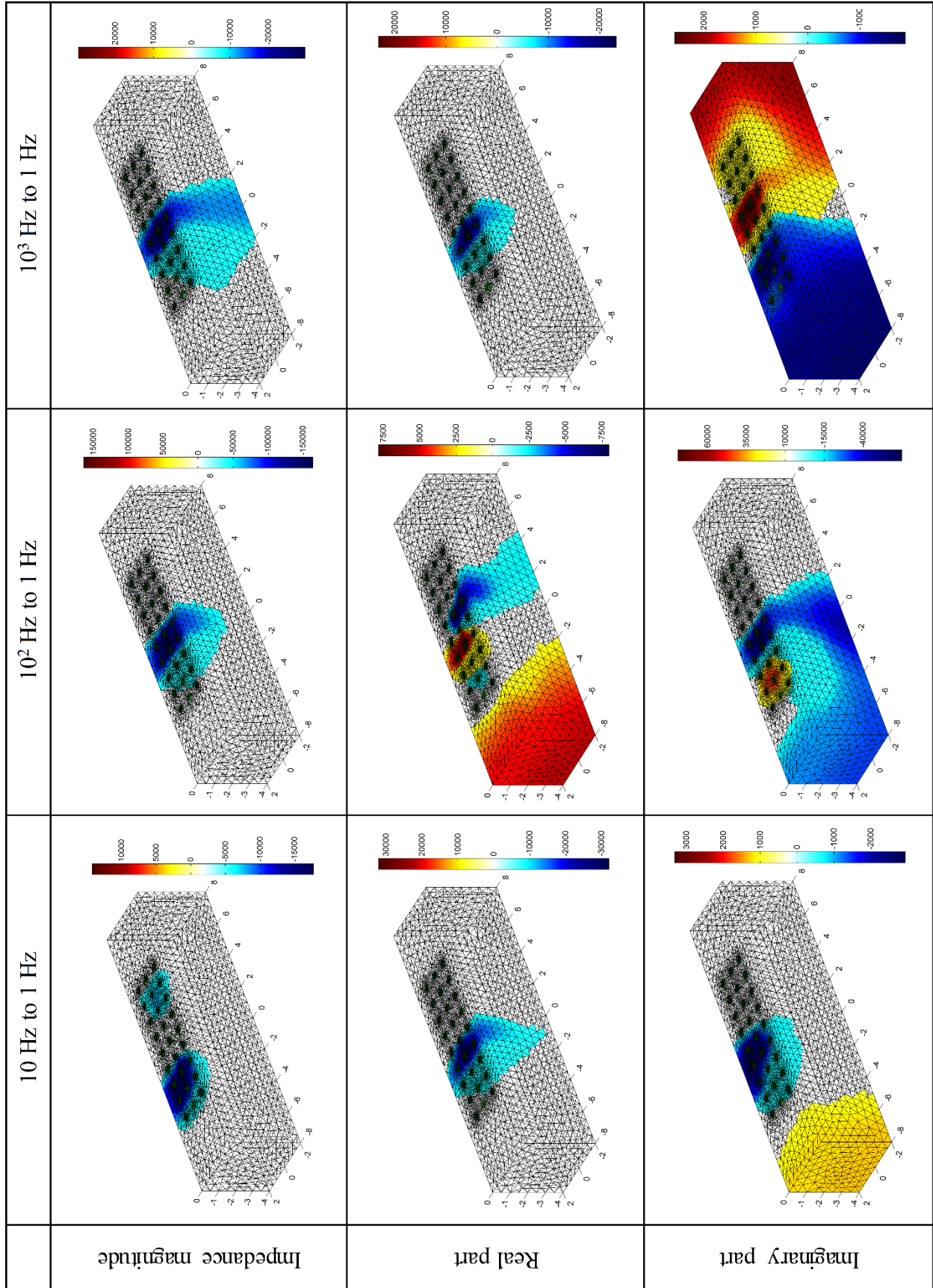
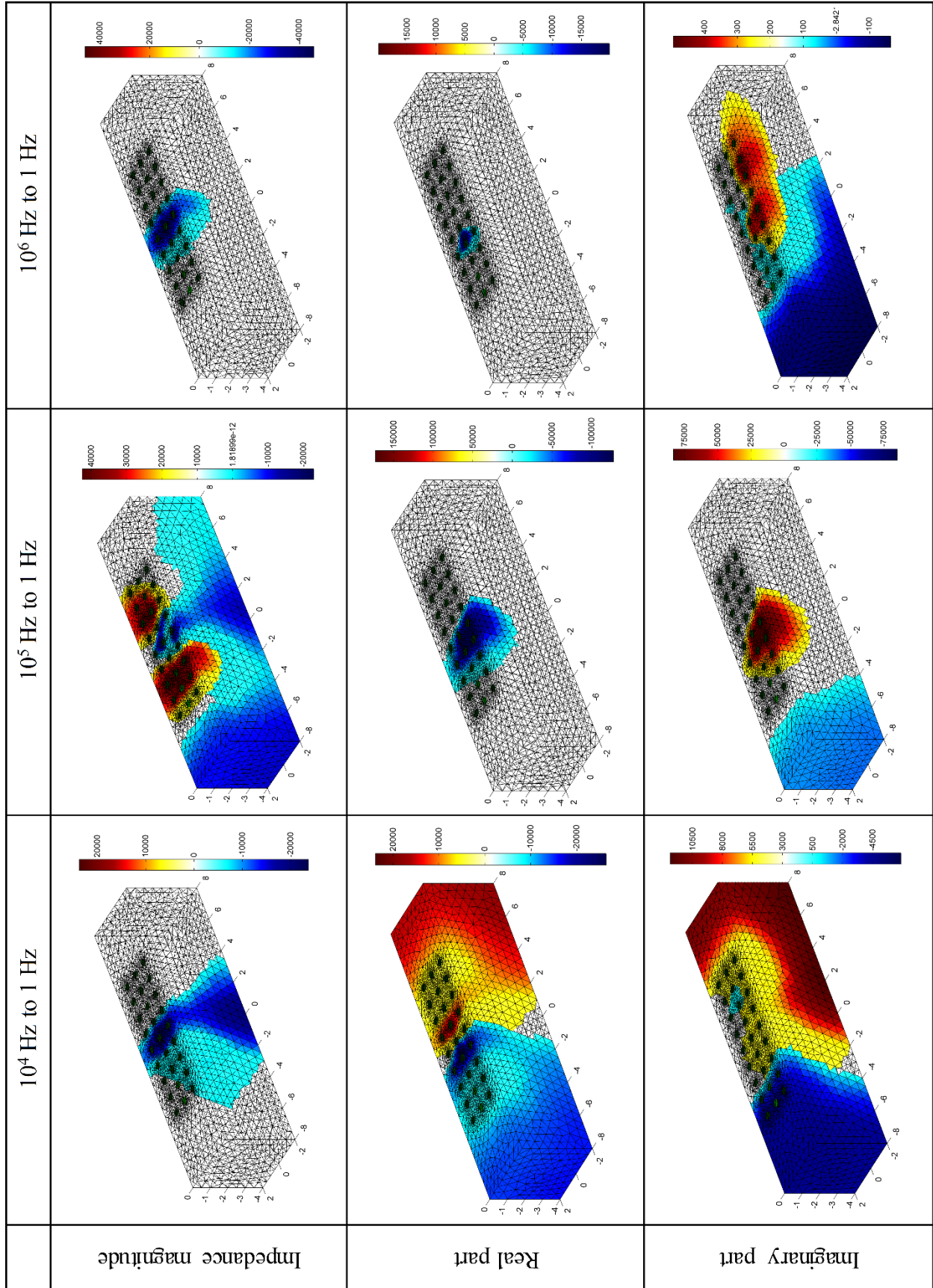
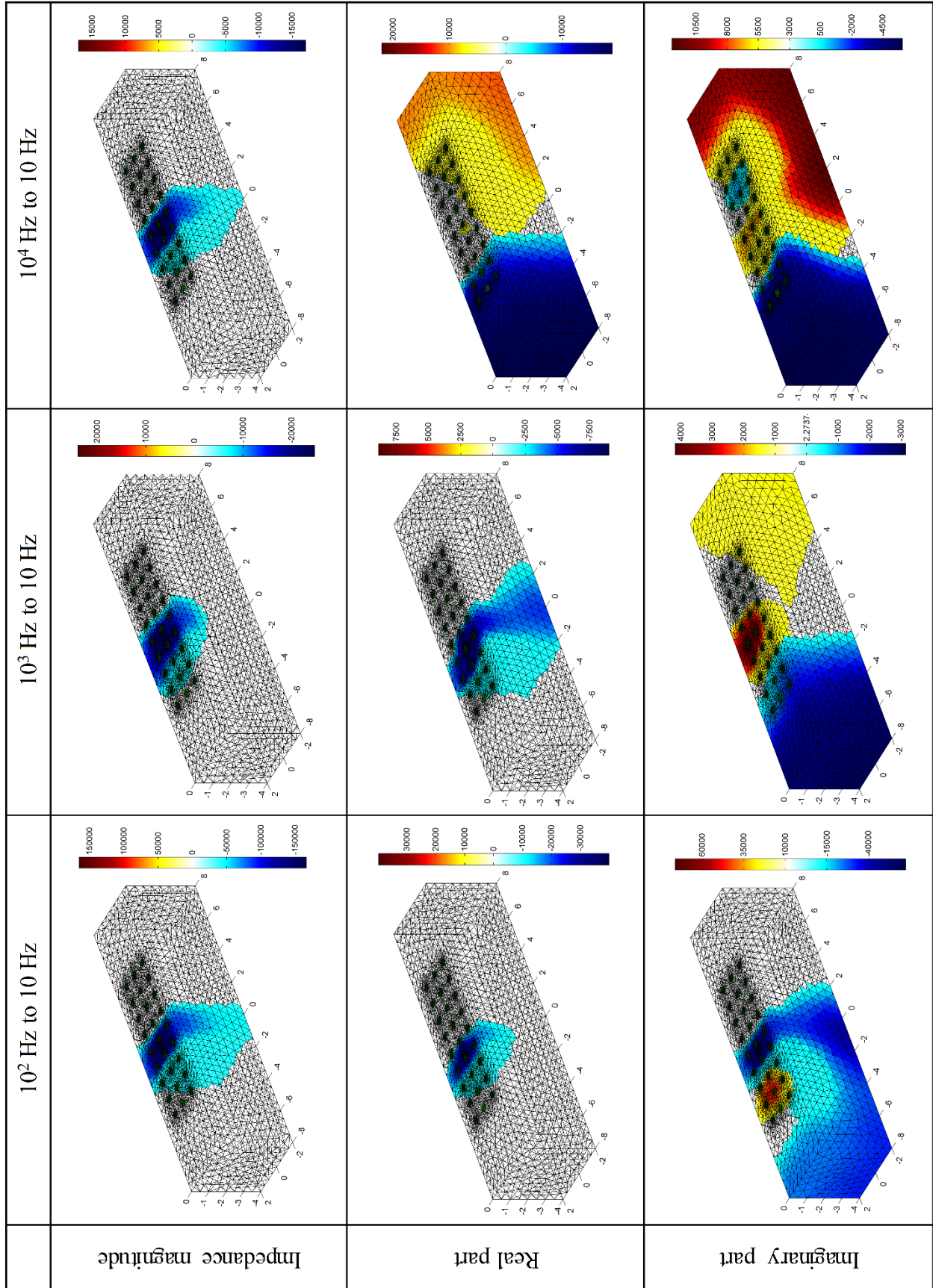


Figure 7.21 localized damage in the beam specimen

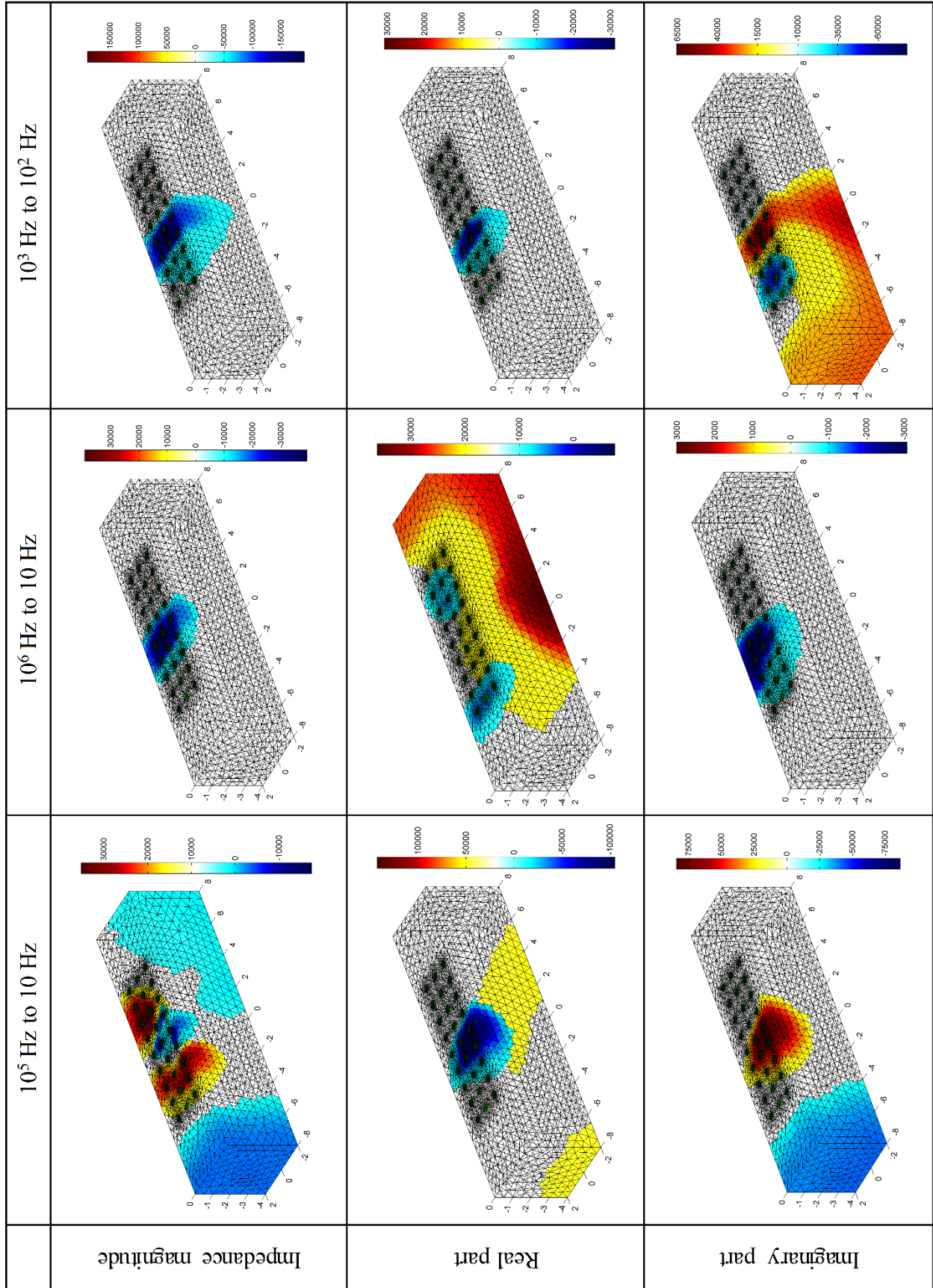
Figure 7.21 illustrates the damage pattern in the MSC specimen. After four-point bending test, there was one single crack in the middle of the specimen, with the crack width of 1.9 mm and the depth of 74 mm. 24 electrodes were mounted on the tension side of the specimen in three rows and eight columns for frequency different EIT data collection. The damage was located near 5<sup>th</sup> column of the electrode. Figure 7.22 shows the image reconstructions based on impedance magnitude, real part and imaginary part. Results depict that impedance magnitude and real part of the impedance provide image reconstructions with higher quality than imaginary part of the impedance. For image reconstructions based on imaginary part, the optimal frequency pairs include one at 100 kHz and the other from 1 Hz to 10 kHz. For image reconstructions based on impedance magnitude, the optimal frequency pairs are composed as follows. One frequency is between 1 Hz and 1 MHz; the other frequency is between 1 Hz and 100 Hz. For real part, the optimal frequency pairs are formed as follows. One frequency is between 1 Hz and 1 kHz; the other frequency is between 1 Hz and 100 Hz. Therefore, the optimum frequency range for impedance magnitude is wider than real part and imaginary part.

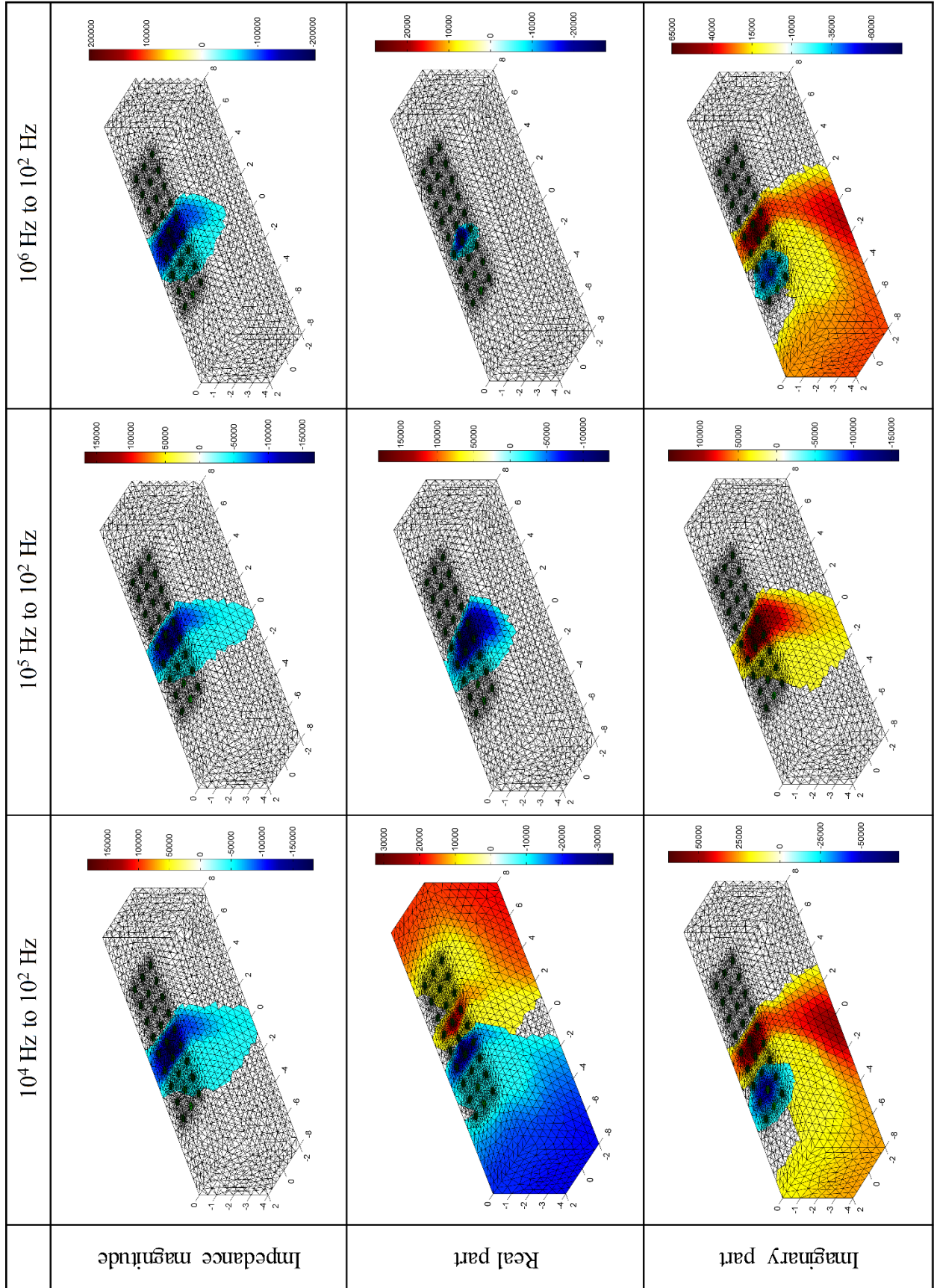


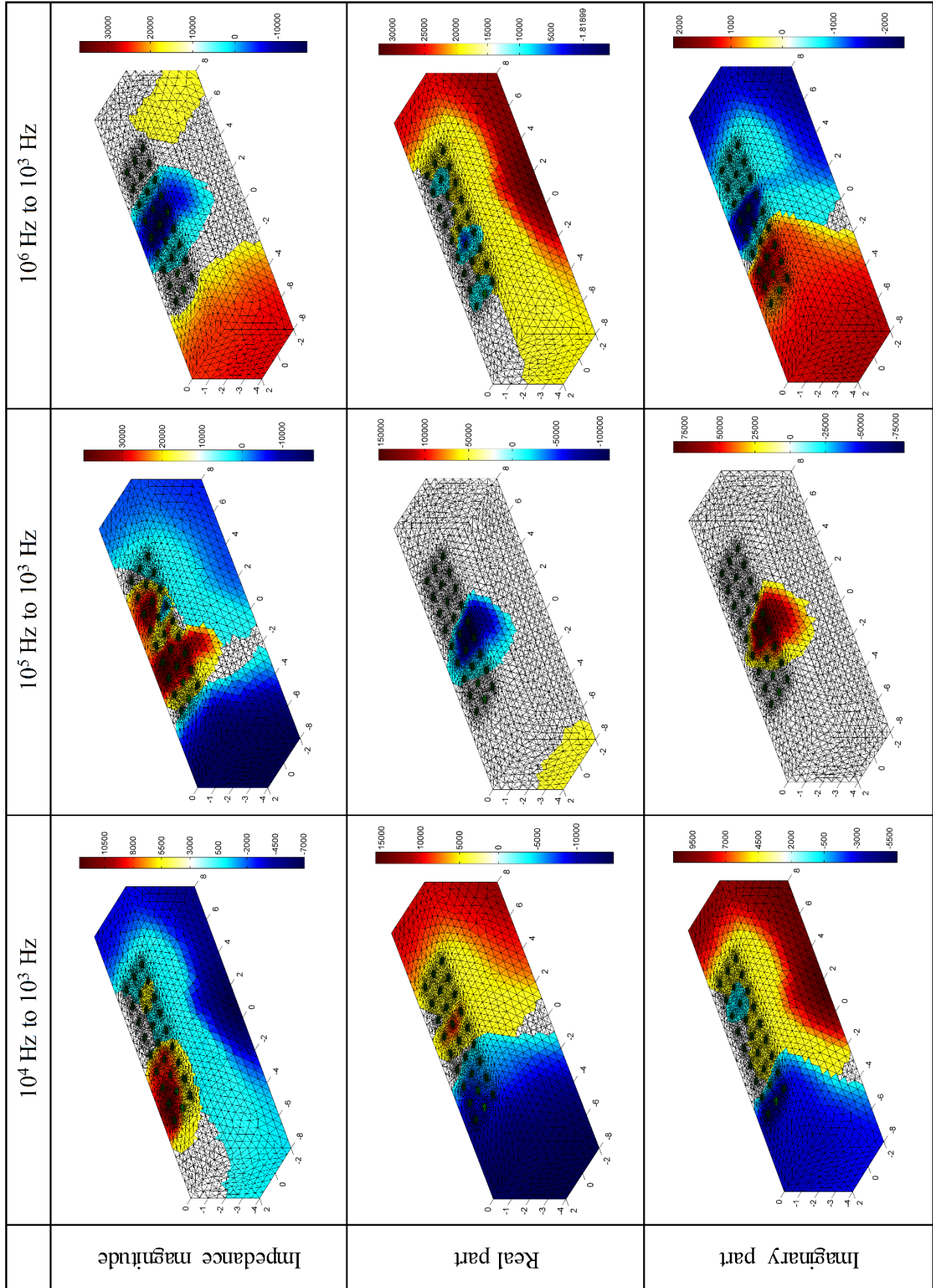












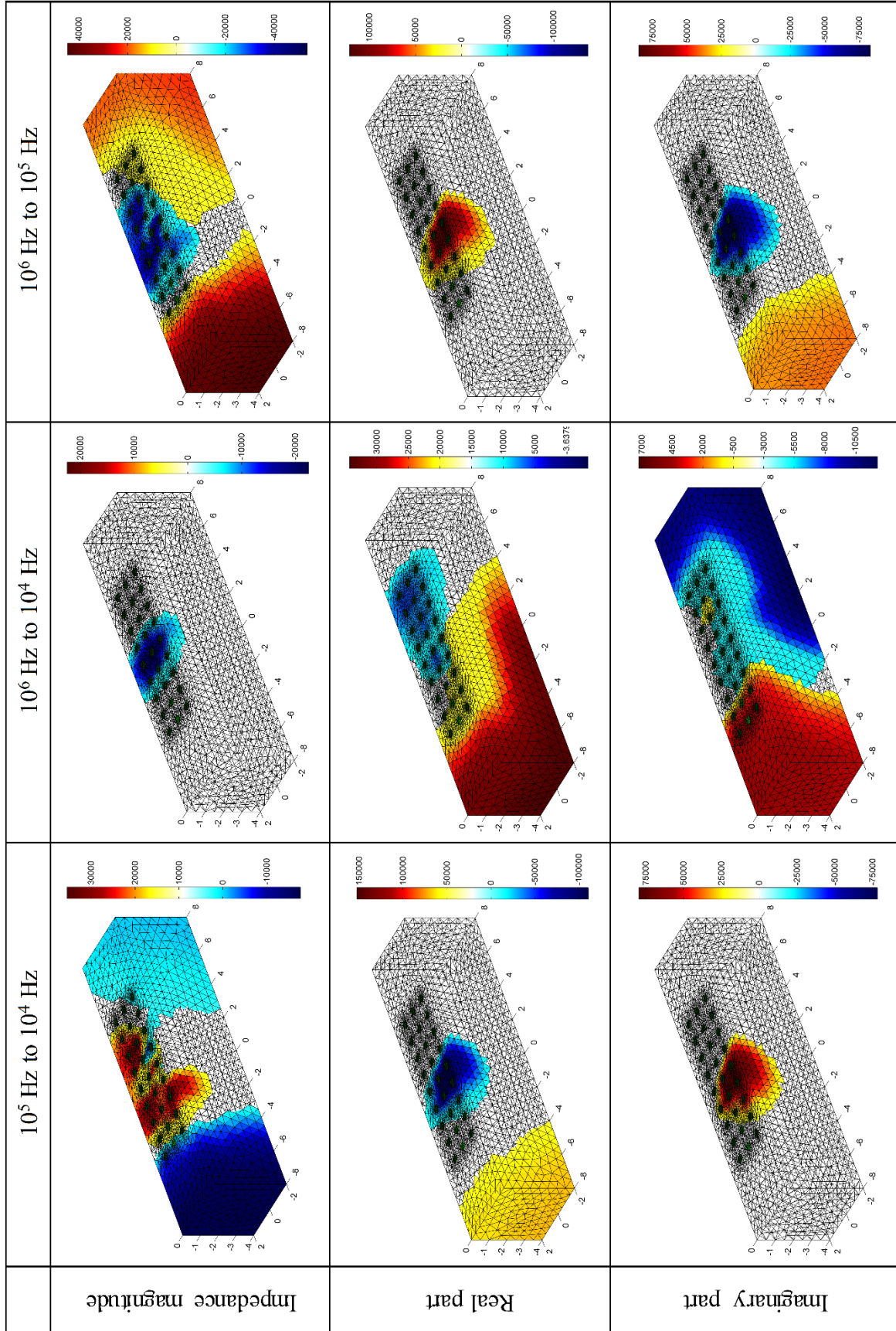


Figure 7.22 Image reconstructions of beam based on frequency-difference EIT

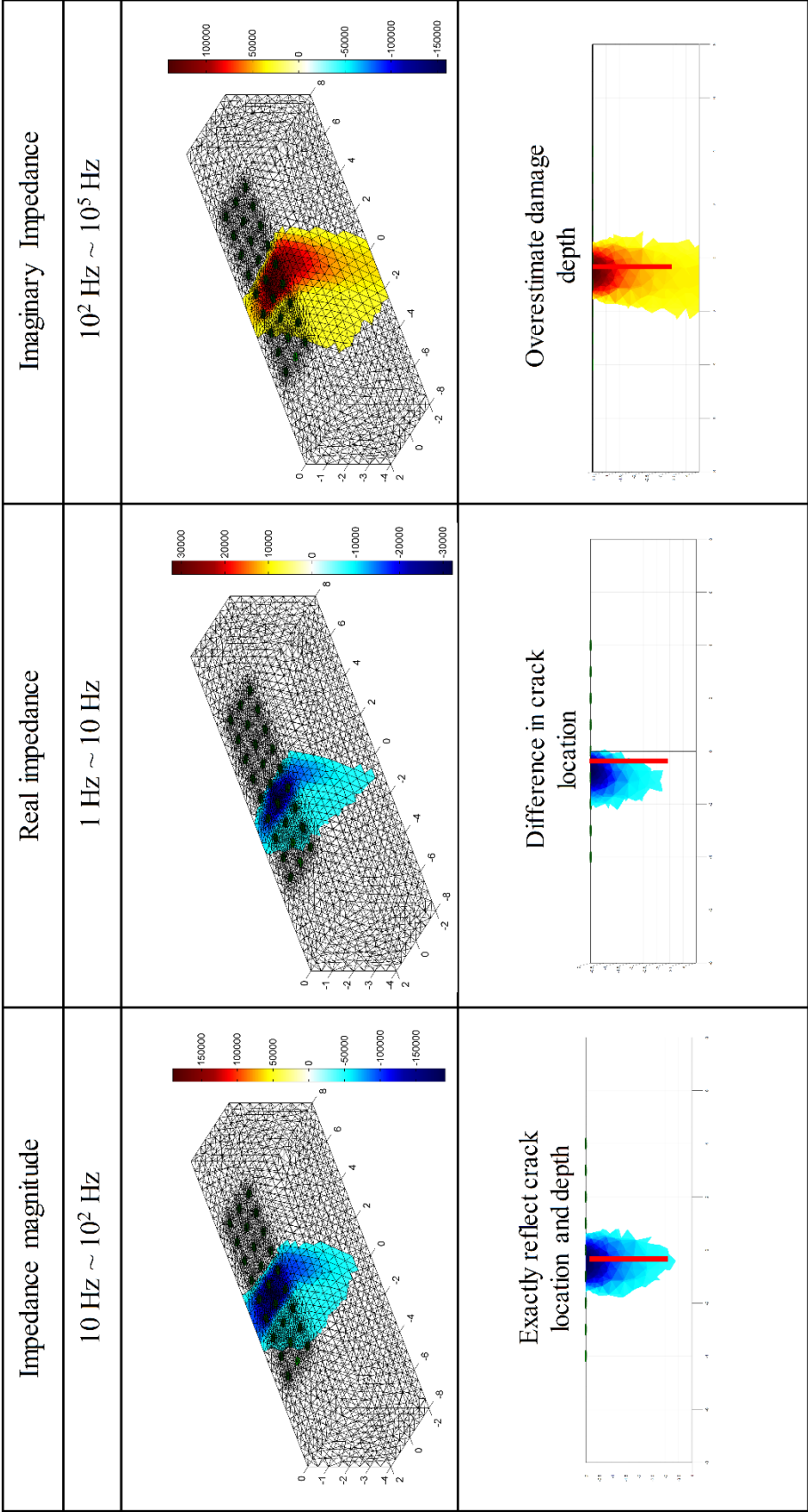


Figure 7.23 Image reconstructions for damage depth detection

Figure 7.23 compares the image reconstructions based on impedance magnitude, the real part, and the imaginary part. The best image reconstructions from each impedance type are plotted. It can be observed that image reconstruction based on impedance magnitude reflects the damage location and depth. For real part, the crack location was not exactly captured but the damage depth was able to be captured. For the imaginary part, The crack location was able to be reflected but the damage depth was overestimated.

## 7.6 Conclusions

The following conclusions are drawn from this chapter:

1. This chapter proposes the concept of frequency-difference EIT on cementitious materials. The evolution of frequency dependent impedance in terms of single crack opening shows that increasing damage level results into an increase in frequency dependency of the impedance. The differences of impedance at different frequencies can be used to reconstruct the conductivity distribution within the object.

2. The multifrequency EIT system established in Chapter 6 can be used for frequency-difference EIT. The available frequency range is from  $10^{-2}$  Hz to  $3.2 \times 10^7$  Hz, and the commonly used frequency range for the cementitious material is from 1 Hz to 1 MHz. The commonly used frequency range is determined by (1) presence of high-frequency arc in Nyquist plot of cementitious materials and (2) measurement time. The frequency-difference EIT system is validated by image reconstructions of damaged specimens.

3. A frequency-difference image reconstruction algorithm is established. Image reconstruction results validate this algorithm. The successful use of this algorithm relies on the frequency-dependent impedance characteristics of MSC: impedance becomes more frequency dependent with increasing damage level.

4. Image reconstructions of two-dimensional localized damage, two-dimensional distributed damage, and three-dimensional localized damage validate the applicability of frequency-difference EIT on damage sensing.

5. For the two-dimensional localized damage, frequency-difference EIT is able to detect the damage details as Time-difference EIT (Chapter 6). For image reconstructions based on impedance magnitude and real part of impedance, the low-frequency range (1 Hz ~ 10 kHz) is preferred. Image reconstructions in the high-frequency range (100 kHz and 1 MHz) display noise only. However, for image reconstructions based on imaginary part of impedance, the high-frequency range is preferred (100 Hz ~ 1 MHz). This is due to the fact that capacitor effect of MSC becomes obvious at the high-frequency range and imaginary part of impedance is directly related to the capacitor effect.

6. For the two-dimensional distributed damage, frequency-difference EIT is also able to detect the damage details. Although each microcrack cannot be identified, the distribution of multiple cracks is shown clearly. Image reconstructions involving 100 kHz shows noise only, which is due to low signal-to-noise ratio of 100 kHz measurement.

7. For the three-dimensional damage in the beam, frequency-difference EIT is able to capture the crack depth and crack location exactly. Unlike two-dimensional image reconstructions, impedance magnitude, the real part and imaginary part of impedance yield critically different image reconstructions. Image reconstructions based on real part of impedance accurately reflect the crack depth but the damage location is not exactly captured. Image reconstructions based on imaginary part capture the damage location but overestimate the damage depth and extent a lot. On the other hand, image reconstructions based on impedance magnitude clearly detect damage depth and location.

8. Different pairs of frequencies result into different image reconstructions. For impedance magnitude, the optimal frequency pairs are composed as follows: one frequency is between 1 Hz and 1 MHz, the other frequency is between 1 Hz and 100 Hz. For real part and imaginary part, the optimal frequency range is much narrower than impedance magnitude.



## CHAPTER 8: CORROSION SENSING IN MSCS

### 8.1 Introduction

Corrosion impact to steel inside the concrete has been studied from many aspects since it is the major cause affecting the early deterioration. Although reinforcing steel bars embedded in concrete usually could be against corrosion damage by the high alkalinity of pore water, while chloride ions approaching the surface of rebar can still pass through it then leads to critical corrosion [234]. In general, the phenomenon of corrosion happens on the steel embedded in concrete cover can be separated into three stages (Figure 8.1). The initial stage, which is a chemical reaction at the first place caused by adventive ions attacking steel. Subsequently, the reaction would change the chemical composite of steel and then lead to the secondary stage. In the second stage, the expansion of reinforcing steel bars would be against the concrete cover inducing tensile stress to create longitudinal cracks in the concrete matrix along the direction of embedded steel. In the third stage, further damage would be introduced to the system due to concrete crack and further corrosion of the steel. The first stage, corrosion initiation stage, takes the longest time compared to other stages. The third stage takes the shortest time but causes most significant damage to reinforced concrete structures. Corrosion effect does not only locally undermine the strength of embedded steel, but also brings out the severe cracking of the structure. Therefore, the degree of corrosion is a considerable parameter to predict the service life of the concrete structure.

Due to such significant effect caused by corrosion, researchers came out some methods to detect the deterioration of concrete and corrosion of embedded steel. For the purpose of measuring corrosion rate of steel bar in concrete, the non-destructive and electrochemical

techniques can be used to monitor corrosion of steel in the concrete structure. Some common ways to monitor corrosion rely on electrical techniques like concrete resistance measurement, electrochemical impedance spectroscopy (EIS) method, etc. EIS is a well-known technique which has been used by researchers to quantify corrosion phenomenon of steel bar [80, 89, 168, 169, 235-237].

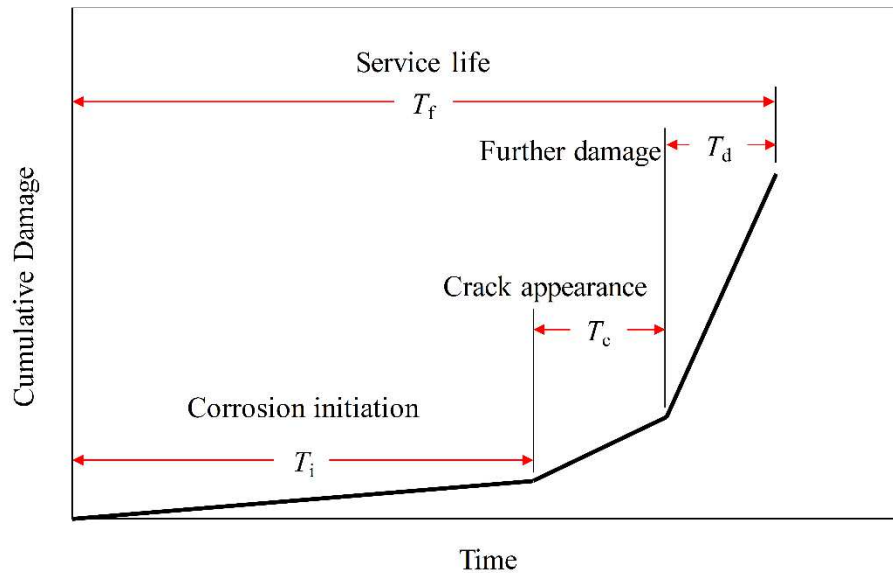


Figure 8.1 Comparisons of image reconstructions in terms of damage detection

In addition, inputting constant electricity into the specimen immersed in salt water environment allows rapid corrosion which was known as accelerated corrosion test. From the recorded electric current variation, people could observe a rapid increase in current after giving a constant electric potential for hours. The dramatic rise of current due to a reduction in electrical resistance indicates the occurrence of the second stage of corrosion. The occurrence of large cracks allows the conductive NaCl solution to come straight into concrete cover to directly contact with steel surface [238-240]. Therefore, this method not only provides an effective way

to introduce corrosion but also indicates when the second stage of corrosion occurs in the test sample.

This study aims to evaluate corrosion resistance of developed MSCs, and then utilize EIT to detect corrosion in the MSCs. MSCs have been designed to achieve high damage tolerance and high tensile ductility as described in previous chapters. Unlike ordinary concrete materials, MSC strain-hardens after initial cracking, which is as similar as metal materials, and displays a strain capacity 300 to 500 times higher than normal cementitious materials. As shown in Figure 3.14, a distributed multiple microcracking pattern was observed on the surface of the coupon specimen with the average crack width less than 65  $\mu\text{m}$ . Such kind of cracking pattern will allow ECC exhibiting nearly the same permeability as sound concrete [241, 242]. Previous studies showed that, due to high tensile strain capacity and microcracking behaviors, strain-hardening cementitious composites critically prolonged the corrosion propagation period while enhancing the ability to maintain the load capacity of the beam [238].

This study includes three parts. First, a feasibility study was conducted to evaluate the chemical sensing behavior of EIT on MSCs. In the initial stage of reinforcement corrosion, chloride penetration is an important process. In order to evaluate chloride penetration, it is therefore critical to first detect the presence of chloride. Second, chloride penetration process in MSCs was evaluated using EIT. A specific test setup was designed. Third, corrosion test was conducted on MSCs and then EIT scan was conducted so that image reconstructions were able to reflect the corrosion damage.

## **8.2 Chemical Sensing: a feasibility study**

Feasibility study for chemical sensing based on Electrical Impedance Tomography was conducted in the following way. A circular plate specimen (diameter = 76 mm; thickness = 10

mm) made from 5% MSC was prepared for chemical sensing test. The 5% MSC material was prepared following the same procedure described in chapter 3 and then cast into cylinder specimen (diameter = 76 mm; height = 152 mm). The specimen was cured at room temperature of 25 °C and constant relative humidity of 95% for 24 hours and then the specimen was demolded. Thereafter, the specimen was cured at room temperature of 25 ± 2 °C and relative humidity of 55 ± 5 % until the age of 28 days. Then a circular plate was cut from the cylinder specimen for the test.

In order to facilitate EIT measurement on the cylinder plate specimen, 24 electrodes were placed on the side surface of the specimen, as shown in Figure 8.2 (a). The electrodes were made via applying a thin layer of colloidal silver paste directly to the side surface of the specimen after sanding the surface, then attaching a layer of copper tape (width = 3.2 mm) on the top of the silver paint. The silver paint layer was intended to smooth the specimen surface and to minimize the contact impedance. The distance between each adjacent pair of electrodes was constant. Afterward, the insulated tape was used to wrap the side surface of the specimen so that connecting alligator clips did not result in loss of contact between the electrodes and the specimen surface

EIT scan was conducted following adjacent current injection and voltage measurement pattern. Alternating current (frequency = 1500 Hz) was injected into the specimen via a pair of two adjacent electrodes, such as 1~2, 2~3, ..., and 23~24, and then voltage measurement was conducted via the other pairs of adjacent electrodes. Therefore, for this scenario, there were a total of  $24 \times 21$  measurements.

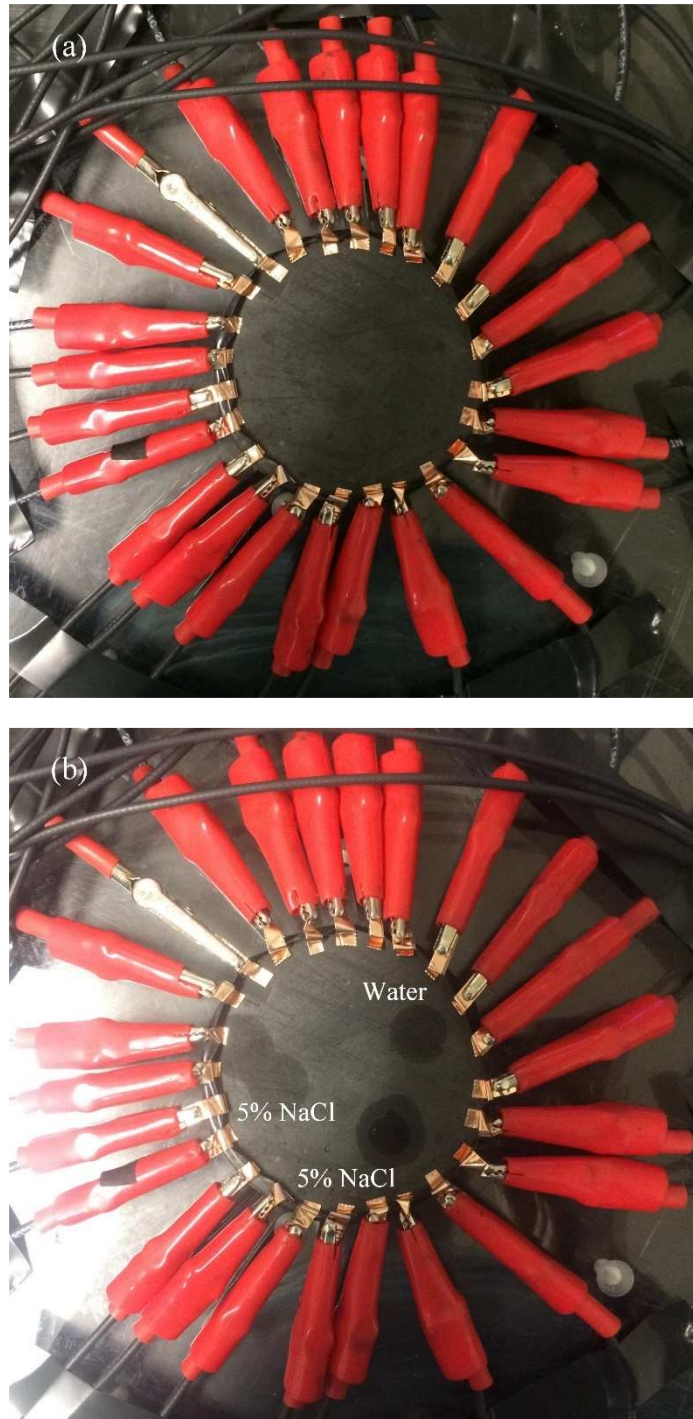


Figure 8.2 Chemical sensing test setup: (a) before dropping the liquid; (b) after dropping the water and 5% NaCl solution

After an initial scan of EIT, three drops of solutions were applied on the surface of the specimen as shown in Figure 8.2 (b). Two drops were 5% NaCl solution, and one drop was pure

water. Three drops were applied simultaneously. Thereafter, the other EIT scan was performed so that Time-difference EIT image reconstructions can be conducted.

Figure 8.3 shows the FEM model for image reconstructions. Three-node triangular element was utilized. There was a total of 14431 elements and 3563 nodes. Several trials have been done so that further increasing mesh number did not increase image reconstruction accuracy.

Figure 8.4 plots the image reconstruction results based on collected EIT data. It can be found that the location of the watermark on the surface of the specimen can be clearly captured by the image reconstructions, although slight difference can be found. There is noise observed in the image reconstructions, which does not interfere the presence of water and NaCl solutions. Also, it is found that the left and bottom watermarks had the higher conductivity than the watermark on the right side, suggesting that the presence of water and NaCl solution can be differentiated by EIT technology.

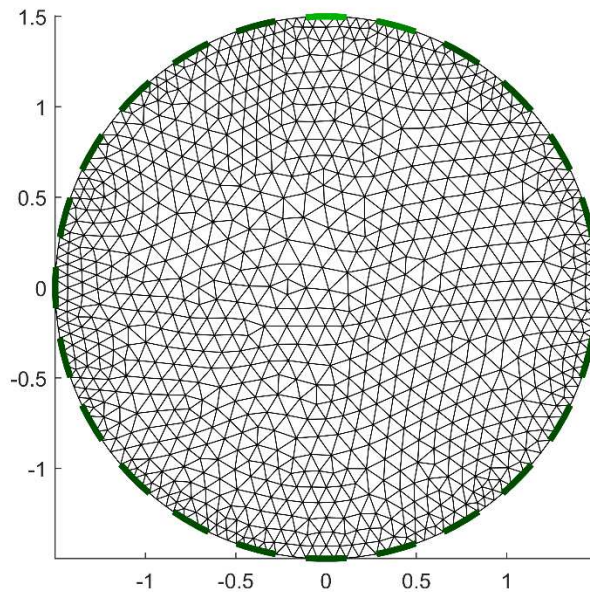


Figure 8.3 FEM model for image reconstruction

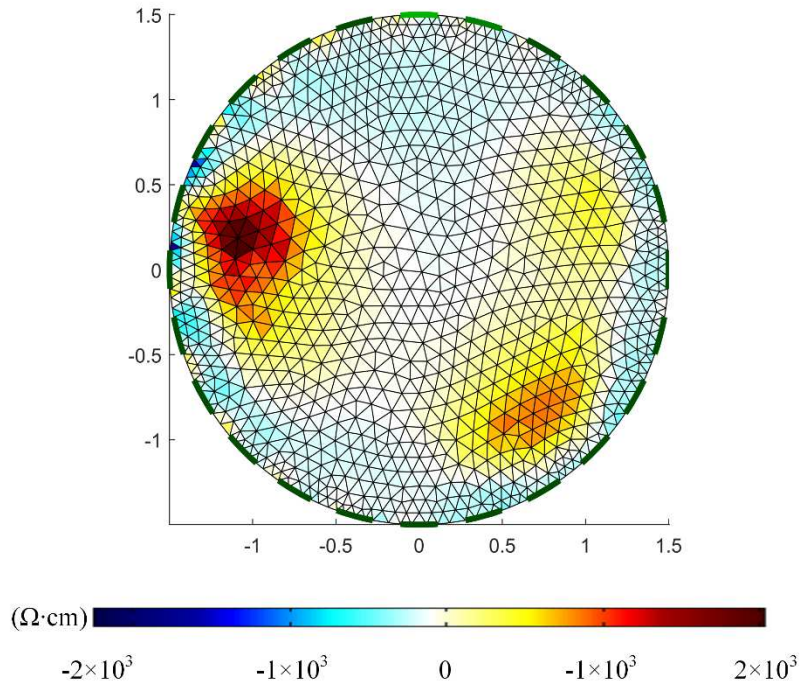


Figure 8.4 Image reconstruction for chemical sensing

### 8.3 Tracking Chloride Penetration

The previous section describes that concrete is effective in protecting embedded steel from corrosion. However, when the chloride concentration in the concrete reaches a certain level, the protective environment in the concrete will be destroyed. Currently, there are several methods to evaluate the chloride penetration resistance of the cementitious material, such as salt ponding test, bulk diffusion test, rapid chloride permeability test, electrical migration techniques, pressure penetration techniques, etc. Most of the tests are able to directly or indirectly estimate chloride penetration ability of the concrete material.

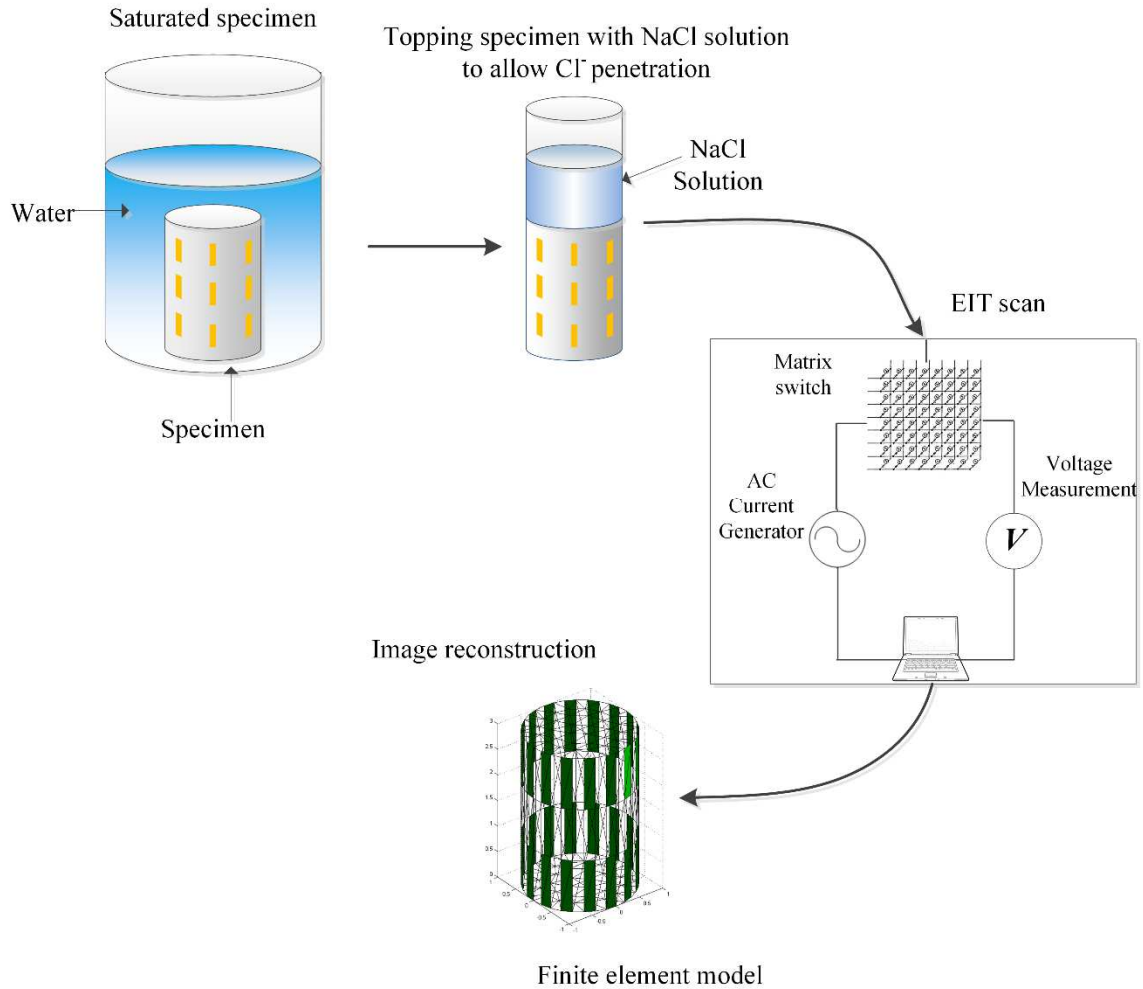


Figure 8.5 Chloride penetration monitoring using EIT technology

Figure 8.5 shows the specifically designed test to monitor chloride penetration in cementitious composites using EIT. First, the cylinder specimen was put into water to allow full saturation. Afterward, the specimen was topped with a plastic mold so that 5% NaCl solution can be placed upon the top surface of the specimen to form a salt pond. Copper electrodes were applied on the surface of the specimen. Image reconstructions were performed based on the collected EIT data.



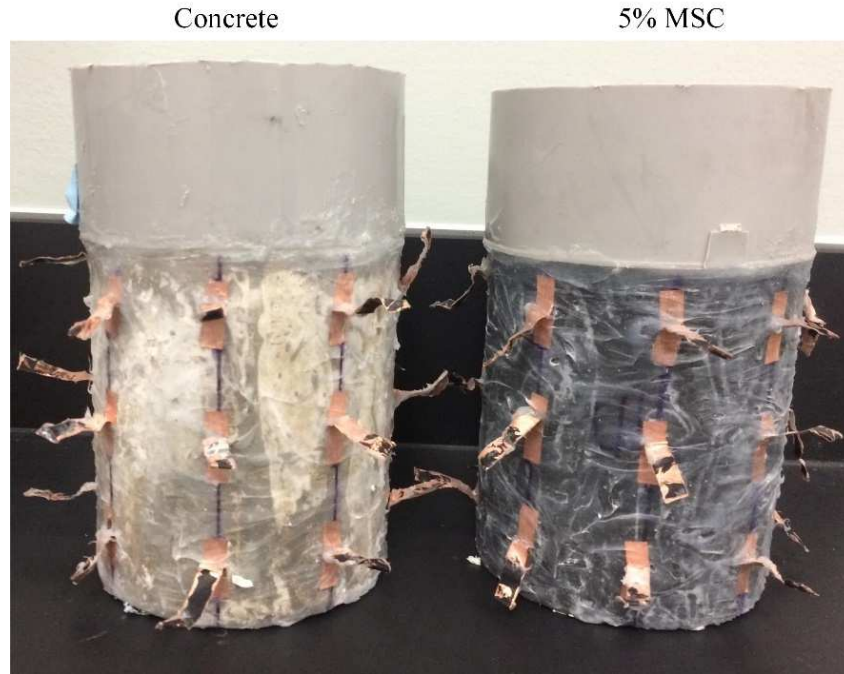


Figure 8.6 Chloride penetration monitoring using EIT

Figure 8.6 shows the specimens made from concrete and 5% MSC. Processing 5% MSC follows the same procedure as shown in Chapter 3. The concrete material was designed with the same water binder ratio as 5% MSC but without fiber. The fresh mixture was cast into cylinder specimen with the diameter of 101 mm and a height of 116 mm. After casting, the specimens were demolded after 24 hours and then were air cured under the room temperature of  $25 \pm 5$  °C and relative humidity of  $50 \pm 5$  % until the age of 28-day. The specimens were exposed to an outdoor environment until the age of 42 days for testing.

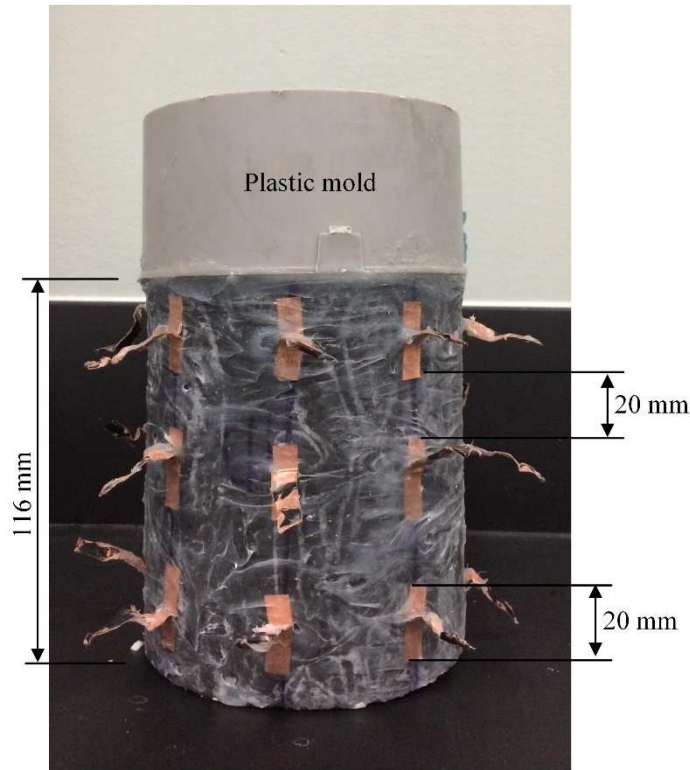


Figure 8.7 Specimen details and electrode setup

Figure 8.7 shows the specimen details and electrode setup for this test. 24 electrodes were mounted on the surface of the specimen in three layers, with eight electrodes in one layer. The distance between the adjacent electrodes in one layer is a constant. The distance between adjacent layers is 20 mm. First, a thin layer of colloidal silver was applied on the surface of the specimen, and then a layer of copper tape (width = 3.2 mm) was attached on the top of the silver paste. The silver paint layer was intended to smooth the specimen surface and to minimize the contact impedance. The copper tape is the copper foil (thickness = 0.038 mm) with an acrylic conductive adhesive (thickness = 0.032 mm). The length of each electrode, as shown in Figure 8.7, is 20 mm. After mounting electrodes, silicone was applied on the surface of the electrodes and specimen to avoid leakage from the specimen surface and loss of contact between the electrodes and the specimen. A plastic mold was installed on the top of the specimen to create the dam for chloride solution. The specimens with dams were subjected to continuous ponding

with 5% NaCl solutions to a depth of 15 mm for 45 days. The top of plastic mold was sealed with plastic wrap to minimize evaporation, and the additional solution was added if necessary to maintain the 15 mm depth.

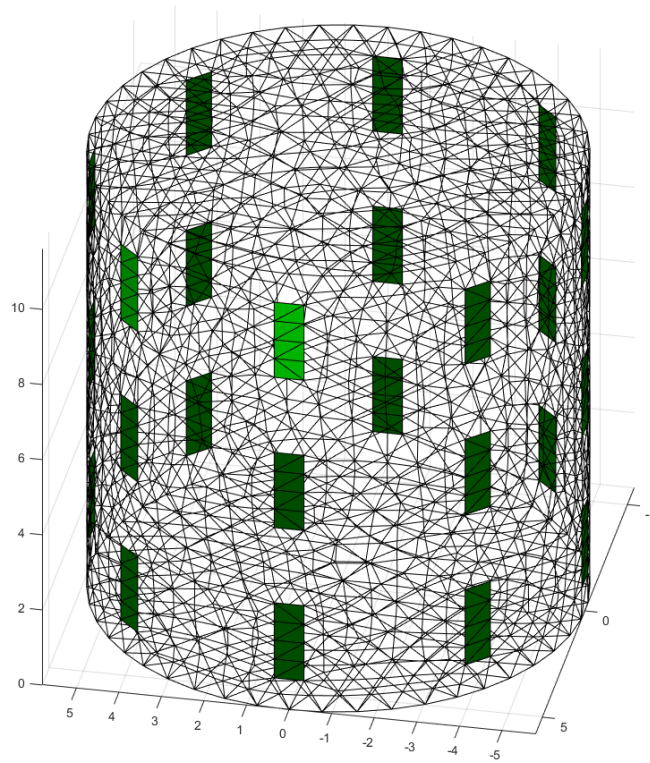
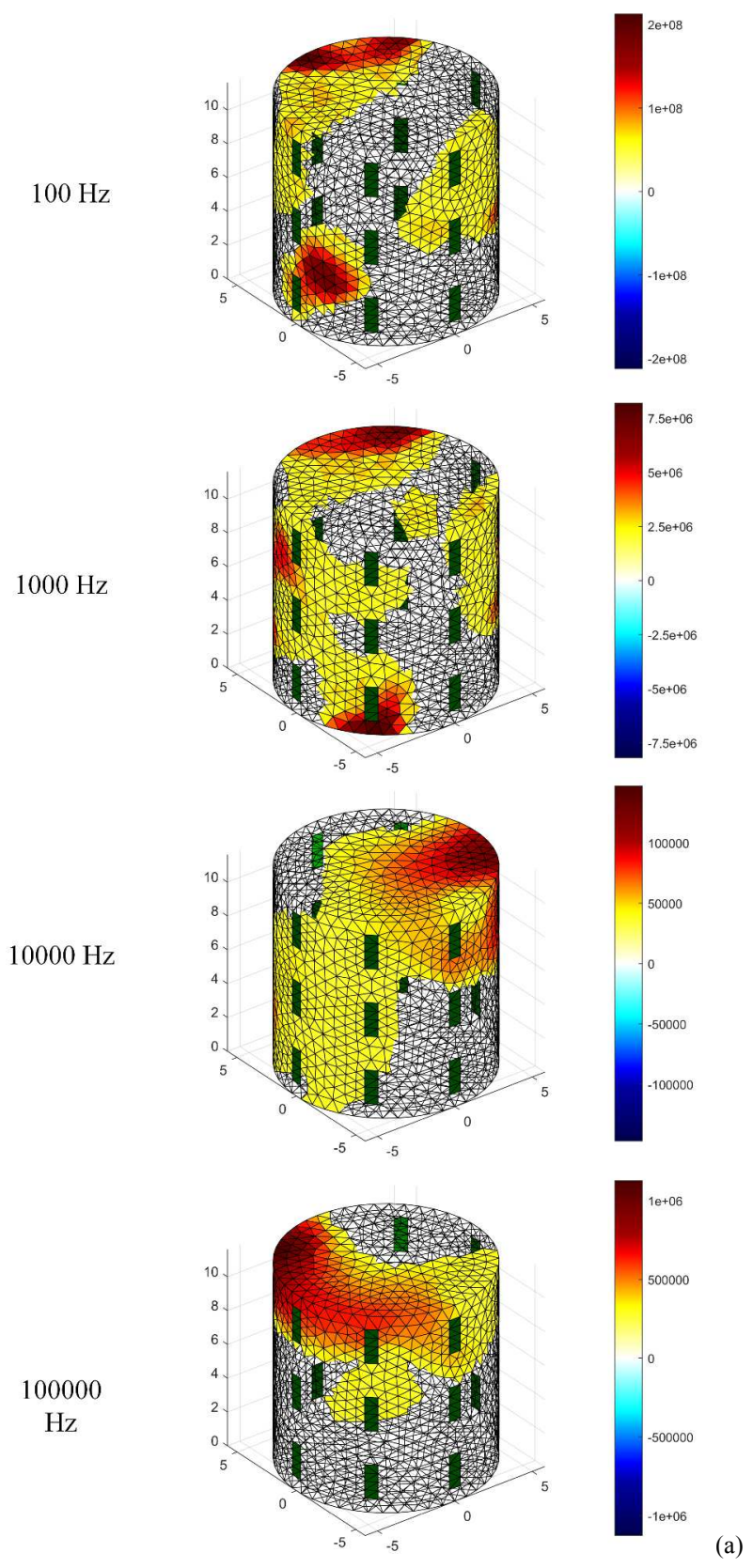
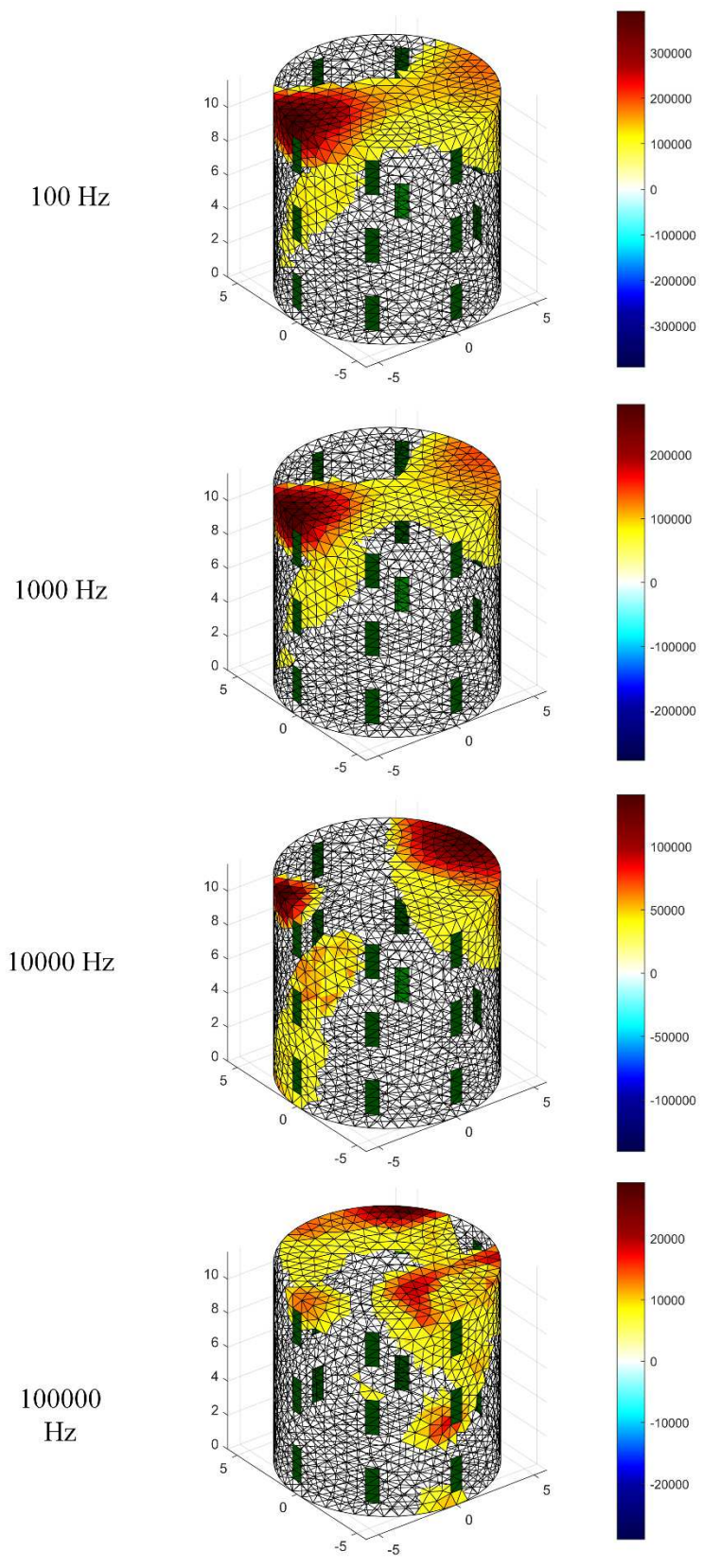


Figure 8.8 FEM model for image reconstructions

One FEM model was established for image reconstructions. This model contains 3894 nodes and 18973 elements. 24 electrodes were modeled. The light color electrode was numbered as one in this study. Image reconstruction results were plotted in Figure 8.9. It is found that for both concrete and 5% MSC, the top side of the specimen experienced an increase in conductivity, suggesting that there was more chloride content on the top side of the specimen. It is also observed that conductivity increase is more dominated for 5% MSC than concrete at the top side of the specimen, suggesting the porosity of 5% MSC is higher than concrete.





(b)

Figure 8.9 Image reconstructions for (a) 5% MSC (b) concrete.

## 8.4 Spatial Corrosion Sensing Using EIT

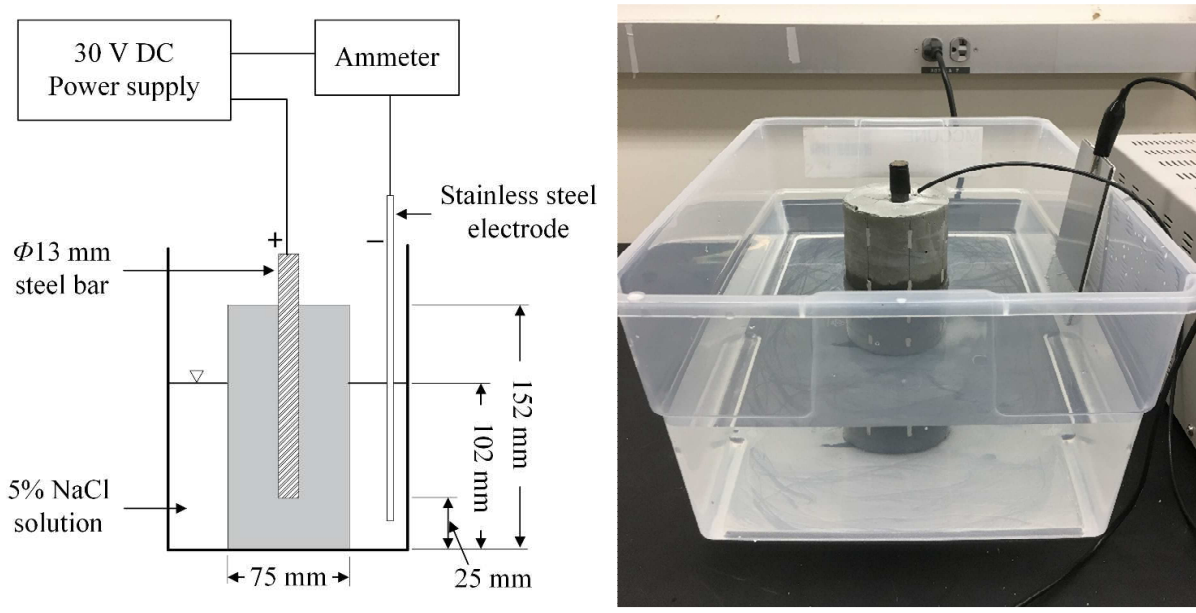
In order to evaluate the corrosion resistance of MSCs and detect the corrosion occurrence within cementitious materials, a test scheme was established. The test scheme included two critical aspects: the first aspect is the accelerated corrosion test; the second aspect is the EIT test.

### 8.4.1 Materials and test setup

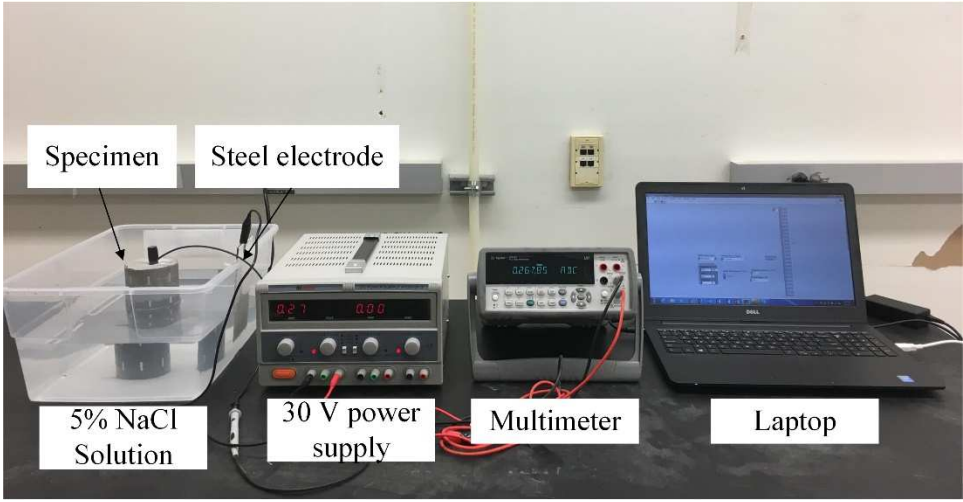
Four types of cementitious materials were prepared in this study (Table 8.1). The first material is a normal SHC material. Second material (0% Mortar) has the same mix design as 0% SHC but without fibers. The third material is 5% MSC and the fourth material is same as 5% MSC but without fibers. The materials were prepared as same as chapter 3. The materials were cast into cylinder molds with the diameter of 75 mm and the height of 152 mm. A steel rebar (#4) was embedded in the center of the specimen and located at 25 mm high from bottom of the specimen. Figure 8.10(a) and Figure 8.11 show the cylinder specimen. From those conditions above, it makes the distances are all equal from the surface of rebar to the boundary of the specimen, which allows a reasonable situation that chloride ions must travel same distance reaching the steel [243].

Table 8.1 Mix design

Design	Water kg/m <sup>3</sup>	Cement kg/m <sup>3</sup>	Sand kg/m <sup>3</sup>	Fly ash kg/m <sup>3</sup>	Carbon Black kg/m <sup>3</sup>	Superplast icizer kg/m <sup>3</sup>	Fiber Vol-%	Silica fume kg/m <sup>3</sup>
0% SHC	312	292	456	935	0	2.7	2	0
0% Mortar	312	292	456	935	0	2.7	0	0
5% MSC	296	243	380	600	25	3.5	2	115
5% Mortar	296	243	380	600	25	3.5	0	115



(a)

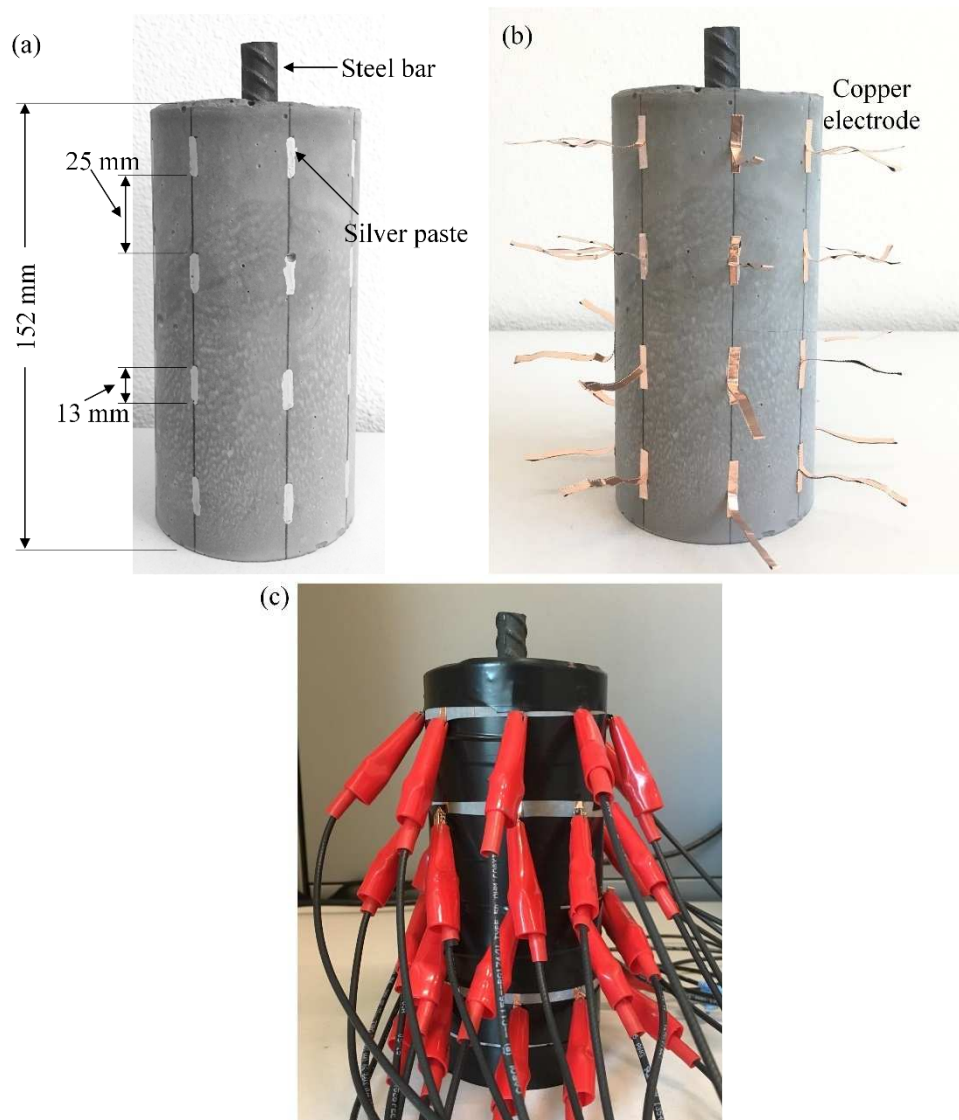


(b)

Figure 8.10 Accelerated corrosion test setup: (a) corrosion test up details; (b) overview of the corrosion test setup

Figure 8.10(a) shows the schematic diagram for test setup of accelerated corrosion test. In order to mimic a seawater environment, specimens were partially immersed in 5% sodium

chloride (NaCl) solution up to 102 mm during the test. A 30-volt DC power supply was used to provide constantly stable current to the system. The positive terminal was connected to the steel rebar and the negative terminal was connected to a stainless steel plate. Thus, the negative charges,  $\text{Cl}^-$  ions were attracted to positive terminal accelerating the corrosion occur inside the specimens. The current flow meanwhile was continuously logged by ammeter to approximately detect corrosion and crack appearance. Figure 8.10 also shows a picture of the test setup. A 0% Mortar sample was placed in the tank with NaCl solution. Labview software was used to control the data collection rate of the multimeter.







this study, Time-difference EIT is not able to be used due to change of conductivity of the specimen from time to time.

EIT scan followed the current injection and voltage measurement pattern as shown in Figure 8.13. The electrode was numbered following the figure in the first column of Figure 8.13. Then for each measurement, the current was injected from a pair of electrodes with an adjacent number, i.e., 1~2, 2~3, etc. (see the third column in Figure 8.13), and the voltage measurements were conducted via the rest pairs of electrodes (fourth column in Figure 8.13). In total, there were  $32 \times 29 = 928$  measurements.

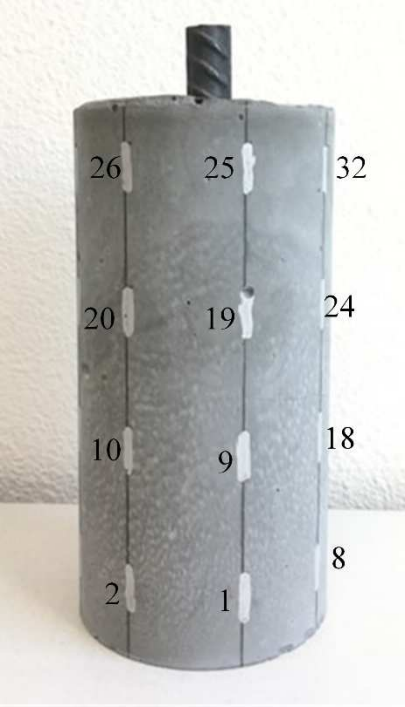
Electrode number	No.	Current injection	Voltage measurement
	1	1~2	3~4, 4~5, ..., 31~32
	2	2~3	4~5, 5~6, ..., 32~1
	...	...	...
	32	32~1	2~3, 3~4, ..., 30~31

Figure 8.13 Current injection and voltage measurement pattern

#### 8.4.2 Corrosion test results

Figure 8.14 shows the accelerated corrosion test results of different specimens. Figure 8.15 ~ Figure 8.18 shows the test results of 0% SHC, 5% MSC, 0% Mortar, and 5% Mortar, separately, and the pictures of specimens at different stages during corrosion test. The change of current as a function of corrosion time under the fixed potential for each specimen is the average of three specimens. This curve allows to determine the corrosion initiation and observe the corrosion development. As observed from Figure 8.14, the differences between mortar materials and MSC or SHC materials are significant. Once the test was stopped, the specimens were immersed in NaCl solution for another month to allow non-accelerated corrosion.

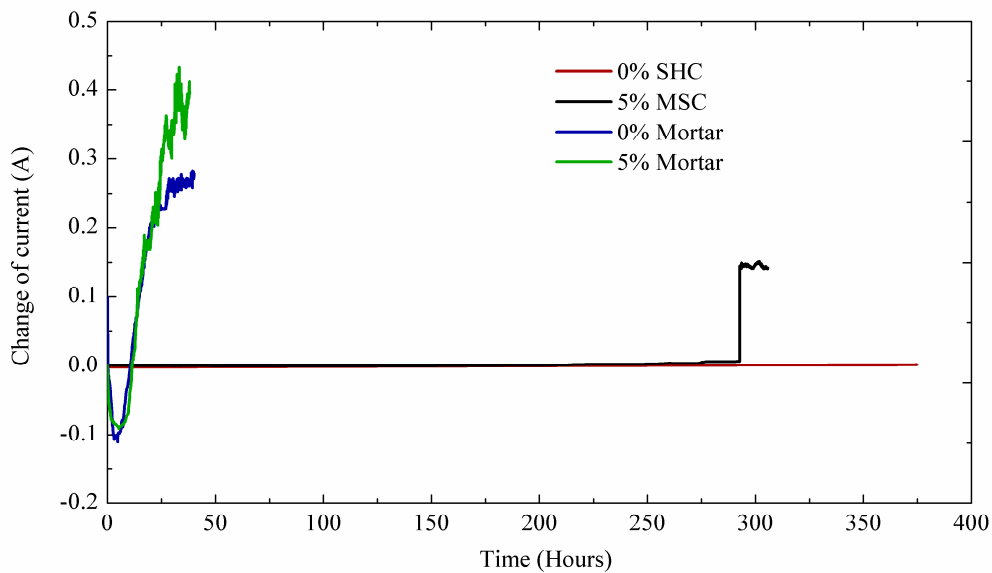
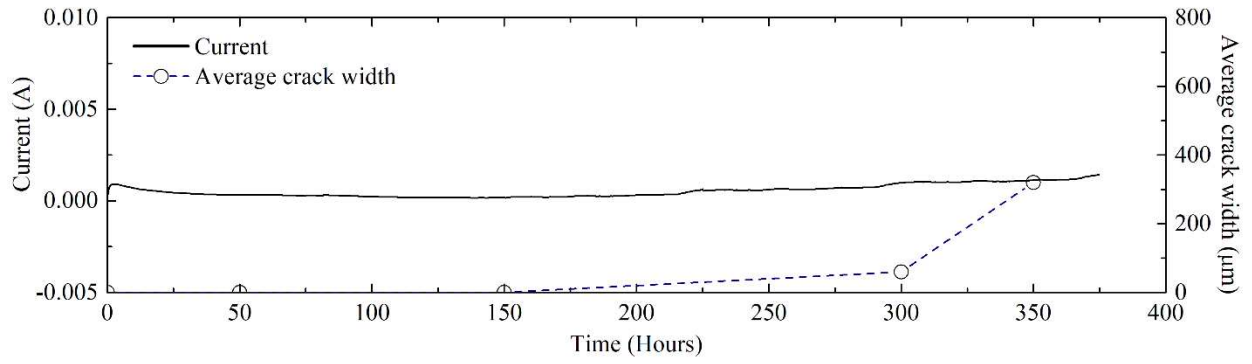


Figure 8.14 Change of current in terms of time for different specimens



50 h

150 h

300 h

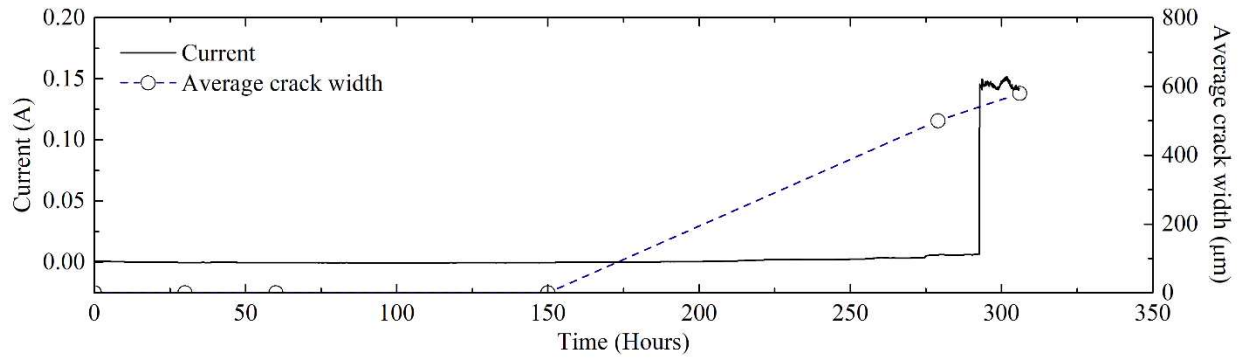
350 h

(a)



(b)

Figure 8.15 0% SHC at different corrosion stage. (a) during accelerated corrosion test; (b) one month under non-accelerated corrosion



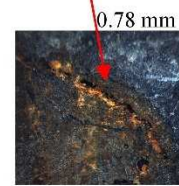
60 h

150 h

275 h

310 h

(a)



(b)

Figure 8.16 5% MSC at different corrosion stage. (a) during accelerated corrosion test; (b) one month under non-accelerated corrosion

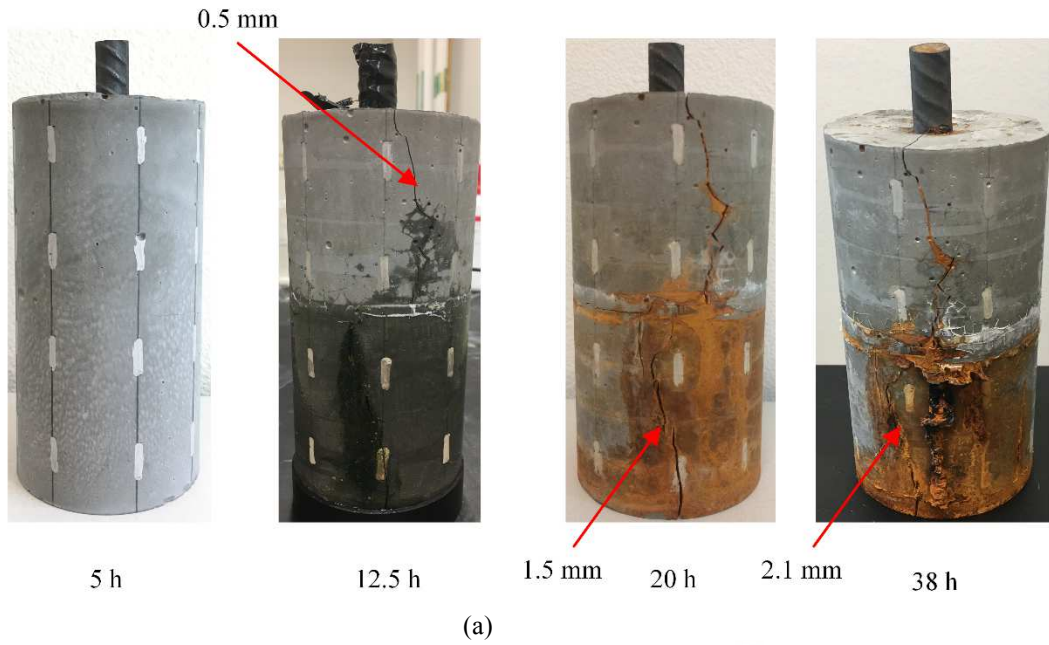
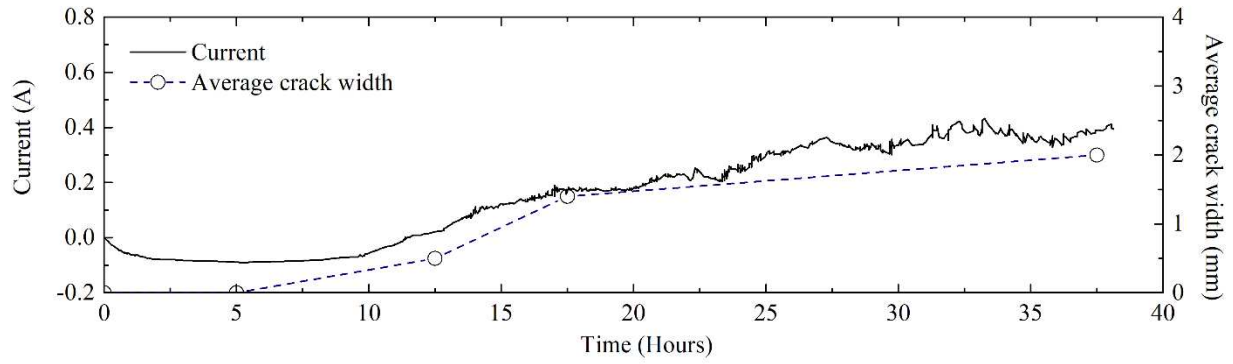
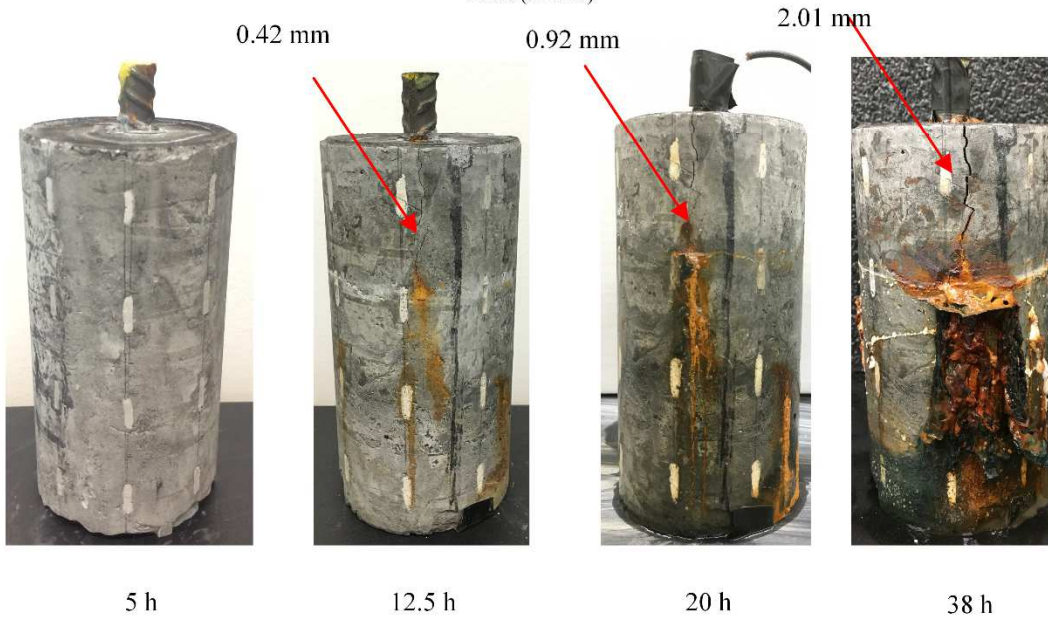
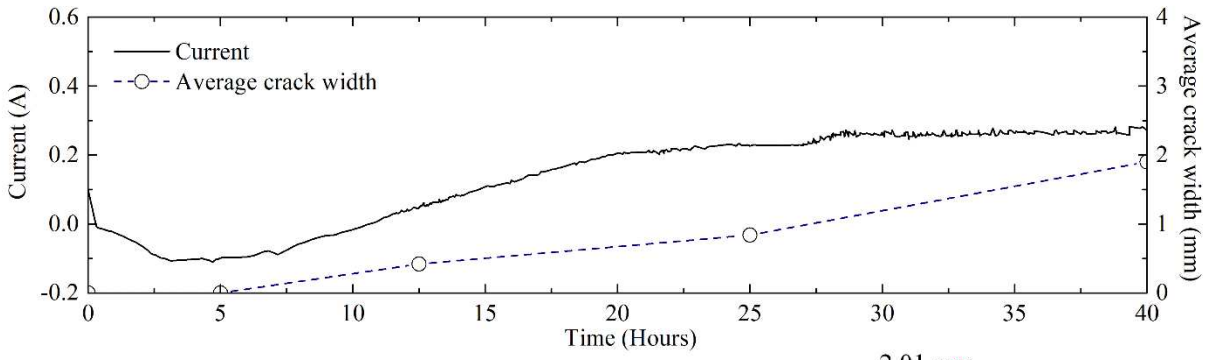


Figure 8.17 0% Mortar at different corrosion stage. (a) during accelerated corrosion test; (b) one month under non-accelerated corrosion



(a)



(b)

Figure 8.18 5% Mortar at different corrosion stage. (a) during accelerated corrosion test; (b) one month under non-accelerated corrosion

For 0% Mortar and 5% Mortar samples, the current decreased a little bit initially until approximately 10 hours, and then an instant increase was observed, suggesting that concrete cover cracked. Figure 8.17 and Figure 8.18 shows the pictures of Mortar specimens. For 0% Mortar, initial crack was observed after around 10 hours of corrosion, accompanied by the increase in current. At 12.5 h, a 0.5 mm wide vertical crack was observed on the surface of the specimen. At 20 h, the crack became wider (1.5 mm), and there was yellow rust leaking from the crack. At 38 h, the damage became more severe. The crack actually penetrates the whole specimen. The phenomena observed for 5% Mortar sample was similar to 0% Mortar. The current firstly decreased and then increased to around 5 h. That means that the specimen was cracked. At 12.5 h, the surface crack was 0.42 mm wide. At 20 h, yellow rust leaked from the crack and the crack became as wide as 0.92 mm, indicating further corrosion within the sample. The accelerated corrosion test was paused at 38 h. The crack was 2.01 mm wide and a large amount of rust leaking from the crack.

For 0% SHC and 5% MSC, the current steadily increased all through the test. However, for 5% MSC, at 280 h, there was one rapid change in current, suggesting that there was one obvious crack emerged. For 0% SHC, microcracks were not observed until 150 h. At 300h, although there was steel rust observed on the surface of the specimen, the average crack width was still as low as 70  $\mu\text{m}$ . At 350 h, there was some steel rust observed on the surface of the specimen. After one-month non-accelerated corrosion, the specimen did not damage at all. For 5% MSC, same as 0% SHC, initial microcracks on the surface the specimen was first noted after 150 hours. Instant change in current indicated the occurrence of obvious cracks, forming a penetrating path so that NaCl solution was able to directly contact with the embedded steel, speeding up the steel corrosion. After accelerated corrosion test and nonaccelerated corrosion



test, there were still no large cracks found on the surface of 5% MSC specimen. The largest cracks in 5% MSC samples have the crack width as large as 0.21 mm and 0.78 mm. Since the change in current indicated the corrosion degree occurred in steel, it can be found that the corrosion degree of 0% and 5% Mortar was 40 times higher than 5% SHC and 5% SHC at the same time.

Above test results validate the high corrosion resistance of 5% MSC and 0% SHC. At different corrosion stages, EIT scan was conducted. Image reconstructions were reported here to verify whether frequency-difference EIT technology and the image reconstruction algorithm in this study was able to monitor the corrosion development or not.

#### *8.4.3 EIT image reconstructions*

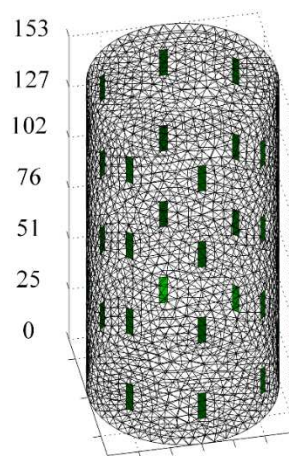


Figure 8.19 FEM model used for image reconstructions

Figure 8.19 shows the FEM model for image reconstructions. The model contains 3788 points and 18654 elements. The lightest electrode in the model is the 1<sup>st</sup> electrode. The model completely simulates the specimen dimension and electrode setup.

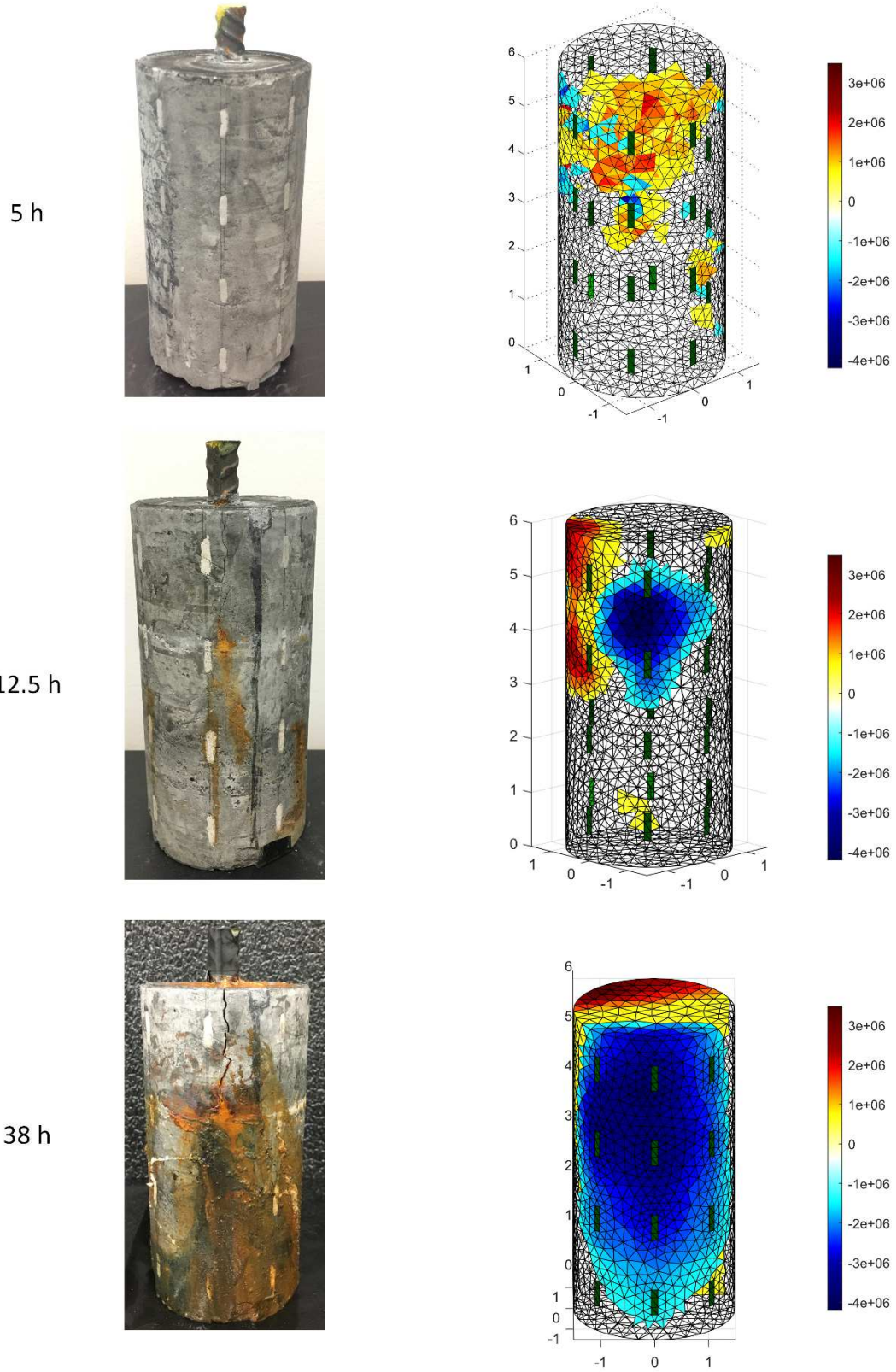


Figure 8.20 Image reconstructions for corrosion sensing of 5% Mortar

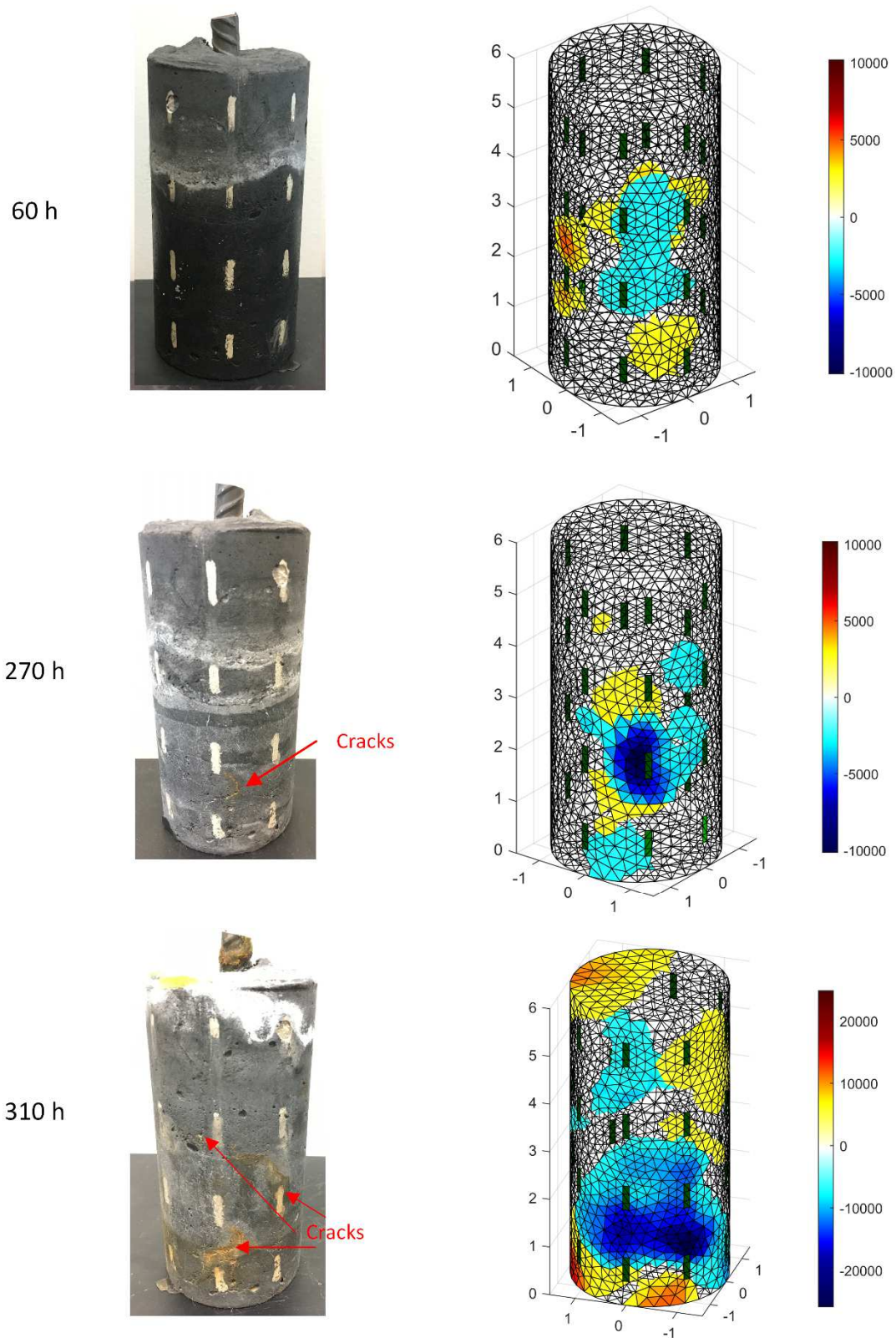


Figure 8.21 Image reconstructions for corrosion sensing of 5% MSC

Frequency-difference EIT image reconstructions were performed to track the corrosion damage in 5% MSC and 5% Mortar. Figure 8.20 and Figure 8.21 shows the image reconstruction results at different corrosion stage. The blue color in the figures represents the presence of low conductivity, indicating the cracks and corrosion damage in this scenario. It should be noted that image reconstructions based on different frequencies were obtained but only representative images were reported to compare with real damage pattern.

Figure 8.20 shows that image reconstructions were able to track the corrosion-induced damage in the 5% Mortar specimen. At 5 h, image reconstruction shows high conductivity only, which might be due to the steel or corrosion. At 12.5 h, image reconstruction captured a localized crack in the specimen. At 38 h, the low conductivity distribution became significant, suggesting that the localized damage and corrosion damage became severe.

Figure 8.21 plots the image reconstructions to monitor the corrosion damage in 5% MSC specimen. At 60 h, although there were no cracks observed on the surface of the specimen, the image reconstruction captured the low conductivity distribution inside the specimen, suggesting that EIT image reconstruction was able to reflect internal damage induced by corrosion or microcracks. At 270h, the surface emerged cracks were captured by image reconstructions. The damage shape was overestimated. At 310 h, the damage became more severe and image constructions showed a large area of low conductivity.

It should be mentioned that the resolution of corrosion sensing is not as high as the damage sensing in the beam or coupon specimen. There are two reasons: (1) corrosion damage is highly distributed in the specimen. (2) The difference image algorithm considers linear assumption in Taylor Expansion. However, for this scenario, the damage was complicated, and

the background conductivity was not uniform. Therefore, a nonlinear assumption is preferred. However, the damage occurrence, location, and severity can still be revealed clearly.

## 8.5 Conclusions

The following conclusions are drawn from this chapter:

1. One test is devised to evaluate the chloride sensing behavior of MSC using Time-difference EIT. Image reconstructions are able to differentiate the presence of water and 5% NaCl solution in MSC materials. Compared with water, NaCl solution results into higher conductivity distribution as reflected by image reconstructions. The conductivity change captured by EIT allows chemical sensing to detect the presence of chloride ions.

2. One test setup is designed to monitor the chloride penetration within cementitious materials using Time-difference EIT. Image reconstructions are able to reflect the conductivity change within the cementitious materials during chloride penetration. The top side of the specimen becomes more conductive after 45 days salt ponding, which can be captured by the EIT. 5% MSC has more volumes in the specimen with increasing conductivity, suggesting the 5% MSC has higher porosity than control specimen. Therefore, EIT is able to track chloride penetration of cementitious materials.

3. One test is proposed to evaluate the corrosion resistance of MSCs and monitor the corrosion of the reinforced MSC. 5% MSC and 0% SHC have the supreme advantages in terms of corrosion resistance compared with 0% Mortar and 5% Mortar. Corrosion-induced crack width of 5% mortar and 0% mortar specimens increase with time as corrosion progresses. At higher levels of corrosion (corrosion time was around 40-hour), the crack width becomes around 2 mm and then the specimens are damaged totally. However, for 0% SHC and 5% MSC specimen, initial cracks are observed after 150 hours. At 300h, the average crack width of 0%

SHC specimen is around 65  $\mu\text{m}$ , and a number of microcracks are observed on the surface of the specimen. At 300h, the average crack width of 5% MSC specimen is about 600  $\mu\text{m}$ . There are a number of microcracks and one large crack. The observation shows that 0% SHC and 5% MSC have significant anti-spalling ability compared with control specimens. The service life of reinforced MSC and reinforced SHC are more than 10 times higher than the reinforced mortar.

4. The image reconstruction results show that EIT is capable of detecting complex corrosion damage in the 5% MSC and 5% mortar. This requires using advanced computational methods and utilizing frequency-difference EIT technology. For corrosion monitoring, the change of the background conductivity with corrosion time makes it difficult to apply Time-difference EIT. On the other hand, frequency-difference EIT does not rely on reference measurements before corrosion and allowed reconstructing conductivity distribution within the specimen, clearly reflecting the corrosion damage details, i.e., extent, location, and severity. Even if the surface damage is not observed, EIT image reconstructions are able to show corrosion damage inside the specimen.

## CHAPTER 9: CONCLUSIONS AND FUTURE RESEARCH

### 9.1 Conclusions

This dissertation developed a distributed, direct damage and strain sensing approach based on novel multifunctional strain-hardening cementitious materials (MSCs). The dissertation (Chapter 2) generated fundamental understandings on how the composition and microstructure affect the frequency-dependent electrical response of cementitious materials. Electrical impedance spectroscopy revealed the frequency-dependent electrical behavior of cementitious materials. Equivalent circuit modeling correlated the material frequency-dependent impedance to its microstructure. Equivalent circuit parameters were analyzed to reveal the effects of chemical composition on the material electrical microstructure and the electrical parameters. It was also found that aging led to a refinement of pore structure and the increase in the heterogeneity of hydration products, thus increasing material impedance at different frequencies. Third, the “impedance” of a cementitious crack to electrical current was found to be frequency-dependent. While resistance is nonlinearly related to crack opening, capacitance is nearly linearly related to crack opening. Fourth, the frequency-dependent electrical response of cementitious materials can be tailored through carbon-based nanoparticles.

This dissertation (Chapter 3) developed novel multifunctional cementitious composite materials that integrate self-sensing functionality with a pseudo-strain-hardening behavior accompanied by multiple steady-state microcracking process. The successful design of MSC was achieved through tailoring material electrical microstructure as well as micromechanical parameters. Impedance spectroscopy and equivalent circuit analysis played an important role for quantifying electrical microstructure and its frequency dependency. The electrical parameters of

the cementitious matrix, and the interfaces between polymeric fibers and cementitious matrix were tailored by incorporating carbon black nanoparticles within an optimum range to achieve a strong piezoresistive behavior with a high signal-to-noise ratio. MSCs exhibited gage factors larger than 40 (elastic strain sensing), and tensile strain-hardening behavior with strain capacity more than 3% (damage tolerance).

This dissertation (Chapter 4 & 5) elucidated the electromechanical behavior of MSCs and mechanisms through electromechanical experiments and a modeling framework coupling micromechanics theory with equivalent circuit analysis. MSC exhibits strongly-coupled, high signal-to-noise electromechanical behavior under monotonic and cyclic loading. MSC possesses high gage factors for strain sensing during elastic stage. During the post-cracking stage, the nonlinear electromechanical behavior of MSC allows differentiating between strain-hardening (multiple steady-stage cracking) and tension-softening (localized fracture failure) stages. The distinctive electromechanical behavior of MSC, in comparison with regular strain-hardening cementitious composite, is explained by a newly developed modeling framework combining micromechanics with equivalent circuit model. The model links length scale from the electromechanical behavior of a single fiber debonding and pullout, to a single cracking opening, and to the multiple cracking process. The model reveals the capacitance effect and resistance effect of cracks in cementitious materials.

This dissertation (Chapter 6, 7 and 8) achieved and demonstrated spatial sensing and visual depiction of damage through advanced EIT methods newly established for MSCs. Two EIT approaches, time-difference EIT and frequency-difference EIT were established and successfully demonstrated in MSC specimens with different damage stimuli (due to mechanical loading or due to corrosion), with different damage pattern (localized crack or distributed



multiple microcracks), and with different geometries (2D damage or 3D damage). Image reconstructions based on EIT methods were demonstrated at different frequencies (from 1 Hz to 1 MHz), with different impedance parameters (impedance magnitude, real part of impedance, or imaginary part of impedance), and using different probing methods. Compared with time-difference EIT, frequency-difference EIT method eliminates the need for reference state and is nearly unaffected by ambient environmental conditions. Furthermore, MSCs exhibited high corrosion resistance as well as corrosion self-sensing capacity. Image reconstructions based on frequency-difference EIT showed that location and extent of corrosion damage in reinforced MSC specimen were clearly identified.

## **9.2 Future Research**

Future research is suggested in the following directions:

(1) nonlinear frequency-difference EIT algorithm for improving spatial resolution for smaller microcracks needs to be developed. A nonlinear assumption would increase the accuracy of highly distributed and dense microcracking damage for a material with nonuniform background impedance.

(2) Further investigation is needed for chemical sensing and deterioration sensing in multifunctional cementitious materials and structures. The sensing results need to be correlated to structural remaining service life.

(3) Scale-up study of damage, strain and deterioration sensing in MSC structural components is needed. Challenges need to be addressed regarding the MSC processing in large scale, performing large-scale testing, and attaining spatial damage sensing in large structural members based on limited boundary measurements.

(4) It is important to achieve 3-D real-time and distributed sensing network for structural

system, centered on the developed MSC materials and EIT methods.

(5) It is necessary to link damage and deterioration sensing data to structural safety and reliability, and to decision making.

## References

- [1] American Society of Civil Engineers, 2017 Infrastructure report card: a comprehensive assessment of America's infrastructure, 2017.
- [2] CNN, Civil engineers say fixing infrastructure will take \$4.6 trillion. 2017. <http://money.cnn.com/2017/03/09/news/infrastructure-report-card/index.html>.
- [3] McKinsey Global Institute, Infrastructure productivity: How to save \$1 trillion a year, 2013.
- [4] American Society of Civil Engineers, Failure to act: closing the infrastructure investment gap for America's economic future, 2016.
- [5] Center for Economics and Business Research, The future economic and environmental costs of gridlock in 2030: an assessment of the direct and indirect economic and environmental costs of idling in road traffic congestion to households in the UK, France, Germany and the USA, 2014.
- [6] European Cyclist's Federation, The darker side of traffic jams: congestion costs billions to world economy, 2011.
- [7] D. Schrank, B. Eisele, T. Lomax, J. Bak, 2015 urban mobility scorecard, The Texas A&M Transportation Institute and INRIX, 2015.
- [8] Eltis, Congestion costs billions to world economy, 2014. <http://www.eltis.org/discover/news/congestion-costs-billions-world-economy-0>.
- [9] Portland Cement Association, Green in practice 102-Concrete, Cement, and CO<sub>2</sub>, 2017.
- [10] National Ready Mixed Concrete Association, Concrete CO<sub>2</sub> fact sheet, 2012.
- [11] The International Energy Agency (IEA), CO<sub>2</sub> capture in the cement industry, 2008.
- [12] L.J. Hanle, K.R. Jayaraman, J.S. Smith, CO<sub>2</sub> emissions profile of the US cement industry, Washington DC: Environmental Protection Agency (2004).
- [13] P.K. Mehta, Durability -- critical issues for the future, ACI Concrete International 19(7) (1997).
- [14] Business Roundtable, Road to growth: The case for investing in America's transportation infrastructure, 2015.
- [15] New York Times, America's infrastructure is getting worse, 2016. <https://www.nytimes.com/interactive/2016/09/16/business/economy/infrastructure-gdp-age-traffic.html>.

- [16] E.J. Wallbank, The performance of concrete in bridges, A survey of 200 highway bridges. (1989).
- [17] World Economic Forum, Strategic infrastructure steps to operate and maintain infrastructure efficiently and effectively, 2014.
- [18] The Department of Treasury With the Council of Economic Advisers, An economic analysis of infrastructure investment, 2010.
- [19] Z.P. Bažant, M.T. Kazemi, Size dependence of concrete fracture energy determined by RILEM work-of-fracture method, *International Journal of Fracture*, 51 (1991) 121-138.
- [20] F. Bangert, S. Grasberger, D. Kuhl, G. Meschke, Environmentally induced deterioration of concrete: physical motivation and numerical modeling, *Engineering Fracture Mechanics*, 70 (2003) 891-910.
- [21] D. Adams, Health monitoring of structural materials and components, Wiley, Hoboken, NJ, 2007.
- [22] D. Frangopol, M. Liu, Maintenance and management of civil infrastructure based on condition, safety, optimization, and life-cycle cost, *Structure and Infrastructure Engineering*, 3 (2007) 29-41.
- [23] D. Balageas, C. Fritzen, A. Guemes, Structural health monitoring, Wiley, Newport beach, CA.
- [24] D. Pettersson, S. Thelandersson, Crack development in concrete structures due to imposed strains—part I: modelling, *Materials and Structures*, 34 (2011) 7-13.
- [25] D.D.L. Chung, Self-monitoring structural materials, *Materials Science and Engineering*, R22 (1998) 1998.
- [26] P.C. Chang, A. Flatau, S.C. Liu, Review paper: health monitoring of civil infrastructure, *Structural Health Monitoring*, 2 (2007) 257-267.
- [27] Federal Highway Administration, National bridge inspection standards, 2004.
- [28] J. Lynch, K.J. Loh, A summary review of wireless sensors and sensor networks for structural health monitoring, *The Shock and Vibration Digest*, 38 (2006) 91-128.
- [29] K.J. Loh, J. Kim, J.P. Lynch, N.W.S. Kam, N.A. Kotov, Multifunctional layer-by-layer carbon nanotube-polyelectrolyte thin films for strain and corrosion sensing, *Smart Materials and Structures*, 16 (2007) 429-438.

- [30] H. Sohn, C.R. Farrar, F.M. Hemez, J.J. Czarnecki, A review of structural health monitoring literature 1996-2001, in: T.W.C.o.S. Control (Ed.), pp. 1-7.
- [31] F. Santosa, Inverse problems of acoustic and elastic waves, Siam, Philadelphia, PA, 1984.
- [32] P. Delsanto, Universality of nonclassical nonlinearity: applications to non-destructive evaluations and ultrasonic, Springer, Torino, Italy, 2006.
- [33] M. Gherlone, P. Cerracchio, M. Mattone, M. Sciuva, A. Tessler, An inverse finite element method for beam shape sensing: theoretical framework and experimental validation, *Smart Materials and Structures*, 23 (2014) 045027.
- [34] K.C. Park, G. Reich, Model-based health monitoring of structural systems: progress, potential and challenges, *Proceedings of the 2nd International Workshop on Structural Health Monitoring*, 1999, pp. 82-95.
- [35] B. Glisic, N. Verma, Very dense arrays of sensors for SHM based on large area electronics, *Structural Health Monitoring: Condition based Maintenance and Intelligent Structures*, 2 (2011) 1409-1416.
- [36] V. Bhatia, A.M. Vengsarkar, Optical fiber long-period grating sensors, *Optics letters*, 21 (1996) 692-694.
- [37] B. Lee, Review of the present status of optical fiber sensors, *Optical fiber technology*, 9 (2003) 57-79.
- [38] S. Zheng, Long-period fiber grating moisture sensor with nano-structured coatings for structural health monitoring, *Structural Health Monitoring*, 14 (2014) 148-157.
- [39] W. Chung, D. Kang, Full-scale test of a concrete box girder using FBG sensing system, *Engineering Structures*, 30 (2008) 643-652.
- [40] M. Majumder, T.K. Gangopadhyay, A.K. Chakraborty, K. Dasgupta, D.K. Bhattacharya, Fibre Bragg gratings in structural health monitoring—Present status and applications, *Sensors and Actuators A: Physical*, 147 (2008) 150-164.
- [41] L. Ren, H.N. Li, J. Zhou, D.S. Li, L. Sun, Health monitoring system for offshore platform with fiber Bragg grating sensors, *Optical Engineering*, 45 (2006) 084401-084401.
- [42] T.L. Yeo, T. Sun, K.T.V. Grattan, Fibre-optic sensor technologies for humidity and moisture measurement, *Sensors and Actuators A: Physical*, 144 (2008) 280-295.
- [43] F. Wu, Debond detection using embedded piezoelectric elements in reinforced concrete structures-part I: experiment, *Structural Health Monitoring*, 5 (2006) 5-15.

- [44] F. Wu, F.K. Chang, Debond detection using embedded piezoelectric elements for reinforced concrete structures-Part II: Analysis and algorithm, *Structural Health Monitoring*, 5 (2006) 17-28.
- [45] M. Papaelias, L. Cheng, M. Kogia, A. Mohimi, V. Kappatos, C. Selcuk, T.H. Gan, Inspection and structural health monitoring techniques for concentrated solar power plants, *Renewable Energy*, 85 (2016) 1178-1191.
- [46] P.C. Chang, A. Flatau, S.C. Liu, Health monitoring of civil infrastructure, *Structural health monitoring*, 2 (2003) 257-267.
- [47] D. Corr, M. Accardi, L. Graham-Brady, S. Shah, Digital image correlation analysis of interfacial debonding properties and fracture behavior in concrete, *Engineering Fracture Mechanics*, 74 (2007) 109-121.
- [48] S.Y. Alam, J. Saliba, A. Loukili, Fracture examination in concrete through combined digital image correlation and acoustic emission techniques, *Construction and Building Materials*, 69 (2014) 232-242.
- [49] J. Kozicki, J. Tejchman, Experimental investigations of strain localization in concrete using Digital Image Correlation (DIC) technique, *Archives of Hydro-Engineering and Environmental Mechanics*, 54 (2007) 3-24.
- [50] S.G. Shah, J.C. Kishen, Fracture properties of concrete–concrete interfaces using digital image correlation, *Experimental mechanics*, 51 (2011) 303-313.
- [51] B. Gencturk, K. Hossain, A. Kapadia, E. Labib, Y.L. Mo, Use of digital image correlation technique in full-scale testing of prestressed concrete structures, *Measurement*, 47 (2014).
- [52] P.E. Mix, *Introduction to nondestructive testing: a training guide*, John Wiley & Sons, 2005.
- [53] A. Carpinteri, G. Lacidogna, N. Pugno, Structural damage diagnosis and life-time assessment by acoustic emission monitoring, *Engineering Fracture Mechanics*, 74 (2007) 273-289.
- [54] A. Farhidzadeh, E. Dehghan-Niri, S. Salamone, B. Luna, A. Whittaker, Monitoring crack propagation in reinforced concrete shear walls by acoustic emission, *Journal of Structural Engineering*, 139 (2012) 04013010.
- [55] H.A. Elfergani, R. Pullin, K.M. Holford, Damage assessment of corrosion in prestressed concrete by acoustic emission, *Construction and Building Materials*, 40 (2013) 925-933.

- [56] T. Shiotani, D.G. Aggelis, O. Makishima, Global monitoring of large concrete structures using acoustic emission and ultrasonic techniques: case study, *Journal of Bridge Engineering*, 14 (2009) 188-192.
- [57] G. Song, H. Gu, Y.L. Mo, Smart aggregates: multi-functional sensors for concrete structures—a tutorial and a review, *Smart Materials and Structures*, 17 (2008) 033001.
- [58] H. Gu, G. Song, H. Dhonde, Y.L. Mo, S. Yan, Concrete early-age strength monitoring using embedded piezoelectric transducers, *Smart Materials and Structures*, 15 (2006) 2006.
- [59] Q. Kong, S. Hou, Q. Ji, Y.L. Mo, G. Song, Very early age concrete hydration characterization monitoring using piezoceramic based smart aggregates, *Smart Materials and Structures*, 22 (2013) 085025.
- [60] J. Zhu, S.C.M. Ho, Q. Kong, D. Patil, Y.L. Mo, G. Song, Estimation of impact location on concrete column, *Smart Materials and Structures*, 26 (2017) 055037.
- [61] G. Song, H. Gu, Y.L. Mo, T.T.C. Hsu, H. Dhonde, Concrete structural health monitoring using embedded piezoceramic transducers, *Smart Materials and Structures*, 16 (2007) 959.
- [62] Q. Feng, Q. Kong, L. Huo, G. Song, Crack detection and leakage monitoring on reinforced concrete pipe, *Smart Materials and Structures*, 24 (2015) 115020.
- [63] Q. Kong, R.H. Robert, P. Silva, Y.L. Mo, Cyclic crack monitoring of a reinforced concrete column under simulated pseudo-dynamic loading using piezoceramic-based smart aggregates, *Applied Sciences*, 6 (2016) 341.
- [64] Q. Kong, Q. Feng, G. Song, Water presence detection in a concrete crack using smart aggregates, *International Journal of Smart and Nano Materials*, 6 (2015) 149-161.
- [65] L. Zeng, S.M. Parvasi, Q. Kong, L. Huo, M. Li, G. Song, Bond slip detection of concrete-encased composite structure using shear wave based active sensing approach, *Smart Materials and Structures*, 24 (2015) 125026.
- [66] Q. Kong, S. Fan, X. Bai, Y.L. Mo, G. Song, A novel embeddable spherical smart aggregate for structural health monitoring: Part I. Fabrication and electrical characterization, *Smart Materials and Structures*, 26 (2017) 095050.
- [67] Q. Kong, S. Fan, Y.L. Mo, G. Song, A novel embeddable spherical smart aggregate for structural health monitoring: Part II. Numerical and experimental verifications, *Smart Materials and Structures*, 26 (2017) 095051.

- [68] J. Zhu, L. He, Study on piezoelectric wave propagation based nondestructive monitoring method of concrete, *Electric Technology and Civil Engineering (ICETCE)*, 2011 International Conference on IEEE, 2011, pp. 764-767.
- [69] T.P. Philippidis, D.G. Aggelis, Experimental study of wave dispersion and attenuation in concrete, *Ultrasonics*, 43 (2005) 584-595.
- [70] J.M. Berthelot, S.M. Ben, J.L. Robert, Study of wave attenuation in concrete, *Journal of Materials Research*, 8 (1993) 2344-2353.
- [71] J. Thongrueng, T. Tsuchiya, K. Nagata, Lifetime and degradation mechanism of multilayer ceramic actuator, *Japanese Journal of Applied Physics*, 37 (1998) 5306.
- [72] S. Mall, T.L. Hsu, Electromechanical fatigue behavior of graphite/epoxy laminate embedded with piezoelectric actuator, *Smart Materials and Structures*, 9 (2000) 78.
- [73] T. Tanimoto, K. Okazaki, Fatigue degradation and reliability of piezoelectric ceramics, *Japanese Journal of Applied Physics*, 30 (1991) 2410.
- [74] P.C. Chang, S.C. Liu, Recent research in nondestructive evaluation of civil infrastructures, *Journal of Materials in Civil Engineering*, 15 (2003) 298-304.
- [75] J. Zhou, A study of acoustic emission technique for concrete damage detection, Michigan Technological University, 2011.
- [76] N.M. Nor, N.M. Bunnori, A. Ibrahim, S. Shahidan, S.N.M. Saliyah, An observation of noise intervention into acoustic emission signal on concrete structure, 2011 IEEE 7th International Colloquium on Signal Processing and its Applications, 2011, pp. 7-10.
- [77] A. Nair, C.S. Cai, Acoustic emission monitoring of bridges: Review and case studies, *Engineering Structures*, 32 (2010) 1704-1714.
- [78] P. Beck, Quantitative damage assessment of concrete structures using acoustic emission, Cardiff University, 2004.
- [79] D.M. McCann, M.C. Forde, Review of NDT methods in the assessment of concrete and masonry structures, *NDT & E International*, 34 (2001) 71-84.
- [80] H.W. Song, V. Saraswathy, Corrosion monitoring of reinforced concrete structures, *International Journal of Electrochemical Science*, 2 (2007) 1-28.
- [81] E.J. Garboczi, Three-dimensional mathematical analysis of particle shape using X-ray tomography and spherical harmonics: Application to aggregates used in concrete, *Cement and Concrete Research*, 32 (2002) 1621-1638.



- [82] D. Fukuda, Y. Nara, Y. Kobayashi, M. Maruyama, M. Koketsu, D. Hayashi, K. Kaneko, Investigation of self-sealing in high-strength and ultra-low-permeability concrete in water using micro-focus X-ray CT, *Cement and Concrete Research*, 42 (2012) 1494-1500.
- [83] S. Fan, M. Li, X-ray computed microtomography of three-dimensional microcracks and self-healing in engineered cementitious composites, *Smart Materials and Structures*, 24 (2014) 015021.
- [84] C. Andrade, V.M. Blanco, A. Collazo, M. Keddad, X.R. Nóvoa, H. Takenouti, Cement paste hardening process studied by impedance spectroscopy, *Electrochimica Acta*, 44 (1999) 4313-4318.
- [85] J.M. Cruz, I.C. Fita, L. Soriano, J. Payá, M.V. Borrachero, The use of electrical impedance spectroscopy for monitoring the hydration products of Portland cement mortars with high percentage of pozzolans, *Cement and Concrete Research*, 50 (2013) 51-61.
- [86] G. Dotelli, C.M. Mari, The evolution of cement paste hydration process by impedance spectroscopy, *Materials Science and Engineering: A*, 303 (2001) 54-59.
- [87] J.M. Torrents, J. Roncero, R. Gettu, Utilization of impedance spectroscopy for studying the retarding effect of a superplasticizer on the setting of cement, *Cement and Concrete Research*, 28 (1998) 1325-1333.
- [88] M. Cabeza, M. Keddad, X.R. Nóvoa, I. Sánchez, H. Takenouti, Impedance spectroscopy to characterize the pore structure during the hardening process of Portland cement paste, *Electrochimica Acta*, 51 (2006) 1831-1841.
- [89] D.A. Koleva, J.H.W. de Wit, K. van Breugel, L.P. Veleva, E. van Westing, O. Copuroglu, A.L.A. Fraaij, Correlation of microstructure, electrical properties and electrochemical phenomena in reinforced mortar. Breakdown to multi-phase interface structures. Part II: Pore network, electrical properties and electrochemical response, *Materials Characterization* 59(6) (2008) 801-815.
- [90] W.J. McCarter, R. Brousseau, The A.C. response of hardened cement paste, *Cement and Concrete Research*, 20 (1990) 891-900.
- [91] S. Nathan, D. Matthew, N. Narayanan, Electrical conductivity based characterization of plain and coarse glass powder modified cement pastes, *Cement and Concrete Composites*, 29 (2007) 656-666.

- [92] P. Chen, D.D.L. Chung, Carbon fiber reinforced concrete for smart structures capable of non-destructive flaw detection, *Smart Materials and Structures*, 2 (1993) 22-30.
- [93] P. Chen, D.D.L. Chung, Improving the electrical conductivity of composites comprised of short conducting fibers in a non-conducting matrix: the addition of a non-conducting particulate filler, *Journal of Electronic Materials*, 24 (1995) 47-51.
- [94] J. Ou, B. Han, Piezoresistive Cement-based Strain Sensors and Self-sensing Concrete Components, *Journal of Intelligent Material Systems and Structures*, (2008) 1-8.
- [95] F. Reza, G. Batson, J. Yamamuro, J. Lee, Resistance Changes during Compression of Carbon Fiber Cement Composites, *Journal of Materials in Civil Engineering*, 15 (2003) 476-483.
- [96] X. Fu, D.D.L. Chung, Contact electrical resistivity between cement and carbon fiber: Its decrease with increasing bond strength and its increase during fiber pull-out, *Cement and Concrete Research*, 25 (1995) 1391-1396.
- [97] D.D.L. Chung, Strain sensors based on the electrical resistance change accompanying the reversible pull-out of conducting short fibers in a less conducting matrix, *Smart Materials and Structures* 4(1995) 59-61.
- [98] X. Fu, D.D.L. Chung, Self-monitoring of fatigue damage in carbon fiber reinforced cement, *Cement and Concrete Research*, 26 (1996) 15-20.
- [99] X. Fu, D.D.L. Chung, Effect of Curing Age on the Self-monitoring Behavior of Carbon Fiber Reinforced Mortar, *Cement and Concrete Research*, 27 (1997) 1313-1318.
- [100] D.D.L. Chung, Self-monitoring structural materials, *Materials Science and Engineering: R: Reports*, 22 (1998) 57-78.
- [101] X. Fu, W. Lu, D.D.L. Chung, Improving the strain-Sensing ability of carbon fiber-reinforced cement by Ozone Treatment of the fibers *Cement and Concrete Research*, 28 (1998) 183-187.
- [102] S. Wen, D.D.L. Chung, Piezoresistivity in continuous carbon fiber cement-matrix composite, *Cement and Concrete Research*, 29 (1999) 445-449.
- [103] S. Wen, D.D.L. Chung, Uniaxial tension in carbon fiber reinforced cement, sensed by electrical resistivity measurement in longitudinal and transverse directions, *Cement and Concrete Research*, 30 (2000) 1289-1294.

- [104] D. Bontea, D.D.L. Chung, G.C. Lee, Damage in carbon fiber-reinforced concrete, monitored by electrical resistance measurement, *Cement and Concrete Research*, 30 (2000) 651-659.
- [105] S. Wen, D.D.L. Chung, Uniaxial compression in carbon fiber-reinforced cement, sensed by electrical resistivity measurement in longitudinal and transverse directions, *Cement and Concrete Research* 31 (2001) 297-301.
- [106] J. Cao, D.D.L. Chung, Carbon fiber reinforced cement mortar Improved by using acrylic dispersion as an admixture, *Cement and Concrete Research*, 31 (2001) 1633-1637.
- [107] J. Cao, S. Wen, D.D.L. Chung, Defect dynamics and damage of cement-based materials, studied by electrical resistance measurement, *Journal of Materials Science*, 36 (2001) 4351-4360.
- [108] S. Wen, D.D.L. Chung, Effect of carbon fiber grade on the electrical behavior of carbon fiber reinforced cement, *Carbon*, 39 (2001) 369–373.
- [109] S. Wen, D.D.L. Chung, Electric polarization in carbon fiber-reinforced cement, *Cement and Concrete Research* 31 (2001) 141-147.
- [110] B. Wu, X. Huang, J. Lu, Biaxial compression in carbon-fiber-reinforced mortar, sensed by electrical resistance measurement, *Cement and Concrete Research*, 35 (2005) 1430-1434.
- [111] B. Chen, J. Liu, K. Wu, Electrical responses of carbon fiber reinforced cementitious composites to monotonic and cyclic loading, *Cement and Concrete Research*, 35 (2005) 2183-2191.
- [112] S. Wen, D.D.L. Chung, Strain-sensing characteristics of carbon fiber-reinforced cement, *ACI Materials Journal*, 102 (2005) 244-248.
- [113] S. Wen, D.D.L. Chung, Self-sensing of flexural damage and strain in carbon fiber reinforced cement and effect of embedded steel reinforcing bars, *Carbon*, 44 (2006) 1496-1502.
- [114] S. Wen, D.D.L. Chung, Spatially resolved self-sensing of strain and damage in carbon fiber cement, *Journal of Materials Science*, 41 (2006) 4823-4831.
- [115] S. Wen, D.D.L. Chung, Effects of Strain and Damage on Strain-sensing Ability of Carbon Fiber Cement, *Journal of Materials in Civil Engineering*, 18 (2006) 355-360.
- [116] S. Wen, D.D.L. Chung, Piezoresistivity-Based Strain Sensing in Carbon Fiber-Reinforced Cement, *ACI Materials Journal*, 104 (2007) 171-179.
- [117] S. Zhu, D.D.L. Chung, Theory of piezoresistivity for strain sensing in carbon fiber reinforced cement under flexure, *Journal of Materials Science*, 42 (2007) 6222-6233.

- [118] B. Chen, J. Liu, Damage in carbon fiber-reinforced concrete, monitored by both electrical resistance measurement and acoustic emission analysis, *Construction and Building Materials*, 22 (2008) 2196-2201.
- [119] D.G. Meehan, S. Wang, D.D.L. Chung, Electrical-resistance-based Sensing of Impact Damage in Carbon Fiber Reinforced Cement-based Materials, *Journal of Intelligent Material Systems and Structures*, 21 (2009) 83-105.
- [120] S. Wen, D.D.L. Chung, A comparative study of steel- and carbon-fibre cement as piezoresistive strain sensors, *Advances in Cement Research*, 15 (2003) 119-128.
- [121] B. Han, Y. Yu, B. Han, J. Ou, Development of a wireless stress/strain measurement system integrated with pressure-sensitive nickel powder-filled cement-based sensors, *Sensors and Actuators A: Physical*, 147 (2008) 536-543.
- [122] B. Han, B. Han, J. Ou, Experimental study on use of nickel powder-filled Portland cement-based composite for fabrication of piezoresistive sensors with high sensitivity, *Sensors and Actuators A: Physical*, 149 (2009) 51-55.
- [123] X. Liu, S. Wu, N. Li, B. Gao, Self-monitoring application of asphalt concrete containing graphite and carbon fibers, *Journal of Wuhan University of Technology-Mater. Sci. Ed.*, 23 (2008) 268-271.
- [124] Y. He, L. Lu, S. Jin, S. Hu, Conductive aggregate prepared using graphite and clay and its use in conductive mortar, *Construction and Building Materials*, 53 (2014) 131-137.
- [125] H. Li, H. Xiao, J. Ou, Effect of compressive strain on electrical resistivity of carbon black-filled cement-based composites, *Cement and Concrete Composites*, 28 (2006) 824-828.
- [126] S. Wen, D.D.L. Chung, Partial replacement of carbon fiber by carbon black in multifunctional cement–matrix composites, *Carbon*, 45 (2007) 505-513.
- [127] H. Li, H. Xiao, J. Ou, Electrical property of cement-based composites filled with carbon black under long-term wet and loading condition, *Composites Science and Technology*, 68 (2008) 2114-2119.
- [128] H. Xiao, H. Li, J. Ou, Modeling of piezoresistivity of carbon black filled cement-based composites under multi-axial strain, *Sensors and Actuators A: Physical*, 160 (2010) 87-93.
- [129] B. Han, L. Zhang, J. Ou, Influence of water content on conductivity and piezoresistivity of cement-based material with both carbon fiber and carbon black, *Journal of Wuhan University of Technology-Mater. Sci. Ed.*, 25 (2010) 147-151.

- [130] M. Li, V. Lin, J. Lynch, V.C. Li, Multifunctional carbon black Engineered Cementitious Composites for the protection of critical infrastructure, *High Performance Fiber Reinforced Cement Composites* 6, 2 (2012) 99-106.
- [131] Y. Ding, Z. Chen, Z. Han, Y. Zhang, F. Pacheco-Torgal, Nano-carbon black and carbon fiber as conductive materials for the diagnosing of the damage of concrete beam, *Construction and Building Materials*, 43 (2013) 233-241.
- [132] M. Li, V. Lin, J. Lynch, V.C. Li, Carbon black Engineered Cementitious Composites - mechanical and electrical characterization, *ACI Special Publication*, 292 (2013).
- [133] G. Li, P. Wang, X. Zhao, Pressure-sensitive properties and microstructure of carbon nanotube reinforced cement composites, *Cement and Concrete Composites*, 29 (2007) 377-382.
- [134] B. Han, X. Yu, E. Kwon, A self-sensing carbon nanotube/cement composite for traffic monitoring, *Nanotechnology*, 20 (2009) 445501.
- [135] H.K. Kim, I.S. Park, H.K. Lee, Improved piezoresistive sensitivity and stability of CNT/cement mortar composites with low water–binder ratio, *Composite Structures*, 116 (2014) 713-719.
- [136] X. Yu, E. Kwon, A carbon nanotube/cement composite with piezoresistive properties, *Smart Materials and Structures*, 18 (2009) 055010.
- [137] X. Yu, E. Kwon, carbon nanotube based self-sensing concrete for pavement structural health monitoring, 2012.
- [138] F. Azhari, N. Banthia, Cement-based Sensors with Carbon Fibers and Carbon Nanotubes for Piezoresistive Sensing, *Cement and Concrete Composites*, 34 (2012) 866-876.
- [139] M. Saafi, K. Andrew, P. Tang, D. McGhon, S. Taylor, M. Rahman, S. Yang, X. Zhou, Multifunctional properties of carbon nanotube/fly ash geopolymetric nanocomposites, *Construction and Building Materials*, 49 (2013) 46-55.
- [140] A. Hehr, Y. Song, B. Suberu, J. Sullivan, V. Shanov, M. Schulz, Embedded Carbon Nanotube Sensor Thread for Structural Health Monitoring and Strain Sensing of Composite Materials, (2014) 671-712.
- [141] H.K. Kim, I.W. Nam, H.K. Lee, Enhanced effect of carbon nanotube on mechanical and electrical properties of cement composites by incorporation of silica fume, *Composite Structures*, 107 (2014) 60-69.

- [142] R.N. Howser, H.B. Dhonde, Y.L. Mo, Self-sensing of carbon nanofiber concrete columns subjected to reversed cyclic loading, *Smart Materials and Structures*, 20 (2011) 085031.
- [143] D. Gao, M. Sturm, Y.L. Mo, Electrical resistance of carbon-nanofiber concrete, *Smart Materials and Structures*, 20 (2011) 049501.
- [144] D.D.L. Chung, Carbon materials for structural self-sensing, electromagnetic shielding and thermal interfacing, *Carbon*, 50 (2012) 3342-3353.
- [145] F.J. Baeza, O. Galao, E. Zornoza, P. Garcés, Effect of aspect ratio on strain sensing capacity of carbon fiber reinforced cement composites, *Materials & Design*, 51 (2013) 1085-1094.
- [146] O. Galao, F.J. Baeza, E. Zornoza, P. Garcés, Strain and damage sensing properties on multifunctional cement composites with CNF admixture, *Cement and Concrete Composites*, 46 (2014) 90-98.
- [147] S. Gupta, J.G. Gonzalez, K.J. Loh, Self-sensing concrete enabled by nano-engineered cement-aggregate interfaces, *Structural Health Monitoring*, 16 (2016) 309-323.
- [148] A. Peled, J. Torrents, T. Mason, S. Shah, E.J. Garboczi, Electrical Impedance Spectra to monitor damage during tensile loading of cement composites, *ACI Materials Journal*, 98 (2001) 313-322.
- [149] M. Li, V.C. Li, Rheology, fiber dispersion, and robust properties of Engineered Cementitious Composites, *Materials and Structures*, (2012).
- [150] T.C. Hou, J. Lynch, Conductivity-based strain monitoring and damage characterization of fiber reinforced cementitious structural components, *Proceedings of SPIE 12 Annual International Symposium on Smart Structures and Materials* 5765 (2005) 419-429.
- [151] R. Ranade, J. Zhang, J.P. Lynch, V.C. Li, Influence of micro-cracking on the composite resistivity of Engineered Cementitious Composites, *Cement and Concrete Research*, 58 (2014) 1-12.
- [152] C.B. J., Microstructure studies of hydrating portland cement-based materials using impedance spectroscopy, *Civil Engineering*, Northwestern University, Evanston, Illinois, 1993.
- [153] F. Rajabipour, Fundamental Investigations on Utilizing Electrical Sensing to Improve Life Cycle Modeling of Concrete Structures, *Civil Engineering*, Purdue University, 2003.
- [154] H. Ma, D. Hou, J. Liu, Z. Li, Estimate the relative electrical conductivity of C-S-H gel from experimental results, *Construction and Building Materials*, 71 (2014) 392-396.

- [155] W.J. McCarter, The a.c. impedance response of concrete during early hydration, *Journal of Materials Science*, 31 (1996) 6285-6292.
- [156] P. Gu, P. Xie, J.J. Beaudoin, R. Brousseau, AC Impedance Spectroscopy II Microstructural characterization of hydration cement silica fume systems, *Cement and Concrete Research*, 23 (1993) 157-168.
- [157] S.W. Tang, Z.J. Li, H.Y. Shao, E. Chen, Characterization of early-age hydration process of cement pastes based on impedance measurement, *Construction and Building Materials*, 68 (2014) 491-500.
- [158] L. Xiao, Z. Li, Early-age hydration of fresh concrete monitored by non-contact electrical resistivity measurement, *Cement and Concrete Research*, 38 (2008) 312-319.
- [159] L. Xiao, Z. Li, New understanding of cement hydration mechanism through electrical resistivity measurement and microstructure investigations, *Journal of Materials in Civil Engineering* 21(8) (2009) 368-373.
- [160] B.J. Christensen, T.O. Mason, H.M. Jennings, Influence of silica fume on the early hydration of portland cements using impedance spectroscopy, *Journal of the American Ceramic Society*, 75 (1992) 939-945.
- [161] N. Schwarz, M. DuBois, N. Neithalath, Electrical conductivity based characterization of plain and coarse glass powder modified cement pastes, *Cement and Concrete Composites*, 29 (2007) 656-666.
- [162] S.W. Tang, Z.J. Li, E. Chen, H.Y. Shao, Impedance measurement to characterize the pore structure in Portland cement paste, *Construction and Building Materials*, 51 (2014) 106-112.
- [163] S.W. Tang, Z.J. Li, H.G. Zhu, H.Y. Shao, E. Chen, Permeability interpretation for young cement paste based on impedance measurement, *Construction and Building Materials*, 59 (2014) 120-128.
- [164] I. Sánchez, C. Antón, G. de Vera, J.M. Ortega, M.A. Climent, Moisture Distribution in Partially Saturated Concrete Studied by Impedance Spectroscopy, *Journal of Nondestructive Evaluation*, 32 (2013) 362-371.
- [165] I. Sánchez, X.R. Nóvoa, G. de Vera, M.A. Climent, Microstructural modifications in Portland cement concrete due to forced ionic migration tests. Study by impedance spectroscopy, *Cement and Concrete Research*, 38 (2008) 1015-1025.

- [166] N. Neithalath, J. Weiss, J. Olek, Characterizing Enhanced Porosity Concrete using electrical impedance to predict acoustic and hydraulic performance, *Cement and Concrete Research*, 36 (2006) 2074-2085.
- [167] J.M. Loche, A. Ammar, P. Dumargue, Influence of the migration of chloride ions on the electrochemical impedance spectroscopy of mortar paste, *Cement and Concrete Research*, 35 (2005) 1797-1803.
- [168] I. Sánchez, M.P. López, J.M. Ortega, M.Á. Climent, Impedance spectroscopy: An efficient tool to determine the non-steady-state chloride diffusion coefficient in building materials, *Materials and Corrosion*, 62 (2011) 139-145.
- [169] P. Gu, Y. Fu, P. Xie, J.J. Beaudoin, Characterization of surface corrosion of reinforcing steel in cement paste by low frequency impedance spectroscopy, *Cement and Concrete Research*, 24 (1994) 231-242.
- [170] H. Ammari, J.K. Seo, T. Zhang, L. Zhou, Electrical Impedance Spectroscopy-based nondestructive testing for imaging defects in concrete structures, *ARXIV*, (2014).
- [171] Y. Li, C. Sui, Q. Ding, Study on the cracking process of cement-based materials by AC impedance method and ultrasonic method, *Journal of Nondestructive Evaluation*, 31 (2012) 284-291.
- [172] J.F. Lataste, C. Sirieix, D. Breysse, M. Frappa, Electrical resistivity measurement applied to cracking assessment on reinforced concrete structures in civil engineering, *NDT & E International*, 36 (2003) 383-394.
- [173] M. Cabeza, P. Merino, X.R. Nóvoa, I. Sánchez, Electrical effects generated by mechanical loading of hardened portland cement paste, *Cement and Concrete Composites*, 25 (2003) 351-356.
- [174] P. Chen, D.D.L. Chung, Carbon fiber reinforced concrete for smart structures capable of non-destructive flaw detection, *Smart Materials and Structures*, 2 (1993) 22.
- [175] W.J. Mccarter, The AC response of hardened cement paste, *Cement and Concrete Research*, 20 (1990) 891-900.
- [176] P. Gu, P. Xie, J.J. Beaudoin, R. Brousseau, AC Impedance Spectroscopy I A new equivalent circuit model for hydrated portland cement paste, *Cement and Concrete Research*, 22 (1992) 833-840.



- [177] P. Xie, P. Gu, Z. Xu, J.J. Beaudoin, A rationalized A.C. Impedance Model for Microstructural Characterization of Hydrating Cement Systems, *Cement and Concrete Research*, 23 (1993) 359-367.
- [178] Z. Xu, P. Gu, P. Xie, J.J. Beaudoin, Application of A.C. impedance techniques in studies of porous cementitious materials (I): Influence of Solid Phase and Pore Solution on High Frequency Resistance, *Cement and Concrete Research*, 23 (1993) 853-862.
- [179] Z. Xu, P. Gu, P. Xie, J.J. Beaudoin, Application of A.C. Impedance techniques in studies of porous cementitious materials (II) Relationship between ACIS behavior and the porous microstructure, *Cement and Concrete Research*, 23 (1993) 853-862.
- [180] G. Song, Equivalent circuit model for AC electrochemical impedance spectroscopy of concrete, *Cement and Concrete Research*, 30 (2000) 1723-1730.
- [181] M. Cabezaa, P. Merinoa, A. Mirandab, X.R. No'voaa, I. Sancheza, Impedance spectroscopy study of hardened portland cement paste, *Cement and Concrete Research*, 32 (2002) 881-891.
- [182] A. Raghavan, C.E.S. Cesnik, Review of guided-wave structural health monitoring, *Shock and Vibration Digest*, 39 (2007) 91-114.
- [183] X. Li, M. Li, G. Song, Energy-dissipating and self-repairing SMA-ECC composite material system, *Smart Materials and Structures*, 24 (2015) 025024.
- [184] A.R. Payne, The dynamic properties of carbon black loaded natural rubber vulcanizates. Part I, *Journal of applied polymer science*, 6 (1962) 57-63.
- [185] J.B. Donnet, A. Voet, *Carbon black: physics, chemistry, and elastomer reinforcement*, M. Dekker 1976.
- [186] G.D. Parfitt, *Dispersion of powders in liquids*, (1969).
- [187] P.A. Hartley, G.D. Parfitt, L.B. Pollack, The role of the van der Waals force in the agglomeration of powders containing submicron particles, *Powder technology*, 42 (1985) 35-46.
- [188] S.P. Rwei, I. Manas-Zloczower, D.L. Feke, Observation of carbon black agglomerate dispersion in simple shear flows, *Polymer Engineering & Science*, 30 (1990) 701-706.
- [189] L. Karasek, M. Sumita, Characterization of dispersion state of filler and polymer-filler interactions in rubber-carbon black composites, *Journal of materials science*, 31 (1996) 281-289.

- [190] Q. Li, D.L. Feke, I. Manas-Zloczower, Influence of aggregate structure and matrix infiltration on the dispersion behavior of carbon black agglomerates, *Rubber Chemistry and Technology*, 68 (1995) 836-841.
- [191] E.M. Dannenberg, Carbon black dispersion and reinforcement, *Rubber Chemistry and Technology*, 25 (1952) 843-857.
- [192] O.A. Al-Hartomy, F. Al-Solamy, A. Al-Ghamdi, N. Dishovsky, M. Ivanov, M. Mihaylov, F. El-Tantawy, Influence of carbon black structure and specific surface area on the mechanical and dielectric properties of filled rubber composites, *International Journal of Polymer Science*, 2011 (2011) 521985.
- [193] V.C. Li, Y. Wang, S. Backer, A micromechanical model of tension-softening and bridging toughening of short random fiber reinforced brittle matrix composites, *Journal of the Mechanics and Physics of Solids*, 39 (1991) 607-625.
- [194] V.C. Li, C.K. Leung, Steady-state and multiple cracking of short random fiber composites, *Journal of Engineering Mechanics*, 118 (1992) 2246-2264.
- [195] E.H. Yang, Designing added functions in Engineered Cementitious Composites, Department of Civil and Environmental Engineering, University of Michigan, 2008.
- [196] M. Li, Multi-scale design for durable repair of concrete structures, Department of Civil and Environmental Engineering, University of Michigan, 2009.
- [197] S.W. Victor C. Li, W. Cynthia, Tensile Strain-Hardening Behavior of Polyvinyl Alcohol Engineered Cementitious Composite (PVA-ECC), *ACI Materials Journal*, 98 (2001).
- [198] ASTM E399, Standard Test Method for Linear-Elastic Plane-Strain Fracture Toughness  $K_{Ic}$  of Metallic Materials, ASTM International, 2012.
- [199] S.P. Shah, Determination of fracture parameters ( $K_{Ic}$  and  $CTOD_c$ ) of plain concrete using three-point bend tests, *Materials and Structures*, 23 (1990) 457-460.
- [200] C. Redon, V.C. Li, C. Wu, H. H., T. Saito, A. Ogawa, Measuring and modifying interface properties of PVA fibers in ECC matrix, *Journal of Materials in Civil Engineering*, 13 (2001).
- [201] V.C. Li, C. Wu, S. Wang, A. Ogawa, T. Saito, Interface tailoring for strain-hardening polyvinyl alcohol-engineered cementitious composite (PVA-ECC), *ACI Materials Journal*, 99 (2002) 463-472.
- [202] W.J.K. M. Taya, K. Ono, Piezoresistivity of a short fiberrelastomer matrix composite, *Mechanics of Materials*, 28 (1998) 53-59.

- [203] A. Godman, A. Bentur, Bond Effects in High-Strength Silica Fume Concretes, *ACI Materials Journal*, 86 (1989) 440-449.
- [204] X.H. Wang, S. Jacobsen, S.F. Lee, J.Y. He, Z.L. Zhang, Effect of silica fume, steel fiber and ITZ on the strength and fracture behavior of mortar, *Materials and Structures*, 43 (2009) 125.
- [205] J. Zhang, C.K.Y. Leung, Y. Gao, Simulation of crack propagation of fiber reinforced cementitious composite under direct tension, *Engineering Fracture Mechanics*, 78 (2011) 2439-2454.
- [206] S. Wen, D.D.L. Chung, Model of piezoresistivity in carbon fiber cement, *Cement and Concrete Research*, 36 (2006) 1879-1885.
- [207] A. Peled, J. Torrents, T. Mason, S. Shah, E.J. Garboczi, Electrical Impedance Spectra to monitor damage during tensile loading of cement composites, *ACI Materials Journal*, 98 (2001) 313-322.
- [208] J.L. Le, H. Du, S.D. Pang, Use of 2D Graphene Nanoplatelets (GNP) in cement composites for structural health evaluation, *Composites Part B: Engineering*, 67 (2014) 555-563.
- [209] T.C. Hou, J.P. Lynch, Electrical Impedance Tomographic Methods for Sensing Strain Fields and Crack Damage in Cementitious Structures, *Journal of Intelligent Material Systems and Structures*, 20 (2008) 1363-1379.
- [210] T.C. Hou, *Wireless and Electromechanical Approaches for Strain Sensing and Crack Detection in Fiber Reinforced Cementitious Materials*, University of Michigan, 2008.
- [211] R. Ranade, J. Zhang, J. Lynch, V.C. Li, Influence of micro-cracking on the composite resistivity of Engineered Cementitious Composites, *Cement and Concrete Research*, 58 (2014) 1-12.
- [212] E.H. Yang, S. Wang, Y. Yang, V.C. Li, Fiber-Bridging Constitutive Law of Engineered Cementitious Composites, *Journal of Advanced Concrete Technology*, 6 (2008) 181-193.
- [213] B. Liliana, Electrical impedance tomography, *Inverse Problems*, 18 (2002) R99.
- [214] M. Cheney, Isaacson, D., J.C. Newell, Electrical impedance tomography, *SIAM review*, 41 (1999) 85-101.
- [215] G.J. Saulnier, R.S. Blue, J.C. Newell, D. Isaacson, P.M. Edic, Electrical impedance tomography, *IEEE Signal Processing Magazine*, 18 (2001) 31-43.
- [216] L. Borcea, Electrical impedance tomography, *Inverse Problems*, 18 (2002) R99.

- [217] M. Buettner, A. Ramirez, W. Daily, Electrical resistance tomography for imaging concrete structures, Structural Materials Technology and NDT Conference San Diego, CA, 1996, pp. 8.
- [218] M. Buettner, A. Ramirez, W. Daily, Electrical resistance tomography for imaging the spatial distribution of moisture in pavement section, Structural Materials Technology and NDT Conference San Diego, CA, 1996, pp. 8.
- [219] T.C. Hou, K.J. Loh, J.P. Lynch, Spatial conductivity mapping of carbon nanotube composite thin films by electrical impedance tomography for sensing applications, Nanotechnology, 18 (2007) 315501.
- [220] K. Karhunen, A. Seppänen, A. Lehtikoinen, P.J.M. Monteiro, J.P. Kaipio, Electrical Resistance Tomography imaging of concrete, Cement and Concrete Research, 40 (2010) 137-145.
- [221] K. Karhunen, A. Seppänen, A. Lehtikoinen, J. Blunt, J.P. Kaipio, P.J.M. Monteiro, Electrical resistance tomography for assessment of cracks in concrete, ACI Materials Journal, 107-M60 (2010) 523-531.
- [222] M. Hallaji, M. Pour-Ghaz, A new sensing skin for qualitative damage detection in concrete elements: Rapid difference imaging with electrical resistance tomography, NDT & E International, 68 (2014) 13-21.
- [223] M. Hallaji, A. Seppänen, M. Pour-Ghaz, Electrical impedance tomography-based sensing skin for quantitative imaging of damage in concrete, Smart Materials and Structures, 23 (2014) 085001.
- [224] M. Hallaji, A. Seppänen, M. Pour-Ghaz, Electrical resistance tomography to monitor unsaturated moisture flow in cementitious materials, Cement and Concrete Research, 69 (2015) 10-18.
- [225] D. Smyl, R. Rashetnia, A. Seppänen, M. Pour-Ghaz, Can Electrical Resistance Tomography be used for imaging unsaturated moisture flow in cement-based materials with discrete cracks?, Cement and Concrete Research, 91 (2017) 61-72.
- [226] K.J. Loh, T.C. Hou, J.P. Lynch, N.A. Kotov, Carbon Nanotube Sensing Skins for Spatial Strain and Impact Damage Identification, Journal of Nondestructive Evaluation, 28 (2009) 9-25.
- [227] A. Andy, R.B.L. William, Uses and abuses of EIDORS: an extensible software base for EIT, Physiological Measurement, 27 (2006) S25.

- [228] P. Nick, R.B.L. William, A Matlab toolkit for three-dimensional electrical impedance tomography: a contribution to the Electrical Impedance and Diffuse Optical Reconstruction Software project, *Measurement Science and Technology*, 13 (2002) 1871.
- [229] O. Luppi Silva, R. Gonzalez Lima, T. Castro Martins, F. Silva de Moura, R. Seiji Tavares, M. Sales Guerra Tsuzuki, Influence of current injection pattern and electric potential measurement strategies in electrical impedance tomography, *Control Engineering Practice*, 58 (2017) 276-286.
- [230] B.M. Graham, A. Adler, Objective selection of hyperparameter for EIT, *Physiological Measurement*, 27 (2006) S65.
- [231] S. Jin Keun, L. Jeehyun, K. Sung Wan, Z. Habib, W. Eung Je, Frequency-difference electrical impedance tomography (fdEIT): algorithm development and feasibility study, *Physiological Measurement*, 29 (2008) 929.
- [232] H. Griffiths, A. Ahmed, A dual-frequency applied potential tomography technique: computer simulations, *Clinical Physics and Physiological Measurement*, 8 (1987) 103.
- [233] X. Li, M. Li, Effect of cracking and fracture on the electromechanical response of HPFRCC, 9th International Conference on Fracture Mechanics of Concrete and Concrete Structures, 2016.
- [234] K. Tuutti, Corrosion of steel in concrete, 1982.
- [235] D.D. Macdonald, M.C. McKubre, M. Urquidi-Macdonald, Theoretical assessment of AC impedance spectroscopy for detecting corrosion of rebar in reinforced concrete, *Corrosion*, 44 (1988) 2-7.
- [236] M.F. Montemor, A.M.P. Simoes, M.M. Salta, M.G.S. Ferreira, The assessment of the electrochemical behaviour of flyash-containing concrete by impedance spectroscopy, *Corrosion Science*, 35 (1993) 1571-1578.
- [237] P. Lay, P.F. Lawrence, N.J.M. Wilkins, D.E. Williams, An AC impedance study of steel in concrete, *Journal of Applied Electrochemistry*, 15 (1985) 755-766.
- [238] M. Sahmaran, V.C. Li, C. Andrade, Corrosion resistance performance of steel-reinforced engineered cementitious composite beams, *ACI Materials Journal*, 105 (2008) 243-250.
- [239] A.H.J. Al-Tayyib, M. Mesfer, A. Zahrani, Corrosion of steel reinforcement in polypropylene fiber reinforced concrete structures, *ACI Materials Journal*, 87 (1990) 108-113.

- [240] M. Olivia, H. Nikraz, Corrosion performance of embedded steel in fly ash geopolymer concrete by impressed voltage method, Proceedings of the 21st Australian Conference on the Mechanics of Structures and Materials, 2011.
- [241] M. Sahmaran, M. Li, V.C. Li, Transport properties of engineered cementitious composites under chloride exposure, ACI Materials Journal, 104 (2007) 604-611.
- [242] S. Miyazato, Y. Hiraishi, Transport properties and steel corrosion in ductile fiber reinforced cement composites, Proceedings of the Eleventh International Conference on Fracture, 2005, pp. 20-25.
- [243] Florida Department of Transportation, Manual of Florida Sampling and Testing Methods, An accelerated laboratory method for corrosion of reinforced concrete using impressed current, Tallahassee, FL, 2000, p. 6.